Cyclical Varying Pitch Propeller

Freiberg, Uffe Sjølund

Publication date:
2020

Document Version
Publisher's PDF, also known as Version of record

CYCLICAL VARYING PITCH PROPELLER

BY
UFFE SJØLUND FREIBERG

DISSERTATION SUBMITTED 2020

AALBORG UNIVERSITY
DENMARK

Cyclical Varying Pitch Propeller

Ph.D. Dissertation

Uffe Sjølund Freiberg

Dissertation submitted June 14, 2020

Dissertation submitted: June 14, 2020

PhD supervisor: Prof. Torben Ole Andersen
Aalborg University, Aalborg, Denmark

Company PhD supervisor: Senior Engineer. Jens Ring Nielsen
MAN Energy Solutions, Frederikshavn, Denmark

PhD committee: Associate professor Thomas Condra (chair)
Aalborg University

Associate professor Poul Andersen
Technical University of Denmark

Dr. Sc. TECHN Dirk Büche
MAN Energy Solutioins

PhD Series: Faculty of Engineering and Science, Aalborg University

Department: Department of Energy Technology

ISSN (online): 2446-1636
ISBN (online): 978-87-7210-541-3

Published by:
Aalborg University Press
Langagervej 2
DK – 9220 Aalborg Ø
Phone: +45 99407140
aauf@forlag.aau.dk
forlag.aau.dk

Printed in Denmark by Rosendahls, 2020

Preface

This dissertation has been submitted to the Faculty of Engineering and Science at Aalborg University in partial fulfilment of the requirements for the degree of Doctor of Philosophy, as a monograph. The work has been carried out at MAN Energy Solutions and the Institute of Energy Technology at Aalborg University. The project has been funded by Innovationsfonden (Grant No. 5016-0017B) and MAN Energy Solutions.

I would like to thank my supervisor Torben Ole Andersen at Aalborg University for the opportunity of doing this research and for the many interesting discussions. Furthermore, I would like to thank my supervisor at MAN Energy Solutions Jens Ring Nielsen for always being available with his expertise within ship propulsion. Also, I would like to thank my co-supervisors Kurt Plough and Steffen Martin Jacobsen from MAN Energy Solutions and Brian Thomsen from MARTEC for contributing with their expertise.

In addition I would like to thank my colleagues at MAN Energy Solutions for many enjoyable hours discussing both on and off-topics and for always being helpful. Furthermore, I would also like to thank my colleagues at Aalborg University. In particular the ones I've had the pleasure of sharing an office with through the years, Niels Henrik Pedersen, Remzija Ćerimagić, Jeppe Haals Christensen and Esben Bach-Sørensen.

I would like to express my gratitude towards "Den Dansk Maritime Fond" for their financial support for the experimental work conducted during my research (Grant Nos. 2016-048 and 2017-094). Without their support it would not have been possible to realise the project. Through this funding a model scale wake pitching propeller has been designed, constructed and tested. I would also like to thank FORCE Technology for being flexible and helpful with their expertise during the testing of the propeller.

Finally, I would like to thank my family for their support and patience through the last four years.

Uffe Sjølund Freiberg

Abstract

The cyclical varying pitch (CVP) propeller is a propeller which pitches the propeller blades cyclically. This is to compensate for the non-uniform wake field that the propeller operates in behind the ship hull. Conventional propellers on the market today are either a fixed pitch (FP) propeller or a controllable pitch (CP) propeller. Common for both of these propellers is that the blades pitch cannot be adapted in a cyclical manner. The CVP propeller is not available on the market today, but it has the potential to improve the performance of the propeller with respect to efficiency, shaft vibrations, cavitation, pressure pulses and noise.

Through a state-of-art review four challenges, in realising the CVP propeller, are identified. These challenges are: how to design the optimum propeller blades for the CVP propeller, how to determine the optimum pitch trajectory for the CVP propeller blades, how to design the cyclical pitch mechanism and how to ensure the reliability of the CVP propeller. These different challenges are, to some degree, coupled with each other. For example the design of the propeller blades is a trade-off between the propeller efficiency and the cavitation extent. This trade-off depends on the cyclical pitch trajectory and the power consumption for the cyclical pitch mechanism. In this dissertation some of the problems associated with the identified challenges are addressed.

One of the problems addressed in this dissertation is how to determine the required power and torque to pitch the propeller blades according to a desired pitch trajectory. This is in order to be able to account for the power consumption of the cyclical pitch mechanism in the design of the CVP propeller and make requirements for the cyclical pitch mechanism. This is addressed by making a model which is able to determine the forces and torques acting on the propeller blades during the cyclical pitching. The model established is applied to a CVP propeller case previously considered in another study. Two different pitch trajectories are investigated and compared to the propeller blades being fixed. Using the model no gain in the propulsion efficiency is obtained because the blade geometry is the same for each of the pitch trajectories. Furthermore, it was found that the pitch trajectory, which

should minimise the variation in the blade thrust, increases the variations instead.

Another problem addressed in this dissertation is how to determine the optimum pitch trajectory for the CVP propeller. The optimum pitch trajectory investigated in this dissertation is the pitch trajectory which minimises the variation in the hydrodynamical forces and torques acting on the propeller blades when the propeller geometry and operating conditions are known. Ideally, the efficiency, cavitation, etc. should also be included when determining the optimum pitch trajectory but they are not, because of the limitations in the model established. Using the model established in an iterative manner to determine the optimum pitch trajectory, is computationally expensive and therefore four alternative models are proposed. These models require fewer computational resources to evaluate and are therefore more suitable for determining the optimum pitch trajectory. Each of the models has their own pros and cons, but the most appropriate models are used to determine a series of optimum pitch trajectories. The validation of these optimum pitch trajectories is to be made in the future.

Experimental open-water and self-propulsion tests are made with a CVP propeller and a CP propeller to compare the relative difference between the two propellers. The experiments are made in model scale to reduce the financial costs. The test setup used for the experiments was designed and fabricated for this project. There were two purposes for making the experiments. One was to validate the performance improvement of the CVP propeller experimentally. The results showed an improvement in the efficiency, but the improvement was generally not large enough to be outside the uncertainty bounds of the experiments. The other purpose of the experiments was to get experimental data which could be used to validate the model established for the CVP propeller. The reliability of the experimental results was not good enough to be able to validate the different model components for the CVP propeller. This has to be addressed in the future.

Resumé

En "cyclical varying pitch" (CVP) propeller er en skibspropel, hvor stigningen på propellens blade kan ændres cyklisk. Dette bruges til at kompensere for det ikke-ensartede medstrømningsfelt, som propellen opererer i bag skibsskroget. De konventionelle propeller på markedet i dag er enten en "fixed pitch" (FP) propeller eller en "controllable pitch" (CP) propeller. Fælles for disse propellere er, at bladstigningen ikke kan tilpasses cyklisk. CVP propellen er ikke tilgængelig på markedet i dag, men den har potentiale til at forbedre ydelsen af propellen med hensyn til effektivitet, akselvibrationer, kavitation, trykimpulser og støj.

Gennem en "state-of-the-art" analyse identificeres fire udfordringer for at kunne realisere CVP propellen. Disse udfordringer er: hvordan designes de optimale propelblade til CVP propellen, hvordan bestemmes det optimale cykliske stigningsforløb for CVP propelbladene, hvordan designes den cykliske stigningsmekanisme, og hvordan sikres pålideligheden af CVP propellen. Disse udfordringer er til dels koblet med hinanden. Eksempelvis, så er designet af propelbladene en afvejning mellem propellens effektivitet og dens kavitation. Denne afvejning afhænger af det cykliske stigningsforløb og effektforbruget for den cykliske stigningsmekanisme. I denne afhandling adresseres nogle af problemerne for de identificerede udfordringer.

Et af problemerne adresseret i denne afhandling er, hvordan bestemmes den krævede effekt og moment, der skal bruges på, at propelbladene følger det ønskede stigningsforløb. Dette er for at kunne redegøre for effektforbruget af den cykliske stigningsmekanisme i designet af CVP propelbladene og for at kunne opstille krav til den cykliske stigningsmekanisme. Dette løses ved at lave en model, der er i stand til at bestemme kræfterne og momenterne, der påvirker propelbladene under det cykliske stigningsforløb. Modellen anvendes på et casestudie af en CVP propel, der tidligere er blevet undersøgt i et andet studie. Heri undersøges to forskellige stigningsforløb som sammenlignes med fikserede propelbladene. Ved anvendelse af modellen observeres der ingen forbedring i fremdrivningseffektiviteten, fordi bladgeometrien er den samme for hvert af de undersøgte stigningsforløb. Det findes endvidere,

at stigningsforløbet, som skulle minimere variationen i propelbladets fremdrivningskraft, i stedet for øger variationen.

Et andet problem adresseret i denne afhandling er, hvordan bestemmes det optimale stigningsforløb for CVP propellen. Det optimale stigningsforløb, der undersøges i denne afhandling, er det stigningsforløb, som minimerer variationerne i de hydrodynamiske kræfter og momenter, der påvirker propelbladene, når propelgeometrien og driftsbetingelserne er kendte. Ideelt set bør effektiviteten, kavitationen osv. også inkluderes, når det optimale stigningsforløb bestemmes, men det er det ikke på grund af begrænsningen i den etablerede model. At bruge modellen til at bestemme det optimale stigningsforløb iterativt er beregningsmæssigt tungt, og derfor foreslås fire alternative modeller. Disse modeller kræver færre ressourcer og er derfor mere egnede til at bestemme det optimale stigningsforløb. Modellerne har deres fordele og ulemper, men de bedst egnede modeller bruges til at bestemme en serie af optimale stigningsforløb. Valideringen af disse stigningsforløb skal foretages i fremtiden.

Eksperimentelle åbenvands- og selvfremdriftstests er udført med en CVP propel og en CP propel for at kunne sammenligne den relative forskel mellem de to propeller. Eksperimenterne er udført i modelskala for at reducere de økonomiske omkostninger. Opstillingen brugt til forsøgene er designet og fremstillet til dette projekt. Eksperimenterne har to formål. Det ene formål er at validere ydelsesforbedringen ved at bruge en CVP propel eksperimentielt. Resultaterne viser en forbedring i fremdrivningseffektiviteten, men forbedringen er ikke stor nok til at være udenfor usikkerhedsgrænsen for eksperimenterne. Det andet formål med eksperimenterne er at få eksperimentelle data, der kan bruges til at validere de etablerede modeller for CVP propellen. Pålideligheden af disse eksperimentelle resultater er ikke god nok til at kunne validere de forskellige elementer af modellen for CVP propellen. Dette skal addresseres i fremtiden.

Contents

Chapter 1

Introduction

"The maritime industry is seeking to decrease the costs of their operations. Especially, in the shipping industry which has experienced a decline in freight rates in recent years. The shipping industry is therefore seeking more energy efficient solutions to increase their profit [93]. Shipowners are not the only ones who are interested in improving the energy efficiency of their vessels. The international community is also interested in reducing the emission of greenhouse gases, due to global warming and other polluting gases and particles. The shipping industry was responsible for approximately 2.2% of the global CO_2 emission in 2012 [93]. The International Maritime Organization (IMO) has made the Energy Efficiency Design Index (EEDI) for new build ships and the Ship Energy Efficiency Management Plan (SEEMP) in order to make the shipping industry focus on energy efficient solutions" [31][1].

"The EEDI is a measure of the CO_2 emission to the transported cargo in gram CO_2 per ton mile $[{}^{gCO_2}/_{ton\ mile}]$. A low EEDI is equivalent to a high energy efficiency of the vessel and a high EEDI is equivalent to low energy efficiency of the vessel" [31]. The EEDI requirements for bulk carriers, tankers and container ships are shown in Figure 1.1. From Figure 1.1 it is seen that the EEDI requirements for new build ships will become more strict in the future. "For example a new build container carrier with 100,000 DWT built before 2015 may emit $\approx$ 15 $[^{gCO_2}$ / *ton mile*$]$, a container carrier built after 2025 may only emit $\approx$ 10 $[^{gCO_2}$ / *ton mile*$]$" [31]. In order to fulfil the EEDI requirements it is necessary to focus on improving the energy efficiency of the ship propulsion for new built ships.

"Decreasing the EEDI of a vessel also leads to a reduction of emission gases such as NO_x, SO_x and particles. New emission limits are continuously being introduced for the emission of NO_x and SO_x gasses" [31].

[1]The paper [31] is cited throughout the introduction in order to avoid self-plagiarism.

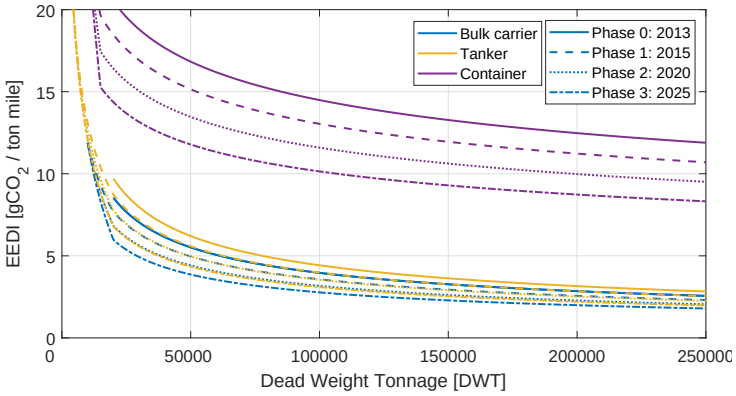

Figure 1.1: EEDI reference line for bulk carrier, tanker and container made from the data in [41]. The different phases shows the year for which the EEDI requirements are valid for new vessels.

"Reducing the EEDI of a vessel can be accomplished by many means, like changing the fuel, more efficient engine, more efficient hull design and more efficient propulsor" [31]. In this project the focus will be on the propulsor of the ship.

1.1 Propulsors

Propellers have been used for ship propulsion for many decades. Over the years the propeller design has continuously developed and it is still in a process of development to this day. A number of the different kinds of propellers has been developed over the years: see Figure 1.2. Many different forms of propulsion technologies have been developed: Figure 1.2 shows just a selection of some of these.

The fixed pitch (FP) propeller, shown in Figure 1.2a, and the controllable pitch (CP) propeller in Figure 1.2b are the two fundamental propeller types. The propellers are usually uniquely designed for each vessel or vessel series. The FP propeller has the largest market share of the two, but the CP propeller has gained a larger part of the market over the last couple of decades [20]. The other propulsion technologies such as the ducted, azimuth, podded and contra rotating propellers use either a FP or a CP propeller. The FP propeller can be made in one piece as shown in Figure 1.2a. Alternatively, the FP propeller can be made with detachable blades for replacement in case of damage, or a change in the desired operation of the propeller. The CP propeller incorporates a mechanism which enables a change in the pitch of all the blades simultaneously during the operation of the ship and this gives a better manoeuvrability compared to a FP propeller. The thrust of a CP propeller can be controlled by pitching the propeller blades, whereas the thrust from a FP

(a) Fixed Pitch Propeller [67].

(b) Controllable Pitch Propeller [67].

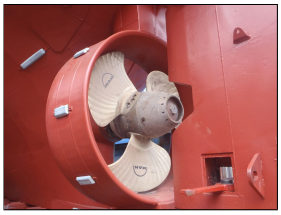

(c) Ducted propeller [67].

(d) Azimuth/Podded Propeller [11].

(e) Contra-rotating propeller [48].

(f) Paddle-Wheel [95].

(g) Cycloidal propeller also called a Voith-Schneider Propeller [91].

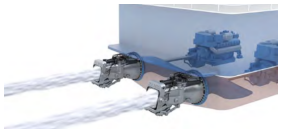

(h) Waterjet [78].

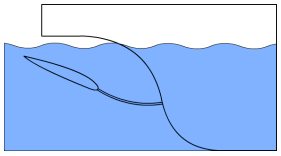

(i) Oscillating foil or animal inspired propulsion [61].

Figure 1.2: Different propulsion technologies for driving marine vessels.

propeller is changed by changing the rotational speed of the shaft. Therefore the thrust response of the FP propeller has a larger time constant due to the inertia of the shaft and motor. This is especially disadvantageous when stopping the ship or in a reversing manoeuvre. With the CP propeller it is possible to have a constant shaft speed whilst controlling the thrust from the propeller by pitching the blades. This is an advantage when the propulsion shaft drives a generator whereby a constant shaft speed can be maintained with the CP propeller while still being able to manoeuvre the ship. The FP propeller usually has a slightly better efficiency than the CP propeller. This is due to the ratio between the hub diameter and the propeller diameter for the FP propeller is lower than the ratio for the CP propeller [20]. The bigger the ratio, the lower the efficiency. The hub of the CP propeller is usually bigger because it contains the mechanism for changing the pitch.

The ducted propeller in Figure 1.2c, the azimuth/podded propeller in Figure 1.2d and the contra-rotating propeller in Figure 1.2e all consist of either a FP or a CP propeller. Ducts are used to either accelerate, deaccelerate

or smoothen the inflow into the propeller [20]. This makes it possible to increase the bollard pull or to design more efficient propellers. The difference between an azimuth and podded propeller is in the location of the motor. For azimuth propellers the motor is inside the ship hull and for the podded propeller the electrical motor is placed in the propeller pod itself [20]. The azimuth/podded propellers have the advantage that they give a better manoeuvrability of the ship compared to the more conventional solutions. The contra-rotating propeller comprises of two propellers, each rotating in the opposite direction of each other and thereby helping to balance the torque. The aft propeller recovers some of the rotational energy from the ahead propeller [20] thereby increasing the efficiency. Similar propeller concepts such as the overlapping and tandem propellers can be found in [20].

The other propulsors; the paddle wheel in Figure 1.2f, the cycloidal propeller in Figure 1.2g, the animal inspired oscillating foil Figure 1.2i and the waterjet propulsor in Figure 1.2h are all alternative propulsors to the conventional FP and CP propellers. The paddle wheel does not see much application anymore and is therefore not discussed further. The cycloidal propeller is a vertical propeller placed on the hull bottom and can provide a high manoeuvrability by controlling the cycloidal variation in the pitch. The waterjet propulsor uses a pump to increase the momentum of the incoming water before it is discharged aft ship. The change in momentum creates the thrust. The animal inspired oscillating foil propulsor is still under research and has not found commercial application.

The typical performance criteria used to evaluate the performance of a propeller are:

- Thrust
  - The propeller should satisfy the thrust requirement for the ship to move at the required speed by overcoming the ship resistance.
- Efficiency
  - To minimise fuel consumption it is desired to maximise the efficiency of the propulsion system. This includes the motor, shaft line, propeller and hull.
- Shaft vibrations
  - Because the propeller operates in a non-uniform flow field (elaborated below) the forces and torques affecting the blades and the propeller varies with time. The mechanical parts of the propeller should therefore be designed such that they do not have the same natural frequency as the force/torque oscillation. The parts should also be dimensioned to avoid fatigue failure.

- Cavitation
  - The thrust of the propeller is generated by having a pressure difference over the propeller. The propeller blades are divided into a pressure side and a suction side. On the suction side, the pressure may become lower than the vapour pressure of the water and the water therefore changes phase from liquid to vapour. This is called cavitation. The performance of the propeller is degraded by cavitation and in some cases it results in erosion of the propeller. Erosion occurs when the vapour gets into a zone close to the blade surface with a pressure higher than the vapour pressure of the water, the vapour therefore collapses/implodes. This implosion close to the blade surface can destroy the blade and erode it.
- Pressure pulses
  - Because the propeller has a finite number of blades, the pressure towards the ship hull pulsates. This is because the pressure towards the ship hull is lower when there is a blade towards the hull and the pressure is higher when the blade has passed. The pressure therefore pulsates towards the ship hull and thereby induces vibrations throughout the ship.
- Noise
  - The primary sources of noise are cavitation, propeller singing and machinery, where cavitation induced noise is usually the dominant source [77]. Propeller singing is due to vortex shedding resonances with the natural frequency of the blade.
  - "Requirements for the noise depends on the ship type. For merchant ships there are requirements for the noise due to the work environment of the crew and guidelines have been made by IMO [21]. For cruise ships and ferries it is desired to minimise the noise to ensure a more comfortable trip for the passengers. Research ships have requirements for the noise to minimise the influence on the measurement devices on board the ship. Naval ships and submarines want to minimise the noise to make it harder to detect the vessel by sonars etc." [31].
  - "It is believed that the noise from ships also influences the life of marine mammals. IMO has therefore issued guidelines for the noise emission to reduce the impact on the life of marine mammals [42]" [31].

- Reliability
  - "Reliability of a propeller is a major concern for the owner of the vessel. If the propeller is unreliable, the vessel has to be docked more often and the probability of unexpected breakdowns increases. Docking a vessel is expensive and an unexpected breakdown and following docking means that the vessels cannot be in operation. Taking the vessel out of operation means that the owner cannot create a revenue with the vessel in this period and has to cancel contracts on planned work. The FP propeller is normally considered to be more reliable than a CP propeller. The CP propeller contains more parts which can break and it has a number of parts which moves relative to each other. This introduces wear which over time can make the propeller break down" [31].

The above performance parameters for the propeller depends on the propeller design, the ship hull and the operating conditions for the vessel. "The operating conditions of the ship and the ship hull design influences the flow into the propeller because the propeller operates behind the ship hull i.e. in the wake of the ship. The flow field in which the propeller operates is called the wake field. An example of the wake field for a single screw ship is shown in Figure 1.3 as the velocity ratio between the local axial velocity (v_a) of the wake field and the ship speed (V_s). A larger ratio equals a higher axial velocity and a lower ratio equals a lower axial velocity" [31].

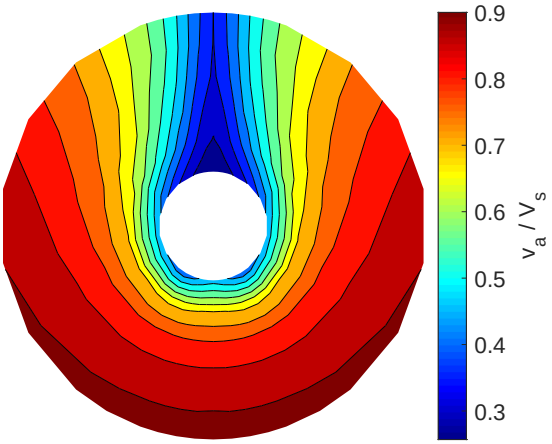

Figure 1.3: Wake field for a single screw ship. The clear center is where the propeller hub is located.

The velocity distribution in a ship's wake field is typically non-uniform as shown in Figure 1.3. The wake field shown in Figure 1.3 is for a single screw ship and these wake fields are usually symmetric about the 12, 6 o'clock axis. Ships with twin screw propellers do not have symmetric wake fields and they usually have smaller velocity variations in the wake field. Because of the velocity variations in the wake field, the flow conditions around each propeller blades varies cyclically as the propeller rotates. The varying flow conditions results in shaft vibrations and transient cavitation. The transient cavitation typically occurs when the blade is in the wake peak (12 o'clock position in the wake field in Figure 1.3).

The design engineer has to consider the propeller thrust, efficiency, vibrations, pressure pulses and cavitation when designing the propeller blades. The thrust that the propeller should be able to generate is typically specified beforehand by the operating conditions of the ship. The thrust should be large enough to maintain the desired ship speed. While satisfying the requirement for the propeller thrust the designer should optimise the propeller with respect to the efficiency. The obtainable efficiency is typically a trade-off with the cavitation and vibrational performance of the propeller. To understand this trade-off, it is necessary to understand the fundamentals of the hydrodynamics of propellers which there is given a short introduction to in the following. For more details about the hydrodynamics of ship propellers the reader is referred to [21,56].

A conventional propeller blade is a cascade of foils of different sizes and alignments relative to each other as shown in Figure 1.4. The left hand side of Figure 1.4 shows the expanded view of the foil's shape over the span of the propeller blade. The right hand side of Figure 1.4 shows the foils projected onto concentric cylindrical surfaces with their center in the propeller shaft. This projection of the foils is usually used for propeller blades. An example

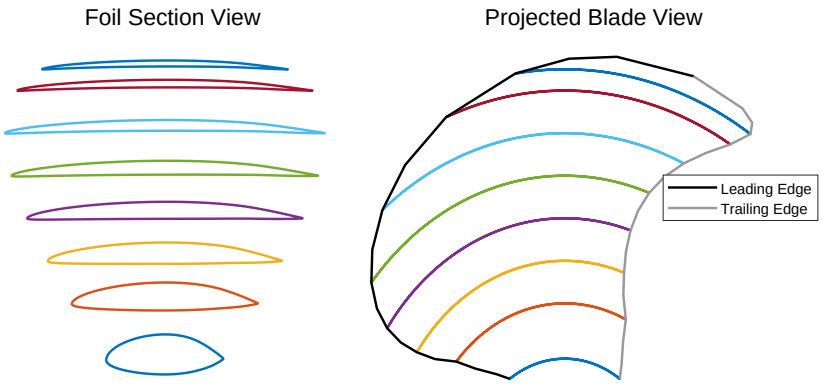

Figure 1.4: Cascade of foils which forms a propeller blade.

of a foil that could be used for a propeller blade is shown in Figure 1.5. There are a number of different standard foils which can be used to form the propeller blade. One of these is the well known NACA series developed by the National Advisory Committee for Aeronautics (NACA), later renamed to National Aeronautics and Space Administration (NASA). The choice of foil shape depends on the desired performance characteristics but the common shapes used for marine propellers are the NACA16-series and NACA6-series. The alignment of the foils relative to each other is described by the three

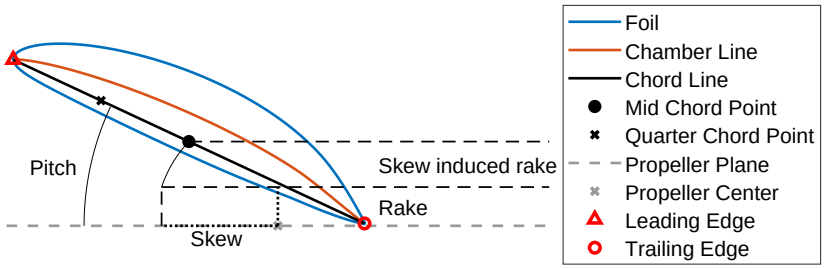

Figure 1.5: NACA 16 foil.

parameters, skew, rake and pitch, as shown in Figure 1.5. The size of the foil is described by the three parameters, chord, camber and thickness. All six of these parameters vary with the radial position of the foil segment in order to form the blade. The design problem for a propeller blade is to determine the radial distribution of these six parameters in order to satisfy the performance criteria of the propeller.

The loads acting on a propeller blade are due to pressure and viscous effects acting on the blade due to the relative motion between the blade and the fluid. Considering a 2D foil section of a blade (Figure 1.6a), the loading per unit span is determined as [21]:

$$F_L = \frac{1}{2}\,\rho\, c\, C_L\left(\alpha_a\right)\, v_r^2 \tag{1.1}$$

$$F_D = \frac{1}{2}\,\rho\, c\, C_D\left(\alpha_a\right)\, v_r^2 \tag{1.2}$$

$$M_p = \frac{1}{2}\,\rho\, c^2\, C_M\left(\alpha_a\right)\, v_r^2 \tag{1.3}$$

F_L is the lift force per unit span which is acting perpendicularly to the resulting velocity vector, see Figure 1.6a. F_D is the drag force per unit span which is acting parallel to the resulting velocity vector. M_p is the pitching torque about the aerodynamic center located at a quarter chord length from the leading edge. c is the chord length of the foil. ρ is the density of the fluid. v_r is the resulting velocity and is a result of the local axial velocity v_a due to the ship's advance in the water and the velocity due to the rotation of

the blade segment $\omega_p\, r$. C_L, C_D and C_M are the lift, drag and pitch-moment coefficient respectively, which depend on the angle of attack, α_a. An example of these coefficients dependency on the angle of attack is shown in Figure 1.6b. α_a is the angle between the incoming fluid velocity and the chord line of the foil. β is the advance angle of the incoming fluid and α_p is the pitch angle of the foil. To determine the thrust from the propeller blade and the

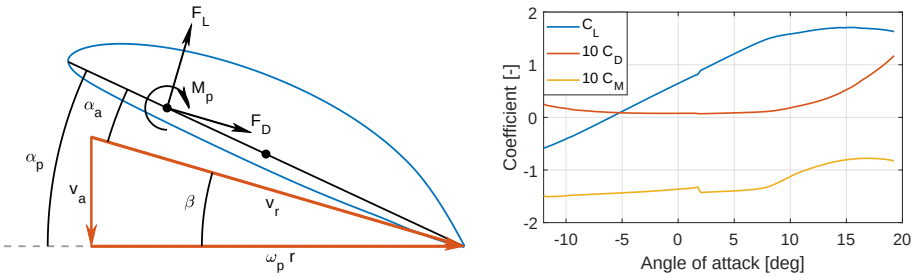

Figure 1.6: (a) Flow condition about foil section of the propeller blade. **(b)** Lift, drag and pitch-moment coefficient for NACA6412 [12].

blade's contribution to the shaft torque, the forces have to be projected onto the appropriate axis and integrated over the radius as:

$$T = \int_{r_{hub}}^{r_p} F_L(r)\, \cos\left(\beta(r)\right) - F_D(r)\, \sin\left(\beta(r)\right) dr \tag{1.4}$$

$$Q = \int_{r_{hub}}^{r_p} \left(F_L(r)\, \sin\left(\beta(r)\right) + F_D(r)\, \cos\left(\beta(r)\right)\right) r\, dr \tag{1.5}$$

T is the blade thrust. Q is the blade's contribution to the shaft torque. To determine the propeller thrust and torque, the contribution for each blade should be added together. r_{hub} and r_p are the radius of the hub and propeller, respectively. r is the radial integration variable.

The above approach is called the blade element theory and describes the general principle for the propeller, but as it is stated, it does not account for the induced velocities which are important when it comes to propellers. The induced velocities are generated due to the spanwise lift distribution along the blade and the finite span which are commonly accounted for using the lifting line theory. To determine the induced velocities, it is necessary to introduce the Kutta-Joukowski theorem which describes the relationship between lift force and circulation. The Kutta-Joukowski theorem is stated as [21]:

$$F_L = \rho\, v_r\, \Gamma \tag{1.6}$$

Γ is the circulation around the foil. The principle of the lifting line theory is to replace the cascade of foils with a line vortex, whose strength varies along its span. This is illustrated in Figure 1.7. The strength of the line vortex is called the bound circulation Γ_b. There is also a free circulation Γ_f which is shed from the blade into the blade's wake due to the bound circulation varying along its span and that circulation is conserved which is stated in Kelvin's theorem. The Kutta-Joukowski and Kelvin's theorems assume an inviscous fluid. The presence of the circulation shown in Figure 1.7 induces

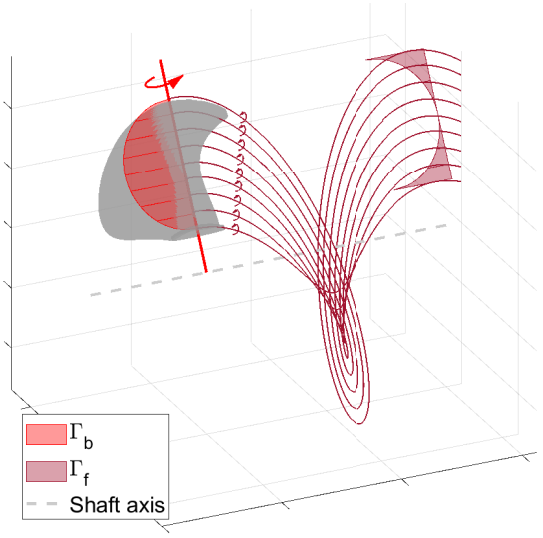

Figure 1.7: Principle of lifting line theory.

velocities in the fluid. The induced velocity at a point from a line segment with a circulation Γ can be determined using the Biot-Savart law as [21]:

$$d\mathbf{v}_i = \frac{\Gamma}{4\,\pi}\,\frac{d\mathbf{l}\times\mathbf{r}}{|\mathbf{r}|^3} \tag{1.7}$$

$\mathbf{v}_i$ is the induced velocity vector. $\mathbf{l}$ is the line segment vector and $\mathbf{r}$ is the distance vector from the line segment to the point. To calculate the collective induced velocity, all the bounded and free circulations have to be considered. This means that each blade influences the other blades.

The induced velocities change the velocity triangle shown in Figure 1.6a to that shown in Figure 1.8a. Instead of using the previous advance angle, β, to calculate the angle of attack, the hydrodynamic pitch angle, β_i is used instead. In Figure 1.8a an additional tangential velocity, v_t, has been added due to the propeller operating in the non-uniform wake field of the ship. The wake field shown in Figure 1.8b also includes the in-plane transverse velocities which

were previously omitted to simplify the explanation. The transverse velocities can be divided into a tangential and radial velocity component which vary with time due to the propeller's rotation. The advance velocity varies radially

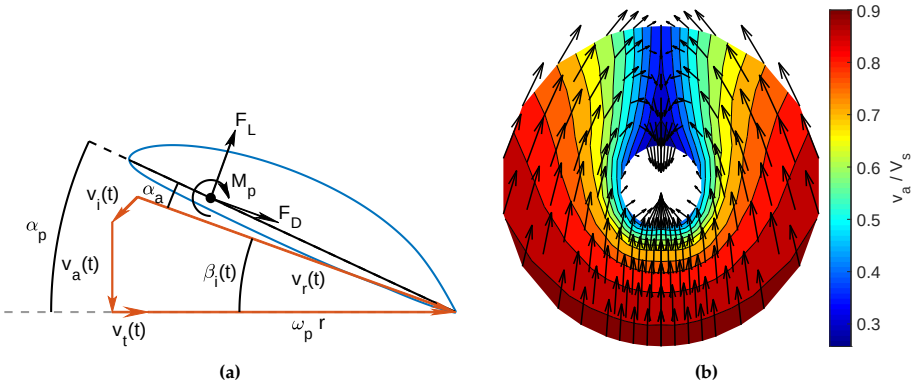

Figure 1.8: (a) Velocity triangle acting on a foil including the induced velocities. **(b)** Wake field of a single screw ship.

and circumferentially which makes the advance velocity for each foil segment vary with time as the propeller rotates. The advance velocity is lowest in the wake peak. The lower advance velocity gives a large angle of attack and the lift and drag force on the foil therefore increase in the wake peak.

As previously discussed, then the performance of the propeller is a trade-off between the efficiency, the cavitation and the vibrational performance of the propeller. For example if the propeller cavitates too much, then the engineer can decrease the pitch or the camber of the blade. By decreasing the pitch or camber, the blade is not as heavily loaded, but this also decreases the thrust of the propeller. To compensate for this decrease the chord, has to be increased which, in turn, increases the area of the propeller blades and this results in an increase in the viscous drag on the propeller, and this reduces the efficiency of the propeller. The engineer can also add skew to the blade in order to reduce the vibration and change the transient cavitation. The skew makes the different sections of the blade enter and exit the wake peak at different times and this smoothens the effect of the wake peak on the propeller blade's performance.

The efficiency of a propeller may be improved by using energy saving devices. Some of these energy saving devices are presented in Figure 1.9 with their potential energy savings [65, 72]. The propeller and the energy saving devices interact with each other which typically results in them being designed at the same time. The aim for most of the energy saving devices is to reduce the rotational energy shed into the fluid or to recover some of it. Transferring rotational energy to the fluid does not contribute to the

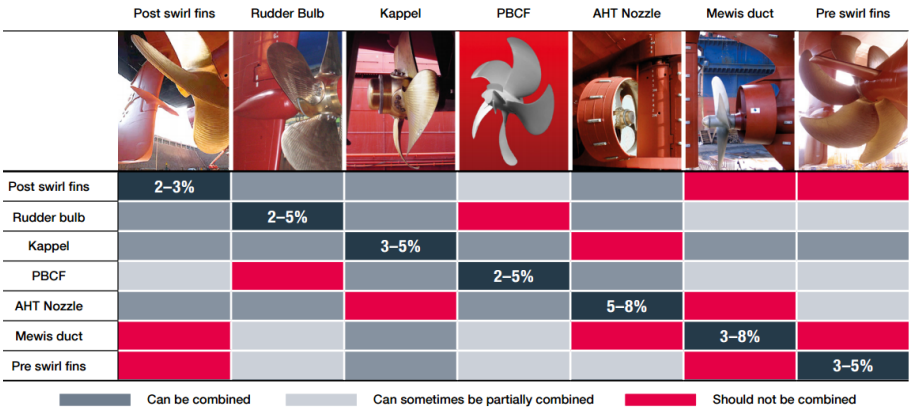

Figure 1.9: Energy saving devices and their potential efficiency gain and the combination possibilities from [65].

propulsion of the ship. The rotational energy shed into the fluid has different sources which means that different concepts may be combined and others not. The concepts that cannot be combined regain the same source for the rotational energy.

The post-swirl fins, pre-swirl fins and Mewis duct affect the flow conditions for the propeller which can contribute to less rotational energy being shed into the fluid. Improving the flow conditions for the propeller may make it possible to design a better performing propeller including the efficiency. The rudder bulb and the propeller boss cap fins (PBCF) reduce the rotational energy shed from the hub. The Kappel propeller blades and the nozzle both reduce the tip vortex from the propeller blades by which the rotational energy shed into the fluid is reduced. The duct can also be used to improve the flow condition around the propeller thereby making it possible to design more favourable blades for the propeller. Furthermore, with the duct it is also possible to get more thrust at lower ship speeds. A more detailed overview can be found in [10] showing the influence of the energy saving devices on the different energy sources.

1.2 Cyclical Varying Pitch Propeller Concept

"Common for both the FP and CP propeller is that they are not able to adapt to the local flow conditions in the wake field. This means that the angle of attack varies with the blade's position in the wake field, thus introducing some problems such as transient cavitation, increased pressure pulses, increased noise, lower efficiency, shaft vibrations and larger fatigue stresses for the propeller blades" [31].

A propeller which adjusts the pitch of the propeller blades individually to adapt to the flow conditions of the wake field is called a cyclical varying pitch (CVP) propeller. The CVP propeller should be able to reduce vibrations, pressure pulses, transient cavitation, fatigue stresses, noise etc. when compared to the FP or CP propeller. This should make it possible to design a CVP propeller which is more efficient than a FP or CP propeller. "The FP propeller may be more efficient than the CVP propeller if a significantly larger hub is required for the CVP propeller or more power is required to pitch the blades than is saved with the CVP propeller. The operational principle of the CVP propeller is shown in Figure 1.10 for a section of the propeller blade operating in a non-uniform wake field" [31].

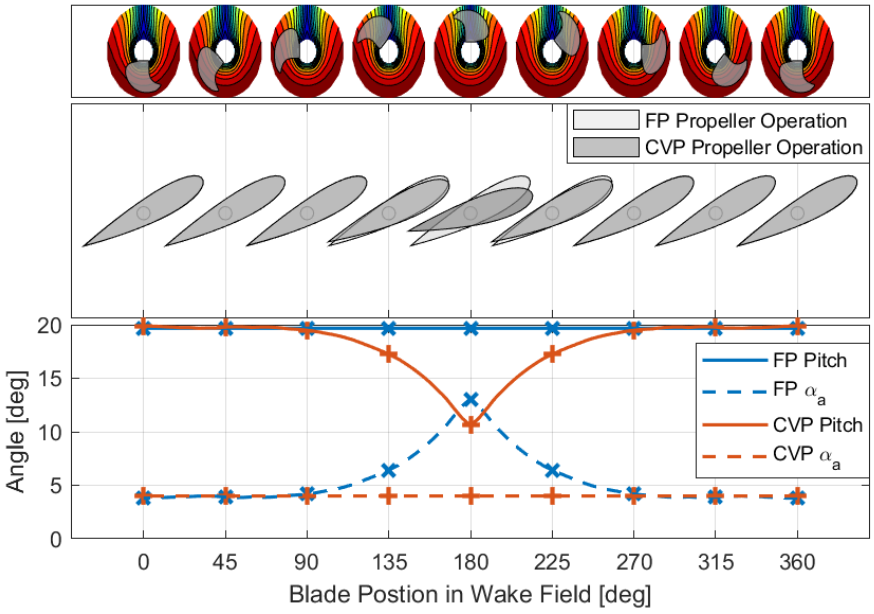

Figure 1.10: Illustration of the operational principle of the CVP propeller. [31]

"Figure 1.10 is divided into three figures. The top figure shows the wake field of the ship and the position of blade in the wake field. The middle figure shows the pitch motion of a foil section of the propeller blade for both the FP and CVP propeller. The foil section of the FP propeller blade is fixed during one revolution of the propeller. The foil section of the CVP propeller blade is changing with the blade's position in the wake field. The pitch of the foil section for the CVP propeller decreases as the blade comes closer to the wake peak (shown in the center of the figure) and increases after having passed the wake peak. This operation for the CVP propeller is repeated for each revolution of the propeller. The bottom figure shows the pitch angle and the

angle of attack for the foil sections as the propeller rotates in the wake field. It is seen that the pitch of the FP propeller is fixed during a revolution and that the angle of attack varies" [31][1]. If the angle of attack varies significantly then transient cavitation can occur. "For the CVP propeller it is seen that the pitch angle changes and the angle of attack is therefore kept constant. This eliminates the issue with transient cavitation, vibrations, etc. The pitch trajectory for the CVP propeller, shown in Figure 1.10, is the pitch trajectory which makes the angle of attack constant for that section of the blade. This pitch trajectory may not be the same for all the sections of the blade and the optimum pitch trajectory is therefore a trade-off of the performance for all the sections of the propeller blade" [31].

With the principle of the CVP propeller accounted for and its potential to improve the performance of the propeller, the hypothesis for this dissertation is stated as:

Can the CVP propeller be realised to improve the performance of the propeller?

1.3 Review of Cyclical Varying Pitch Propeller Concept

"The idea of a CVP propeller is not new and the idea of cyclical varying pitch is already utilized in other applications. The cyclical varying pitch is already utilized in helicopters, wind turbines and small automated underwater vehicles/submarines (AUV) [73]. For the shipping industry no commercially available CVP propeller has been found which is able to pitch the blades individually. However, the CVP propeller has been researched as a potential propulsion for the shipping industry, where different designs have been proposed through the years" [31]. The proposed designs are divided into four types as:

- Thrust balanced propeller
- Swash plate propeller
- Passively controlled individual pitch propeller
- Actively controlled individual pitch propeller

"Besides the above four types of CVP propellers, there is also the flexible blade propeller. The flexible blade propeller differs from the four above types of CVP propellers by that the blade deforms to adapt to the local flow condition, where the other CVP propellers pitches the whole blade" [31]. In this dissertation the focus is on the CVP propeller where the whole propeller blade pitches. The flexible blade propeller is not considered further, but for the interested reader reviews of the propeller can be found in [1–3, 5, 7, 9].

1.3.1 Thrust Balance Propeller

"The thrust balance (TB) propeller is a propeller with an even number of blades and it has been proposed and/or discussed in [25, 75, 76, 80, 88]. The designs of the TB propeller proposed in [25, 75, 76, 80, 88] are all similar to each other. An example of the design of a four bladed TB propeller is shown in Figure 1.11. The blades opposite each other are connected through the hub by a shaft and the blades are designed such that the center of pressure is placed between the blade's spindle axes and its trailing edge. The spindle torque of the blade should therefore always tend to decrease the pitch of the blade" [31].

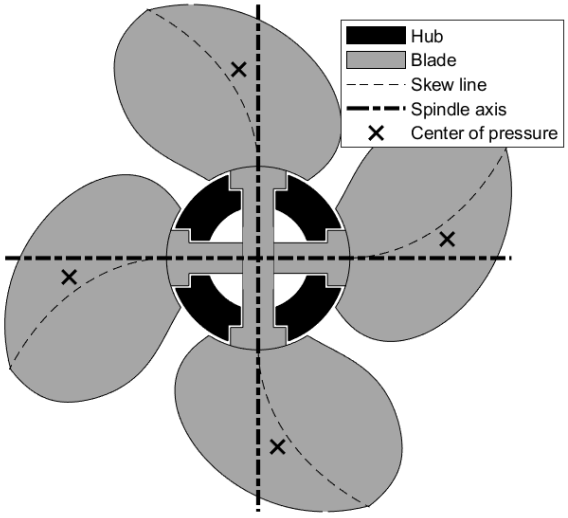

Figure 1.11: Sketch of a trust balance propeller. The propeller is seen from aft of the ship and rotates clockwise. [31]

"Due to the local velocity variations in the wake field the thrust acting on each blade varies with its position in the wake field. The thrust will have a minimum in the bottom half of the wake field and will increase as the blade moves towards the wake peak where the thrust is at a maximum" [31].

"The difference in the thrust on each blade pair results in a torque inequality on the blade pair assembly. This torque inequality will reduce the pitch of the blade in the upper part of the wake field and increase the pitch of the blade in the lower part of the wake field. This reduces the torque inequality of the blade pair assembly until the torque affecting each blade has equalized" [31].

"The TB propellers in [25, 75, 80] are patents and only present the mechanical design of the TB propeller. Analysis and performance results are not presented in [25, 75, 80] but they postulate on some of the performance

improves of the TB propeller. In [25,80] it is postulated that the TB propeller can reduce ship vibration which includes both pressure pulses and shaft vibrations. No comment is given with respect to efficiency, cavitation, noise or reliability. In [75] it is postulated that the TB propeller can increase the propeller's efficiency, reduce shaft vibrations, cavitation, pressure pulses and noise. With respect to the reliability in [75] only the blade and shaft are considered. It is postulated in [75] that the blade's thickness and shaft diameter can be reduced due to the reduced load variations with the TB propeller. The patent in [75] also includes a locking mechanism for the blades which adds the possibility of controlling when the blades can make the cyclic pitching motion" [31].

"The study in [76] is a theoretical study of the feasibility and performance of the TB propeller. The feasibility study was made to determine whether the blade pitch is able to adapt to the non-uniform wake field to yield a performance improvement. The investigation is made by making a second-order dynamical model for the blade pitch motion. The model accounts for the moment of inertia of the blade, the variation in the centrifugal force due to the pitch displacement and the variation in the hydrodynamics due to the pitching motion using [81]. The friction in the blade bearing is neglected. The second-order system is excited by the variation in the hydrodynamical spindle torque which is based on measurements. The model is applied to a single propeller design. For this propeller design the maximum difference between the pitch and the hydrodynamic pitch is reduced by 38% during a revolution when using the TB propeller instead of a FP propeller. From these results [76] assumes that the propeller efficiency will increase. Furthermore, [76] expects the TB propeller to give an improvement in cavitation performance and that the TB propeller may improve the general vibration level on board the ship i.e. pressure pulses and shaft vibrations. No direct performance improvement, by using the TB propeller, is shown in [76], they are only inferred based on the reduced maximum variation in the difference between the pitch and the hydrodynamic pitch, i.e. the angle of attack" [31].

"In [88] the performance of the TB propeller proposed in [75] is evaluated. The performance assessment is made with a series of piecewise linear pitch trajectories with the same slope but different pitch offsets. The pitch trajectories are made such that the pitch decreases towards the wake peak and increases towards the bottom of the wake field. All the pitch trajectories have the same amplitude of 6°[2]. The performance of the TB propeller is compared to the same propeller with fixed blades (i.e. a FP propeller), where one of the pitch trajectories has the same mean pitch as the FP propeller. To evaluate the performance of the TB propeller, an unsteady lifting surface program is used. The program does not account for the cyclical pitch motion of the

[2]Amplitude is peak to peak difference

blade but does account for the unsteadiness of the non-uniform wake field. To evaluate the performance of the TB propeller a series of evaluations of the performance for FP propellers are made. The FP propellers are all geometric similar except for their pitch, which is displaced for each FP propeller to cover the range of the defined pitch trajectories. The performance evaluation of the TB propeller is made by interpolating the results for the different FP propellers performance using the pitch trajectories. Presentation of the results for the TB propeller mostly focuses on the pitch trajectory which has the same mean pitch as the FP propeller. For this pitch trajectory the efficiency is increased by 1.5%, the cavitation is slightly reduced in the wake peak, the pressure pulses are reduced by approx. 50% and the average transverse loads are reduced. Furthermore, the propeller thrust and torque are increased. No direct data is given with respect to shaft vibrations, noise or reliability" [31].

1.3.2 Swash Plate Propeller

"The swash plate propeller uses the same principle utilized in many helicopter rotors to manoeuvre the helicopter. In helicopters a swash plate is used to control the collective pitch and the cyclical pitch of the rotor blades. The collective pitch is the mean pitch for all the blades and the cyclical pitch is an overlying local pitch which depends on the blade's position in the rotor field. It is the cyclical pitch that makes the pilot able to steer the helicopter" [31].

"In marine propellers the concept of cyclical pitch has primarily been utilized in the cycloidal/Voith–Schneider propeller and for autonomous vehicle propulsion (AUV) [73]" [31]. The cycloidal/Voith–Schneider propeller is described in Section 1.1. "In AUVs the cyclic pitch is used to manoeuvre the ship/vehicle because the sailing speed is low which makes use of control surfaces such as rudders inefficient. The propeller is normally not used to adapt the pitch to the local velocities in the wake field due to the wake field being more uniform than for single screw ships see [36]" [31].

"Utilizing a swash plate propeller for ships is investigated in [84–86] and is called the pinnate propeller. The pinnate propeller is shown in Figure 1.12 and it connects the opposite blade to each other through the hub to minimise friction. To each blade pair two push-pull rods are attached which extend out and make contact with the swash plate. The swash plate is then angled relative to the propeller shaft in order to get the cyclical pitching of the propeller blades. Using this swash plate principle makes the pitch trajectory sinusoidal" [31].

"Propulsion and cavitation model tests with the pinnate propeller were made in [84] with the sinusoidal pitch trajectory with a minimum pitch 10° before the 12 o'clock position due to the phase shift between the pitch change and lift response. Depending on the amplitude (amplitude between $2^\circ - 5^\circ$

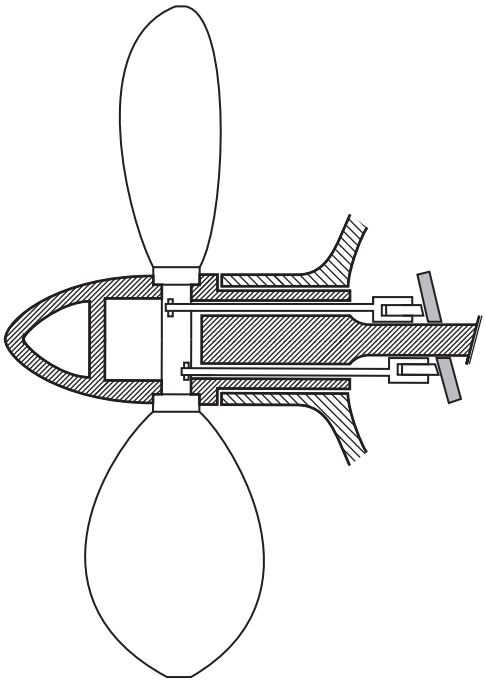

Figure 1.12: The pinnate propeller from [31].

with 1° increments) of the sinusoidal pitch trajectory either a small loss or a small gain was obtained with the pinnate propeller with respect to a FP propeller. The difference in efficiency was $-0.2\%, -1\%, 0.7\%$ and 0.6% for the different amplitudes which are within the uncertainties of the experiments [84]. The cavitation tests were made with an amplitude of 4.2° and under different operating conditions. For all of the operating conditions, the cavitation performances was improved in the wake peak but for some conditions the cavitation was more severe in the bottom of the wake field (6 o'clock position). During the cavitation test the pressure pulses were measured at four points on the ship hull. The pressure pulses were reduced by $30 - 45\%$ for all the points when using the pinnate propeller. The tests were made with a modified ship hull which improved the flow conditions for the pinnate propeller and reduced the resistance by 1%. Using the modified hull with the pinnate propeller yielded a 3.6% increase in efficiency compared to using the unmodified ship hull with a FP propeller" [31].

"The study in [85] includes the results from [84] and extends upon them experimentally and documents the theoretical considerations made during the study. The cavitation tests are extended with pitch trajectory with amplitudes of $4^\circ, 5.4^\circ, 5.4^\circ$ and 5.4° with a minimum pitch at $20^\circ, 0^\circ, 10^\circ$ and 20°

before the 12 o'clock position, respectively. The cavitation is reduced in the wake peak for all pitch trajectories but with more cavitation at the 6 o'clock position and face cavitation at the 9 o'clock position. For the load analysis, measurements of the hydrodynamical loads are used for the steady part and the dynamical part is model by the method in [81] with compensation for the low aspect ratio of the propeller blades" [31][1].

"The pinnate propeller was tested in full scale in [86] on a Swedish navy patrol boat. The boat has a length of 23 meters, a normal service speed of 24 knots and is equipped with twin screws on inclined shafts. The propellers are four bladed with a diameter of 0.88 meters. During the tests, the cavitation in the wake peak was observed and the pressure pulses were measured at four locations. The cavitation was generally reduced with the pinnate propeller and the speed for thrust breakdown due to cavitation was increased by 2 knots. A small increase in efficiency was obtained at high speeds due to the increased speed before thrust breakdown. The pressure pulses are generally reduced by between $1-50\%$ when using the pinnate propeller. With respect to reliability, the pinnate propeller had some issues during testing. After 500 hours all the seals were replaced due to defective manufacturing which became apparent after 50 hours of testing. In one of the pinnate propellers one of the blade connecting shafts failed due to fatigue after approx. $4 \cdot 10^7$ cycles. The test was continued by replacing the pinnate propeller with the original propeller for the ship. The tests ended after the second propeller had operated for approx. $5.5 \cdot 10^7$ cycles. It is postulated in [86] that it is possible, by careful design, to make a reliable pinnate propeller" [31][1].

"A similar concept to the swash plate is proposed in the patent [63] which is capable of both collective and cyclical pitching by using a hydraulic transmission system instead of mechanical rods. The cyclical pitching is made by having a hydraulic piston pair for each blade. One of the pistons can rotate the blade and the other extends radially out of the propeller shaft inside the ship where it follows an eccentric groove which matches the desired cyclical pitching. Through feedback wires, valves and a collective pitch reference piston a complete collective and cyclical pitching propeller is obtained. It is in [63] postulated that the propeller may reduce the cavitation, shaft vibration, pressure pulses and increase efficiency, but no results are shown" [31][1].

1.3.3 Passively Controlled Individual Pitch Propeller

A passively controlled individual pitch propeller, pitches the propeller blades individually through passive components which cannot be switched on/off. The passively controlled individual pitch propeller has been suggested in [14,37,51,60,80].

"The passive controlled individual pitch propellers proposed in [37,60,80] are from patents. The concepts proposed in [37,60] are similar and consist

of a fixed guide ring around the propeller shaft with a groove in the guide ring which is formed to the desired pitch trajectory, see Figure 1.13a. Pins extend radially out of the propeller shaft. Pull-push rods inside the propeller shaft, which rotate the blades, are connected to these radial extending pins. The pins slide in the groove as the propeller rotates thereby making the pitch adjusting to the local velocities in the wake field. It is postulated in [37, 60] that the propeller can be used to improve the efficiency" [31].

"In the patent [80] a feathering system is proposed using a spring system, as shown in Figure 1.13b, and having the blade's center of pressure behind the spindle axes. When the blade is in the wake peak the thrust and the spindle torque increase which deforms the spring and decreases the pitch of the blade until an equilibrium in the spindle torque is obtained. When the blade has passed the wake peak, the thrust and spindle torque decrease and the pitch increases until an equilibrium in the spindle torque is obtained. In [80] it is postulated that the propeller can reduce ship vibrations which includes both pressure pulses and shaft vibrations but no analysis or test are shown which support the statement" [31].

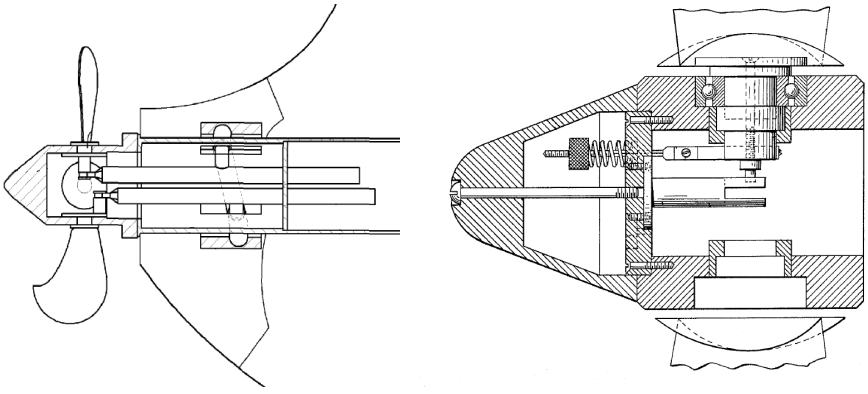

Figure 1.13: (a) Example of cam mechanism from [60]. **(b)** Feathering mechanism from [80].

"In [51] cavitation tests are made with a five bladed propeller, where one of the blades is able to vary the pitch cyclically through a cam mechanism. The propeller was tested in a wake field made by a wake screen which was dominated by second-order harmonic variations. The pitch trajectory was therefore a second-order sinusoidal pitch trajectory. Two cams were made for the tests, one with a 7° amplitude and one with a 3.5° amplitude. The cams were tested at four different operating conditions for the 7° amplitude cam and for three operating conditions for the 3.5° amplitude cam. For the 7° amplitude cam the transient cavitation was almost eliminated for the pitching blade when compared to the fixed blade for all the operating conditions. For

the 3.5° amplitude cam the transient cavitation was significantly reduced for all the operating conditions" [31].

"In [14] cavitation tests are made for a propeller with sinusoidal oscillating blades mounted on an inclined shaft in an uniform flow field. The tests were made in order to reduce cavitation and erosion near the root of the blade. The tests are made for two inclinations of the shaft, amplitudes of the pitch trajectories at 0° and 3° and phase shift of the oscillation at 0° and 30° at different advance coefficients and cavitation numbers. The general tendency of the results was that the oscillating blade, in some cases, could delay the cavitation at the root of the blade, but the cavitation was increased towards the tip" [31].

1.3.4 Actively Controlled Individual Pitch Propeller

An actively controlled individual pitch propeller pitches the propeller blades individually by using active components such as an actuator system with a controller. With the actively controlled individual pitch propeller it is possible to change the amplitude and shape of the pitch trajectory during the operation of the ship. This is not possible with the concepts presented in [37, 51, 60, 63, 84–86]. The concepts in [37, 51, 60] are limited to one shape and amplitude of the pitch trajectory. The concepts in [63, 84–86] are limited in the shape of the pitch trajectory, but can vary the amplitude of the pitch trajectory during operation. An actively controlled individual pitch propeller is presented in [40, 90, 98] and one of the concepts from [98] is sketched in Figure 1.14.

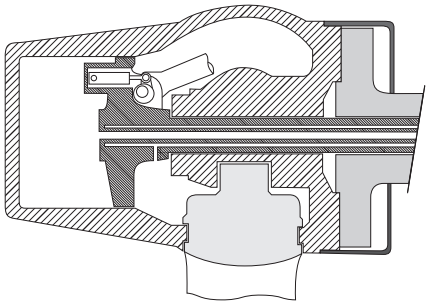

Figure 1.14: Sketch of the individual blade pitching mechanism proposed in [98]. The sketch is from [31]

"The proposed propeller in [98] has the servo piston known from CP propellers which can make a collective pitching of the blades. Smaller servo pistons are attached to the large servo piston which controls the cyclical pitch of the individual blades. Furthermore, it is proposed that the servo pistons can be replaced with a vane actuator or a motor. It is postulated in [98] that

the propeller can be used to improve the efficiency of the propeller but no results are shown for it. Similarly, the patent in [40] proposes the propeller to increase the efficiency" [31].

"The performance of an active CVP propeller, compared to a FP propeller, is made in [33]. The pitch trajectory is determined in order to remove the time varying components of the axial forces, by using unsteady thin foil theory [81] and compensating for the low aspect ratio of the propeller blades. These theories are linear and by approximating the wake field and pitch trajectory by Fourier series, a number of linear equations needs to be solved in order to determine the optimum pitch trajectory. The performance evaluation of the CVP propeller is made by using an unsteady lifting surface program modified to include the pitching motion of the blade. The propeller used in the evaluation is a five bladed propeller with a diameter of 6.2 meters. The performance of the CVP propeller is compared to the performance of the FP propeller. The performance evaluation shows a 3% increase in efficiency for the CVP propeller compared to the FP propeller, due to an increase in the mean thrust. The mean values of the transverse loads are reduced by $8\% - 40\%$ for the CVP propeller and the variation in propeller thrust is reduced. The pressure pulses up to the fourth harmonic are determined at five points above the propeller. The pressure pulses are reduced by between $15\% - 60\%$ for the CVP propeller. The extent of the cavitation is generally reduced with the CVP propeller. It is therefore proposed in [33] to reduce the area ratio of the propeller to increase the efficiency while maintaining the same cavitation performance as for the FP propeller" [31][1]. The propulsion efficiency is determined as:

$$\eta_D = \underbrace{\frac{T\,V_a}{\omega_p\,Q}}_{\eta_p}\,\underbrace{\frac{1-t_d}{1-w}}_{\eta_h} \tag{1.8}$$

η_D is the propulsion efficiency. η_p is the propeller efficiency. η_h is the hull efficiency. T is the propeller thrust. V_a is the advance velocity. ω_p is the rotational speed of the propeller. Q is the propeller torque. t_d is the thrust deduction factor. w is the wake coefficient. The thrust deduction factor is due to the suction pressure of the propeller pulling the ship backwards. Both w and t_d may be different for the CVP propeller than they are for a FP/CP propeller [33].

The improved cavitation performance with the CVP propeller is utilized in [66] to reduce the area ratio of the propeller and thus improve the efficiency. The investigation in [66] considers modifying a CP propeller, with a diameter of 5.4 meters, to a CVP propeller. The wake field for the ship considered in [66] is shown in Figure 1.3. Two pitch trajectories are determined in [66] and the performance of the propeller with these pitch trajectories is

shown in Table 1.1, where they are compared to a normal constant pitch trajectory. The pitch of the blades depends on their position in the wake field as shown in Figure 1.15. A blade position equal to 180° is when the blade is in the wake peak, i.e. 12 o'clock position.

Table 1.1: Propeller performance determined in [66]. Pi is the pitch in [m]. D_p is the propeller diameter in [m].

Trajectory	Pi/D_p at $r/r_p = 0.7$	Thrust per blade [kN]	Power per blade [kW]	η_p	Area ratio
Constant	0.8039	143.0	1506.6	0.5847	0.64
Variable	0.8144	143.0	1418.5	0.6396	0.50
Cosine	0.8098	143.1	1436.0	0.6222	0.57

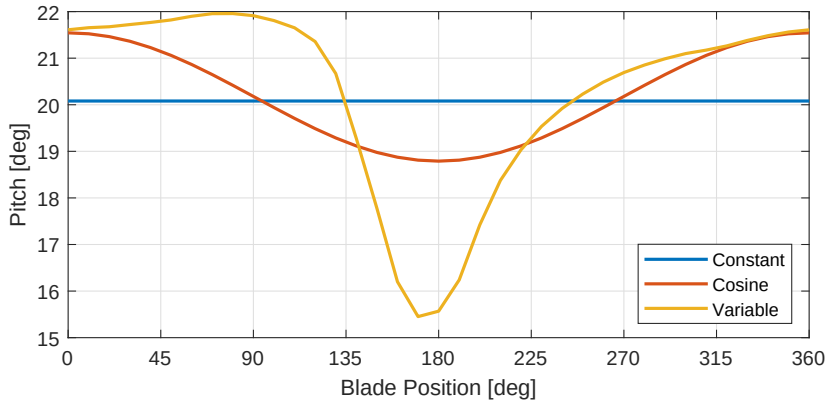

Figure 1.15: Pitch trajectories for the CVP propeller determined in [66].

"The investigation has been made such that the average thrust is the same for all the pitch trajectories, using a quasi-steady lifting line to evaluate them. The area ratio of the propeller is decreased due to the better cavitation performance and small changes in the blade design were made to ensure an optimum design [66]. From Table 1.1 it is seen that the efficiency is increased by 9.4% for the variable pitch trajectory and by 6.4% for the cosine pitch trajectory relative to the constant pitch trajectory" [31].

In [90] a theoretical feasibility study of the actively controlled individual pitch propeller is presented. The work in [90] considers the propeller considered in [66] and includes the work needed to pitch the propeller blades in the evaluation of the propulsion efficiency. With the actuator system designed in [90], the propulsion efficiency is decreased when using the variable pitch trajectory in Figure 1.15. For the cosine pitch trajectory in Figure 1.15 the propulsion efficiency is slightly increased. The actuator system presented in [90] is similar to the concepts presented in [98] and shown in Figure 1.14.

The system consists of a hydraulic cylinder to pitch each of the propeller blades. The variable pitch trajectory in Figure 1.15 is used to design the cylinders and the proportional valves controlling them. Because the components are placed in the hub, it requires that the hub is extended along the propeller shaft in order to fit the components inside the hub.

1.3.5 Summing up on Cyclical Varying Pitch Propeller Performance

Studies focusing on the CVP propeller are limited as evident from the review above. Many of the studies are concepts presented in the patents [25,37,40, 55,60,63,75,80,80,98]. Actual studies are restricted to [14,33,51,66,84–86,88]. Theoretical studies are made in [33,66,76,88]. Model scale tests are made in [14,51,84,85] and [86] is a full scale test. "The performance results of the CVP propeller of these studies are summarized in Table 1.2 which only considers the actual performance shown in the studies and not postulated/inferred performance improvements" [31].

Table 1.2: Summarization of CVP propeller performance excluding the reliability. The reliability is excluded since none of the studies have focused on the reliability. T is for theoretical studies, MS is model scale testing and FS is full scale testing. TB is the thrust balance propeller, SP is the swash plate propeller, PCIP is the passive CVP propeller and ACIP is the active CVP propeller. *Only considers the variation in the thrust. [31]

Citation	[88]	[84], [85]	[86]	[51]	[14]	[33]	[66]
CVP propeller concept	TB	SP	SP	PCIP	PCIP	ACIP	ACIP
Efficiency							
Cavitation							
Shaft vibration						*	*
Pressure pulses							
Noise							
Type of study	T	MS	FS	MS	MS	T	T

Improved	May improve	Not investigated or commented	No change	Worsened

"From Table 1.2 it is, in general, seen that the performance of the CVP propeller is improved compared to a FP propeller" [31].

"However, the type of vessel could also have significant influence on the usability of the CVP propeller. If the CVP propeller proves to improve all of the performance parameters in Table 1.2, then the CVP propeller is suitable for all types of vessels if the down payment for the propeller is tolerable and the reliability is reasonable. If the CVP propeller does not yield an efficiency improvement but only improves the cavitation performance and noise, then

the type of vessel that the CVP propeller is appropriate for changes. Because an efficiency improvement is not obtained, the CVP propeller is not desirable for cargo transporting vessels. The vessels that could still benefit from using the CVP propeller are: navy ships, research vessels, seismic vessels, cruise ships and ferries. These types of vessels typically prioritise to some degree having a quiet propulsion system" [31]. Navy ships desire a quiet propulsion system in order to not be detected by the enemy, research and seismic vessels want quiet propulsion systems such that the noise does not influence the measuring equipment and cruise ships and ferries want quiet propulsion systems in order to increase the comfort of the passengers.

"An obvious question is then why is the CVP propeller not on the market yet? There are at least two reasons" [31].

"The first reason is to consider the energy loss due to the pitching motion of the blades. To assess the feasibility of a CVP propeller to increase the propulsion efficiency, a dynamic model is necessary which accounts for the dynamics of the pitching motion and the actuator system. This has not been considered in any of the above studies except for in [90], which is a preliminary study and the dynamic model used in [90] has to be extended to get more accurate results. By using the dynamic model an optimal pitch trajectory can be found which accounts for the needed work to turn the blades. The dynamic model can also be used to evaluate the feasibility and requirements of different topological designs of the pitching system. Experimental test are needed in order to validate the dynamic model and determine its accuracy. The effect of the CVP propeller on the hull efficiency needs to be investigated. This includes the CVP propeller's effect on the thrust deduction factor and the wake coefficient. If the hull efficiency decreases with the CVP propeller then the CVP propeller may only be desirable due to its improved cavitation behaviour" [31].

"The second reason is related to the cost of the CVP propeller. The down payment is likely to be larger for the CVP propeller compared to the FP and CP propellers due to the increased complexity of the propeller with the individual pitch mechanism. The efficiency of the propeller should therefore be greater than the efficiency of a FP and CP propeller in order to ensure a reasonable payback time. If this is not the case then the CVP propeller should yield performance improvements compared to the FP and CP propeller which justify the use of a CVP propeller instead of a FP or CP propeller" [31].

1.4 Challenges in Cyclical Varying Pitch Propeller

"From the above analysis the CVP propeller has the potential to improve the propeller performance when compared to the FP and CP propeller, but there are a number of challenges that have to be addressed before the CVP propeller can be used commercially. The challenges in realising the CVP propeller are" [31]:

- **Blade design**
  - *"How should the propeller blades be designed for the CVP propeller compared to the design rules followed for the FP and CP propeller?"* [31]
    "None of the studies [14,33,51,76,84–86,88] consider how the blades for the CVP propeller should be designed. The studies consider an existing blade design and use it for a CVP propeller. The optimum blade design for the CVP propeller is likely to differ from the optimum blade design for the FP and CP propeller" [31]. Adapting the blade design for the CVP propeller is considered in [66]. It has to be determined if this method is suitable to use. If it is not then a suitable method has to be determined before the CVP propeller can be realised.
- **Pitch trajectory**
  - *"How should the pitch trajectory be for a CVP propeller to obtain the optimum performance for the propeller?"* [31]
    The pitch trajectories considered in [14,51,85,86] are limited to only include a single harmonic. In [88] the pitch trajectory is assumed to be piece-wise linear. Limiting the pitch trajectory to these types of pitch trajectories may not yield the optimum performance for the CVP propeller. Considering pitch trajectories with a multitude of harmonics may yield a better performance of the CVP propeller. Such pitch trajectories are considered in [33, 66] where the pitch trajectory is determined to obtain a specific performance with the CVP propeller. It has to be validated whether the methods used to determine the pitch trajectories in [33, 66] are appropriate. "Alternatively, new methods have to be developed to determine the optimum pitch trajectory. The optimum pitch trajectory is likely coupled with the blade design and vice versa. The coupling between these should be investigated and included in the determination of the optimum pitch trajectory and the blade design for the CVP propeller" [31].
- **Individual blade pitching mechanism**
  - *"Can a mechanism be designed for the CVP propeller which is able to pitch the blades individually in a cyclic manner during one rotation?"*

[31]
"Several different mechanisms for the CVP propeller have been proposed in [25,37,60,63,75,76,80,80,84–86,90,98]. Each of these mechanisms have their own pros and cons but only the mechanisms, with the limitation of the pitch trajectory to one harmonic, have been realised [14,51,84–86]. The only mechanism realised in a real application is [86] which had a couple of breakdowns. The types of mechanisms that can be utilized for the CVP propeller are going to depend on the required loads acting on the blade when it pitches according to the desired pitch trajectory and the propeller size. When having designed the individual pitch mechanism, the propulsion efficiency can be evaluated with the power consumption of the individual pitch mechanism included. Then it can be evaluated if an efficiency improvement is obtained with the CVP propeller when compared to a FP and CP propeller" [31].

- **Reliability**
  - *"How does the reliability of the CVP propeller change compared to the FP and CP propeller?"* [31]
    "The only study that has tested the CVP propeller in a real application is [86]. The propeller was tested for almost an year (approx. 55 million cycles) and during this year it experienced a couple of breakdowns which required servicing of the propeller. In [86] it is believed that a more reliable propeller could be made by reevaluating the design. For commercial application of the CVP propeller, the number of pitch cycles the propeller experiences is approx. 1.3 billion for a twenty-year lifetime with a rotational speed of the propeller of 120 rpm. This is a large increase compared to the CP propeller which is only exposed to approx. 10 million cycles under similar condition. Wear and fatigue of the propeller components are therefore going to be even more significant for the CVP propeller than it is for the CP propeller. It is therefore necessary to investigate how reliable the CVP propeller is and if something can be done to improve the reliability of the CVP propeller. If it is not possible to improve the reliability of the CVP propeller, then it may have to be serviced more regularly than a CP propeller" [31].

1.5 Main Contributions of this Dissertation

The main contributions of the research in this dissertation are:

- Reviewing the literature related to the CVP propeller and thereby identifying the challenges in realising the CVP propeller.
- Establishing a modelling approach to determine the forces and torques acting on the CVP propeller blades.
- Establishing a series of alternative modelling approaches for the hydrodynamical loads. These models are suitable to determine the optimum pitch trajectory for the CVP propeller which minimises the variation in the hydrodynamical loads.
- Designing and fabricating a model scale propeller test setup for the CVP propeller which is able to pitch the propeller blades cyclical whilst measuring a selection of the unsteady loads acting on the propeller and its blades.
- Making tank tests with the fabricated test setup for the CVP propeller to show the efficiency improvement with the CVP propeller.

1.6 Outline of Dissertation

The outline of the dissertation is as follows:

Chapter 2: Modelling of Cyclical Varying Pitch Propeller:
Common for all the challenges is that they all require a framework which is able to determine the loads acting on the propeller depending on the propeller design and operating conditions. In this chapter a model is made which can determine the loads acting on the CVP propeller blades during the individual cyclical pitching of the blades. The model is applied to determine the requirements for the individual pitch mechanism such as the required pitching power and torque. The application of the model is made with the CVP propeller in [66] where the geometry, operating conditions and pitch trajectories are known.

Chapter 3: Pitch Trajectory for Cyclical Varying Pitch Propeller:
In Chapter 2 it is found that the pitch trajectories determined in [66] are likely not the optimal pitch trajectories for the CVP propeller. It is therefore required to establish a method to determine the optimum pitch trajectory for the CVP propeller. The method considers known geometry and operating conditions. The model established in Chapter 2 is too computationally

expensive to determine the optimum pitch trajectory using an iterative optimization algorithm. Four different simplified models are established which are less computationally expensive than the method in Chapter 2. These models are compared with the model from Chapter 2 and the models with the best correspondence are used to determine the optimum pitch trajectory. The optimum pitch trajectory is defined as the trajectory which minimises the variations in the hydrodynamical load/loads acting on the propeller blade.

Chapter 4: Experimental Testing of Cyclical Varying Pitch Propeller:
To validate the performance of the CVP propeller and the hydrodynamical model established in Chapter 2, experimental tests of the CVP propeller were made. Since there is no standard test bench for testing the CVP propeller, a custom model scale CVP propeller with two blades was made which was able to measure the propeller thrust, torque and blade spindle torque. The CVP propeller was tested in open-water and behind hull conditions. To test the CVP propeller in behind hull conditions, a ship hull has been designed and fabricated for the tests. The CVP propeller tests were made with two different blade designs for the propeller. One blade design was made for a traditional CP propeller and the other blade design was made for the CVP propeller. The propellers are also tested with a number of different pitch trajectories. The results for the two blade design are used to establish if the CVP propeller can yield an efficiency improvement and the results were used to validate the hydrodynamical model in Chapter 2.

Chapter 5: Conclusion and Future Work:
This chapter summarizes the work of this dissertation and discusses the future work needed in order to realise the CVP propeller.

Chapter 2

Modelling of Cyclical Varying Pitch Propeller

This chapter presents the modelling of the loads acting on the CVP propeller blades during the cyclical pitching of the blades. The model is used to determine the propeller efficiency, the required power to make the cyclical pitching of the propeller blades and the required loads for the cyclic pitch mechanism. The model consists of a series of different contributing factors which are evaluated through the chapter as they are presented. To make these evaluations the vessel and propeller considered in [66] are used. This is a 1,000 TEU container vessel with a controllable pitch propeller. The operational, design and performance parameters for the propeller are given in Table 2.1. The propeller blade is shown in Figure 2.1a and the wake field of the container vessel is shown in Figure 2.1b.

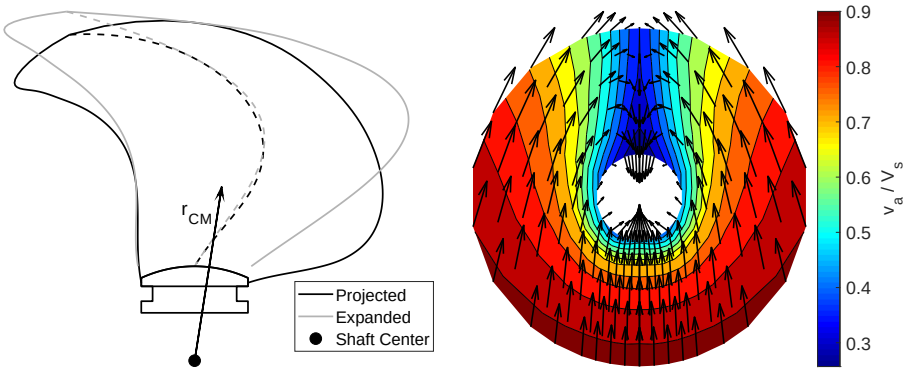

Figure 2.1: (a) Projected and expanded blade view. **(b)** Wake field of the vessel.

Propeller			
Propeller diameter	D_p	5400	$[mm]$
Number of blades	Z_b	4	$[-]$
Power	P_D	5838.8	$[kW]$
Hub diameter	D_{hub}	1460	$[mm]$
Propeller speed		121	$[rpm]$
	n_p	≈ 2.02	$[rps]$
	ω_p	≈ 12.67	$[rad/s]$
Blade area ratio		0.64	$[-]$
Shaft immersion	h_s	5070	$[mm]$
Blade			
Pi/D_p at $r/r_p = 0.7$		0.7861	$[-]$
Skew		40°	$[-]$
Forward skew		19°	$[-]$
Rake		0	$[mm]$
Center of mass $^+$	$\mathbf{r}_{CM}$	$\begin{bmatrix} 117.0 \\ -176.0 \\ 1197.6 \end{bmatrix}$	$[mm]$
Blade mass $^+$	m_b	3048.77	$[kg]$
Blade moment of inertia $^+$	$\mathbf{I}_b$	$\begin{bmatrix} 6100.0 & 275.4 & -450.2 \\ 275.4 & 5634.6 & 677.6 \\ -450.2 & 677.6 & 811.6 \end{bmatrix}$	$[kg\,m^2]$
Operating conditions			
Ship speed (for	V_s	16.55	$[knots]$
hydrodynamic design)		≈ 8.51	$[m/s]$
Ship speed (for strength)	V_s	18.5	$[knots]$
		≈ 9.52	$[m/s]$
Water density	ρ	1025.5	$\left[kg/m^3\right]$
Kinematic viscosity of water	v	$1.191\,10^{-6}$	$\left[m^2/s\right]$
Thrust *	T	559.0	$[kN]$
Torque *	Q	460.8	$[kNm]$
Efficiency *	η_p	0.576	$[-]$

Table 2.1: Propeller data. $^+$ data is determined through a CAD program with respect to the shaft center and includes the flange on which the blade is mounted, see Figure 2.1a. * calculated through MAN Energy Solutions internal design programs at $V_s = 16.55\,[knots]$.

Three different pitch trajectories are proposed in [66]. A constant pitch trajectory, a cosine pitch trajectory and a variable pitch trajectory. The constant pitch trajectory is the same operation as a traditional CP propeller. The pitch trajectories are elaborated further in Section 2.2. In [66] a new blade design is made for each of the pitch trajectories where the area ratio has been

reduced because of the improved cavitation performance. The reduction in the area ratio of the propeller results in a more efficient propeller.

Throughout this chapter the results from the modelling of the CVP propeller are presented by applying it to the three pitch trajectories. The results presented will not account for the change in the blade design for cosine and variable pitch trajectory.

Before going into details with the modelling of the CVP propeller it is necessary to present some definitions. The coordinate systems used to model the CVP propeller are defined as well as the pitch trajectories, with their corresponding velocities and accelerations. These definitions will be used throughout this chapter.

2.1 Coordinate Systems

To make the modelling of the blade motion easier three coordinate systems are defined. The three coordinate systems are shown in Figure 2.2 and are defined as:

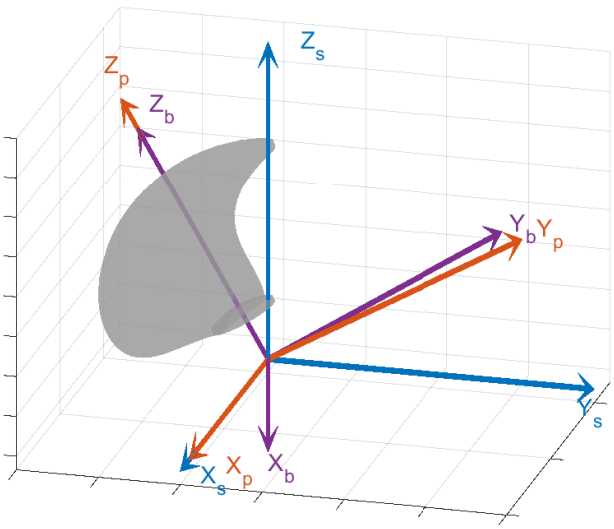

Figure 2.2: The three coordinate system used in the modelling of the CVP propeller.

- Ship coordinate system: X_s, Y_s, Z_s - blue coordinate system in Figure 2.2.
  - The coordinate system is fixed to the ship and with origin in the center of the propeller as shown in Figure 2.2. The direction of X_s is in the ahead direction of the ship, the direction of Y_s is to the port side and the direction of Z_s is upward.

- Propeller coordinate system: $X_{p,i}$, $Y_{p,i}$, $Z_{p,i}$ - red coordinate system in Figure 2.2.
  - The coordinate system is fixed to the propeller and with origin in the center of the propeller as shown in Figure 2.2. The coordinate system is fixed to the propeller and therefore rotates with it. There are multiple propeller coordinate systems, one for each blade which the subscript i indicates. Each of the propeller coordinate system's x-axis is aligned with the ship coordinate system's x-axis. The direction of the z-axis is aligned with the blade's spindle axis as shown in Figure 2.2.
- Blade coordinate system: $X_{b,i}$, $Y_{b,i}$, $Z_{b,i}$ - purple coordinate system in Figure 2.2.
  - There are multiple blade coordinate systems, one for each blade which is noted by the subscript i. The coordinate system is fixed to the blade meaning that the coordinate system rotates with the blades as it pitches and rotates with the propeller. This makes the inertia matrix constant. The coordinate system has its origin in the center of the propeller and is aligned with the propeller coordinate system when the blade pitch is equal to the design pitch.

The displacement of the coordinate systems with respect to each other is defined by the two angles θ_b and θ_p. θ_b is the blade position in the wake field and is the angular displacement between the ship coordinate system and the propeller coordinate system. θ_b is defined to be the angle between the negative z-axis in the ship coordinate system and the positive z-axis in the propeller coordinate system as shown in Figure 2.3a. θ_p is the pitch displacement of the blade, which is relative to the design pitch ($\alpha_{p,d}$) of the blade as shown in Figure 2.3b. The pitch displacement is the angle between the x-axis of the propeller coordinate system and the x-axis of the blade coordinate system. The y-axes of the propeller and blade coordinate system can also be used to define θ_p.

To transform vectors from one coordinate system to another, the transformation matrices, $\boldsymbol{T}_{x,y}$ are used. The transformation matrices are defined with two indices in the subscript. The first index is the coordinate system that the vector is transformed from and the second index is the coordinate system that the vector is transformed to. The subscripts s, p and b designate the ship, propeller and blade coordinate system, respectively. Two examples of the transformation matrix are shown in Eq. 2.1 and Eq. 2.2.

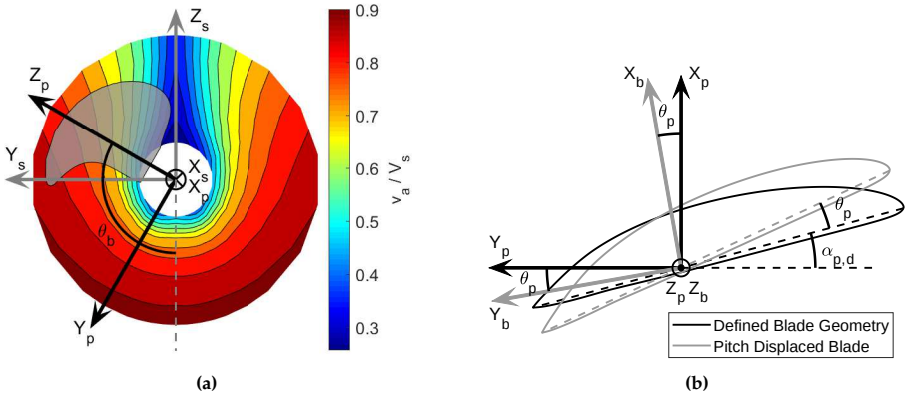

Figure 2.3: **(a)** Definition of the blade's position in wake field θ_b. **(b)** Definition of the blade's pitch displacement θ_p.

$$\begin{bmatrix} X_{p,i} \\ Y_{p,i} \\ Z_{p,i} \end{bmatrix} = \underbrace{\begin{bmatrix} 1 & 0 & 0 \\ 0 & -\cos\theta_{b,i} & -\sin\theta_{b,i} \\ 0 & \sin\theta_{b,i} & -\cos\theta_{b,i} \end{bmatrix}}_{\mathbf{T}_{s,p}(\theta_{b,i})} \begin{bmatrix} X_s \\ Y_s \\ Z_s \end{bmatrix} \tag{2.1}$$

$$\begin{bmatrix} X_{b,i} \\ Y_{b,i} \\ Z_{b,i} \end{bmatrix} = \underbrace{\begin{bmatrix} \cos\theta_{p,i} & -\sin\theta_{p,i} & 0 \\ \sin\theta_{p,i} & \cos\theta_{p,i} & 0 \\ 0 & 0 & 1 \end{bmatrix}}_{\mathbf{T}_{p,b}(\theta_{p,i})} \begin{bmatrix} X_{p,i} \\ Y_{p,i} \\ Z_{p,i} \end{bmatrix} \tag{2.2}$$

In Eq. 2.1 the transformation matrix $\boldsymbol{T}_{s,p}$ transforms a vector from the ship coordinate system to the propeller coordinate system. In Eq. 2.2 the transformation matrix $\boldsymbol{T}_{p,b}$ transforms a vector from the propeller coordinate system to the blade coordinate system. The transformation matrices $T_{p,s}$ and $T_{b,p}$ are the inverse of the matrices $T_{s,p}$ and $T_{p,b}$ as:

$$\mathbf{T}_{s,p}(\theta_{b,i})^{-1} = \mathbf{T}_{p,s}(\theta_{b,i}) = \mathbf{T}_{s,p}(-\theta_{b,i}) \tag{2.3}$$

$$\mathbf{T}_{p,b}(\theta_{p,i})^{-1} = \mathbf{T}_{b,p}(\theta_{p,i}) = \mathbf{T}_{p,b}(-\theta_{p,i}) \tag{2.4}$$

The above defined coordinate systems and transformation matrices will be used throughout this chapter.

2.2 Pitch Trajectories

The pitch trajectories, determined in [66], are defined as the pitch at the non-dimensional radius equal to 0.7 for each 10° in the wake field. It is desired to define the pitch trajectories as continuous differentiable functions of the blade position in the wake field instead of discrete points. By defining the pitch trajectories as a continuous differentiable function, the pitch rate and acceleration can be determined by the first and second time derivatives of the function. The continuous differentiable function used to define the pitch trajectories is a Fourier series of the form:

$$\alpha_p\left(\theta_b\right) = a_0 + \sum_{n=1}^{N} a_n \cos\left(n\,\theta_b\right) + b_n \sin\left(n\,\theta_b\right) \tag{2.5}$$

$\alpha_p\left(\theta_b\right)$ is the Fourier series of the blade's pitch angle at the 0.7 non-dimensional radius of the propeller. a_0 is the constant term in the Fourier series. n is the harmonic of the Fourier series. N is the largest harmonic included in the Fourier series. a_n is the n'th order coefficient for the n'th cosine term. b_n is the n'th order coefficient for the n'th sine term. The coefficients a_0, a_n and b_n are determined by linear least-squares estimation as:

$$\boldsymbol{\theta} = \left(\boldsymbol{\mathcal{F}}^T\,\boldsymbol{\mathcal{F}}\right)^{-1}\,\boldsymbol{\mathcal{F}}^T\,\boldsymbol{y} \tag{2.6}$$

Where,

$$\boldsymbol{\theta} = \begin{bmatrix} a_0 & a_1 & a_2 & \cdots & a_N & b_1 & b_2 & \cdots & b_N \end{bmatrix}^T \tag{2.7}$$

$$\boldsymbol{y} = \begin{bmatrix} \alpha_p\left(0^\circ\right) & \alpha_p\left(10^\circ\right) & \cdots & \alpha_p\left(360^\circ\right) \end{bmatrix}^T \tag{2.8}$$

$$\boldsymbol{\mathcal{F}} = \begin{bmatrix} 1 & 1 & \cdots & 1 \\ \cos\left(0^\circ\right) & \cos\left(10^\circ\right) & \cdots & \cos\left(360^\circ\right) \\ \cos\left(2\cdot 0^\circ\right) & \cos\left(2\cdot 10^\circ\right) & \cdots & \cos\left(2\cdot 360^\circ\right) \\ \vdots & \vdots & \ddots & \vdots \\ \cos\left(N\cdot 0^\circ\right) & \cos\left(N\cdot 10^\circ\right) & \cdots & \cos\left(N\cdot 360^\circ\right) \\ \sin\left(0^\circ\right) & \sin\left(10^\circ\right) & \cdots & \sin\left(360^\circ\right) \\ \sin\left(2\cdot 0^\circ\right) & \sin\left(2\cdot 10^\circ\right) & \cdots & \sin\left(2\cdot 360^\circ\right) \\ \vdots & \vdots & \ddots & \vdots \\ \sin\left(N\cdot 0^\circ\right) & \sin\left(N\cdot 10^\circ\right) & \cdots & \sin\left(N\cdot 360^\circ\right) \end{bmatrix}^T \tag{2.9}$$

The discrete point values of the pitch trajectories are shown in Figure 2.4 together with the linear least-squares estimation of the Fourier series for the pitch trajectories.

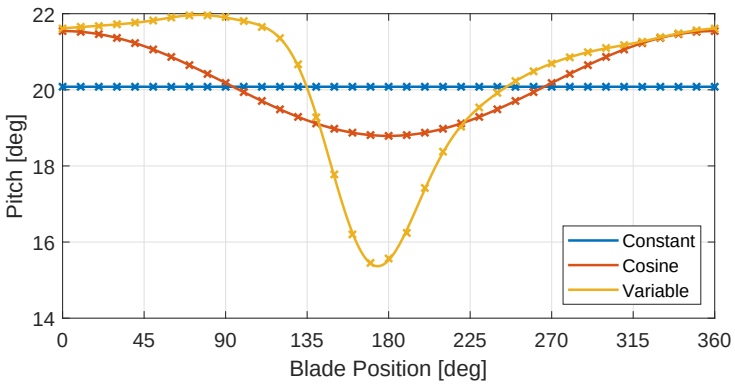

Figure 2.4: Pitch trajectories from [66] shown as x and the estimated Fourier series shown as the lines.

The mean of each of the pitch trajectories in Figure 2.4 differs from each other. This is due to the blade design being adapted to the pitch trajectory in [66]. To make the results for the different pitch trajectories comparable, the mean pitch has to be the same. This is done by defining the pitch trajectories as relative pitch displacements to the design pitch. This was previously defined to be θ_p, which is then defined as:

$$\theta_p(\theta_b) = \sum_{n=1}^{N} a_n \cos(n\,\theta_b) + b_n \sin(n\,\theta_b) \tag{2.10}$$

The coefficients a_n and b_n are the same as determined with the least-squares estimation in Eq. 2.6. The pitch rate and acceleration for the pitch trajectories are obtained by the time derivative of Eq. 2.10 as:

$$\dot{\theta}_p(\theta_b) = \sum_{n=1}^{N} -n\,\omega_p\,a_n \sin(n\,\theta_b) + n\,\omega_p\,b_n \cos(n\,\theta_b) \tag{2.11}$$

$$\ddot{\theta}_p(\theta_b) = \sum_{n=1}^{N} -n^2\,\omega_p^2\,a_n \cos(n\,\theta_b) - n^2\,\omega_p^2\,b_n \sin(n\,\theta_b) \tag{2.12}$$

$\dot{\theta}_p$ is the pitch rate of the trajectory. $\ddot{\theta}_p$ is the pitch acceleration of the trajectory. ω_p is the rate of revolution of the propeller. In the derivation of Eq. 2.12 it is assumed that the revolution rate of the propeller is constant. The relative pitch displacement, pitch rate and pitch acceleration are shown in Figure 2.5,

Figure 2.6 and Figure 2.7, respectively, for all the pitch trajectories defined in [66].

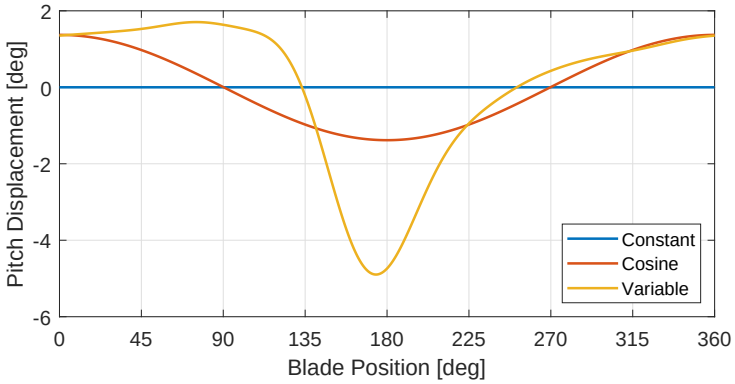

Figure 2.5: Pitch displacement trajectories.

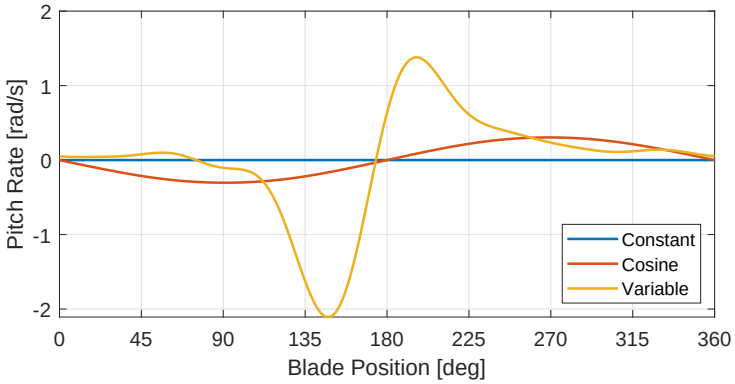

Figure 2.6: Pitch rate trajectories.

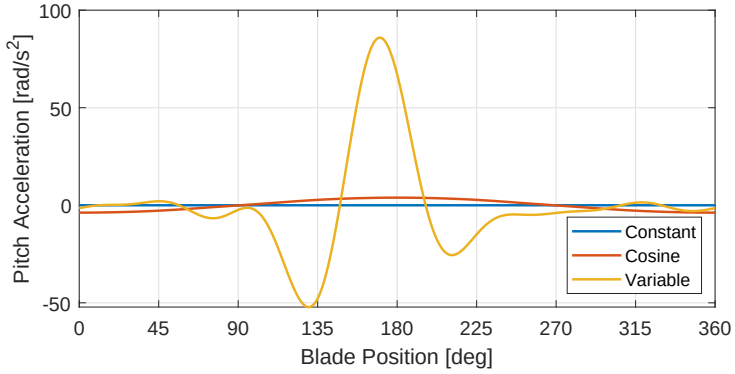

Figure 2.7: Pitch acceleration trajectories.

From the Figure 2.5, Figure 2.6 and Figure 2.7 it is seen that the variable pitch trajectories have the largest pitch rate and acceleration. For the pitch acceleration, the peak of the variable pitch trajectory is approximately 20 times larger than the peak pitch acceleration of the cosine pitch trajectory. The dynamic effects should therefore be the most significant for the variable pitch trajectory.

2.3 CVP Propeller Model Overview

To obtain an overview of the different loads acting on the individual propeller blades, a free-body diagram is made and a sketch of this is shown in Figure 2.8.

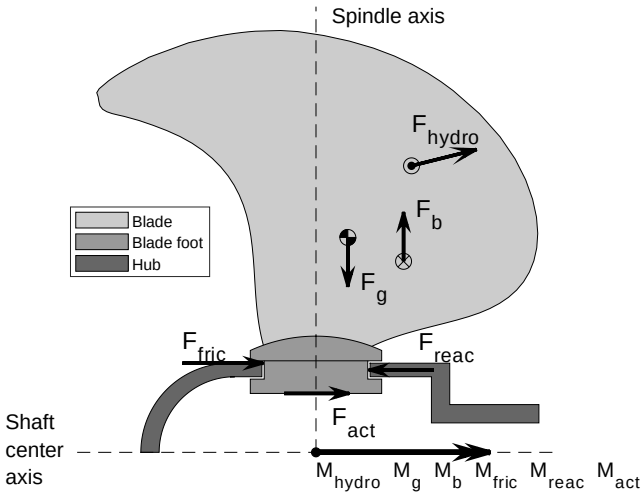

Figure 2.8: Sketch of the free body diagram of a propeller blade.

Figure 2.8 shows one blade of the propeller and a cut-through of its assembly with the hub. The blade is attached to the hub by clamping around the hub with the blade foot. The blade foot is divided into two parts which are bolted together to clamp around the hub. The blade is affected by six different loads. Each of these loads consists of forces and torques in the xyz-directions. The forces and torques are also referred to as the loads, $\boldsymbol{L} = [\boldsymbol{F} \ \ \boldsymbol{M}]^T$. The six loads acting on the blade are:

- **Hydrodynamical loads**, $\boldsymbol{L}_{hydro}$: Due to the relative motion between the blade and the water, a pressure difference over the blade is created and a viscous drag acts on the blade.
- **Gravitational loads**, $\boldsymbol{L}_g$: Due to gravitational acceleration.

- **Buoyancy loads**, $\boldsymbol{L}_b$: Due to the hydrostatic pressure acting on the blade.
- **Frictional loads**, $\boldsymbol{L}_{fric}$: Due to the relative motion between the blade foot and hub.
- **Reactive loads**, $\boldsymbol{L}_{reac}$: Due to the hub bearing exerting a load on the blade.
- **Actuator loads**, $\boldsymbol{L}_{act}$: Due to the actuator used to control the pitch of the blade.

Having determined the loads acting on the propeller blade, Newton's second law of motion can be used to make a model for the blade's motion. In the ship coordinate system the propeller blade has two degrees of freedom in its motion. It rotates about the x-axis due to the propeller rotation and about the blade's spindle axis. The main point of interest is to model the dynamics due to the pitching motion and not the dynamics due to a change in the propeller rotational speed. It is therefore assumed that the propeller rotational speed is constant. The system is therefore modelled as an one degree-of-freedom system where the degree of freedom is the pitch of the blade. The pitching motion of the blade is easier to model in the propeller coordinate system than in the ship coordinate system. The propeller coordinate system is therefore used to model the pitching motion of the blade. Applying Newton's second law of motion on the propeller blade gives:

$$\begin{bmatrix} \sum F_{x,p} \\ \sum F_{y,p} \\ \sum F_{z,p} \\ \sum M_{x,p} \\ \sum M_{y,p} \\ \sum M_{z,p} \end{bmatrix} = \begin{bmatrix} F_{hydro,x,p} + F_{act,x,p} + F_{fric,x,p} + F_{reac,x,p} + F_{g,x,p} + F_{b,x,p} \\ F_{hydro,y,p} + F_{act,y,p} + F_{fric,y,p} + F_{reac,y,p} + F_{g,y,p} + F_{b,y,p} \\ F_{hydro,z,p} + F_{act,z,p} + F_{fric,z,p} + F_{reac,z,p} + F_{g,z,p} + F_{b,z,p} \\ M_{hydro,x,p} + M_{act,x,p} + M_{fric,x,p} + M_{reac,x,p} + M_{g,x,p} + M_{b,x,p} \\ M_{hydro,y,p} + M_{act,y,p} + M_{fric,y,p} + M_{reac,y,p} + M_{g,y,p} + M_{b,y,p} \\ M_{hydro,z,p} + M_{act,z,p} + M_{fric,z,p} + M_{g,z,p} + M_{b,z,p} \end{bmatrix} \tag{2.13}$$

$\sum F_{i,p}$ and $\sum M_{i,p}$ are the sum of forces and torques along/around the xyz-axis in the propeller coordinate system. These forces and torques are also called the inertial forces and torques and will also be noted as $F_{iner,i,p}$ for the forces and $M_{iner,i,p}$ for the torques. The forces and torques in Eq. 2.13 have three indexes in the subscript, where each index is separated by a comma. The first index indicates the load, which is either; hydrodynamical, gravitational, buoyancy, frictional, reactive or actuator. The second index indicates the axis which the force or torque is along or around, and this is either the x-, y- or z-axes. The third index of the subscript indicates which coordinate system the force or torque is defined in. These are s, p and b respectively for the ship, propeller and blade coordinate system. The six equations in Eq. 2.13 are all the sum of six loads except for the torques about the z-axis. The sum of torques about the z-axis does not include a reactive torque. This is because the blade is free to rotate about the z-axis. The blade motion is locked in the

translating direction of the x-, y-, and z-axes and rotationally about the x- and y-axes due to the blade bearing, shown in Figure 2.8. Because the motion is locked about these axes, the reactive forces and torques are included in Eq. 2.13 so that equilibrium can be satisfied. The forces in Eq. 2.13 are defined to be positive in the positive direction of the coordinate system in which they are defined in. The positive direction of the torques in Eq. 2.13 are defined with the right hand rule. Eq. 2.13 only applies for one of the propeller blades. To determine the response from the propeller Eq. 2.14 is used. Eq. 2.14 adds the response for each blade and the hub to get the response from the propeller in the ship coordinate system.

$$\boldsymbol{L}_{prop,s}(\theta_b) = \boldsymbol{L}_{hub,s}(\theta_b) + \sum_{n=0}^{Z_b-1} \left(\boldsymbol{L}_{blade_i,s} \left(\theta_b - n \, \frac{2\,\pi}{Z_b} \right) \right) \tag{2.14}$$

$\boldsymbol{L}_{prop,s}$ is the propeller load in the ship coordinate system, $\boldsymbol{L}_{hub,s}$ is the load contribution from the hub, $\boldsymbol{L}_{blade_i,s}$ is the load contribution from the i'th blade in the ship coordinate system and Z_b is the number of propeller blades. The response of each blade has a phase shift on $360^\circ / Z_b$ with respect to the previous blade. This means that the propeller response due to the propeller blades only has oscillations for the $n\,Z_b$ harmonics due to the other harmonics cancelling each other.

In the following five sections, the loads due to inertia, hydrodynamics, gravity, buoyancy, friction and reactive loads are modelled. The loads due to the actuator depend on the design of the individual pitching mechanism and the other five loads. An example of how the actuator loads is determined is given in Section 2.10.

2.4 Modelling of Inertial Loads

The inertial loads are the required sum of all the forces and torques acting on the blade, so that the blade moves according to the desired pitch trajectory. The inertial loads depend on the motion of the blade i.e. the kinematics of the blade. The kinematics for the blades pitching motion are defined in Section 2.2. The inertial forces and torques are derived by considering the change in linear and angular momentum of the blade in the inertial frame of reference. The inertial frame of reference is the ship coordinate system, thereby assuming that the ship has a constant velocity vector. Furthermore it is assumed that the blade is a rigid body.

The derivation of the inertial loads is made separately for the linear and rotational inertial loads in the following two sections. The derivation of the inertial loads is made such that the inertial loads are defined in the propeller

coordinate system. The results for the modelled inertial loads are presented in Section 2.4.3 for the pitch trajectories defined in Section 2.2.

2.4.1 Linear Inertial Loads

The inertial forces are equal to the change in linear momentum in the ship coordinate system and are expressed as:

$$\boldsymbol{F}_{iner,s} = \dot{\boldsymbol{G}}_s \tag{2.15}$$

$\boldsymbol{F}_{iner,s}$ is the inertial force vector in the ship coordinate system containing the inertial forces $F_{iner,x,s}$, $F_{iner,y,s}$ and $F_{iner,z,s}$. $\dot{\boldsymbol{G}}_s$ is the time derivative of the linear momentum vector, $\boldsymbol{G}_s$, in the ship coordination system. The linear momentum vector for the propeller blade is defined as:

$$\boldsymbol{G}_s = m_b\, \boldsymbol{v}_{CM,s} = m_b\, \dot{\boldsymbol{r}}_{CM,s} \tag{2.16}$$

m_b is the mass of the blade, see Table 2.1. $\boldsymbol{v}_{CM,s}$ is the velocity vector of the center of mass of the blade which is equal to the time derivative of the vector $\boldsymbol{r}_{CM,s}$. $\boldsymbol{r}_{CM,s}$ is the vector from the shaft center to the center of mass of the propeller blade defined in the ship coordinate system. In Table 2.1 $\boldsymbol{r}_{CM}$ is defined in the blade coordinate system. The vector $\boldsymbol{r}_{CM}$ has to be transformed to the ship coordinate system to determine the linear momentum. $\boldsymbol{r}_{CM,s}$ is determined using the transformation matrices as:

$$\boldsymbol{r}_{CM,s} = \boldsymbol{T}_{p,s} \boldsymbol{T}_{b,p}\, \boldsymbol{r}_{CM} \tag{2.17}$$

Eq. 2.16 and Eq. 2.17 are substituted into Eq. 2.15 to determine the linear inertial forces as:

$$\begin{aligned}
\boldsymbol{F}_{iner,s} &= \dot{\boldsymbol{G}}_s \\
&= m_b\, \ddot{\boldsymbol{r}}_{CM,s} \\
&= m_b\, \frac{d^2}{dt^2} \left(\boldsymbol{T}_{p,s} \boldsymbol{T}_{b,p} \right) \boldsymbol{r}_{CM} \\
&= m_b\, \underbrace{\left(\ddot{\boldsymbol{T}}_{p,s}\, \boldsymbol{T}_{b,p} + 2\, \dot{\boldsymbol{T}}_{p,s}\, \dot{\boldsymbol{T}}_{b,p} + \boldsymbol{T}_{p,s}\, \ddot{\boldsymbol{T}}_{b,p} \right)}_{\boldsymbol{T}_{G,s}} \boldsymbol{r}_{CM} \\
&= m_b\, \boldsymbol{T}_{G,s}\, \boldsymbol{r}_{CM}
\end{aligned} \tag{2.18}$$

The inertial forces in the ship coordinate system are defined by using the blade mass, the vector to center of mass and a transformation matrix. The transformation matrix depends on the blade's pitch displacement, pitch rate, pitch acceleration, blade position and the rate of propeller revolutions. The

inertial forces are determined in the ship coordinate system but they have to be defined in the propeller coordinate system for the modelling of the CVP propeller. To get the inertial forces in the propeller coordinate system, the transformation matrix from the ship coordinate system to the propeller coordinate system is used, as:

$$\begin{aligned} \boldsymbol{F}_{iner,p} &= \boldsymbol{T}_{s,p}\, \boldsymbol{F}_{iner,s} \\ &= m_b \underbrace{\boldsymbol{T}_{s,p}\, \boldsymbol{T}_{G,s}}_{\boldsymbol{T}_{G,p}} \boldsymbol{r}_{CM} \\ &= m_b\, \boldsymbol{T}_{G,p}\, \boldsymbol{r}_{CM} \end{aligned} \tag{2.19}$$

2.4.2 Rotational Inertial Loads

The inertial torques are equal to the change in angular momentum in the ship coordinate system and are expressed as:

$$\boldsymbol{M}_{iner,s} = \dot{\boldsymbol{H}}_s \tag{2.20}$$

$\boldsymbol{M}_{iner,s}$ is the inertial torque vector containing the inertial torques $M_{iner,x,s}$, $M_{iner,y,s}$ and $M_{iner,z,s}$. $\dot{\boldsymbol{H}}_s$ is the time derivative of the angular momentum vector, $\boldsymbol{H}_s$, in the ship coordinate system. The angular momentum for the propeller blade in the ship coordinate system is defined as:

$$\boldsymbol{H}_s = \boldsymbol{I}_s\, \boldsymbol{\omega}_s \tag{2.21}$$

$\boldsymbol{I}_s$ is the blade's moment of inertia matrix in the ship coordinate system. The moment of inertia of the blade is defined in Table 2.1 in the blade coordinate system with respect to the origin of the coordinate system where it is constant. $\boldsymbol{\omega}_s$ the angular velocity vector of the blade in the ship coordinate system.

The vector for the angular velocity of the propeller blade is defined in the three coordinate systems as:

$$\boldsymbol{\omega}_p = \begin{bmatrix} \dot{\theta}_b \\ 0 \\ \dot{\theta}_p \end{bmatrix} \tag{2.22}$$

$$\boldsymbol{\omega}_s = \mathbf{T}_{p,s}\, \boldsymbol{\omega}_p = \begin{bmatrix} \dot{\theta}_b \\ \dot{\theta}_p \sin(\theta_b) \\ -\dot{\theta}_p \cos(\theta_b) \end{bmatrix} \tag{2.23}$$

$$\boldsymbol{\omega}_b = \mathbf{T}_{p,b}\, \boldsymbol{\omega}_p = \begin{bmatrix} \dot{\theta}_b \cos(\theta_p) \\ -\dot{\theta}_b \sin(\theta_p) \\ -\dot{\theta}_p \end{bmatrix} \tag{2.24}$$

$\boldsymbol{\omega}_b$, $\boldsymbol{\omega}_p$, $\boldsymbol{\omega}_s$ are the angular velocity vectors in the blade, propeller and ship coordinate systems, respectively. $\dot{\theta}_p$ is the pitch rate. $\dot{\theta}_b$ is the rotational speed of the propeller.

To determine the moment of inertia matrix in the propeller and ship coordinate system, the angular momentum in each coordinate system is determined as:

$$\boldsymbol{H}_b = \boldsymbol{I}_b\,\boldsymbol{\omega}_b \tag{2.25}$$

$$\boldsymbol{H}_p = \boldsymbol{I}_p\,\boldsymbol{\omega}_p \Rightarrow \boldsymbol{T}_{b,p}\,\boldsymbol{H}_b = \boldsymbol{T}_{b,p}\,\boldsymbol{I}_b\,\boldsymbol{\omega}_b = \boldsymbol{T}_{b,p}\,\boldsymbol{I}_b\boldsymbol{T}_{p,b}\,\boldsymbol{\omega}_p \tag{2.26}$$

$$\boldsymbol{H}_s = \boldsymbol{I}_s\,\boldsymbol{\omega}_s \Rightarrow \boldsymbol{T}_{p,s}\,\boldsymbol{H}_p = \boldsymbol{T}_{p,s}\boldsymbol{T}_{b,p}\,\boldsymbol{I}_b\boldsymbol{T}_{p,b}\,\boldsymbol{\omega}_p = \boldsymbol{T}_{p,s}\boldsymbol{T}_{b,p}\,\boldsymbol{I}_b\,\boldsymbol{T}_{p,b}\,\boldsymbol{T}_{s,p}\,\boldsymbol{\omega}_s \tag{2.27}$$

The moment of inertia matrices in the propeller coordinate system ($\boldsymbol{I}_p$) and the ship coordinate system ($\boldsymbol{I}_s$) are:

$$\boldsymbol{I}_p = \boldsymbol{T}_{b,p}\,\boldsymbol{I}_b\,\boldsymbol{T}_{p,b} \tag{2.28}$$

$$\boldsymbol{I}_s = \boldsymbol{T}_{p,s}\,\boldsymbol{T}_{b,p}\,\boldsymbol{I}_b\,\boldsymbol{T}_{p,b}\,\boldsymbol{T}_{s,p} \tag{2.29}$$

Substituting Eq. 2.21 and Eq. 2.29 into Eq. 2.20 yields the inertial torque vector in the ship coordinate system as:

$$\begin{aligned}
\boldsymbol{M}_{iner,s} &= \dot{\boldsymbol{H}}_s \\
&= \frac{d}{dt}\,\left(\boldsymbol{I}_s\,\boldsymbol{\omega}_s\right) \\
&= \frac{d}{dt}\,\left(\boldsymbol{T}_{p,s}\,\boldsymbol{T}_{b,p}\,\boldsymbol{I}_b\,\boldsymbol{T}_{p,b}\,\boldsymbol{T}_{s,p}\,\boldsymbol{\omega}_s\right) \\
&= \underbrace{\begin{pmatrix} \dot{\boldsymbol{T}}_{p,s}\,\boldsymbol{T}_{b,p}\,\boldsymbol{I}_b\,\boldsymbol{T}_{p,b}\,\boldsymbol{T}_{s,p} \\ +\ \boldsymbol{T}_{p,s}\,\dot{\boldsymbol{T}}_{b,p}\,\boldsymbol{I}_b\,\boldsymbol{T}_{p,b}\,\boldsymbol{T}_{s,p} \\ +\ \boldsymbol{T}_{p,s}\,\boldsymbol{T}_{b,p}\,\boldsymbol{I}_b\,\dot{\boldsymbol{T}}_{p,b}\,\boldsymbol{T}_{s,p} \\ +\ \boldsymbol{T}_{p,s}\,\boldsymbol{T}_{b,p}\,\boldsymbol{I}_b\,\boldsymbol{T}_{p,b}\,\dot{\boldsymbol{T}}_{s,p} \end{pmatrix}}_{\boldsymbol{I}_{s,\omega}}\boldsymbol{\omega}_s + \underbrace{\boldsymbol{T}_{p,s}\,\boldsymbol{T}_{b,p}\,\boldsymbol{I}_b\,\boldsymbol{T}_{p,b}\,\boldsymbol{T}_{s,p}}_{\boldsymbol{I}_{s,\dot{\omega}}}\dot{\boldsymbol{\omega}}_s \\
&= \boldsymbol{I}_{s,\omega}\,\boldsymbol{\omega}_s + \boldsymbol{I}_{s,\dot{\omega}}\,\dot{\boldsymbol{\omega}}_s
\end{aligned} \tag{2.30}$$

For the modelling of the CVP propeller, the loads are desired in the propeller coordinate system. The inertial torque vector, in the propeller coordinate system, is determined as:

$$\begin{aligned}
\boldsymbol{M}_{iner,p} &= \boldsymbol{T}_{s,p}\,\left(\boldsymbol{I}_{s,\omega}\,\boldsymbol{\omega}_s + \boldsymbol{I}_{s,\dot{\omega}}\,\dot{\boldsymbol{\omega}}_s\right) \\
&= \underbrace{\boldsymbol{T}_{s,p}\,\boldsymbol{I}_{s,\omega}\,\boldsymbol{T}_{p,s}}_{\boldsymbol{I}_{p,\omega}}\,\boldsymbol{\omega}_p + \underbrace{\boldsymbol{T}_{s,p}\,\boldsymbol{I}_{s,\dot{\omega}}\,\boldsymbol{T}_{p,s}}_{\boldsymbol{I}_{p,\dot{\omega}}}\,\dot{\boldsymbol{\omega}}_p \\
&= \boldsymbol{I}_{p,\omega}\,\boldsymbol{\omega}_p + \boldsymbol{I}_{p,\dot{\omega}}\,\dot{\boldsymbol{\omega}}_p
\end{aligned} \tag{2.31}$$

2.4.3 Inertial Loads

From Eq. 2.19 and Eq. 2.31 the inertia model in the propeller coordinate system is:

$$\begin{bmatrix} \boldsymbol{F}_{iner,p} \\ \boldsymbol{M}_{iner,p} \end{bmatrix} = \begin{bmatrix} m_b \, \boldsymbol{T}_{G,p} \, \mathbf{r}_{CM} \\ \mathbf{I}_{p,\omega} \, \boldsymbol{\omega}_p + \mathbf{I}_{p,\dot{\omega}} \, \dot{\boldsymbol{\omega}}_p \end{bmatrix} \tag{2.32}$$

Applying the inertia model in Eq. 2.32 for the three pitch trajectories defined in Section 2.2 and the operating condition in Table 2.1 gives the inertial loads in Figure 2.9.

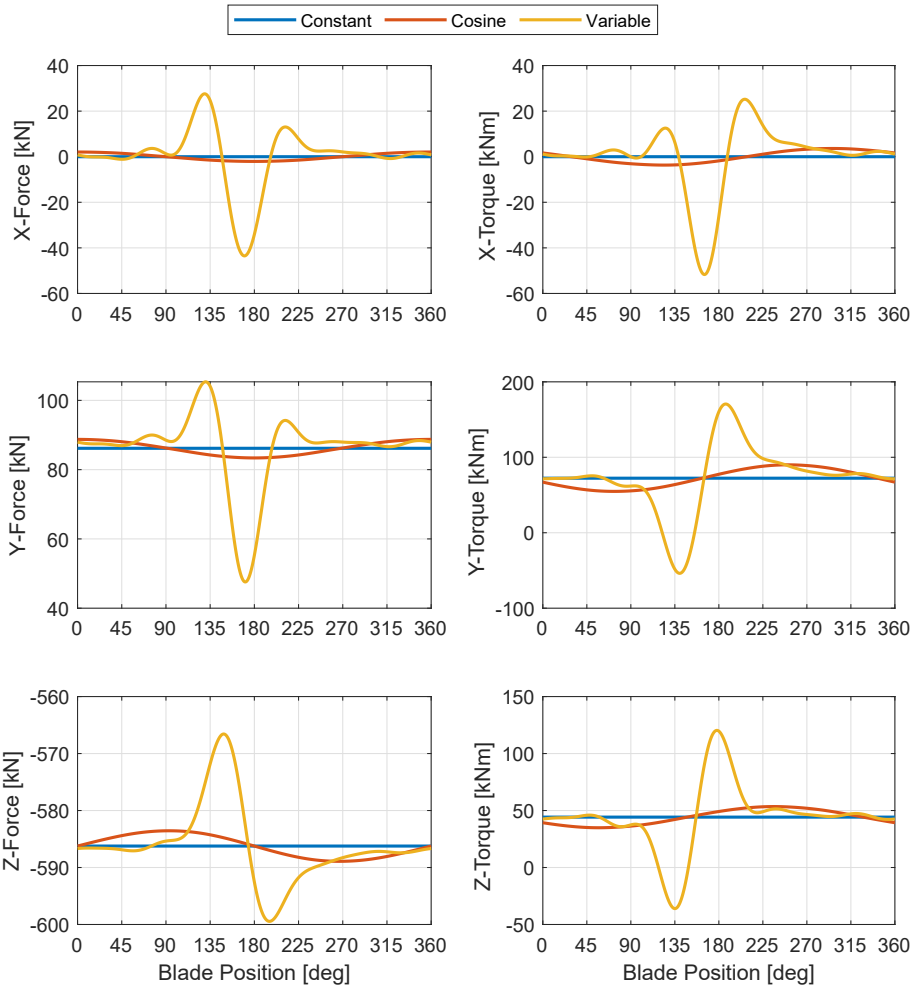

Figure 2.9: The inertial forces and torques acting on the propeller blade for the pitch trajectories determined in Section 2.2.

From Figure 2.9 it is seen that the inertial loads varies the most for the variable pitch trajectory. The constant offset in the inertial loads is due to the rotation of the propeller and the cyclical variations are due to the pitching of the blade. It is seen that the variation in the inertial forces in the x- and y-direction and the inertial torque about the x-axis, has a shape which is similar to the pitch acceleration. The other inertial loads are shaped similar to the pitch rate, which shows the coupling between the pitch rate and acceleration in the inertial loads.

2.5 Modelling of Hydrodynamical Loads

In this section the hydrodynamical loads acting on the CVP propeller blades, when operating in a non-uniform wake field, are determined through the use of computational fluid dynamics (CFD) simulations. The CFD simulations were made for the three pitch trajectories described in Section 2.2. The complete description of the setup of the simulations, uncertainty study and simulation results are given in Appendix A. This section summarizes the methods used and the results from Appendix A. For more details see Appendix A.

The CFD simulations were made using the program STAR-CCM+ 12.02.010. The simulations of the CVP propeller were made as unsteady single phase simulations assuming an incompressible fluid and using the segregated flow solver. The turbulence is accounted for by using the SST kω RANS turbulence model.

The domain of the simulation is shown in Figure 2.10 with the dimensions; $L_r = 10.5D_p$, $L_b = 12.7\,D_p$ and $L_f = 4\,D_p$. The rotation of the propeller is made using a sliding mesh interface between the stationary region and the rotating propeller region, shown as the yellow region in Figure 2.10. The pitching of the blades is made by morphing the mesh in the propeller region.

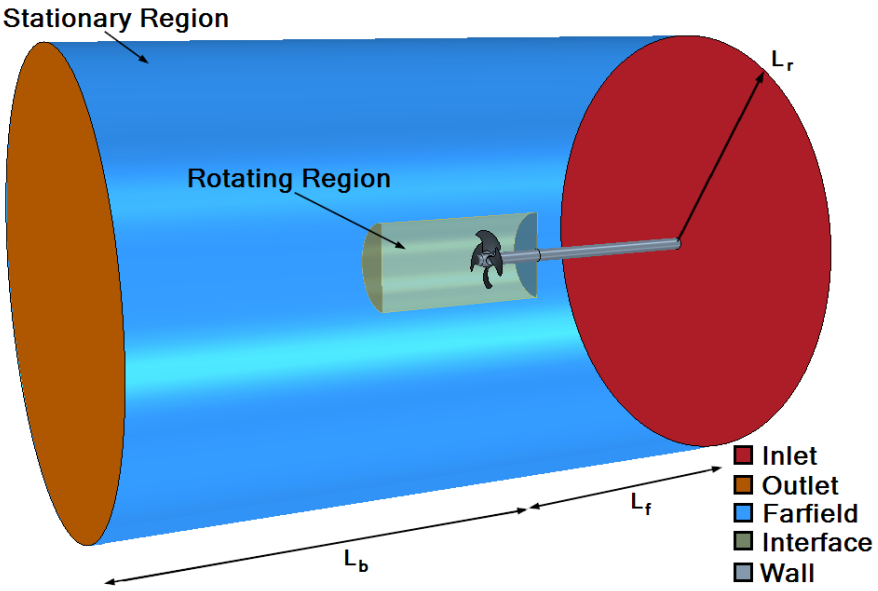

Figure 2.10: The domain used in the CFD simulations of the CVP propeller in a non-uniform wake field.

The discretization of the domain is made using STAR-CCM+'s unstructured polyhedral mesher with prism layer cells near the walls. The prism layer settings are such that the y^+-value is $\approx$ 100 for the first prism layer. Because the viscous sublayer is not resolved, STAR-CCM+'s all y^+ wall function is used. The spatial discretization of the domain is made for five different refinements from $\approx$ 1.5 million cells to $\approx$ 13.6 million cells. Four different temporal discretizations are used in the simulations. These different discretizations are used to determine the uncertainty in the simulation results due to discretization. To determine the discretization uncertainty of the simulations, the method in Appendix C is used for the cycle of the simulations that has obtained periodic convergence. The method used to determine if periodic convergence has been obtained is also described in Appendix C.

The wake field implemented into the CFD simulation is the measured nominal wake field, scaled by using the thrust identity method of [46]. The axial velocity components of the non-uniform wake field are imposed as a boundary condition on the inlet. The transverse velocity components of the non-uniform wake field are made by distributing momentum sources upstream of the propeller (between the inlet and the propeller). The strength of the momentum sources is determined through an iterative process.

The hydrodynamical forces and torques acting on the propeller blade, determined from the CFD simulation with the finest discretization, are shown in Figure 2.11 for the three pitch trajectories.

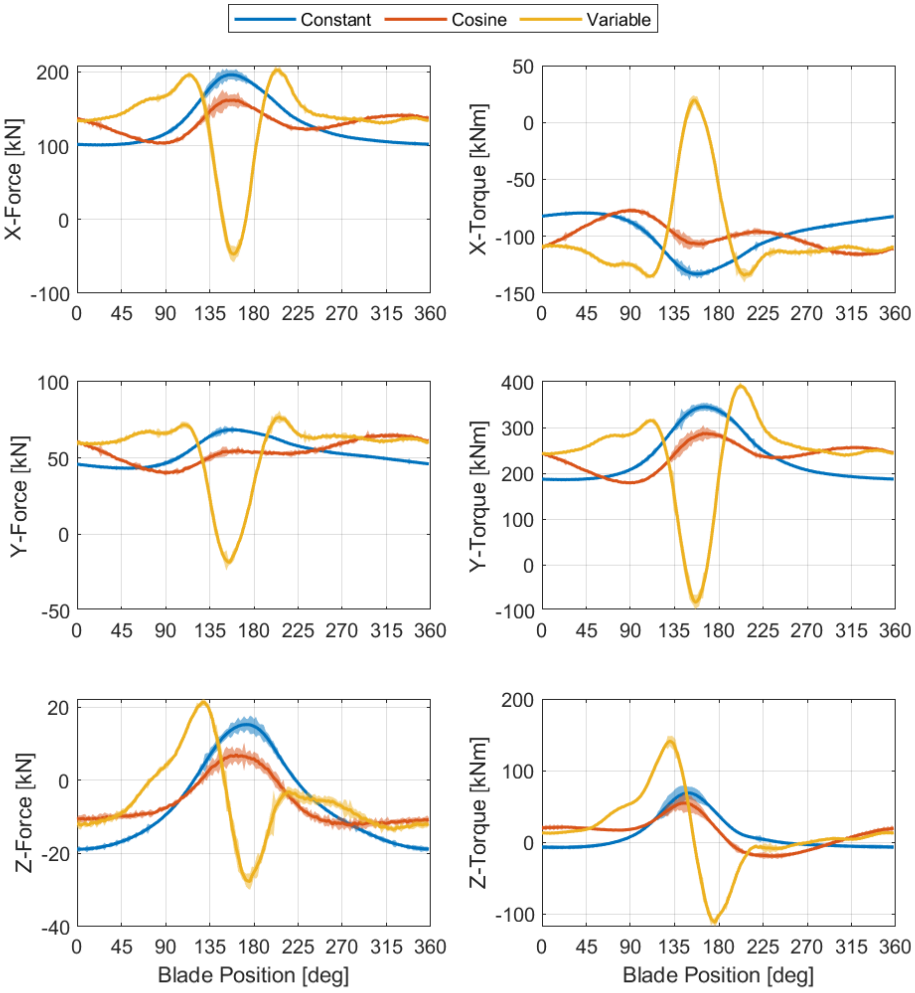

Figure 2.11: The hydrodyanmical forces and torques acting on the propeller blade for the pitch trajectories determined in Section 2.2.

From Figure 2.11 it is seen, for the constant pitch trajectory, that the loads change significantly, around the wake peak (i.e. blade position about 180°) and also that the uncertainty of the CFD simulation is largest around the wake peak. For the cosine pitch trajectory, the change in the loads is generally reduced. This is in agreement with what is expected when using the CVP propeller. With the variable pitch trajectory, according to [66], it is expected that the load variations should be further reduced. This is not the case as can be seen from Figure 2.11. The variation in the loads is largest for the variable pitch trajectory and therefore it cannot be considered as an optimum pitch trajectory for the CVP propeller. This may be due to the quasi-steady

assumption, used in [66] to determine the optimum pitch trajectory, not being an appropriate assumption when the variations in the pitch trajectory are large enough. It may be more appropriate to use the quasi-steady assumption when the variations in the pitch trajectory is limited, as for the cosine pitch trajectory. Considering the shape of the loads for the variable pitch trajectory in Figure 2.11 then it can be seen that the forces and torques in the x- and y-direction are similarly shaped as the pitch acceleration in Figure 2.7. The z-components of force and torque are shaped similar to the pitch rate in Figure 2.6. This indicates that the pitch rate and acceleration influences the load response. The pitch rate and acceleration are not considered under the quasi-steady assumption used in [66].

It is desired to use the CVP propeller as an efficiency improving device for ship propulsion. It is therefore relevant to consider the efficiency of the propeller for the different pitch trajectories even though the same propeller blade design is used for the three pitch trajectories. For the CFD simulations the propeller efficiency, η_p, is determined as:

$$\eta_p = \frac{T\, V_a}{\omega_p\, Q} \tag{2.33}$$

T is the propeller thrust. V_a is the average advance velocity of the water into the propeller. ω_p is the rotational speed of the propeller. Q is the propeller torque. From this the propeller efficiency is determined for each of the pitch trajectories which are given in Table 2.2.

Table 2.2: Propeller efficiency for the different pitch trajectories based on the CFD simulations of the CVP propeller.

	Constant	**Cosine**	**Variable**
η_p	$0.6464 \begin{matrix}\pm 0.0150 \\ \pm 2.3134\%\end{matrix}$	$0.6460 \begin{matrix}\pm 0.0168 \\ \pm 2.5941\%\end{matrix}$	$0.6436 \begin{matrix}\pm 0.0211 \\ \pm 3.2829\%\end{matrix}$

From Table 2.2 it can be seen that there is a small variation in the propeller efficiency for each pitch trajectory. The variations are within the uncertainty bounds of the simulations and therefore no direct conclusion can be made from this. It should be noted that the same blade design has been used for all the CFD simulations and therefore the same results as in [66] cannot be expected. In [66] the blade design is changed for each pitch trajectory. Concluding whether an efficiency gain is obtainable or not, using the CVP propeller with adapted blade design, is therefore not currently possible.

2.6 Modelling of Gravitational Loads

The gravitational force acts in the negative z-direction in the ship coordinate system as:

$$\boldsymbol{F}_{g,s} = \begin{bmatrix} 0 \\ 0 \\ -m_b\, g \end{bmatrix} \tag{2.34}$$

g is the gravitational acceleration. To get the gravitational forces in the propeller coordinate system, the transformation from the ship coordinate system to the propeller coordinate system is as:

$$\boldsymbol{F}_{g,p} = \boldsymbol{T}_{s,p}\, \boldsymbol{F}_{g,s} \tag{2.35}$$

The torques due to the gravitational force are determined using the cross product of the gravitational force vector and the position vector for the center of mass. The torque due to the gravitational force is:

$$\boldsymbol{M}_{g,s} = \boldsymbol{F}_{g,s} \times \boldsymbol{r}_{CM,s} \tag{2.36}$$

The position vector for the center of mass is constant in the blade coordinate system and it has to be transformed into the ship coordinate system. The gravitational torque is therefore determined as:

$$\boldsymbol{M}_{g,s} = \boldsymbol{F}_{g,s} \times \boldsymbol{T}_{p,s}\, \boldsymbol{T}_{b,p}\, \boldsymbol{r}_{CM} \tag{2.37}$$

To model the CVP propeller the torque is desired in the propeller coordinate system. The torque is therefore transformed into the propeller coordinate system as:

$$\begin{aligned} \boldsymbol{M}_{g,p} &= \boldsymbol{T}_{s,p}\, \boldsymbol{M}_{g,s} \\ &= \boldsymbol{T}_{s,p} \left(\boldsymbol{F}_{g,s} \times \boldsymbol{T}_{p,s}\, \boldsymbol{T}_{b,p}\, \boldsymbol{r}_{CM} \right) \end{aligned} \tag{2.38}$$

Applying the above model for gravitational loads, with the pitch trajectories determined in Section 2.2, gives the gravitational loads in Figure 2.12.

From Figure 2.12 it is seen that the gravitational loads acting on the blade do not change significantly for the different pitch trajectories.

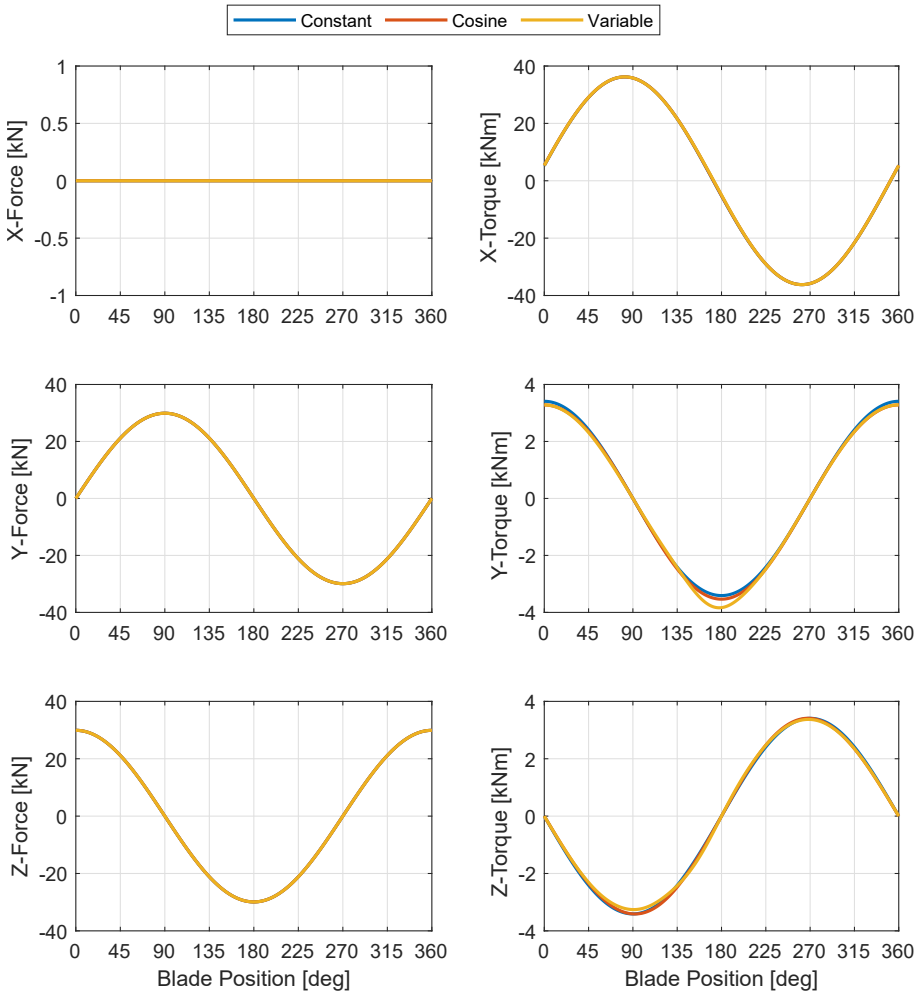

Figure 2.12: The gravitational forces and torques acting on the propeller blade for the pitch trajectories determined in Section 2.2.

2.7 Modelling of Buoyancy Loads

The buoyancy loads acting on the propeller blade are due to the hydrostatic pressure acting on the blade. There are two sources for the hydrostatic pressure: one is for the water surrounding the blade and the other is from the hydrostatic pressure of the lubrication oil in the hub acting on the blade foot. The hydrostatic pressure, p_{hydro}, from the surrounding water is determined in the ship coordinate system as a function of the immersion of the blade, z_s,

as:

$$p_{hydro}(z_s) = p_{sc} - \rho\, g\, z_s \tag{2.39}$$

ρ is the density of the water. p_{sc} is the hydrostatic pressure at the origin of the ship coordinate system. The origin of the ship coordinate system lies in the center of the shaft and p_{sc} is determined as:

$$p_{sc} = \rho\, g\, h_s \tag{2.40}$$

h_s is the immersion of the shaft center relative to the water line and is given in Table 2.1. The force acting on the blade due to the hydrostatic pressure acts normal to the surface of the blade. The surface of the blade is a complex geometry and is difficult to describe in a closed-form expression. The forces and torques due to the hydrostatic pressure are therefore determined numerically. To determine the forces and torques numerically the finest surface mesh of the blade, used to model the hydrodynamic forces and torques in Section 2.5 and Appendix A, is used. The surface mesh of the blade is shown in Figure 2.13.

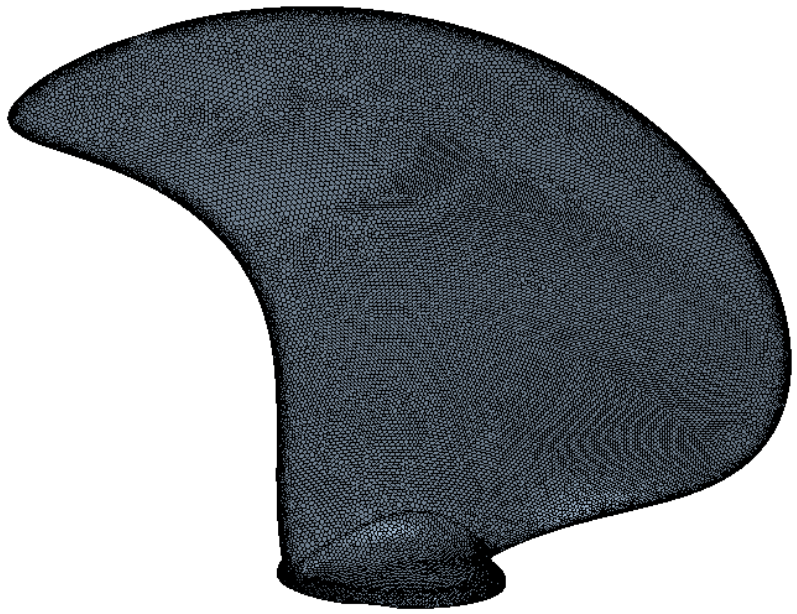

Figure 2.13: Surface mesh of the propeller blade.

The position, $\boldsymbol{r}_A$, and area, $\boldsymbol{A}$, vectors for each face of the blade surface are used to determine the forces and torques due to the hydrostatic pressure from the surrounding water as:

$$\boldsymbol{F}_{b,p} = \boldsymbol{T}_{s,p} \sum_{i=1}^{N_{faces}} p_{hydro,i}(\boldsymbol{T}_{p,s}\,\boldsymbol{T}_{b,p}\,\boldsymbol{r}_{A,z,i})\,\boldsymbol{T}_{p,s}\,\boldsymbol{T}_{b,p}\,\boldsymbol{A}_i \tag{2.41}$$

$$\boldsymbol{M}_{b,p} = \boldsymbol{T}_{s,p} \sum_{i=1}^{N_{faces}} p_{hydro,i}(\boldsymbol{T}_{p,s}\,\boldsymbol{T}_{b,p}\,\boldsymbol{r}_{A,z,i})\,\boldsymbol{T}_{p,s}\,\boldsymbol{T}_{b,p}\,\boldsymbol{A}_i \times \boldsymbol{T}_{p,s}\,\boldsymbol{T}_{b,p}\,\boldsymbol{r}_{A,i} \tag{2.42}$$

In Eq. 2.41 and Eq. 2.42 the vectors $\boldsymbol{r}_A$ and $\boldsymbol{A}$ are defined in the blade coordinate system and therefore they have to be transformed into the ship coordinate system. In the ship coordinate system the hydrostatic pressure is calculated using Eq. 2.40. From the hydrostatic pressure, the forces and torque are determined and transformed to the propeller coordinate system. $\boldsymbol{r}_{A,z,i}$ denotes the z-component of the i'th position vector.

Using this numerical approach to determine the forces and torques acting on the propeller blade does not include the pressure inside the hub. The area under the blade foot inside the hub is filled with lubrication oil which is used to lubricate the blade bearing. The lubrication oil is typically pressurized by elevating the tank with the lubrication oil a couple of meters above the waterline. In the propeller coordinate system this gives a force contribution in the z-direction which is determined as:

$$\boldsymbol{F}_{b,p} = \begin{bmatrix} 0 \\ 0 \\ p_{hub}\,A_{bf} \end{bmatrix} + \boldsymbol{T}_{s,p} \sum_{i=1}^{N_{faces}} p_{hydro,i}(\boldsymbol{T}_{p,s}\,\boldsymbol{T}_{b,p}\,\boldsymbol{r}_{A,z,i})\,\boldsymbol{T}_{p,s}\,\boldsymbol{T}_{b,p}\,\boldsymbol{A}_i \tag{2.43}$$

Where,

$$p_{hub} = \rho_{oil}\,g\,((h_s + h_{tank}) + h_{hb}\,\cos(\theta_b)) \tag{2.44}$$

p_{hub} is the pressure of the lubrication oil inside the hub acting on the bottom of the blade foot. A_{bf} is the area of the bottom of the blade foot. ρ_{oil} is the density of the lubrication oil. h_{tank} is the evaluation of the lubrication tank above waterline. h_{hb} is the distance from the hub center to the bottom of the blade foot. Using Eq. 2.42 and Eq. 2.43 for the three pitch trajectories gives the forces and torques due to the hydrostatic pressure shown in Figure 2.14 for both the water and lubrication oil, individually and collected.

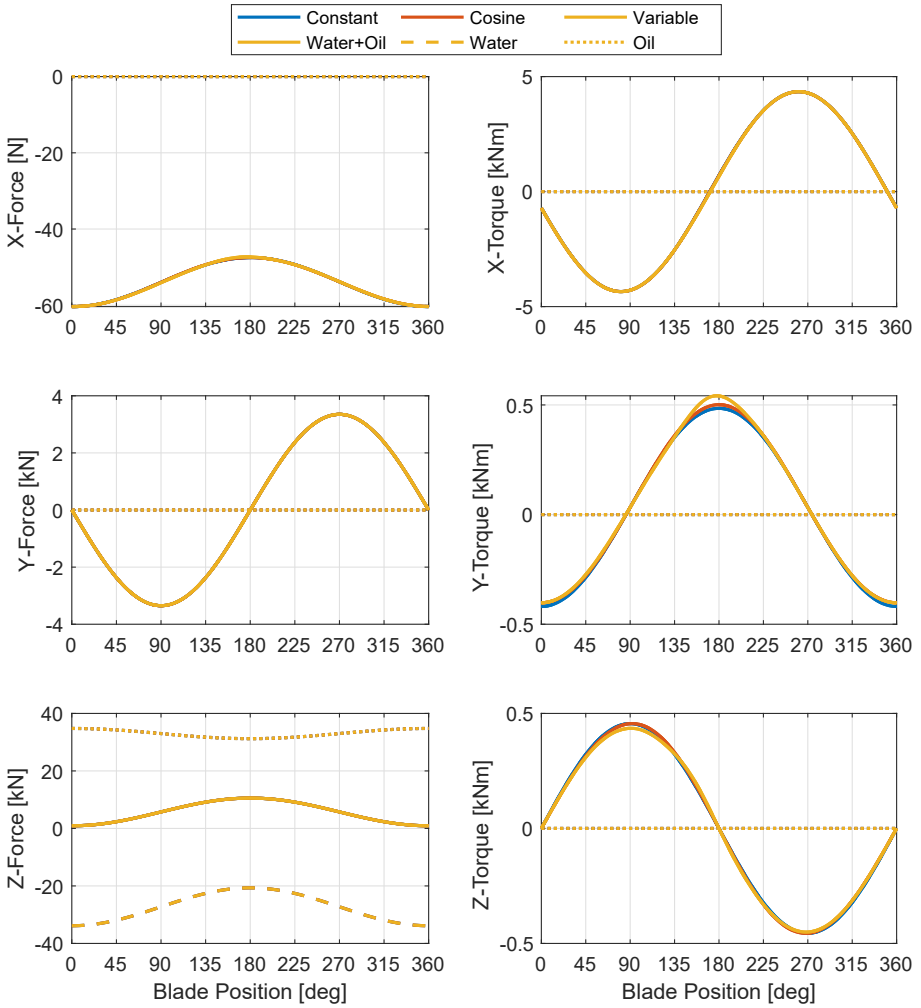

Figure 2.14: The buoyancy forces and torques acting on the propeller blade for the pitch trajectories determined in Section 2.2.

From Figure 2.14 it is seen that the variation in the buoyancy loads for the different pitch trajectories is small. The model used for the hydrodynamics of the CVP propeller in Section 2.5 already includes the hydrostatic pressure from the water acting on the propeller blades. The only pressure acting on the blade that is not accounted for is the pressure of the lubrication oil in the hub. This gives a force in the positive z-direction on $\approx 33[kN]$. Some of the models in Chapter 3 for the hydrodynamics have to determine the buoyancy load separately. This is why there is a longer derivation of the buoyancy loads in this section.

2.8 Modelling of Frictional Loads

The friction is due to the relative motion between the contact surfaces of the blade foot and the hub in the blade bearing. The blade bearing for a CP propeller is illustrated in Figure 2.15. For the modelling of the friction it is assumed that the same blade bearing principle is used for the CVP propeller.

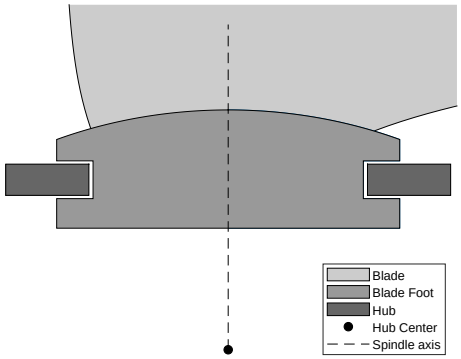

Figure 2.15: Cut view sketch of the blade bearing for a CP propeller. The blade foot is axisymmetric around the spindle axis.

Most experimental data on the friction in CP propeller is based on measuring the pressure difference over the servo piston during pitch changes as in [76, 97]. The friction contribution in these measurements is not only due to the friction in the blade bearing but also due to the friction in the crank-slot/pin-slot mechanism and the bearings supporting the oil pipes to and from the piston chambers.

Modelling of the friction in the blade bearing for CP propellers is presented in [13, 34, 35, 69, 89]. In [13, 69] the modelling is formulated to analyse the dynamic behaviour of CP propellers and [96] uses it for active pitch control to improve performance. In [34, 35, 89] the friction in the blade bearing is modelled to predict the oscillating motion of the blade which can cause fretting wear. Wear due to fretting can result in a failure of the system.

The friction models considered in [13, 35] are both static and dynamic friction models. The main reason for using the dynamic friction model is due to the potential numerical issues when using the static friction model to solve for the motion of the blade. In this section a static friction model is used, since there should not be any issues with numerical stability because the pitch motion of the blade is known. The classical static friction model is a function of the velocity as shown in Figure 2.16 and the normal loading [74].

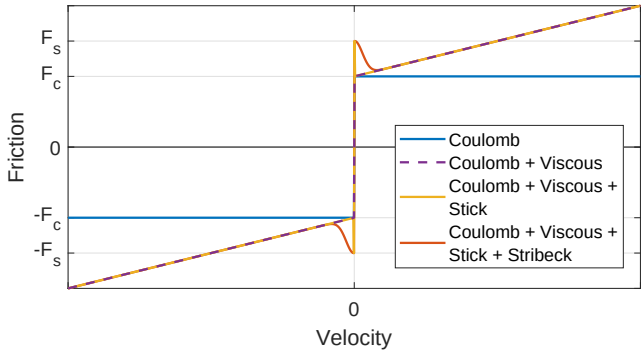

Figure 2.16: Static friction models as a function of the velocity.

In Figure 2.16 there are four different friction components. These components are; Coulomb, viscous, stiction and Stribeck. The simplest friction model has only the contribution from the Coulomb friction, which is discontinuous at zero velocity. At zero velocity the frictional force is equal to the force exciting the motion, if this force is smaller than the Coulomb friction. The friction due to Coulomb is determined as [74]:

$$F_{fric} = \begin{cases} \underbrace{\mu_c F_N}_{F_c} \operatorname{sign}(v) & \text{if } v \neq 0 \\ F_e & \text{if } v = 0 \text{ and } F_e < F_c \\ F_c \operatorname{sign}(F_e) & \text{otherwise} \end{cases} \tag{2.45}$$

F_{fric} is the friction force. μ_c is the Coulomb friction coefficient. F_N is the normal force i.e. the force each body exerts on each other on the bodies contact surfaces. F_c is the Coulomb frictional force. F_e is the force exciting the motion of the body. v is the relative velocity between the two bodies.

The second friction model includes a viscous contribution due to the fluid in the gap between the two bodies. In Figure 2.16 the viscous friction is shown as a linear function of the velocity. The order of the viscous friction may vary depending on the application [74]. The third friction model adds the contribution due to stiction. The stiction is caused by the frictional force required to initialize the motion is larger than the Coulomb friction. The stiction friction is therefore only present when the velocity is zero. The stiction friction force F_s is determined in the same manner as the Coulomb frictional force but instead of using the Coulomb friction coefficient μ_c, the stiction friction coefficient μ_s is used. The last contribution is the Stribeck friction which is the gradual transition from the stiction friction to the Coulomb and viscous friction as shown in Figure 2.16. The friction model including the four com-

ponents is [74]:

$$F_{fric} = \begin{cases} \left(F_c + (F_s - F_c)\ e^{-\left|\frac{v}{v_s}\right|^2} \right) \text{sign}\,(v) + F_v & \text{if } v \neq 0 \\ F_e & \text{if } v = 0 \text{ and } F_e < F_s \\ F_s \,\text{sign}\,(F_e) & \text{otherwise} \end{cases} \tag{2.46}$$

v_s is the Stribeck velocity. F_v is the viscous frictional force. In order to use the friction model in Eq. 2.46, a number of parameters have to be determined for the application. These parameters are: the Coulomb friction coefficient, stiction friction coefficient, Stribeck velocity and the viscous frictional force. The most comprehensive study made for these parameters, with respect to CP propellers, is [35]. In [35] the parameters are fitted to experimental data obtained on a small test bench. The parameters are estimated as $\mu_c \approx 0.1$ and $\mu_s \approx 0.11$.

The aim of the model, presented in this chapter, is to determine the loads acting on the propeller blades and to determine the requirements for the individual pitch mechanism. It is therefore better to overestimate the friction and thereby the requirements for the actuation system than to underestimate the friction. This is especially the case since knowledge about the modelling of the friction and the friction coefficients is still sparse for CP propellers and requires further research. The friction model used is therefore chosen to be the Coulomb friction model with a Coulomb friction coefficient of 0.15 to account for stiction and to be conservative. This friction model may not be conservative enough if the viscous effect is significant. The friction model in Eq. 2.46 is therefore reduced to:

$$F_{fric} = \begin{cases} F_c \,\text{sign}\,(v) & \text{if } v \neq 0 \\ F_e & \text{if } v = 0 \text{ and } F_e < F_c \\ F_c \,\text{sign}\,(F_e) & \text{otherwise} \end{cases} \tag{2.47}$$

Having decided on the friction model used in the modelling of the CVP propeller, the remaining factor to be determined is the normal force F_N. The load the hub exerts on the blade and vice-versa are the reactive loads. To model the reactive loads, a new blade bearing coordinate system is defined as shown in Figure 2.17a. The notation used for the dimensional of the bearing are shown in Figure 2.17b. The dimensions of the blade bearing considered are given in Table 2.3.

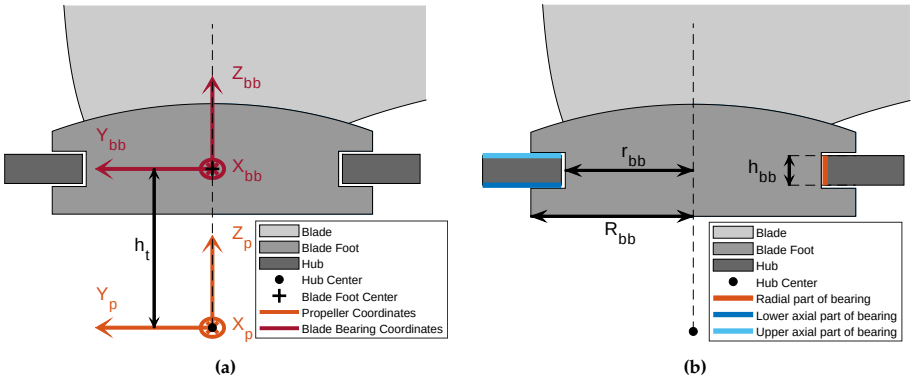

Figure 2.17: (a) The blade bearing coordinate system relative to the propeller coordinate system. **(b)** Notation and definitions used for the blade bearing.

Blade bearing dimensions

Outer radius of blade bearing	R_{bb}	412.5	$[mm]$
Inner radius of blade bearing	r_{bb}	325	$[mm]$
Height of blade bearing	h_{bb}	115	$[mm]$
Translation length	h_t	527.5	$[mm]$

Table 2.3: Blade bearing parameter for the case considered.

The new blade bearing coordinate system (X_{bb},Y_{bb},Z_{bb}) is a translation of the propeller coordinate system along the spindle axis. The translation is such that the origin of the blade bearing coordinate system is located in the middle of the bearing as shown in Figure 2.17a. It is assumed that the origin of the blade bearing coordinate system lies in the blade bearing's center of stiffness. The center of stiffness is the center at which the blade will tilt around due to the torques about the x- and y-axis. To use the blade bearing coordinate system, the forces and torques in the propeller coordinate system have to be transformed to the blade bearing coordinate system. The forces in the blade bearing coordinate system are the same as the forces in the propeller coordinate system. The torque vector in the blade bearing coordinate system ($\boldsymbol{M}_{bb}$) is determined as:

$$\boldsymbol{M}_{bb} = \boldsymbol{M}_p - \boldsymbol{r}_t \times \boldsymbol{F}_p \tag{2.48}$$

$\boldsymbol{M}_p$ is the torque vector in the propeller coordinate system. $\boldsymbol{r}_t$ is the translation vector from the propeller coordinate system to the blade bearing coordinate system. In this case the translation vector $\boldsymbol{r}_t = [0 \;\; 0 \;\; h_t]^T$. $\boldsymbol{F}_p$ is the force vector in the propeller coordinate system.

There are three contact surfaces in the blade bearing, as shown in Figure 2.17b. These surfaces are the upper and lower axial surfaces and the radial surface. The reactive loads can, in principle, act on any of the surfaces. The friction varies depending on which surface the reactive loads act upon. To model the reactive loads some assumptions are made about which surfaces the reactive loads act upon and these assumptions are;

- The reactive forces $F_{reac,x,bb}$ and $F_{reac,y,bb}$ are assumed to act upon the radial surface of the blade bearing.
- The reactive force $F_{reac,z,bb}$ is assumed to act upon the axial surfaces of the blade bearing.

The reactive torques $M_{reac,x,bb}$ and $M_{reac,y,bb}$ can, in principle, act upon either the radial or the axial surfaces depending on the clearance in the blade bearing, if the blade bearing is assumed to be rigid. In reality the blade bearing is not rigid and it is elastic deformed when loaded. If the elastic deformation is considered then the reactive torques $M_{reac,x,bb}$ and $M_{reac,y,bb}$ can act upon all the surfaces at the same time. To determine the influence of which surface the reactive torque acts upon, different loading models are investigated. These models are not limited to which surface the reactive torques act upon but also include different assumptions with respect to the load distribution on these surfaces. Due to the elastic deformation of the blade bearing under loading, the reactive loads may not act at a single point. Instead, the loading may be distributed over an area of the blade bearing surfaces. In total seven different models are investigated. These models are shown in Figure 2.18. The different models in Figure 2.18 will be referred to by their subfigure notation, such as Figure 2.18a is model A, Figure 2.18b is model B, etc.

The models in Figure 2.18 can be divided into two types, one where the resulting reactive torque $M_{reac,xy,bb}$ acts upon the axial surface (model A-D) and the others where the resulting reactive torque $M_{reac,xy,bb}$ acts upon the radial surface (model E-G). For the models where the resulting reactive torque $M_{reac,xy,bb}$ acts upon the axial surface, it is assumed that the surfaces can be viewed as a disc in the xy-plane of the blade bearing coordinate system.

The force and torque vectors F_{xy} and M_{xy} in Figure 2.18 are the force and torque due to the resulting reactive force and torque $F_{reac,xy,bb}$ and $M_{reac,xy,bb}$, respectively. The red shaded areas are the assumed shape of the load distribution, q, for the model. In the models without the red shaded areas the loads are considered to act at points.

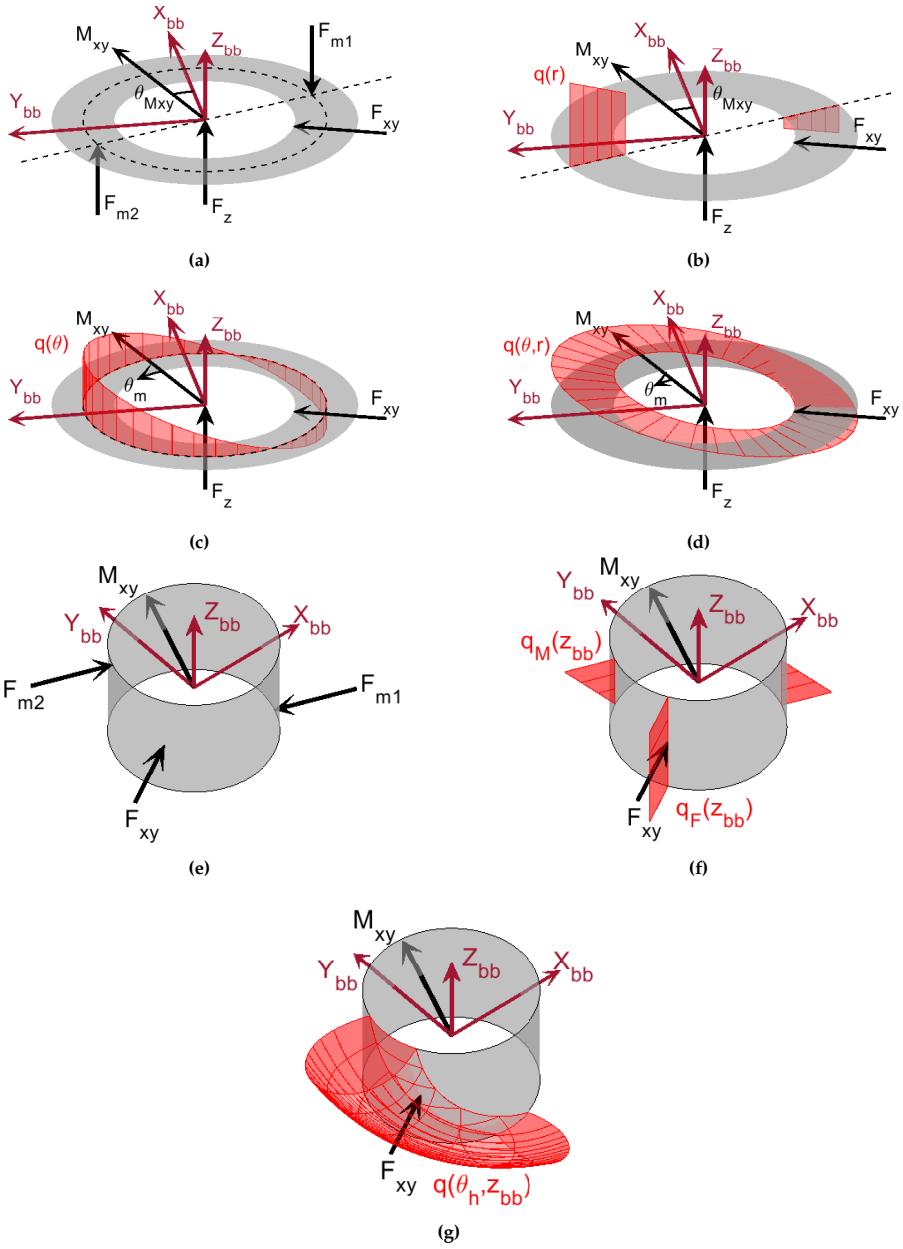

Figure 2.18: Different models for the load distribution of the resulting torque $M_{reac,xy,bb}$ in the blade bearing.

The derivation of the Coulomb friction for the different load distribution models in Figure 2.18 is presented in Appendix B. The derivation of the Coulomb friction in Appendix B results in 13 different models for the Coulomb friction. The increase in models is because additional submodels are used for each model in Figure 2.18. For the models A-D, two assumptions about the load distribution in the radial bearing surface can be made. These two load distribution models are shown in Figure 2.19.

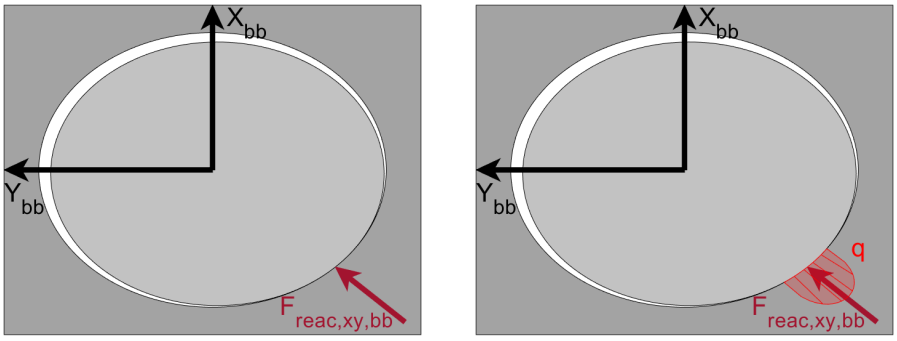

(a) (b)

Figure 2.19: **(a)** Point load on the radial surface. **(b)** Elliptical load distribution on the radial surface.

In Figure 2.19a the load acts at a point and in Figure 2.19b the load has an elliptical distribution over the surface according to Hertzian contact mechanics. The models using the point load assumption are indicated with a subscript "p" as in model B_p and the models using the Hertzian contact assumption are indicated with a subscript "h" as in model B_h. Model A_h is not investigated since the model A assumes point loads which is violated if model A_h is used.

Similar considerations are made for the axial surfaces when the resulting reactive torque $M_{reac,xy,bb}$ is assumed to act on the radial surface only i.e. model E-G. The two cases considered are shown in Figure 2.20.

In Figure 2.20a it is assumed that the reactive force, $F_{reac,z}$ is distributed circumferentially at a fixed radius. This submodel is noted with the subscript "c". In Figure 2.20b it is assumed that the reactive force, $F_{reac,z}$ is distributed uniformly over the whole axial surface. This submodel is noted with the subscript "s".

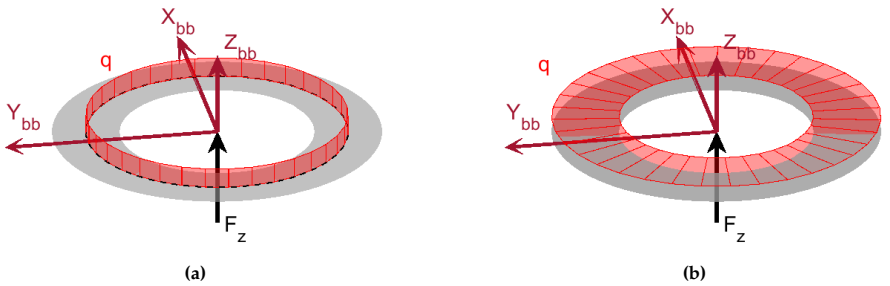

Figure 2.20: (a) Circumferential load distribution over the axial surface. **(b)** Radially and circumferential load distribution over the axial surface.

The friction model implemented into the computation of the friction differs from the one in Eq. 2.47. The friction model implemented is:

$$F_{fric} = \begin{cases} F_c \operatorname{sign}(v) & \text{if } v \neq 0 \\ \kappa F_c \operatorname{sign}(F_e) & \text{if } v = 0 \end{cases} \tag{2.49}$$

Where,

$$\kappa = \min\left(\left|\frac{F_e}{F_c}\right|, 1\right) \tag{2.50}$$

For the case considered, the motion is not excited by a force but by a torque about the z-axis. The excitation torque is determined as:

$$M_{ext,z,bb} = M_{hydro,z,bb} + M_{act,z,bb} + M_{g,z,bb} + M_{b,z,bb} \tag{2.51}$$

The friction model for the pitching motion of the blade is then:

$$\begin{bmatrix} \mathbf{F}_{fric,bb} \\ \mathbf{M}_{fric,bb} \end{bmatrix} = \begin{cases} \begin{bmatrix} \mathbf{F}_{c,bb} \\ \mathbf{M}_{c,bb} \end{bmatrix} \operatorname{sign}(\dot{\theta}_p) & \text{if } \dot{\theta}_p \neq 0 \\ \kappa \begin{bmatrix} \mathbf{F}_{c,bb} \\ \mathbf{M}_{c,bb} \end{bmatrix} \operatorname{sign}(M_{ext,z,bb}) & \text{if } \dot{\theta}_p = 0 \end{cases} \tag{2.52}$$

Where,

$$\kappa = \min\left(\left|\frac{M_{ext,z,bb}}{M_{c,z,bb}}\right|, 1\right) \tag{2.53}$$

$\mathbf{F}_{c,bb}$ and $\mathbf{M}_{c,bb}$ are the Coulomb friction vector determined in Appendix B. The different friction models are compared to each other for each pitch trajectory with respect to the friction about the spindle axis ($M_{fric,z,bb}$) in Figure 2.21. The friction is evaluated using the method described in Section 2.9. The

models which are based on assuming a radius where the load acts on the axial surfaces are shown in Figure 2.21 with a shaded area.

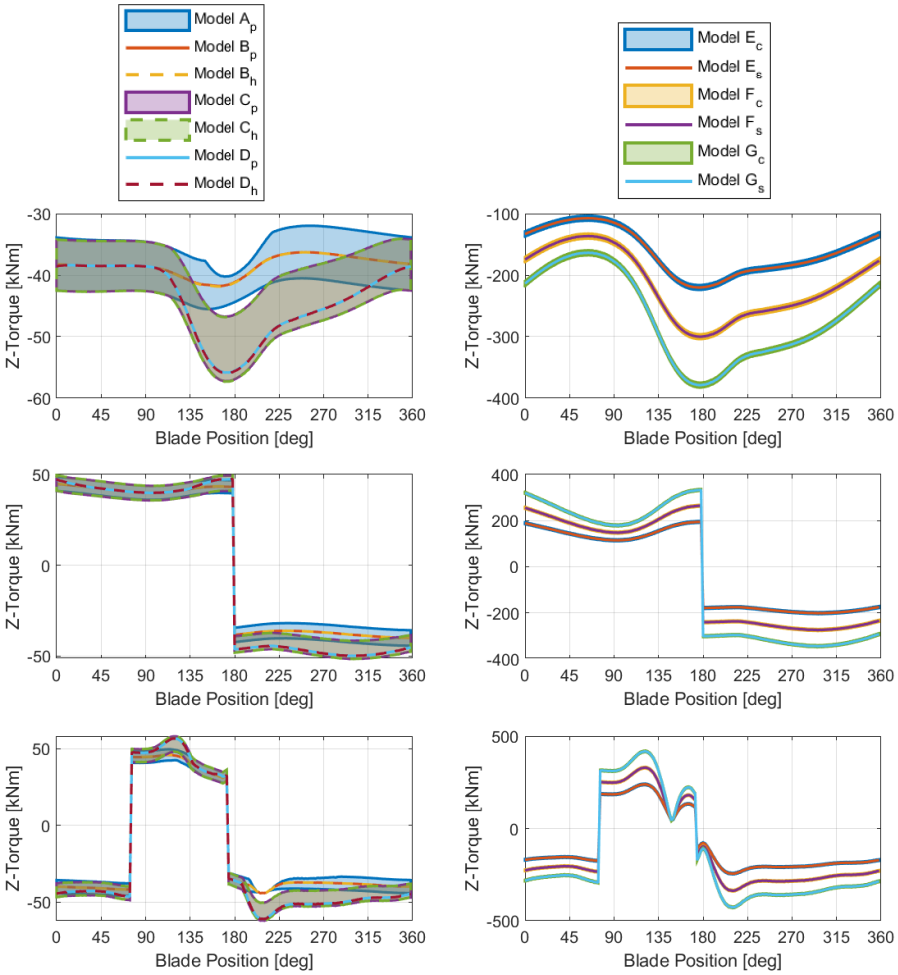

Figure 2.21: Frictional torque about the z-axis for the different friction models. The left column shows the frictional torque using the load distribution models A-D and the right column shows the frictional torque using the load distribution models E-G. The top row plots are for the constant pitch trajectory. The middle row plots are for the cosine pitch trajectory. The bottom row plots are for the variable pitch trajectory.

From Figure 2.21 it is seen that there is little difference between the different submodels for the models B-D. This is because the loading of the radial surface is not large enough for the Hertzian contact modelling to become significant. The same difference is not seen between models F and G where the

difference are approximately a factor of 1.3, which is close to the maximum difference between using Hertzian contact mechanics and a point load.

The models including the Hertzian contact also depend on the clearance between the hub and the blade foot. The smaller the clearance, the larger the friction. The results shown in Figure 2.21 are based on using the maximum allowable clearance due to tolerances. If the smallest allowable clearance is used instead, the frictional torque would increase by a maximum of 162 Nm for the models B_h-D_h. For model G the maximum increase in the frictional torque is 5.5 kNm.

The largest differences between the models is seen between models A-D and the models E-G. These differences are between a factor 2-11. This is a large difference in the friction which depends on the assumptions made for the load distribution in the blade bearing. The models are based on the reactive torque, $M_{reac,xy,bb}$, either acting on the axial or the radial surfaces of the blade bearing. In reality, the reactive torque, $M_{reac,xy,bb}$, more than likely acts partly on both surfaces with a load distribution which differs from the ones investigated here. To investigate this further, it is necessary to make numerical simulations of the elastic deformation of the blade bearing under loading. Such simulations have not been conducted during this work and are left for future work.

The effect of distributing the torque, $M_{reac,xy,bb}$, to both the radial and axial surfaces is investigated with the models presented. This is done by using the axial friction from the models A-D and the radial friction from the models E-G and adding the frictions together. The reactive torque used in the axial friction model is $DR\, M_{reac,xy,bb}$ and the reactive torque used in the radial friction model is $(1 - DR)\, M_{reac,xy,bb}$. DR is the distribution ratio of the reactive torque, $M_{reac,xy,bb}$. The results from using this approach should be bounded by the results shown in Figure 2.21.

The modelling of the friction in the blade bearing is made using the model D for the axial friction and model G for the radial friction. Model D is chosen to be conservative in the determination of the axial friction without having to assume a radius that the load acts upon such as that for model C. For the same reason of being conservative in the determination of the friction, model G is chosen to determine the radial friction. It is assumed that most of the reactive torque acts on the axial surface. The distribution ratio is determined as a function of the geometrical shape of the bearing as:

$$DR = \frac{2\, R_{bb} - h_{bb}}{2\, R_{bb}} \quad \rightarrow \quad DR = 0.86 \tag{2.54}$$

The results for the frictional torque, $M_{fric,z,bb}$, using model D and G are shown in Figure 2.22 for various distribution ratios for the three pitch trajectories.

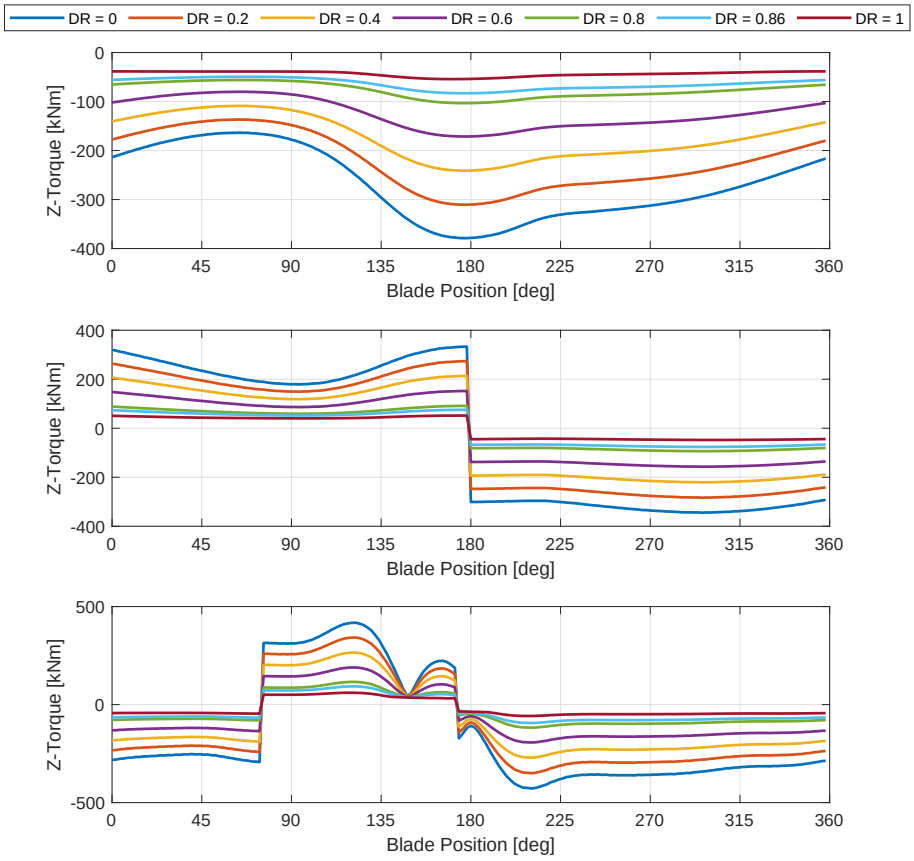

Figure 2.22: Frictional torque about the z-axis by using the model D and G with different load distributions ratios, DR. The top plot is for the constant pitch trajectory. The middle plot is for the cosine pitch trajectory. The bottom plot is for the variable pitch trajectory.

From Figure 2.22 it is seen that at $DR = 1$, the friction is the same as when using model D. For $DR = 0$ the friction is the same as when using model G. A distribution ratio of 0.86 is used for the friction modelling.

2.9 Modelling of Reactive Loads

The reactive loads are the loads that the hub exerts on the blade such that the blade stays in the blade bearing. These loads are determined such that the system of equations in Eq. 2.13, based on Newton's second law of motion, are satisfied. For convenience Eq. 2.13 is shown again in Eq. 2.55.

$$\begin{bmatrix} F_{iner,x,p} \\ F_{iner,y,p} \\ F_{iner,z,p} \\ M_{iner,x,p} \\ M_{iner,y,p} \\ M_{iner,z,p} \end{bmatrix} = \begin{bmatrix} F_{hydro,x,p} + F_{act,x,p} + F_{fric,x,p} + F_{reac,x,p} + F_{g,x,p} + F_{b,x,p} \\ F_{hydro,y,p} + F_{act,y,p} + F_{fric,y,p} + F_{reac,y,p} + F_{g,y,p} + F_{b,y,p} \\ F_{hydro,z,p} + F_{act,z,p} + F_{fric,z,p} + F_{reac,z,p} + F_{g,z,p} + F_{b,z,p} \\ M_{hydro,x,p} + M_{act,x,p} + M_{fric,x,p} + M_{reac,x,p} + M_{g,x,p} + M_{b,x,p} \\ M_{hydro,y,p} + M_{act,y,p} + M_{fric,y,p} + M_{reac,y,p} + M_{g,y,p} + M_{b,y,p} \\ M_{hydro,z,p} + M_{act,z,p} + M_{fric,z,p} + M_{g,z,p} + M_{b,z,p} \end{bmatrix} \tag{2.55}$$

The previous sections have shown how the hydrodynamical, inertial, gravitational, buoyancy and frictional loads are determined. The hydrodynamical, inertial, gravitational and buoyancy loads are determined as functions of the pitch trajectory, the operating condition of the propeller and the design of the propeller blades. The frictional loads depend on the reactive loads and the pitch trajectory. The reactive loads are the loads that the hub exerts on the blade such that the blade stays in the blade bearing and Eq. 2.55 is satisfied. Because the frictional loads depend on the reactive loads, the system of equations in Eq. 2.55 is solved iteratively for each blade position in the wake field. The iterative solving procedure is:

Algorithm 1 Determine the reactive, frictional and actuator loads acting on the CVP propeller blades.

for $\theta_b = 0 \ldots 2\,\pi$ **do**

Compute:

$$\boldsymbol{F}_{hydro,p},\ \boldsymbol{M}_{hydro,p},\ \boldsymbol{F}_{iner,p},\ \boldsymbol{M}_{iner,p},\ \boldsymbol{F}_{g,p},\ \boldsymbol{M}_{g,p},\boldsymbol{F}_{b,p},\ \boldsymbol{M}_{b,p}$$

Minimise:

$$e(F_{reac,x,p}, F_{reac,y,p}, F_{reac,z,p}, M_{reac,x,p}, M_{reac,y,p}, M_{act,z,p})$$

Where,

$$e = \left\| \begin{bmatrix} F_{iner,x,p} - F_{hydro,x,p} - F_{act,x,p} - F_{fric,x,p} - F_{reac,x,p} - F_{g,x,p} - F_{b,x,p} \\ F_{iner,y,p} - F_{hydro,y,p} - F_{act,y,p} - F_{fric,y,p} - F_{reac,y,p} - F_{g,y,p} - F_{b,y,p} \\ F_{iner,z,p} - F_{hydro,z,p} - F_{act,z,p} - F_{fric,z,p} - F_{fric,z,p} - F_{g,z,p} - F_{b,z,p} \\ M_{iner,x,p} - M_{hydro,x,p} - M_{act,x,p} - M_{fric,x,p} - M_{reac,x,p} - M_{g,x,p} - M_{b,x,p} \\ M_{iner,y,p} - M_{hydro,y,p} - M_{act,y,p} - M_{fric,y,p} - F_{reac,y,p} - M_{g,y,p} - M_{b,y,p} \\ M_{iner,z,p} - M_{hydro,z,p} - M_{act,z,p} - M_{fric,z,p} - M_{g,z,p} - M_{b,z,p} \end{bmatrix} \right\|_{L2}$$

end for

The above algorithm computes the hydrodynamical, inertial, gravitational and buoyancy loads using the methods described in the previous sections for each blade position. The reactive loads and the actuation spindle torque $M_{act,z,p}$ are determined through minimising the L2-norm of the error of the system of equations in Eq. 2.55. In the evaluation of the error the friction is determined as in Section 2.8 using the current values of the reactive loads. The five actuator components, $F_{act,x,p}$, $F_{act,y,p}$, $F_{act,z,p}$, $M_{act,x,p}$, and $M_{act,y,p}$ are determined using an actuator model which has not been presented yet. The actuator model depends on the topological design of the pitch mechanism. Since the topological design of the pitch mechanism is not known, the most simple actuator model is used. This is where the five actuator components, $F_{act,x,p}$, $F_{act,y,p}$, $F_{act,z,p}$, $M_{act,x,p}$, and $M_{act,y,p}$ are equal to zero. This is the case if the actuator is a motor which only contributes with a torque about the z-axis to pitch the blades. It is furthermore assumed that there is no friction in the actuator.

Using the above algorithm to determine reactive loads for the different pitch trajectories gives the reactive loads shown in Figure 2.23. The discontinuities in the forces along the x- and y-axes are due to the discontinuities in the friction.

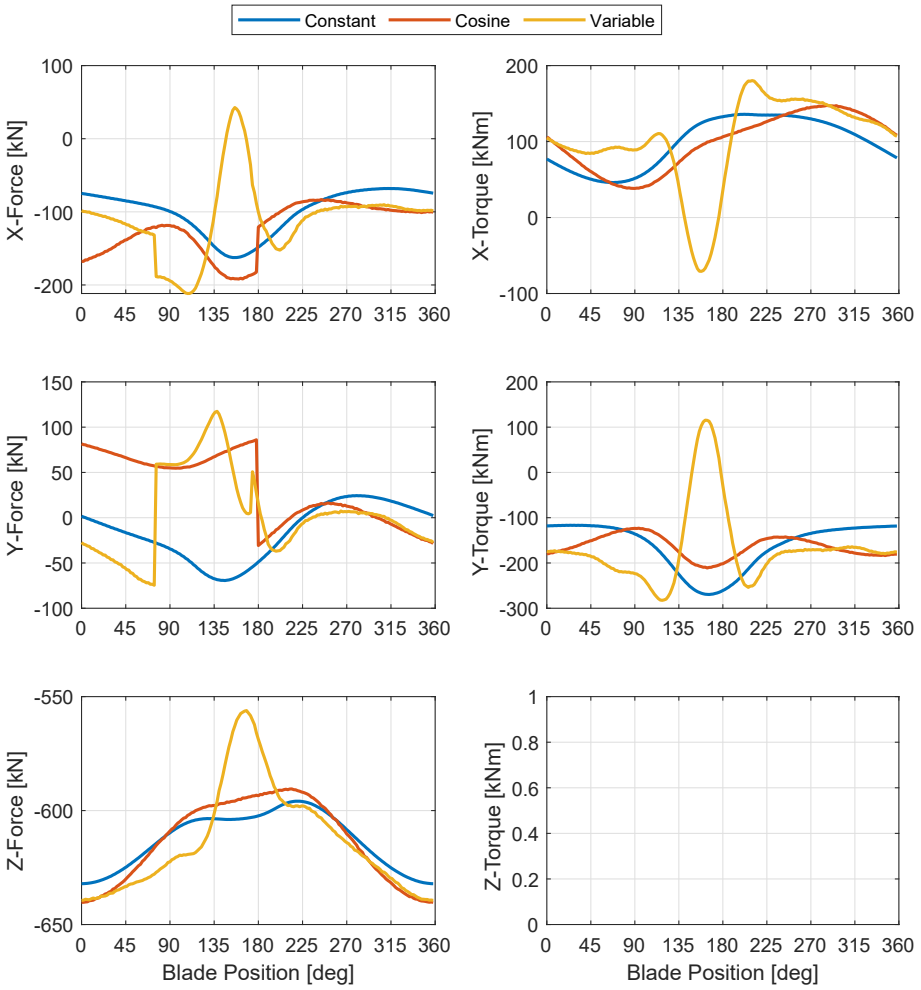

Figure 2.23: The reactive forces and torques acting on the propeller blades for the pitch trajectories determined in Section 2.2.

2.10 Applications of Cyclical Varying Pitch Model

The model for the CVP propeller blades has been derived in the previous sections. The model can be used to determine the required actuator torque to pitch the blade according to the desired pitch trajectory determined in Section 2.2. The actuator torque determined is shown in Figure 2.24 for each pitch trajectory together with the other torques about the z-axis. The actuator model used is the same as the one used in Section 2.9, which is an actuator that only contributes with a torque about the z-axis.

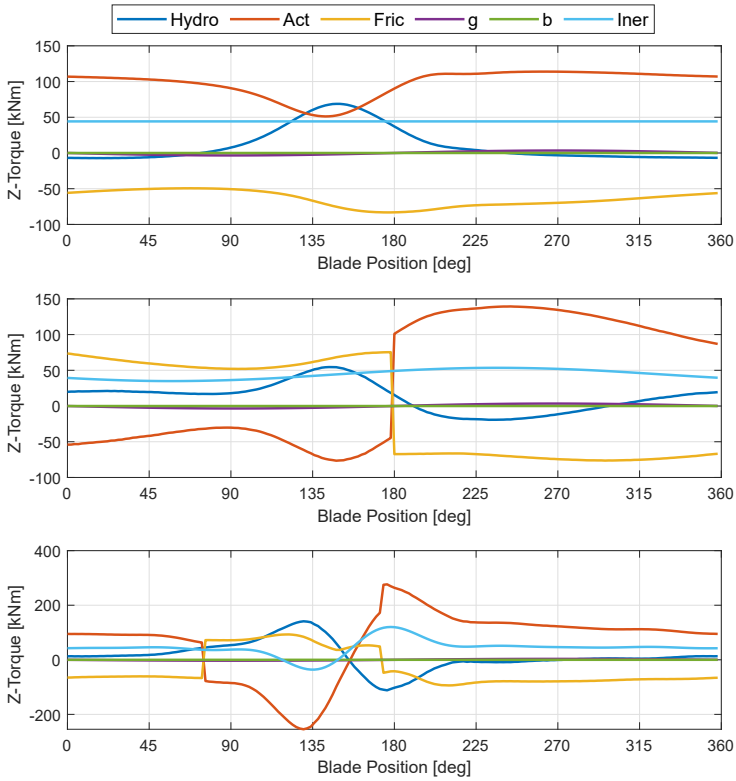

Figure 2.24: Required actuator torque to pitch the blade according to the desired pitch trajectory and the torque constituting the actuator torque.

The top, middle and bottom plots in Figure 2.24 show the torques acting on the propeller blade for it to follow the constant, cosine and variable pitch trajectories, respectively.

For the constant pitch trajectory, the actuator is used to hold the blade. The actuator torque for the cosine pitch trajectory is about the same order of magnitude as for the constant pitch trajectory. This indicates that the dynamics of the cosine pitch trajectory do not increase the magnitude of the actuator torque significantly. The actuator torque for the variable pitch trajectory is larger than the actuator torque for either the constant or the cosine pitch trajectories. The dynamics of the pitch trajectory therefore has a significant effect on the actuator torque. The requirements for the actuator are therefore significantly stricter if it is desired to use the variable pitch trajectory for the CVP propeller.

Another aspect to consider is the required power to make the cyclical pitching of the propeller blades. If the power consumption is larger than the power savings obtained with the CVP propeller then an overall power saving

is not obtained. The CVP propeller may thereby only be desirable due to the improvement in the cavitation performance, as described in Section 1.3.5. The power, P_p, to pitch the blade is determined as:

$$P_p\left(\theta_b\right) = M_{act,z,p}\left(\theta_b\right)\ \dot{\theta}_p\left(\theta_b\right) \tag{2.56}$$

Using the actuator torques in Figure 2.24 and the corresponding pitch trajectories gives the varying and average required pitching power in Figure 2.25. The average, maximum and minimum required pitching powers are given in Table 2.4 for each of the pitch trajectories.

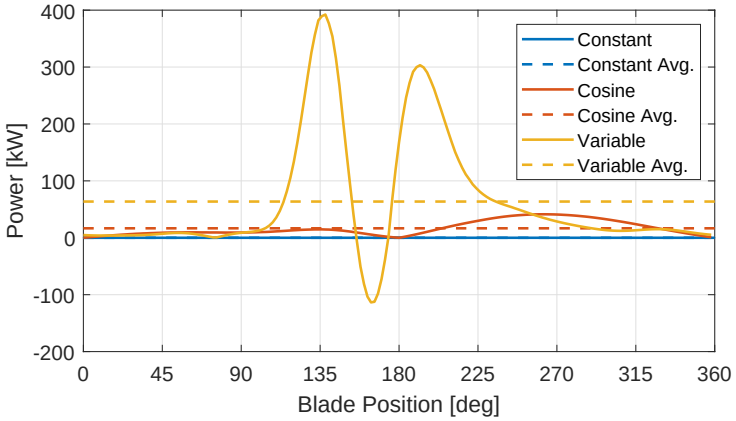

Figure 2.25: Required power to pitch the blade according to the desired pitch trajectory.

Table 2.4: Required average, maximum and minimum pitching powers to pitch the propeller blade.

	Constant	**Cosine**	**Variable**
Average Pitching Power	0.0 [kW]	16.7 [kW]	63.7 [kW]
Maximum Pitching Power	0.0 [kW]	41.3 [kW]	392.3 [kW]
Minimum Pitching Power	0.0 [kW]	0.0 [kW]	−113.5 [kW]

From Figure 2.25 and Table 2.4 it is seen that the average required pitching power for the variable pitch trajectory is 3.8 times the required power for the cosine pitch trajectory. The variation in the required pitching power is also significantly larger for the variable pitch trajectory than for the cosine pitch trajectory. But for the variable pitch trajectory it is possible to regenerate some power just before the wake peak which is included when determining the average pitching power. If the power is not regenerated and the average of the absolute pitching power is used instead, the average pitching power is

71.2 [kW]. Otherwise if the negative power is set to zero, the average pitching power is 67.4 [kW].

The required pitching power is not equal to the required actuation power. This is because there are losses in the actuator system e.g. due to friction. To get an idea of the required efficiency of the actuation system the power savings determined in [66] for the CVP propeller are considered. These power savings are also presented in Section 1.3.4. In [66] the power delivered to each propeller blade is determined for each pitch trajectory and corresponding blade design. Using these calculated powers and the required pitching power, the minimum allowable efficiency, η_{act}, of the actuator system is determined as:

$$\eta_{act} = \frac{P_p}{P_{const} - P_{traj}} \tag{2.57}$$

P_{const} is the delivered power to the propeller blade for the constant pitch trajectory. P_{traj} is the delivered power to the propeller blade for the cosine or the variable pitch trajectory. The delivered power to the propeller blade, pitching power and minimum required actuator efficiency are given in Table 2.5. Note that the pitching power, P_p, is determined using the derived model in this chapter with the blade design for the constant pitch trajectory in [66]. The delivered powers, determined in [66], are based on using a unique blade design for each pitch trajectory. One should therefore be careful not to make any strong conclusions on these minimum required actuator efficiencies in Table 2.5. But, it is expected that the pitching power is reduced if the power was determined using the blade geometry determined for the different pitch trajectories. This is because in [66] the area ratio of the propeller is reduced for the cosine and variable pitch trajectories. If the required pitching power is reduced by using the adapted blade geometries, then the minimum required actuator efficiency is also reduced compared to the values determined in Table 2.5. One should still be careful in drawing any strong conclusions since the delivered blade power from [66] is used. Because it was determined in Section 2.5 that the variable pitch trajectory is not an optimum pitch trajectory, then the method used to determine the performance of the CVP propeller in [66] may not be adequate.

Table 2.5: Minimum required actuator efficiency. Pitching power determined as; * average of the pitching power in Figure 2.25, $^+$ average of the absolute pitching power in Figure 2.25 and ^{x} average of the pitching power in Figure 2.25 where the negative power is set to zero.

Pitch Trajectory	Power per blade [kW]	Pitching Power [kW]	Minimum Actuator Efficiency [-]
Constant	1506.6	0	-
Cosine	1436.0	16.7	0.2359
Variable*	1418.5	63.7	0.7225
Variable$^+$	1418.5	71.2	0.8080
Variable^x	1418.5	67.4	0.7652

From Table 2.5 it is seen that the minimum required efficiency of the actuator system is relatively high for the variable pitch trajectory. If the CVP propeller is to be used as an efficiency improving device, then the efficiency of the actuator system has to be larger than those given in Table 2.5. The minimum required efficiency for the actuation system for the cosine pitch trajectory is relatively low. It should be possible to design an actuation system which has an efficiency of 0.24 or better. Therefore, the cosine pitch trajectory seems the most promising to use to make the CVP propeller an efficiency improving device. The variable pitch trajectory may still be desirable for the CVP propeller if it improves the cavitation performance, assuming that that is the feature sought by the owner of the vessel.

The presented results for the frictional loads in Section 2.8, the reactive loads in Section 2.9 and this section (Section 2.10) have not taken the uncertainties of the hydrodynamical loads into account. These uncertainties are defined with an upper and lower limit. To assess the influence of this uncertainty, the model is evaluated for all of the 64 (2^6) combinations of the uncertainties. The resulting uncertainties in the determined actuator torque and power are shown in Figure 2.26. The solid lines in Figure 2.26 are the actuator torque and power previously presented and the shaded areas are the uncertainties. The average, minimum and maximum values for the actuator torque and power are given in Table 2.6 for the three pitch trajectories.

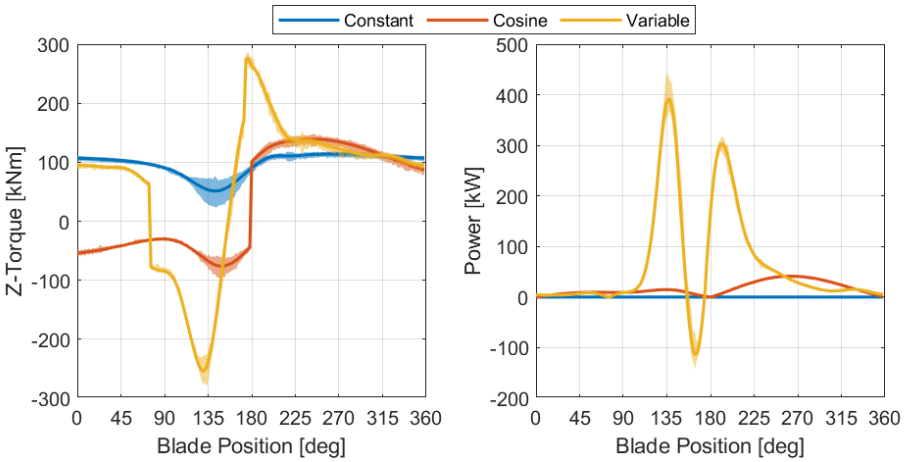

Figure 2.26: Actuator torque and power with their uncertainties due to the uncertainties in the hydrodynamical loads for each of the three pitch trajectories.

Table 2.6: Average, maximum and minimum actuator torque and power with their uncertainties due to the uncertainties in the hydrodynamical loads for each of the pitch trajectories

	Constant	Cosine	Variable
Average Actuator Torque [kNm]	$97.6^{+5.6}_{-7.7}$	$36.6^{+5.8}_{-7.4}$	$63.9^{+7.3}_{-10.0}$
Maximum Actuator Torque [kNm]	$113.9^{+4.6}_{-4.7}$	$139.4^{+8.7}_{-6.6}$	$276.5^{+10.8}_{-6.4}$
Minimum Actuator Torque [kNm]	$51.2^{+17.5}_{-27.8}$	$-76.5^{+13.8}_{-21.1}$	$-254.5^{+23.3}_{-24.7}$
Average Power [kW]	$0.0^{+0.0}_{-0.0}$	$16.7^{+1.1}_{-1.4}$	$63.7^{+7.4}_{-6.2}$
Maximum Power [kW]	$0.0^{+0.0}_{-0.0}$	$41.3^{+2.0}_{-2.2}$	$392.3^{+48.7}_{-23.2}$
Minimum Power [kW]	$0.0^{+0.0}_{-0.0}$	$0.0^{+0.0}_{-0.0}$	$-113.5^{+24.6}_{-28.1}$

From Figure 2.26 and Table 2.6 it is seen that the uncertainties in the actuator torque and power are the largest around the wake peak. This corresponds with the uncertainty of the hydrodynamical loads. The uncertainties in the actuator torque and power have to be accounted for when designing the actuation mechanism for the CVP propeller. A consequence of this uncertainty can lead to overdimensioning the actuator mechanism which can reduce the efficiency of the actuation mechanism at smaller loads.

2.11 Partial Conclusion, Discussion and Future Work

In this chapter a framework has been established which is used to evaluate the loads acting on the CVP propeller blades. The framework established requires the propeller geometry, the pitch trajectory and operating conditions of the propeller to be known in order to evaluate the loads. The loads evaluated are the inertial, hydrodynamical, actuator, frictional, reactive, gravitational and buoyancy loads, and they have been determined for one propeller blade design for each of the three pitch trajectories from [66]. The framework established is used to determine the requirements for the individual pitch mechanism at one operating condition with respect to the actuator torque and power, which is the primary contribution from this chapter. The requirements should be determined for all the operating conditions of the propeller and be included in a sensitivity study for all the parameters which are not strictly known.

The evaluation of hydrodynamical loads acting on the CVP propeller and its blades, have been studied in [33, 88]. In [88] the hydrodynamical loads acting on the CVP propeller blades are modelled using an unsteady lifting surface program. This program accounts for unsteadiness due to the non-uniform wake field but neglects the unsteadiness due to the pitching motion. The hydrodynamical loads due to the cyclical pitching are determined through interpolation of a series of FP propellers with different pitch settings. The model is therefore quasi-steady with respect to the pitch motion. In [33] the hydrodynamical loads acting on the CVP propeller are determined through an unsteady lifting surface program. This program is modified to account for the unsteadiness due to the pitching motion of the CVP propeller blades. The proposed method to determine the hydrodynamical loads in this chapter was to use URANS CFD simulation. The benefits of using a CFD simulation is the capability to account for flows with complex vortex structures and/or viscous effects [2] and the method is therefore not limited by the inviscid flow assumptions used in the lifting surface method. The present method used to determine the hydrodynamical loads can, in the future, be extended to also determine the propeller performance with respect to the cavitation, pressure pulses and noise. This is likely to require additional computational resources. It could also be investigated if other methods are more appropriate to use for the analysis of the CVP propeller with respect to the accuracy and the required computational resources.

The framework established in this chapter is the most comprehensive one to establish the requirements for the individual pitch mechanism of the active controlled CVP propeller. These requirements can be used to determine if the CVP propeller is feasible, in the future especially, when more knowledge has been established with respect to how to design the optimum propeller blades

and pitch trajectory for a CVP propeller. Other feasibility studies were made in [76,90]. The feasibility study in [76] is for the thrust balance propeller and the study in [90] is for the active controlled individual pitch propeller. None of these studies are as comprehensive as the established framework in this dissertation.

The established framework in this chapter is based on inverse rigid body dynamics whereas most previous studies are based on rigid body dynamics when modelling the pitching motion of the blades. These studies are [76] for the CVP propeller and [13,34,35,69,89] for the CP propeller. The studies of the CP propeller all include the loads due to hydrodynamics, centrifugal and friction, where the centrifugal load is equivalent to the inertial load used in this framework. The method used to determine the hydrodynamical loads differs for each of the studies [13,34,35,69,89]. The frictional loads are generally determined using the method from [34,35]. This friction model is equivalent to the derived friction model C_h. In this chapter it is shown that there are a multitude of methods and assumptions that can be used to model the friction which yields vastly different results. Further research has to show which method is the most appropriate one to use to model the friction in the blade bearing. The modelling could also be extended by modelling the elastic deformation of the blade bearing to assess the load distribution in the bearing, including the fluid film in the bearing and by determining the appropriate friction coefficients. Furthermore, the whole framework should be validated through experiments. The established framework can furthermore be adapted to rigid body dynamics by replacing the actuator torque with the pitch acceleration in the solver algorithm. This requires either that the model is coupled with the CFD simulation or that another method is used to evaluate the hydrodynamical loads due to pitch motion, which preferably requires fewer computational resources than the CFD approach presented.

Chapter 3

Pitch Trajectory for Cyclical Varying Pitch Propeller

In Chapter 2 it was found that the variable pitch trajectory determined in [66] is not the optimum pitch trajectory for the CVP propeller. This is because the variable pitch trajectory does not reduce the variations in the hydrodynamical loads which are expected according to [66]. The variations in the hydrodynamical loads are increased significantly instead.A reason for this may be due to the quasi-steady assumption made in [66] is not an appropriate assumption when analysing the CVP propeller. It may also therefore be that the quasi-steady assumption is not appropriate to determine the optimum pitch trajectory for the CVP propeller. To determine the optimum pitch trajectory it is necessary to define what the optimum pitch trajectory is.

The optimum pitch trajectory for the CVP propeller is defined as the pitch trajectory that gives the best performance of the CVP propeller. In Chapter 1 the performance parameters are defined and with respect to these parameters the desired performance with the optimum pitch trajectory are:

- Thrust
  - The mean of the cyclical thrust should equal the desired thrust according to the specified operating conditions.
- Efficiency
  - Maximise the efficiency of the CVP propeller by minimising the required power delivered to the propeller to produce the desired thrust and minimise the required power for the actuator system to pitch the blades individually.
- Shaft vibrations
  - Minimise the variation in the loads acting on the propeller.

- Cavitation
  - Minimise the cavitation over the propeller blades.
- Pressure pulses
  - Minimise the amplitudes of the pressure pulses acting on the ship hull.
- Noise
  - Reduce the noise created by the propeller. Generally done by minimising shaft vibrations, cavitation and pressure pulses.
- Reliability
  - Minimise the load variation on the propeller blade to reduce fatigue stresses. The reliability is not limited to the blade's fatigue stresses but could also include other relevant components.

There are multiple performance parameters for the CVP propeller which have to be considered when determining the optimum pitch trajectory. It is therefore a multi-objective optimization problem that has to be solved. The optimization problem can be defined with five objectives, for the efficiency, shaft vibrations, cavitation, pressure pulses and reliability, as defined above. The thrust is made as an equality constraint and the noise is implied to be included by the shaft vibrations, cavitation and pressure pulses. The design parameters or variables for the optimization problem are the variables used to define the propeller geometry, pitch trajectory and actuator mechanism. These design variables also have their own constraints which should be included in the optimization. Solving this multi-objected optimization problem globally would yield the optimum propeller geometry, pitch trajectory and actuator system for the CVP propeller. Considering the established framework in Chapter 2 then it is not possible to determine the objectives related to cavitation and pressure pulses. These objectives are, to some degree, coupled with the other objectives, such as the shaft and blade vibrations, and minimising these will most likely also minimise the cavitation and pressure pulses. The framework can be used to determine the blade and shaft vibrations, the propeller efficiency and the required minimum actuator power.

Furthermore, in the determination of the optimum pitch trajectory the design variables for the propeller geometry are not included. This is due to the large design space of the propeller geometry and the associated high computational costs. Because the blade geometry is not included, the actuator power cannot be included. This is because when considering the actuator power it has to be considered relative to the optimal solution for the CP propeller, i.e. when the blade's pitch does not vary cyclically, and since the propeller efficiency does not change significantly when the blade geometry is fixed it does not make sense to consider the actuator power when the blade geometry is

not considered. This means that only the shaft and blade vibrations are used to determine the optimum pitch trajectory for the CVP propeller. The modelling of the hydrodynamical loads does not, therefore, need to determine the steady components of the hydrodynamical loads but instead the model only has to be able to determine the unsteady components.

The downside of the framework is that it is computationally expensive due to the method used to evaluate the hydrodynamics and therefore it might not be efficient to use it in an optimization if a solution is desired within a restricted time limit. Therefore, it is desirable to find a less computationally expensive method to determine the hydrodynamical loads acting on the CVP propeller and its blades. Four alternative models, to determine the hydrodynamical loads, are described in Section 3.1 where they are also compared to the hydrodynamical loads determined in Chapter 2.

The optimum pitch trajectory is determined in Section 3.2 for the propeller considered in Chapter 2. The actuator requirements are determined in Section 3.3 when the CVP propeller pitches according to the optimum pitch trajectory. In Section 3.4 the results from this chapter are summarized and discussed together with some of the other aspects for the future work.

3.1 Alternative Hydrodynamic Models

The model used to evaluate the hydrodynamical loads in Chapter 2 is computationally expensive. To determine the optimum pitch trajectory for the CVP propeller it is desired to have a model which is less computationally expensive. Four alternative models for the hydrodynamical loads were investigated. These models are:

- Hydrodynamic modelling of the CVP propeller using the open-water curves for the equivalent CP propeller. Described in Appendix D.
- Hydrodynamic modelling of the CVP propeller using unsteady foil theory. Described in Appendix E.
- Hydrodyanmic modelling of the CVP propeller using empirical transfer function estimation. Described in Appendix F.
- Hydrodynamic modelling of the CVP propeller using a reduced model. Described in Appendix G.

A short summary of the four modelling methods is presented in the following four sections, followed by a section presenting the results for each of the modelling approaches. The details of the four modelling methods are given in appendices D-G.

3.1.1 Hydrodynamic Modelling of CVP Propeller using Open-Water Curves for the CP Propeller

The modelling of the hydrodynamical loads acting on the CVP propeller blades using the open-water curves of the CP propeller is presented in Appendix D. The open-water curves are determined using the equivalent CP propeller i.e. constant pitch trajectory to correspond with traditional open-water tests. The open-water curves are made for a series of pitch settings which cover the span of the pitch trajectory. Furthermore, for modelling the CVP propeller it is required that all six loads acting on the propeller blade are determined. Such measurements have been made in [16, 50]. In Appendix D the open-water curves are determined using quasi-steady RANS CFD simulations of the full scale propeller.

The hydrodynamical loads acting on the CVP propeller blades are determined by interpolating the open-water CFD simulation results depending on the blade's pitch and the local advance coefficient. These vary with the position of the propeller blade in the wake field. The local advance coefficient is a measure of the local flow condition of the propeller blade and is used to account for the non-uniform wake field. Four different methods are used to determine the local advance coefficient in Appendix D. These methods use the average axial velocity over the blade spindle axis, blade area, skew line and leading edge.

The hydrodynamic modelling of the CVP propeller using open-water curves for the CP propeller, determines the loads quasi-statically and does therefore not account for any dynamic effects. The modelling approach is used to determine both the steady and unsteady hydrodynamical load components.

3.1.2 Hydrodynamic Modelling of the CVP propeller using Unsteady Foil Theory

The modelling of the hydrodynamical loads acting on the CVP propeller using unsteady foil theory is presented in Appendix E. The unsteady foil theory is based on the assumption of potential flow whereby different flow solutions can be superimposed onto each other to achieve the solution for more complex flow problems. The modelling is based on decomposing the flow into a steady flow problem, an unsteady problem due to the pitch motion and an unsteady flow problem due to the perpendicular gust. Only the solutions to the two unsteady problems are presented in Appendix E. The two unsteady solutions are used strip-wise for each radial section of the blade from which the response for the blade is determined by integrating over the whole blade.

The two unsteady solutions are determined in the frequency domain which is advantageous to use when the unsteady pitch motion and unsteady gust are known. The unsteadiness due to the pitch motion is determined

using Theodorsen's method [15, 62] where the lift response is divided into a circulative and non-circulative term. The circulative term is determined using the pitch displacement and pitch rate times a gain and Theodorsen's function. Theodorsen's function is a complex function giving phase to the response and it depends on the reduced frequency. The reduced frequency depends on the flow condition and geometry of the foil. The non-circulative term is determined using the pitch rate and the pitch acceleration times a gain. The unsteadiness due to the perpendicular gust is determined using Sears's method [15, 62] where the lift response only depends on the circulative effects. The lift due to the gust is determined as a gain times the gust velocity times Sears's function which describes the dynamics of the response.

The strip-wise application of the unsteady solutions does not account for the finite aspect ratio of the propeller blades. Two different approaches are used to account for the effect of the finite aspect ratio of the propeller blades. One method is to scale the lift response by assuming an elliptically loaded propeller blade. The other method also adapts Theodorsen's and Sears's functions.

3.1.3 Hydrodynamic Modelling of the CVP propeller using Empirical Transfer Function

The modelling of the hydrodynamical loads acting on the CVP propeller using the empirical transfer function is presented in Appendix F. The empirical transfer function is the transfer function of the system determined as the ratio between the frequency components of the output and input signals. The input to the system is the pitch trajectory and the output of the system are the hydrodynamical loads. The input and output used to determine the empirical transfer function are the simulation results from URANS CFD with the variable pitch trajectory in Appendix A. The empirical transfer function for the system is therefore limited to the first seven frequency harmonics since this is the highest harmonic included in the variable pitch trajectory. The frequency components are determined through a least-squares estimation of a Fourier series to the input and output signals.

This model can only be used to determine the unsteady hydrodynamical loads due to the pitching motion. The unsteadiness due to the non-uniform wake field is not determined through the empirical transfer function. These unsteady hydrodynamical loads were determined using the URANS CFD simulation with the constant pitch trajectory.

3.1.4 Hydrodynamic Modelling of the CVP propeller using a Reduced Model

The modelling of the hydrodynamical loads acting on the CVP propeller using the reduced model is presented in Appendix G. The reduced model only models the unsteady hydrodynamical load due to the pitching motion. The formulation of the reduced model is inspired by the modelling of the pitching motion using unsteady foil theory presented in Appendix E. The circulative effects are determined by using a regression model which depends on the effective pitch displacement and effective pitch rate. The regression model is determined through a series of quasi-steady CFD simulations. The CFD simulations each have a unique setting of the pitch displacement and pitch rate, according to a 2^k factorial design with a central composite design for the second-order effects. The regression model is based on the results from 75 quasi-steady CFD simulations. The effective pitch displacement and effective pitch rate are determined by using the convolution integral with the dynamics of the circulative build-up, the pitch displacement and the pitch rate of the blades. The dynamic build-up of the circulative effect is determined through a URANS CFD simulation where one blade makes a step change in the pitch displacement. The two non-circulative gains for the pitch rate and pitch acceleration are determined through a minimisation of the least-squares error between the reduced model and the unsteadiness due to the pitch motion from the CFD simulation of the CVP propeller in Appendix A with the variable pitch trajectory.

3.1.5 Hydrodyanmic Model Comparision for the CVP Propeller

The four models described above to determine the hydrodynamical loads acting on the CVP propeller blades for a new pitch trajectory, are all computationally inexpensive. This reduced computational cost is based on a comparison of making a new URANS CFD simulation of the CVP propeller. The computational costs of making the models differ since some use CFD simulations to a greater or lesser extent and others do not use CFD simulations to make the model. The loads that can be determined with the models also differ. These properties are summarized in Table 3.1 for each of the models.

Table 3.1: Comparision of the properties of the different models to determine the hydrodynamical loads acting on the CVP propeller blades. * OW stands for open-water. ^{x} Analytical is the model which is based on the unsteady foil theory.$^+$ TF stands for transfer function.

Model		URANS CFD	OW*	Analytical^x	TF$^+$	Reduced
Appendix		A	D	E	F	G
Hydrodynamical Load	Steady	Yes	Yes	No	No	No
	Unsteadiness due to non-uniform wake field	Yes	Yes	Yes	No	No
	Unsteadiness due to pitch motion	Yes	Yes	Yes	Yes	Yes
Computational cost for setup		Low	Moderate	None	High	High
Computational cost for new pitch trajectory		High	Low	Low	Low	Low

From Table 3.1 it is seen that only one of the models with reduced computational cost is able to determine the steady component of the hydrodynamical loads. Furthermore, two of the models are not able to determine the unsteady hydrodynamical loads due to the non-uniform wake field. These two models therefore require one of the other models to determine these unsteady load components. For this the URANS CFD simulations with the constant pitch trajectory are used. All of the models are able to determine the unsteady hydrodynamical loads due to the pitch motion of the propeller blades.

By "computational cost for the setup" in Table 3.1 is meant the required computations before the computations with the desired pitch trajectory can be made. For the URANS CFD simulation of the CVP propeller it is necessary to determine the effective wake field beforehand. For the OW model it is necessary to make several quasi-steady open-water simulations to get the open-water curves for different pitch settings. For the analytical model the unsteady hydrodynamical loads are expressed in an explicit form and no prior computations are necessary. The empirical transfer function model requires two evaluations using the URANS CFD model, one with the blades fixed and one with a pitch trajectory with a satisfactory number of harmonics included. The reduced model requires at least 75 quasi-steady simulations and two or more URANS CFD simulations, depending on how the non-circulative terms are determined.

To evaluate the usability of the different models, they are compared to each other on their ability to determine the unsteady hydrodynamical loads due to the pitch motion. For the other components refer to the corresponding appendix for the models. In each of these appendices the models are compared to the URANS CFD simulations of the CVP propeller.

The unsteady hydrodynamical loads, due to the cosine and variable pitch trajectories, are shown in Figure 3.1 and Figure 3.2, respectively, for each of the models. The hydrodynamical loads shown in Figure 3.1 and Figure 3.2 do not include the uncertainty of the models in order to make the figures more clear. The hydrodynamical loads, with their uncertainties, can be found in the appendices. For the open-water models, only one of the models is included in Figure 3.1 and Figure 3.2. For the analytical models all three are included. The open-water model used is the one using the local advance coefficient determined over the blade area.

From Figure 3.1 and Figure 3.2 it can be seen that the unsteady hydrodynamical loads due to the pitch motion are best determined using the empirical transfer function model. This model matches almost exactly the URANS CFD simulation. The reduced model is the model that matches the URANS CFD simulation, second best. These two models have that in common that they are fitted to the URANS CFD simulation to a greater or lesser extent. It is therefore not surprising that these models match the URANS CFD simulation best. The benefit of the reduced model relative to the empirical transfer function model is that the reduced model can be used for any arbitrary pitch trajectory, whereas the empirical transfer function model can only be used for the frequency harmonics included in the input, which in this case it is up to the 7th harmonic.

For the cosine pitch trajectory in Figure 3.1 the open-water model matches the amplitude of the loads reasonably well but there is some phase difference. The analytical model either overestimates or underestimates the URANS CFD simulation. The phase differences between the analytical models and the URANS CFD simulation generally tend to be smallest for the analytical model noted as $2D$. This model uses just the strip-wise application of the unsteady foil theory without any compensation for the finite aspect ratio of the propeller blade. The same is the case when considering the variable pitch trajectory in Figure 3.2. The analytical models capture the general trends of the variable pitch trajectory, except for the z-force. The open-water model does not catch the general trends for the variable pitch trajectory and it underestimates the amplitudes. The application of the open-water model to determine the unsteady hydrodynamical loads, due to the pitch motion, is therefore limited to where the pitch rate and acceleration are not as prominent. Under these conditions the system is closer to the quasi-steady assumption that the open-water model is based upon.

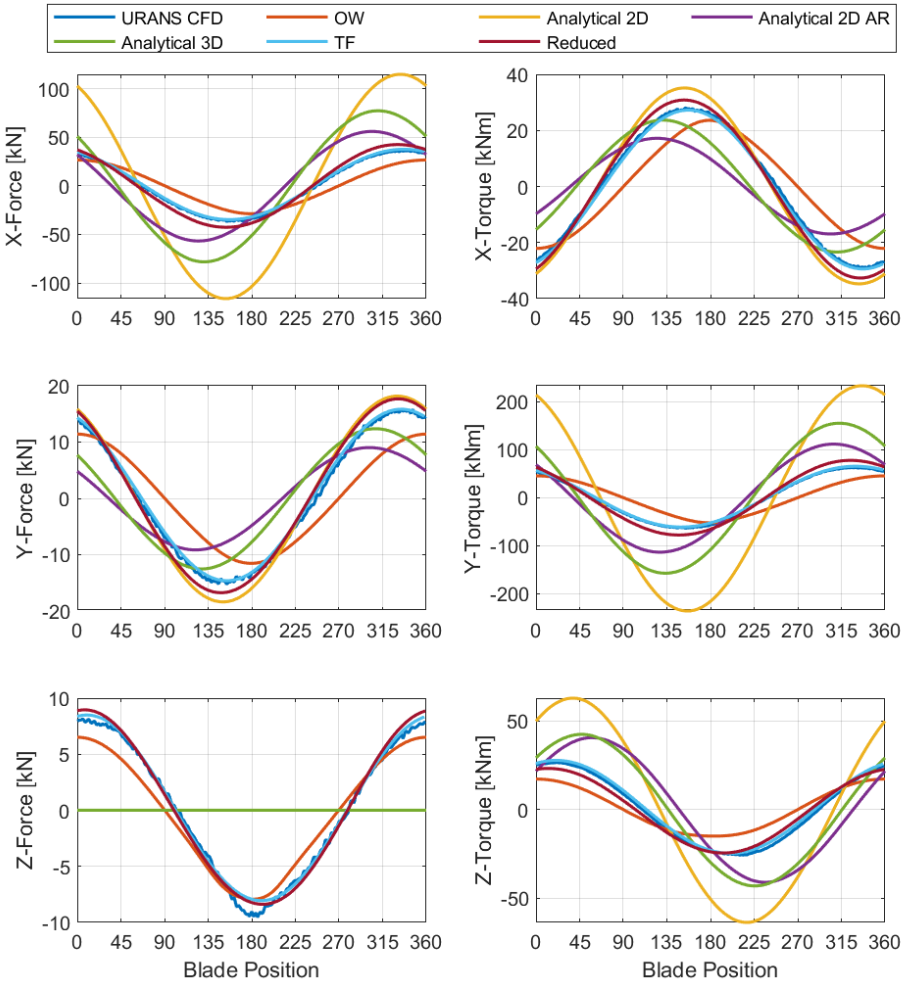

Figure 3.1: Comparision of models for the unsteady hydrodynamical loads due to the pitch motion with the cosine pitch trajectory.

To determine the optimum pitch trajectory for the CVP propeller, based on the minimisation of the load variations, the analytical, empirical transfer function and the reduced model will be considered in the work. The analytical model is probably best suited for determining an initial optimum pitch trajectory. This pitch trajectory can then be used in the URANS CFD simulation of the CVP propeller from which the empirical transfer function can be determined. If the performance of the CVP propeller, with the optimum pitch trajectory using the analytical model, is not satisfactory, then the empirical transfer function can be used to determine a new optimum pitch trajectory. This pitch trajectory should yield a better performance because the empirical

transfer function is better at determining the unsteady hydrodynamical loads of the CVP propeller due to the pitch motion.

Using the open-water model to determine the optimum pitch trajectory has been used in [30] and the method will not be presented further here. In [30] two optimum pitch trajectories are determined, one that maximises the efficiency and one that also maintains the required thrust whihch is similar shaped as the variable pitch trajectory.

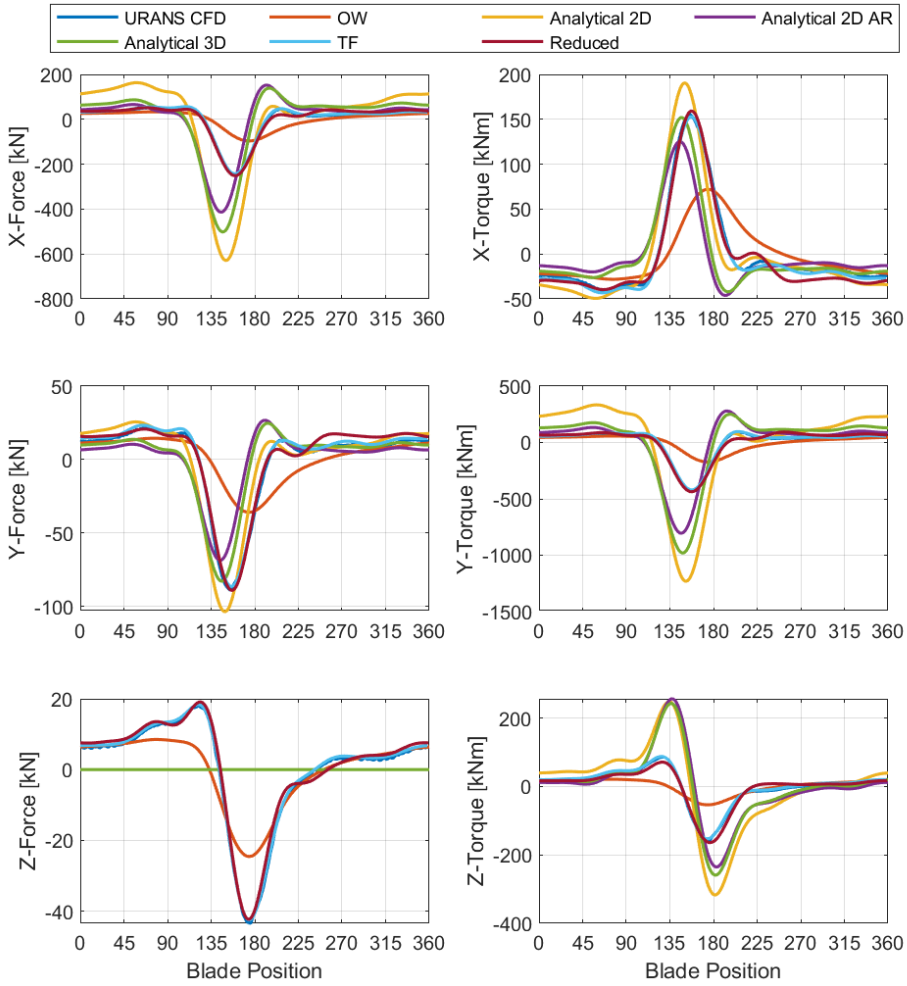

Figure 3.2: Comparision of models for the unsteady hydrodynamical loads due to the pitch motion with the variable pitch trajectory.

3.2 Determination of Optimum Pitch Trajectory

For the optimum pitch trajectory for the CVP propeller, it is desired to compensate the unsteadiness in the hydrodynamical loads, due to the non-uniform wake field with the unsteadiness due to the pitch motion. The sum of the unsteady loads should therefore be equal to zero for the pitch trajectory to be an optimum pitch trajectory. This optimization problem is stated as:

$$\text{Minimise,} \qquad e = \sum_{i}^{6} \sum_{\theta_b=0}^{2\pi} \left(\tilde{L}_{i,wake}(\theta_b) + \tilde{L}_{i,pitch}(\theta_b) \right)^2 \tag{3.1}$$

e is the error which is to be minimised. θ_b is the blade position in the wake field. $\tilde{L}_{i,wake}$ is the i'th unsteady hydrodynamical load due to non-uniform wake field. $\tilde{L}_{i,pitch}$ is the i'th unsteady hydrodynamical load due to the pitching of the propeller blade. One of the problems that can occur with the optimization problem in Eq. 3.1, is that some loads will be weighted more than others because of the differences in the load amplitudes. An alternative approach to the optimization problem in Eq. 3.1 is to optimize the pitch trajectory with respect to the variation in one of the hydrodynamical loads. The optimization problem therefore becomes:

$$\text{Minimise,} \qquad e_i = \sum_{\theta_b=0}^{2\pi} \left(\tilde{L}_{i,wake}(\theta_b) + \tilde{L}_{i,pitch}(\theta_b) \right)^2 \tag{3.2}$$

Approaches similar to Eq. 3.2 are used in [33, 66, 85] to determine the optimum pitch trajectory. These studies only consider the variation in the blade thrust. Both options in Eq. 3.1 and Eq. 3.2 are considered for the optimum pitch trajectory. The resulting optimum pitch trajectories, using these seven approaches, are shown in Figure 3.3 using the analytical model, empirical transfer function model and the reduced model. The unsteadiness due to the non-uniform wake field is for the analytical models determined using the corresponding gust models in Appendix E. The empirical transfer function model and the reduced model use the hydrodynamical loads determined from the URANS CFD simulation of the CVP propeller with the constant pitch trajectory in Appendix A. In Figure 3.3 the title of each plot indicates which load/loads are used to determine the optimum pitch trajectories. The cosine and variable pitch trajectory, that have been considered so far, are also shown in Figure 3.3 for ease of comparison.

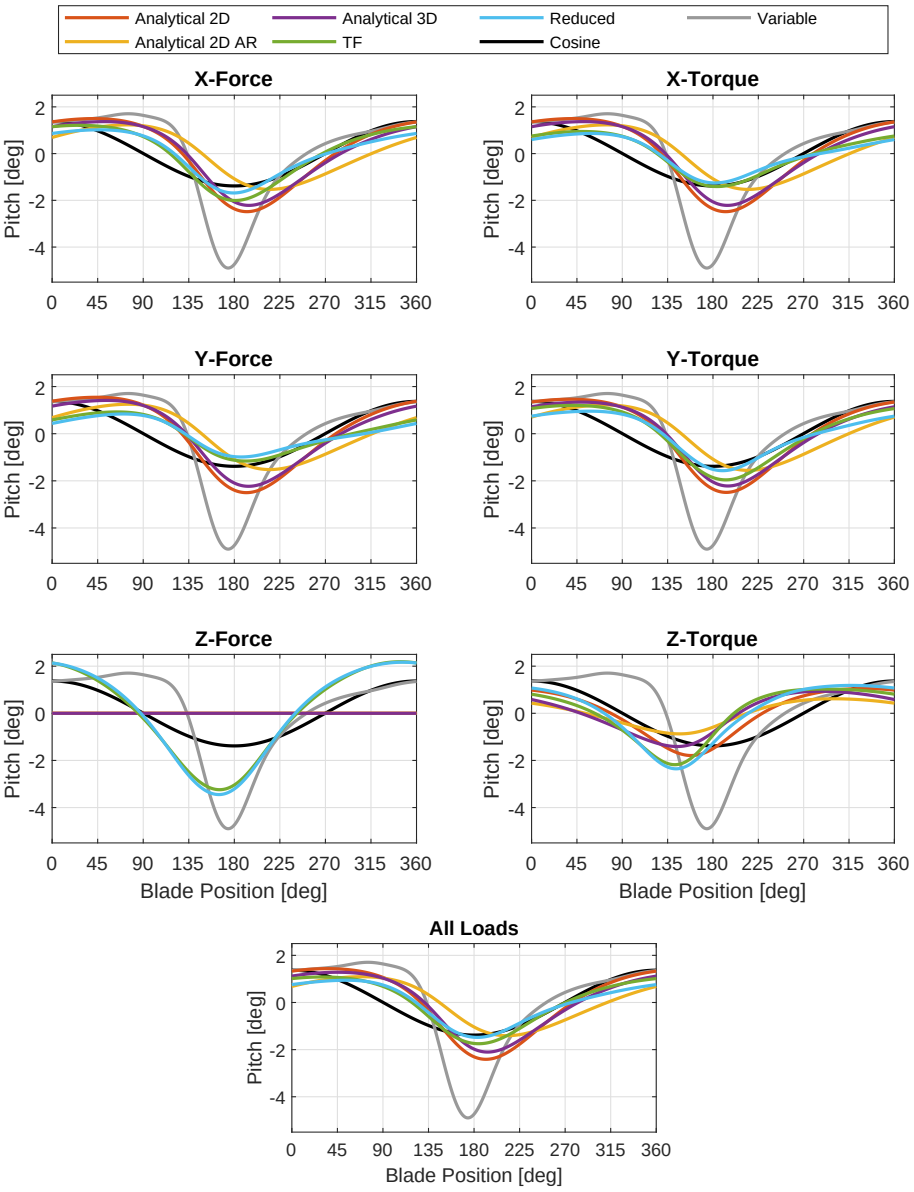

Figure 3.3: Comparision of optimum pitch trajectories using the analytical model, empirical transfer function model, reduced model and the pitch trajectories from Chapter 2.

In Figure 3.3 35 candidates for the optimum pitch trajectory are shown. The optimum pitch trajectories determined using the analytical models are almost identical for all the loads, except when optimised with respect to the z-torque and all the loads together. This is not surprising since all these loads

are determined from the unsteady lift. Minimising the unsteady lift thereby minimises the x and y unsteady loads. The optimum pitch trajectory, determined for all the loads, has a slightly reduced amplitude, and the optimum pitch trajectory determined for the z-torque has a significant phase shift and reduced amplitude.

The optimum pitch trajectory determined using the empirical transfer function model and the reduced model are very similar but with slight differences in the amplitudes. This corresponds well with the model's ability to determine the unsteady hydrodynamical loads due to the pitch motion as shown in Figure 3.1 and Figure 3.2. For the empirical transfer function model and the reduced model there are variations in the optimum pitch trajectory depending on the load used for the optimisation.

Determining the optimum pitch trajectory using the 2D analytical model tends to have the same phase as the optimum pitch trajectory using the empirical transfer function model and the reduced model. Generally, the amplitude is slightly overestimated. The 3D analytical model tends to get a better prediction of the amplitude, but at the cost of worse correspondence in the phase. Therefore, it seems reasonable to use the 2D analytical model to determine an initial optimum pitch trajectory. This trajectory can then be used in a CFD simulation of the CVP propeller from which the empirical transfer function model can be determined and used to determine a new better optimum pitch trajectory.

To validate whether the pitch trajectories in Figure 3.3 are indeed optimum pitch trajectories requires that an URANS CFD simulations of the CVP propeller, as that in Appendix A, is made with the optimum pitch trajectories. This is left as future work for the project.

3.3 Actuator Requirements for the CVP Propeller with an Optimum Pitch Trajectory

Having established a series of candidates for the optimum pitch trajectory that minimise the propeller and blade load variations, the requirements for the actuation system are determined as in Section 2.10. The optimum pitch trajectories determined through the use of the analytical model are not considered further. This is because the analytical model overestimates the unsteady hydrodynamical loads significantly and this will lead to a significant overestimation of the requirements for the actuator system. The optimum pitch trajectories, and corresponding hydrodynamical loads considered, are therefore the ones using the empirical transfer function model and the reduced model. This means that only 14 optimum pitch trajectories are considered henceforth. The empirical transfer function model and reduced model only determine the unsteady hydrodynamical loads due to the pitch motion. These hydrodynamical loads are therefore superimposed onto the hydrodynamical loads for the propeller, with a constant pitch trajectory determined in Appendix A. The hydrodynamical loads, for each of the optimum pitch trajectories using the empirical transfer function model, are shown in Figure 3.4 where they are compared to the hydrodynamical loads for the pitch trajectories used in Appendix A. The hydrodynamical loads for each of the optimum pitch trajectories using the reduced model are not shown in Figure 3.4 in order to not add confusion to the figure. The hydrodynamical loads for the reduced model are similar to the loads shown in Figure 3.4, having the same tendencies but with some differences in the amplitudes. The symbols Fx, Mx, Fy etc. in the legend shows which hydrodynamical load is used to determine the optimum pitch trajectory.

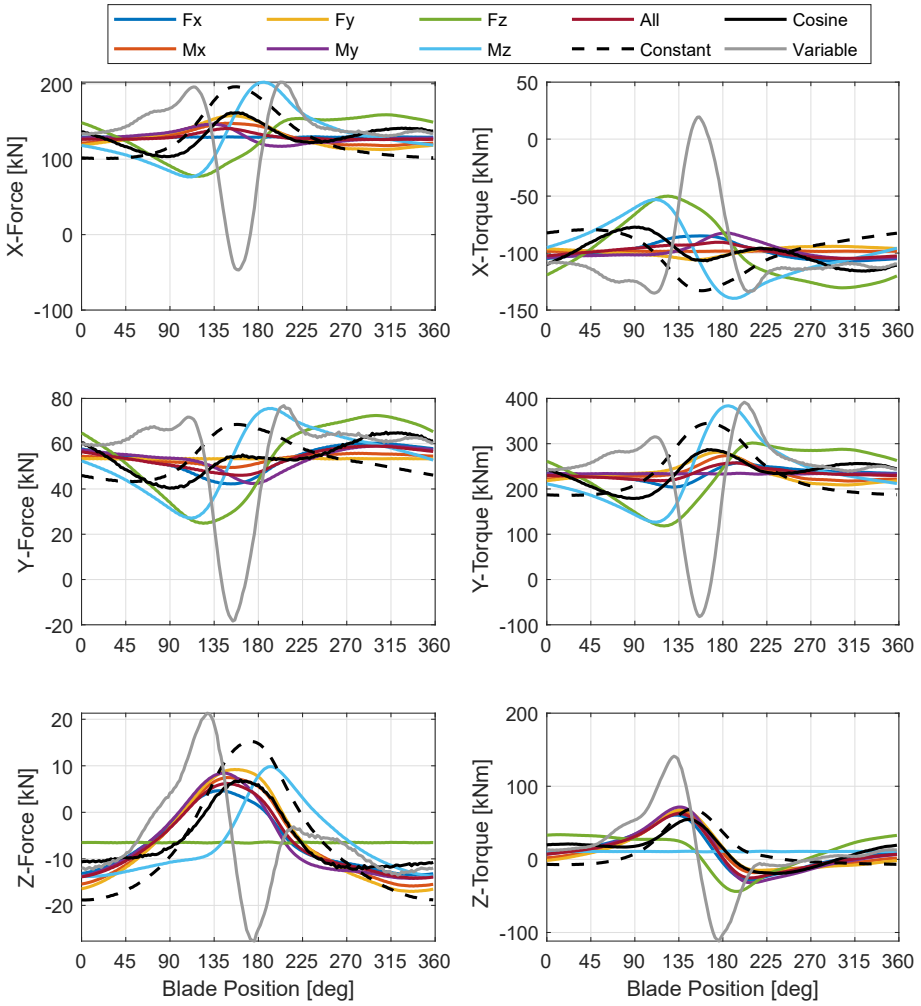

Figure 3.4: Hydrodynamical loads when using the optimum pitch trajectories determined using the empirical transfer function model.

From Figure 3.4 it is seen that all the pitch trajectories optimised for a single load result in the load being constant. The pitch trajectory optimised for all the loads tends to be closely correlated to the optimum pitch trajectories determined for the loads Fx, Fy, Mx, My, which are also correlated to each other. The pitch trajectories, optimised with respect to the loads Fz and Mz, yield unique hydrodynamical loads, which result in large variations in the non-corresponding hydrodynamical loads.

With the hydrodynamical loads determined for each of the optimum pitch trajectories, the required actuator torque and power are determined as in

Section 2.10. The required actuator torque and power are determined using the combined friction model DG with a distribution ration (DR) of 0.86. The actuator torque and power determined are shown in Figure 3.5 for all the optimum pitch trajectories and the three pitch trajectories used in Chapter 2.

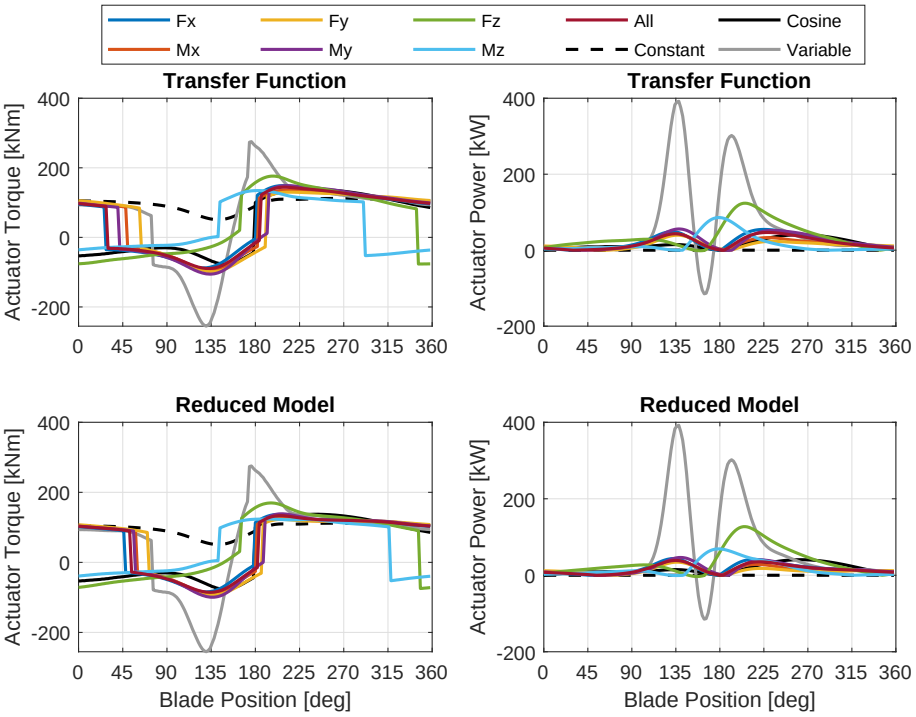

Figure 3.5: Required actuator torque and power for the blade to follow the optimum pitch trajectories.

The actuator torque in Figure 3.5 for the pitch trajectories optimised with respect to the loads Fx, Fy, Mx, My and all for both models correlates well with the actuator torque for the cosine pitch trajectory. For these pitch trajectories the power is more symmetric about the blade position of 180° than the power for the cosine pitch trajectory. The required peak actuator power is seen to be largest for the pitch trajectories optimised for the loads Fz and Mz. In general, all the optimised pitch trajectories require less power for the actuator than for the variable pitch trajectory. This is positive since this makes it more likely that an actuator system can be designed for the CVP propeller by which an increase in the propulsion efficiency can be obtained when also accounting for the actuators power consumption. The peak actuator torques for the optimum pitch trajectories are also smaller than the peak torque for the variable pitch trajectory. This means that a smaller actuator can be used

which is easier to fit inside the propeller hub. It should also be easier to obtain a higher efficiency for the actuator system. The average, maximum and minimum actuator torque and power for each of the pitch trajectories are given in Table 3.2.

Table 3.2: Average, maximum and minimum actuator torque and power for each of the pitch trajectories.

Model	*Load Optimised*	*Avg. Actuator Torque [kNm]*	*Max. Actuator Torque [kNm]*	*Min. Actuator Torque [kNm]*	*Avg. Actuator Power [kW]*	*Max. Actuator Power [kW]*	*Min. Actuator Power [kW]*
Constant		97.6	113.9	51.2	0.0	0.0	0.0
Cosine		36.6	139.4	-76.5	16.7	41.3	0.0
Variable		63.9	276.5	-254.5	63.7	392.3	-113.5
TF	Fx	45.9	148.7	-87.9	22.4	54.7	0.1
TF	Mx	50.2	135.7	-95.2	16.3	42.5	0.0
TF	Fy	50.1	130.0	-98.7	14.6	39.5	0.0
TF	My	44.4	148.7	-105.7	23.0	55.9	-0.3
TF	Fz	42.0	176.1	-76.6	36.4	123.7	-1.5
TF	Mz	30.8	134.6	-52.5	16.6	85.9	-0.1
TF	All	44.3	144.1	-89.5	19.6	46.6	0.0
Reduced	Fx	53.5	136.6	-84.4	17.8	43.6	0.1
Reduced	Mx	54.8	129.0	-89.1	14.0	37.5	0.0
Reduced	Fy	54.8	122.8	-92.7	12.2	34.2	0.1
Reduced	My	51.5	138.6	-99.5	17.3	46.5	-0.0
Reduced	Fz	46.4	169.7	-74.6	35.3	127.1	-3.2
Reduced	Mz	41.5	123.7	-52.5	17.6	68.9	-0.7
Reduced	All	53.1	133.5	-85.6	16.0	38.7	0.0

From Table 3.2 it is seen that the average actuator power for the optimised pitch trajectories is about the same as for the cosine pitch trajectory. The exception to this is the pitch trajectory optimised with respect to the load Fz, where the actuator power required is more than double the power required for the cosine pitch trajectory. Furthermore, it is seen that the minimum required actuator power for most of the pitch trajectories does not become negative at any point which means that it is not possible to make energy recovery as is possible with the variable pitch trajectory.

3.4 Partial Conclusion, Discussion and Future Work

In Chapter 2 it was determined that the variable pitch trajectory is not an optimum pitch trajectory for the CVP propeller because it increases the unsteadiness of the hydrodynamical loads. It is therefore necessary to determine the optimum pitch trajectory using another method. The optimum pitch trajectory is determined by minimising the hydrodynamical load variation of the CVP propeller blades in the non-uniform wake field. The other propeller performance parameters, such as cavitation, pressure pulses, noise and efficiency, are not included. This is because the framework established in Chapter 2 is not able to evaluate the cavitation, pressure pulses and noise. The efficiency is not included because it only changes significantly when the propeller blade design is changed. Only the design parameters for the pitch trajectory are included in the minimisation due to the large computational costs of including the propeller blade geometry.

Previous studies vary in their approach as to how the pitch trajectory is determined. One study assumes a piece-wise linear pitch trajectory [88]. Other studies are limited to pitch trajectories with only one harmonic [14, 51, 84–86]. In [51] the amplitude of pitch trajectory is determined as the amplitude of the variation in the advance angle at $r/r_p = 0.7$. In [14, 84, 86] no details are given as to how the amplitude and phase of the pitch trajectories are determined. In [85] a pitch trajectory, to minimise the transient cavitation, is determined by reducing the first harmonic variations in the angle of attack at the leading edge for each radial section of the blade. For the propeller blade design to be appropriate, the pitch trajectory should not change with the span of the blade. The pitch trajectory to minimise the blade lift variation in [85] is determined using unsteady foil theory similar to the analytical model presented in this chapter. The pitch trajectory used in [85] is a trade-off between using the pitch trajectories from the two methods presented in [85]. In [33, 66] the pitch trajectory is determined as the one which minimises the variation in the blade thrust. The method used in [33], to determine the thrust variation, is based on unsteady foil theory similar to the analytical model used in this chapter. The thrust variation in [66] is determined using a quasi-steady lifting line.

The contribution from this chapter is the development and application of novel modelling approaches to model the unsteady hydrodynamical loads due to the pitch motion of the propeller blades. These models have different degrees of accuracy and require a different amount of computational resources to set up and evaluate. Determining the optimum pitch trajectory by using the method presented in Chapter 2, using an iterative approach, requires a large amount of computational resources, because of the CFD simulation of the CVP propeller that has to be made for each evaluation. To

reduce the required computational resources to determine the optimum pitch trajectory, four different models are presented to determine the unsteady hydrodynamical loads due to the pitch motion. Of these four models two of them are especially of interest, being the analytical model and the empirical transfer function model. The analytical model is derived from unsteady foil theory and the empirical transfer function model estimates the system dynamics from the URANS CFD simulation of the CVP propeller. The analytical model is not as accurate as the empirical transfer function model, but it requires fewer computational resources to evaluate and furthermore the optimum pitch trajectory determined is close to the optimum pitch trajectories determined using the empirical transfer function model. The analytical model is therefore suitable to determine an initial optimum pitch trajectory for the URANS CFD simulation, from which the empirical transfer function model can be made. The empirical transfer function model is then used to determine a new optimum pitch trajectory which should be suitable for the CVP propeller. It has not been validated if this is the case and this remains to be shown in the future. The actuator requirements for the determined optimum pitch trajectories are, in general, slightly larger than the requirements determined for the cosine pitch trajectory in Chapter 2 but significantly smaller than the requirements for the variable pitch trajectory.

In future developments regarding the calculation of the optimum pitch trajectory, the other propeller performance parameters should be included in the objective function for the optimisation, such as cavitation, pressure pulses, noise and efficiency. This requires that the method used to evaluate the hydrodynamics of the propeller have to be adapted or changed. Furthermore, the design variables for the optimization problem should also be extended to include the propeller blade design and actuator design. Also the optimisation should consider the whole range of operating conditions of the propeller and not just limited to a single point as was considered in this chapter.

Chapter 4

Experimental Testing of CVP Propeller

The experimental testing of the CVP propeller serves two purposes. The first is to validate the increase in propulsion efficiency when utilizing the CVP propeller compared to a CP propeller. The second purpose is to get experimental data which can be used to validate the model for determining the hydrodynamical loads. The experiments are made by using a scaled-down model of the ship and propulsion system to reduce the costs of the experiments. The use of scaled-down models for testing is a well-known and common practice in the maritime industry.

The traditional tests made to evaluate the propulsion efficiency are; ship hull resistance test, ship hull wake field measurement, propeller open-water test and self-propulsion test. A short description of the contents of these tests is given in the following four sections.

Ship Hull Resistance Test:
The ship hull resistance test is usually made by towing a scaled down model of the ship hull through the water in a towing tank. While towing the ship hull through the tank, the speed, the horizontal drag force (i.e. towing force) and the heave of the fore and the aft part of the ship are measured as shown in Figure 4.1. The ship hull is towed through the tank at an equal Froude number for both the ship hull model and the full scale ship hull. The equal Froude number condition is in order to ensure that the wave pattern is the same for the ship hull model and full scale ship hull [20]. From the measured towing resistance and towing speed, the full scale towing resistance for the ship hull can be extrapolated according to [47].

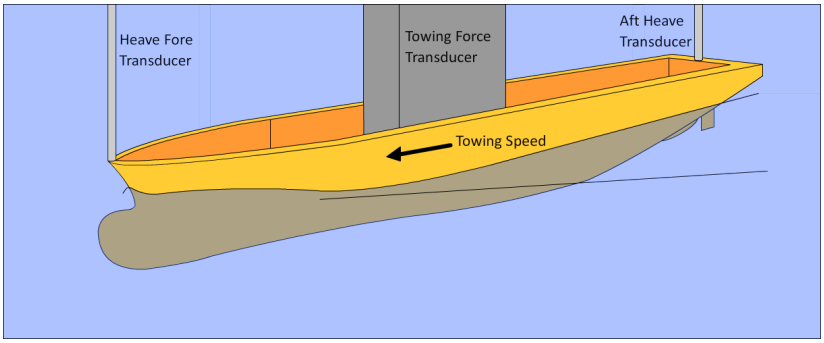

Figure 4.1: Sketch of resistance test in a towing tank.

Ship Hull Wake Field Measurement:
The wake field of the ship hull at the propeller's location is measured using pitot tubes at appropriate positions. The measurements are typically made at one of the ship speeds used for the resistance test. The wake field measurements are used to determine both the nominal wake field coefficient and the velocity distribution in the wake field.

Propeller Open-Water Test:
The propeller open-water test is made using a scaled model of the propeller, where the flow into the propeller is uniformly disturbed. The test is made using an open-water dynamometer as shown in Figure 4.2 and is either made in a towing tank or in a cavitation tunnel. In both cases the measurements made during a open-water test are the carriage speed, the rate of propeller revolution, the propeller thrust and torque as described in [44].

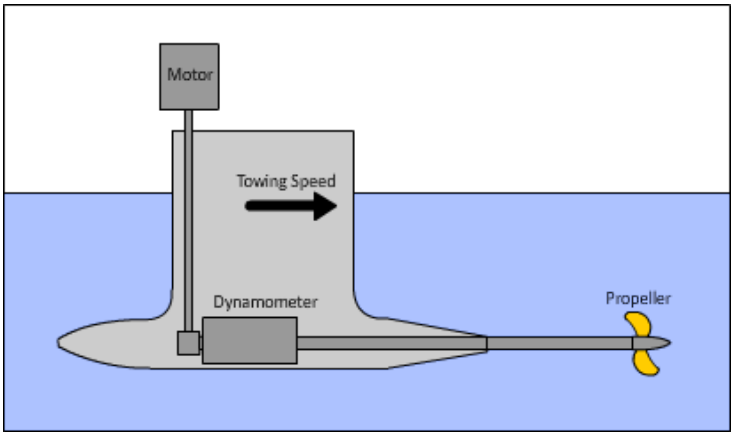

Figure 4.2: Sketch of open-water test in a towing tank.

Self-Propulsion Test:
The self-propulsion test uses the same setup as the resistance test but has the propeller installed in the ship as shown in Figure 4.3. The propeller is driven by a motor through a dynamometer such that the propeller thrust and torque can be measured. In the self-propulsion test the ship hull model is towed through the water at a constant speed and the towing force, heave positions, propeller thrust and torque are measured at different rates of revolutions of the propeller, as described in [43]. The range of the rate of revolutions of the propeller should be such that the point where the towing force equals the skin friction correctional force, is included in the measurements. Ideally, this point is measured but it is also possible to use regression to determine the rate of revolutions of the propeller at the self-propulsion point.

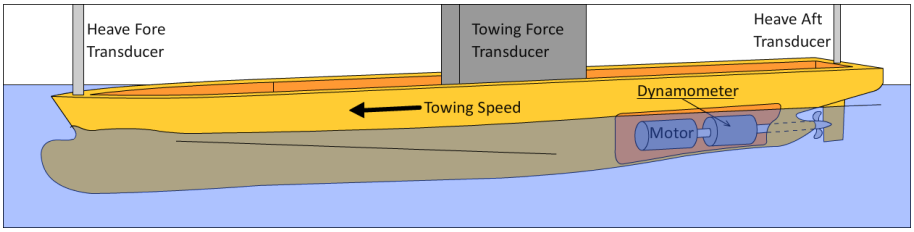

Figure 4.3: Sketch of self-propulsion test in a towing tank.

Additionally, to the above tests it is also common to make cavitation tests in a cavitation tunnel. It has been decided to not make cavitation tests of the CVP propeller in this project. This is both due to the additional costs of cavitation tests but also because results from cavitation tests with the CVP propeller have been presented in other studies see Section 1.3.5.

To validate the improvement in the propulsion efficiency with the CVP propeller, the propeller has to be tested in a self-propulsion test and compared to the performance of a CP propeller in the self-propulsion test. It is therefore necessary to design and make two sets of propeller blades for the tests. One set of propeller blades is designed for a CP propeller and the other set is designed for a CVP propeller. To design appropriate propeller blades, it is necessary to consider a specific case i.e. a specific ship hull model and its operating conditions. A ship hull is therefore designed, constructed and tested through a ship hull resistance test and the wake field is measured, before the propeller blades are designed. Furthermore, before the open-water tests and self-propulsion tests are made, it is necessary to have a test setup which is able to make the cyclical pitching of the propeller blades and measure the required forces and torques etc. This test setup is made in this project, since no known test system exists which is able to satisfy these requirements. The design, construction and testing is financed by "Den Dansk

Maritime Fond" through the grants "2016-048, Prøveopstilling af medstrøm-stilpassende propel" and "2017-094, Medstrømstilpassende skibspropel". The tests are made in the towing tank at FORCE Technology in Kgs. Lyngby, Denmark.

Experimental tests with the CVP propeller are presented in [14,51,84–86]. The studies [14,51] only concern the cavitation test of the CVP propeller but the cavitation performance of the CVP propeller is also considered in [84–86] amongst other performance measurements. These studies generally show reduced cavitation with the CVP propeller. Model scale open-water and self-propulsion tests are presented in [84, 85] and full scale tests are presented in [86]. Common for all these experiments is that the pitch trajectory for the CVP propeller is limited so as to only contain one harmonic and the test concerns the performance of the propeller with and without the cyclical pitching of the blades. None of the studies concern the study of the CVP propeller with multiple harmonics in the pitch trajectory and adapting the propeller blade design for the CVP propeller. This is included in this study and is thereby the novelty of this study.

The second purpose of the experimental tests is to get experimental data to be able to validate the model for the hydrodynamical loads acting on the CVP propeller, i.e. both steady and unsteady components. This validation can be made by using both the experimental results for both the open-water tests and the self-propulsion tests. In a traditional tank test only the steady propeller thrust and torque are measured. To be able to validate the unsteady components of the hydrodynamical loads it is necessary to have a sufficiently high resolution of the measurements during a single propeller revolution. Furthermore, for the CVP propeller it is especially of interest to be able to validate the hydrodynamical loads acting on the propeller blades and not just the whole propeller. Concerning the propeller blade loads, the blades spindle torque about the blades spindle axis i.e. the torque about the z-axis in the propeller coordinate system is especially of interest, because it is one of the main components which determines the requirements for the actuator system.

Measuring the propeller blade loads is not part of the standard tank test. Nonetheless, in previous studies such measurements have been made. In [18,23,32] open-water tests were made where the blade spindle torque, the propeller thrust and torque are measured. The spindle torque is also measured in [59] among four other blade loads under ventilating condition for an azipull thruster. In [76] the steady spindle torque is measured for a series of different blades in behind conditions and under different cavitation conditions. Dynamic measurements of the blade spindle torque, thrust and side force are made in [49] under cavitating conditions for a propeller with an inclined shaft supported by struts. In [17,52] the unsteady propeller loads are measured for different propellers in wake fields with different dominating

harmonics. The novelty of the experiments, described in this chapter, is that the measured hydrodynamical loads are measured during cyclical pitching of propeller blades.

This chapter is divided into six sections, which are:

- Section 4.1 describes the final design and construction of the test system for the CVP propeller.
- Section 4.2 describes the test conditions for the open-water and self-propulsion tests.
- Section 4.4 presents and discusses the results for the open-water tests.
- Section 4.5 presents and discusses the results for the self-propulsion tests.
- Section 4.6 summarizes the chapter contents and discusses the results.

4.1 Test Bench

The design and construction of the test system used to test the CVP propeller has been an iterative process. Only the final version of the test system is presented in this section. The test setup consists of a number of components, which are:

- Ship hull model (described in Section 4.1.1)
- Propeller blades (described in Section 4.1.2)
- Open-water and self-propulsion dynamometer (described in Section 4.1.3)
- Carriage for open-water dynamometer (described in Section 4.1.4)
- Sensors and data acquisition equipment (described in Section 4.1.5)

4.1.1 Ship Hull Model

The ship hull used in this project is designed and built by FORCE Technology in Kongens Lyngby, Denmark. The design and the choice of vessel type have been made in cooperation with MAN Energy Solutions in Frederikshavn, Denmark.

When choosing the vessel type it is desired to choose a vessel type, which gives favourable operating conditions for the CVP propeller and where there could be a market for the CVP propeller. The vessel chosen for this project is a single screw container feeder which was chosen because the variation in the wake field is larger than for a twin or more screw vessel. The container feeder vessel type is chosen because it is a vessel where a CP propeller is commonly used today. This type of vessel could therefore have a significant benefit from the potential efficiency improvement obtained with the CVP propeller.

The ship hull designed by FORCE Technology is shown in Figure 4.4. The designed hull is shown in Figure 4.4a with a close up of the stern in Figure 4.4b and of the bow in Figure 4.4c. The hull model built is shown in Figure 4.4d. It is estimated that the cargo capacity of the vessel is about 1500 TEU. The data for the ship hull is given in Table 4.1 for both full scale and model scale. A scale factor of 1:20 has been used.

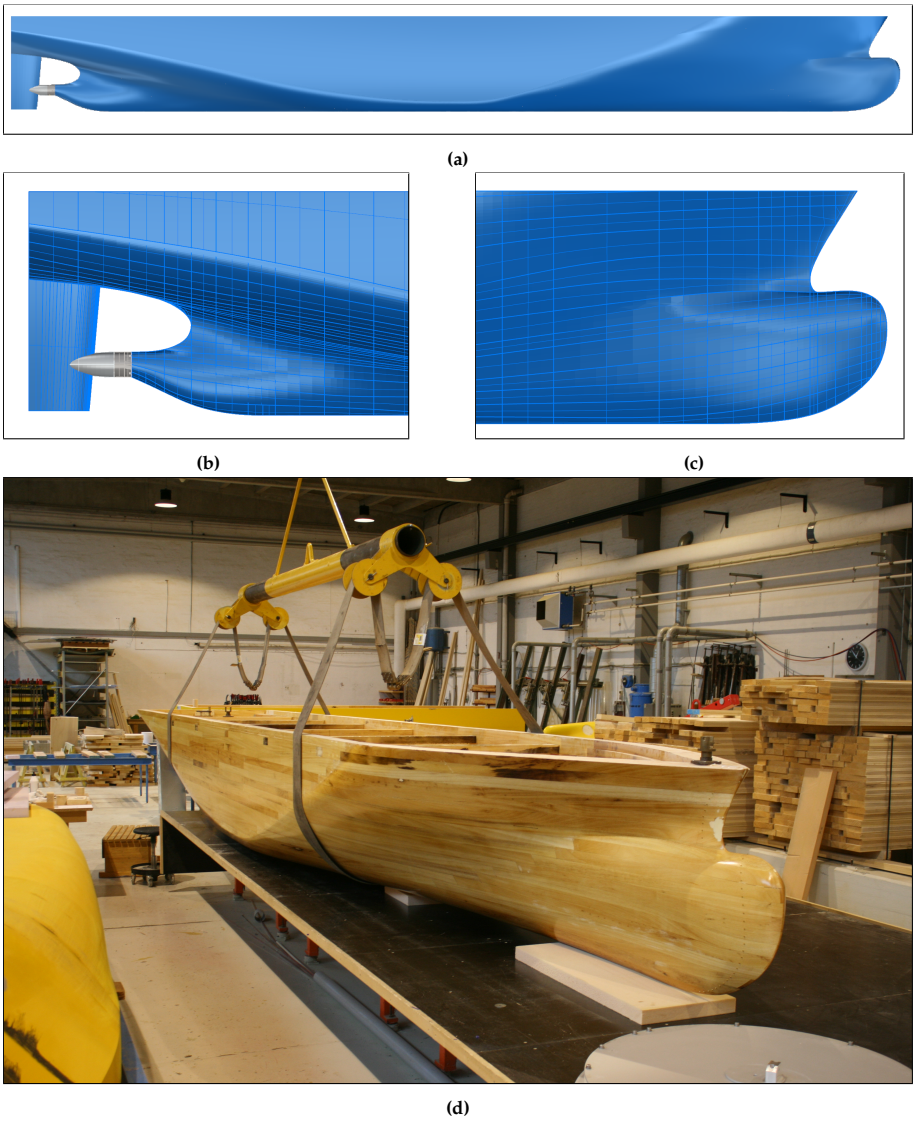

Figure 4.4: (a) Side view of the ship hull as a CAD drawing. **(b)** Side view of the stern as a CAD drawing. **(c)** Side view of the bow as a CAD drawing. **(d)** The build ship hull model.

Table 4.1: Ship hull data for designed container feeder hull in full scale and model scale.

	Full Scale	Model Scale 1:20
Length overall	170 $[m]$	8.5 $[m]$
Length between perpendiculars	160 $[m]$	8 $[m]$
Length on waterline	160.47 $[m]$	8.02 $[m]$
Beam moulded	27.20 $[m]$	1.36 $[m]$
Draught Forward	10 $[m]$	0.5 $[m]$
Draught Aft	10 $[m]$	0.5 $[m]$
Wetted Surface	5804.30 $[m^2]$	$\approx$ 14.51 $[m^2]$
Displacement	28266.19 $[m^3]$	$\approx$ 3.52 $[m^3]$
Shaft immersion	6 $[m]$	0.3 $[m]$
Propeller diameter	8 $[m]$	0.4 $[m]$

Using a scale factor of only 1:20 results in a relatively large ship hull model. The reason for using this scale factor is to get a reasonable ratio between the hub and propeller diameter. Since the hub size is constrained by the requirements to fit the sensors and the pitch mechanism, its diameter could not be reduced further and therefore a smaller scale factor could not be used. It may, in the future, be possible through optimization to design a smaller hub and thereby make it possible to use a smaller model.

Resistance tests were made in FORCE Technology's towing tank using the fabricated hull model. The resistance tests include the ship hull model and a hub dummy, as shown in Figure 4.4b. The results from the resistance tests are shown in Figure 4.5a for the model and in Figure 4.5b for the calculated full scale values, according to the ITTC-57 friction line with a form factor of $1 + k = 1.15$. The calculations were made by FORCE Technology. The results from the resistance tests are used in the design of the propeller blades in Section 4.1.2.

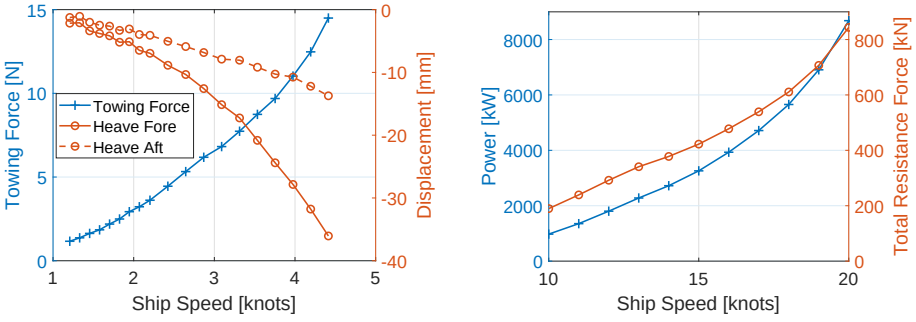

Figure 4.5: (a) Results from the resistance test with the ship hull model. **(b)**Resistance force and power for the ship hull in full scale determine by FORCE Technology.

The wake field of the ship hull model were measured by FORCE Technology. The axial, radial and tangential velocity components of the wake field were measured. The measurements were made for one half of the wake field due to the assumed symmetry in the wake field for a single screw ship. The measurements were made for each 5° and at five radial distances. The wake field measured is shown in Figure 4.6a and Figure 4.6b shows the full wake field. The wake field is shown as the velocity ratio. The wake field measurements were made at a model speed of $\approx 2.07\,[m/s]$ equivalent to a ship speed of 18 $[knots]$ in full scale.

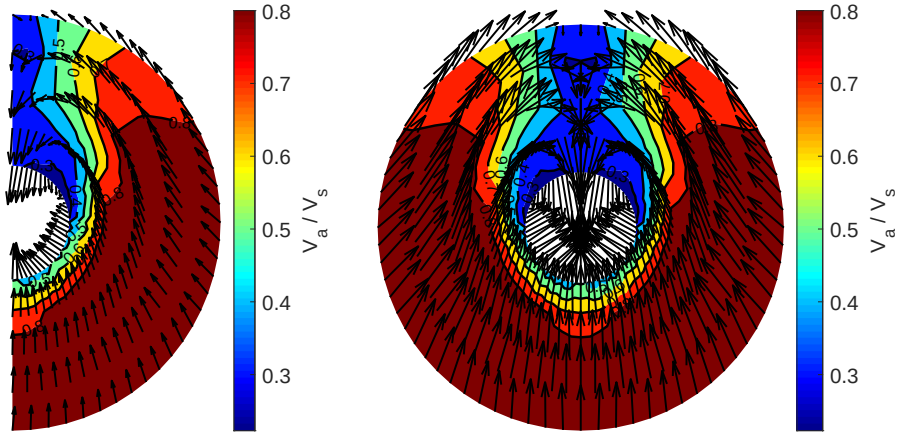

Figure 4.6: (a) Measured three wake velocity fractions of half the wake field. **(b)** The full wake field's wake velocity fractions of hull model assuming symmetry.

The measured wake field, shown in Figure 4.6, is seen to have a large change in the velocity ratio over a relatively short span. It may have been more favourable for the CVP propeller if the change in the velocity ratio was spread over a larger area. This may result in a pitch trajectory with quick changes in the pitch, which requires more power for the pitching motion.

4.1.2 Propeller Blades

Two sets of propeller blades were designed and fabricated for the tests. One set of blades was designed for a CP propeller and the other set for a CVP propeller. The blade designs and the pitch trajectory were made by the propeller design engineer Ege Lundgren at MAN Energy Solutions, Frederikshavn. The blade design and the performance of the propellers are presented in this section.

The first decision for the design of the propeller blades was how many blades the propeller should have. It was decided to design the propeller as a two bladed propeller due to the space constraints in the hub for the sensors and the pitch mechanism. A two bladed propeller is an unconventional propeller to use on merchant ships such as a container feeder. But it was still chosen for the experiments since it allows for more space in the hub to fit sensors, pitch mechanism etc.

The blades for the CP propeller were designed such that propeller power equals the ship power determined from the resistance test with a 10% motor margin and 15% sea margin. To determine the propeller power from the resistance test, the quasi-propulsive coefficient (QPC) was used. The QPC is defined as [20,21]:

$$QPC = \eta_h \, \eta_o \, \eta_r = \underbrace{\frac{1 - t_d}{1 - w}}_{\eta_h} \underbrace{\frac{J_o}{2\,\pi} \frac{K_{T,o}}{K_{Q,o}}}_{\eta_o} \underbrace{\frac{K_{Q,o}}{K_{Q,sp}}}_{\eta_r} \tag{4.1}$$

η_h, η_o and η_r are the hull, open-water and relative rotative efficiency. t_d is the thrust deduction factor. w is the effective wake coefficient. J_o is the advance coefficient. $K_{T,o}$ and $K_{Q,o}$ are the open-water thrust and torque coefficients respectively and $K_{Q,sp}$ is the torque coefficient from the self-propulsion test.

The thrust deduction factor, effective wake coefficient and rotative efficiency were determined by using a similar ship hull in MAN Energy Solutions' database. The open-water efficiency and the rotational speed of the propeller were determined through MAN Energy Solutions' in-house program. The blade design for the CVP propeller was designed such that it has the same thrust as the CP propeller at the same ship speed. This was chosen, in order to make a fair relative comparison of the two propellers' efficiencies.

The pitch trajectory used to design the CVP propeller blades was based on the measured wake field and the skew line of the blade. The skew line was kept equal for the two blade sets. The pitch trajectory was determined as:

$$\alpha_p(\theta_b) = \text{atan}\left(\frac{Pi/D_p}{\pi\, r/r_p}\right) + \beta(\theta_b) - \bar{\beta} + \alpha_T \tag{4.2}$$

Where,

$$\beta(\theta_b) = \text{atan}\left(\frac{V_s\,(1 - w_a(\theta_b))}{2\,\pi\,\omega_p\,r - V_s\,w_t(\theta)}\right) \tag{4.3}$$

α_p is the pitch angle as a function of the blade's position in the wake field (θ_b). Pi/D_p is the non-dimensional pitch at the non-dimensional radial section r/r_p. The radial section considered is at $r/r_p = 0.75$. β is the advance angle of the incoming fluid with $\bar{\beta}$ being the circumferential mean value both at the radial section r/r_p. α_T is a offset angle adjusted to ensure equal thrust for the two blade sets. V_s is the ship speed. w_a is the average axial wake velocity coefficient over the skew line and corrected with the effective wake coefficient, defined using the Tayler method. ω_p is the rotational speed of the propeller. w_t is the tangential wake velocity coefficient defined using the ratio method. Using Eq. 4.2 for the measured wake field and the blade design gives the pitch trajectory shown in Figure 4.7 which is determined for each 10° in the wake field.

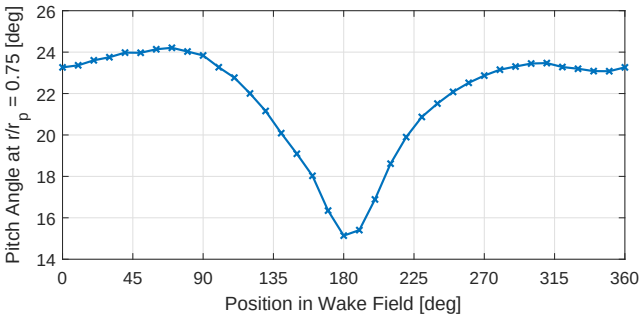

Figure 4.7: Pitch trajectory used in the design process for the CVP propeller blades.

The two sets of propeller blades were designed using MAN Energy Solutions' in-house propeller design program. The design program is based on a quasi-steady lifting line. Furthermore, the propeller was designed to satisfy the classification requirements from Lloyd's register. The propeller blades designed and their main parameters are given in Table 4.2 for their geometric shape and in Table 4.3 for their average performance values. The appropriate engine for this ship and propeller would be a 12 MW two-stoke MAN B&W G50M 7 cylinder engine.

Table 4.2: Main dimensions and operating condition for the two designed blade sets.

		CP	CVP	
Propeller				
Propeller diameter	D_p	8000	8000	$[mm]$
Number of blades	Z	2	2	$[-]$
Hub diameter	D_{hub}	2020	2020	$[mm]$
Blade area ratio		0.411	0.300	$[-]$
Shaft immersion	h_s	6000	6000	$[mm]$
Blade				
Pi/D_p at $r/r_p = 0.7$		0.8486	0.8696	$[-]$
Skew		25°	25°	$[deg]$
Rake		0	0	$[mm]$
Blade mass	m_b	7231	6245	$[kg]$
Operating conditions				
Ship speed	V_s	18.75	18.75	$[knots]$
		≈ 9.65	≈ 9.65	$[^m/_s]$
Shaft speed		87.3	86.7	$[rpm]$
	n_p	≈ 1.46	≈ 1.45	$[rps]$
	ω_p	≈ 9.14	≈ 9.07	$[rad/s]$

Blade Outline

CP CVP

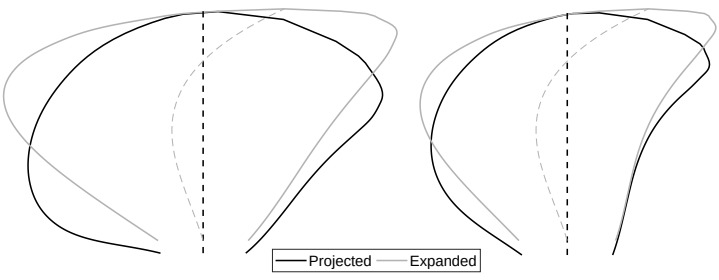

Table 4.3: Propeller performances for the two designed blade sets with and without individual pitching of the blades. The individual pitching of the blades is indicated in the table with "Moving Blade" and "Fixed Blade" indicates that the blades are fixed.

Power [kW]	CP	CVP
Fixed Blade	9823	9565
Moving Blade	9754	9511
Thrust [kN]		
Fixed Blade	931	933
Moving Blade	931	931
Efficiency [-]		
Fixed Blade	0.6513	0.6786
Moving Blade	0.6753	0.6926
Relative Efficiency Increase [%]		
Fixed Blade	-	4.19%
Moving Blade	3.68%	6.34%

The performance data in Table 4.3 are the average values over one propeller revolution. It is seen that the efficiency of the CVP propeller is increased by 6.34% relative to the CP propeller design. The CP propeller design obtains a 3.68% relative increase in efficiency by changing from a fixed blade to a cyclically varying pitch. The unsteady performance of the blade sets, with respect to the thrust, power and efficiency is shown in Figure 4.8 for both the fixed and moving blades.

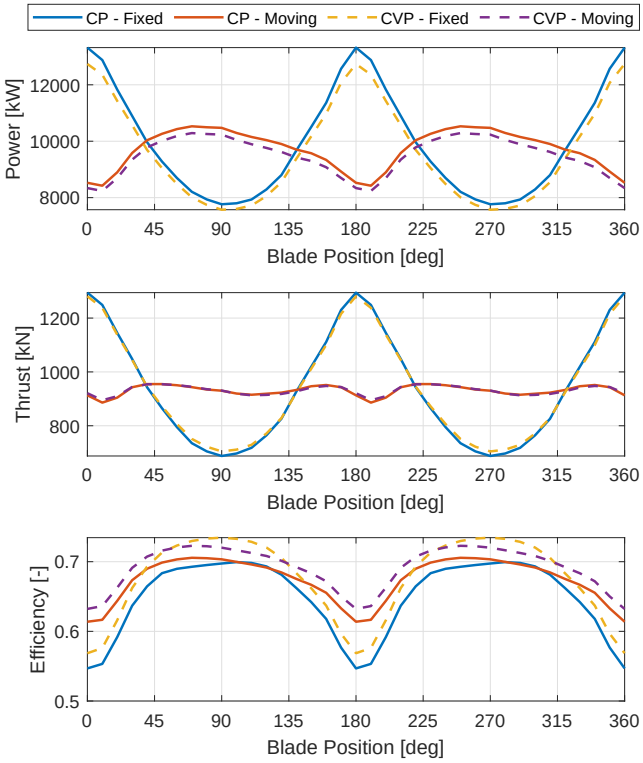

Figure 4.8: Unsteady performance of the design blade sets.

From Figure 4.8 it is clearly seen that the propellers have two blades due to the unsteadiness being dominated by a second-order harmonic. The propellers with fixed blades have larger variations in the performance parameters than the propellers with moving/pitching blades. The reduced thrust variation for the CVP propeller means that the variation in the pressure difference over the blades is reduced. This should give a better cavitation performance for the propeller with moving/pitching blades. The cavitation performance of the CP propeller blades is shown in Table 4.4 for both the fixed and moving blade and in Table 4.5 for the CVP propeller blades. The wake peak in Table 4.4 and Table 4.5 is at $\theta_b = 180°$. The green areas in the images in Table 4.4 and Table 4.5 are where there is sheet cavitation. The cavitation extent was determined through MAN Energy Solutions' in-house program.

Table 4.4: Sheet cavitation in the wake peak for the CP propeller blades with fixed and moving blades.

θ_b	Fixed Blade	Moving Blade	θ_b	Fixed Blade	Moving Blade
80°	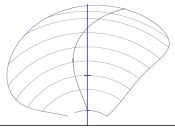	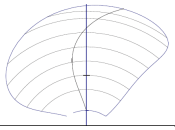	180°	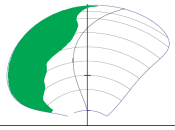	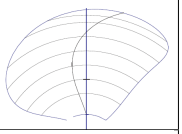
90°	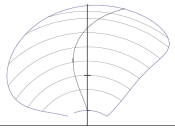	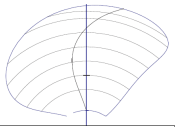	190°	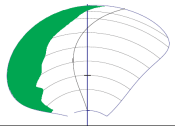	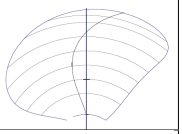
100°	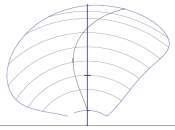	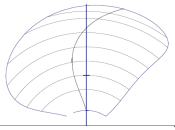	200°	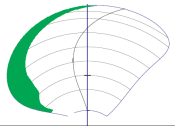	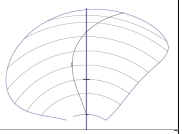
110°	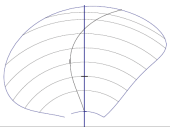	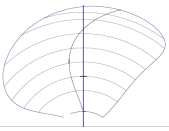	210°	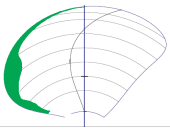	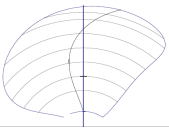
120°	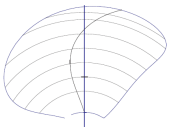	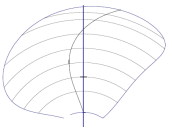	220°	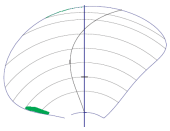	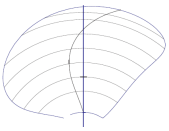
130°	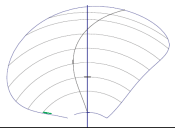	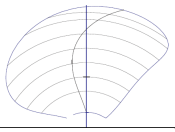	230°	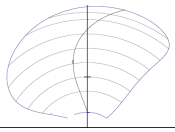	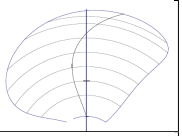
140°	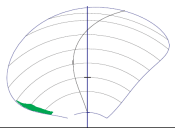	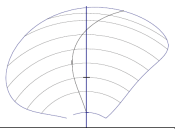	240°	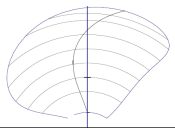	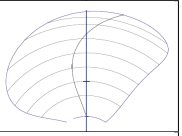
150°	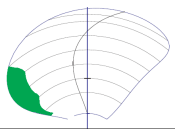	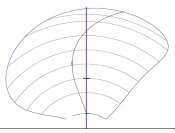	250°	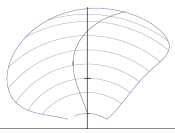	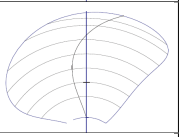
160°	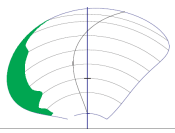	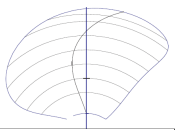	260°	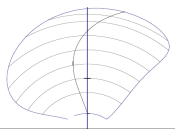	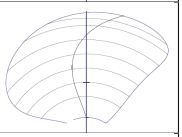
170°	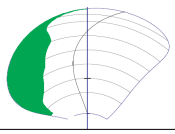	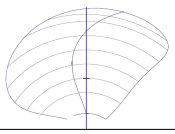	270°	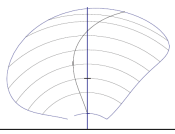	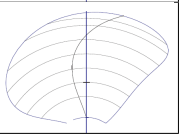

Table 4.5: Sheet cavitation in the wake peak for the CVP propeller blades with fixed and moving blades.

θ_b	Fixed Blade	Moving Blade	θ_b	Fixed Blade	Moving Blade
80°	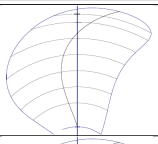	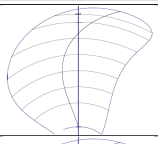	180°	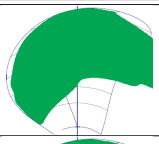	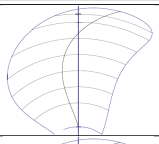
90°	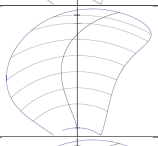	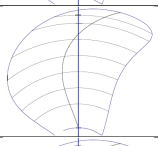	190°	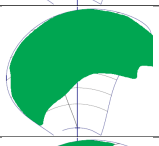	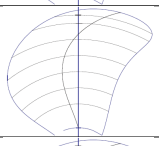
100°	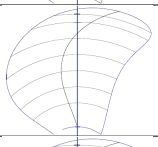	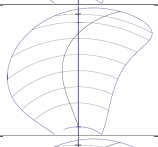	200°	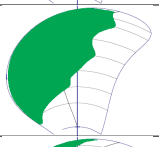	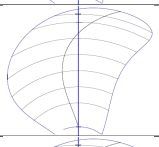
110°	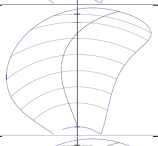	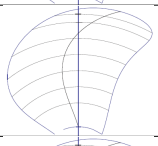	210°	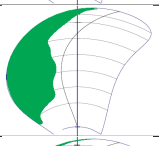	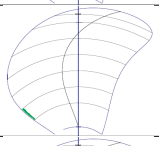
120°	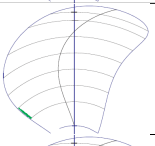	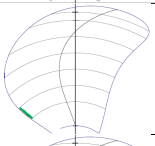	220°	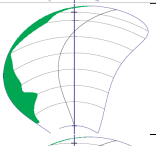	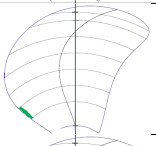
130°	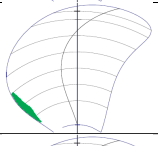	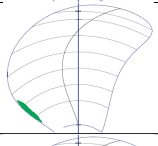	230°	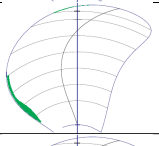	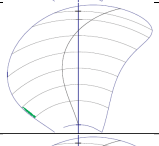
140°	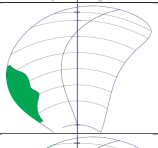	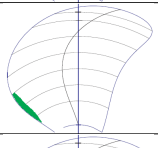	240°	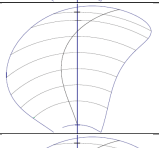	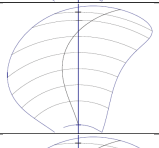
150°	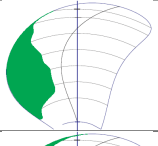	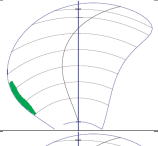	250°	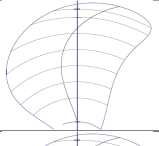	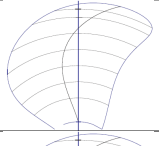
160°	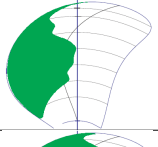	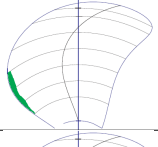	260°	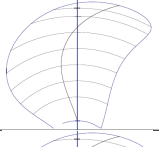	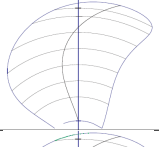
170°	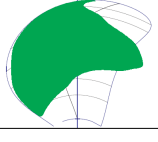	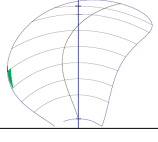	270°	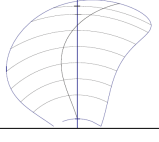	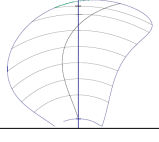

From Table 4.4 and Table 4.5 it is seen that the sheet cavitation for the moving blade is almost eliminated for both the CP and CVP propeller blades. The reduction in the sheet cavitation is the reason for allowing a reduction in the area ratio of the CVP propeller blades compared to the CP propeller blades. Reducing the area ratio means that the pitch or camber for the CVP propeller blade has to be increased compared to the CP propeller blade design, to achieve the same thrust from the propeller. The increase in the pitch/camber for the CVP propeller blade design increases the cavitation when the blade is not moving/pitching as shown in Table 4.5.

4.1.3 Open-Water and Self-Propulsion Dynamometer

The dynamometer should be able to measure the propeller thrust, torque and blade spindle torque dynamically to enable a validation of a model for the hydrodynamical loads for the CVP propeller. Also, the dynamometer should contain a mechanism that can pitch the propeller blades individually according to the desired pitch trajectory. To reduce the financial costs in association with the experimental work it was chosen to design a single dynamometer which could be used for both the open-water and self-propulsion tests.

The development of the test setup can be divided into three phases, over a period from 2016 to 2019. The first phase consisted of a topology study of the cyclical pitch mechanism and sensors and the construction of a prototype for concept validation. This prototype was used to validate the cyclical pitch mechanism concept in air. At the end of the first phase a satisfactory performance was obtained for the concept and it was used in the further development. The second phase consisted of the further development of the cyclical pitch mechanism and sensor from phase one and the manufacturing of it. Furthermore, the second phase also included the development and construction of the open-water carriage and installation of the dynamometer in the ship model. During the second phase the test setup was tested in air and in water to ensure the functionality of the test setup before making the tests at FORCE Technology. The test in water were made at the Aalborg University Department of Civil Engineering in their wave basin and wave flume. At the end of the second phase, in the Summer of 2018, the test setup was transported to FORCE Technology to make the open-water and self-propulsion tests. During these tests a number of problems occurred with the test setup which made it impossible to make the tests during this period. Amongst the problems that occurred were: problems with seals which resulted in water leaking into the test system and causing problems with the data acquisition, long setup time to ensure the correct pitch setting of the propeller blades and reliability of the test system since wires broke off the blade sensor due to fatigue. The third phase consisted of redesigning the problematic components and remaking the tests. The redesigned components consisted of all the pro-

peller components at the end of the shaft except for the propeller blades and the cyclical pitch mechanism. The final design of the dynamometer which was used for the testing is shown in Figure 4.9.

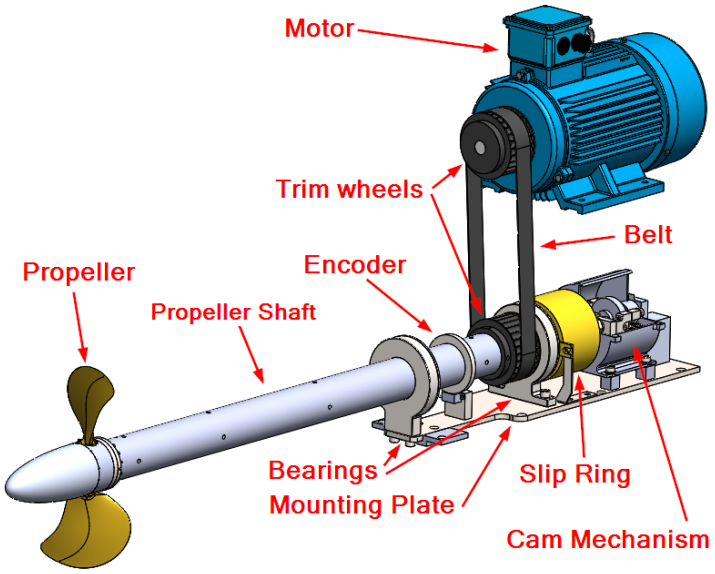

Figure 4.9: Dynamometer for the open-water and self-propulsion tests.

The dynamometer and propeller was driven by a three-phase AC motor through a belt and a pair of trim wheels with a gear ratio on one. The motor was controlled by a Danfoss FC-302 7.5 kW motor controller. The dynamometer was mounted on a mounting plate which was installed either in the open-water carriage or in the ship model, depending on the test. Two bearings were mounted on the mounting plate which supported the propeller shaft. On the outer radial surface of the shaft a magnetic encoder, trim wheel and a slip ring were mounted. The encoder was used to determine the position of the propeller in the wake field and the slip ring was used to transfer the data signals from the rotating shaft to the data acquisition setup. At the end of the propeller shaft, the propeller is mounted and at the other end the cyclical pitch mechanism. The cyclical pitch mechanism was made using a cam mechanism which is shown in Figure 4.10.

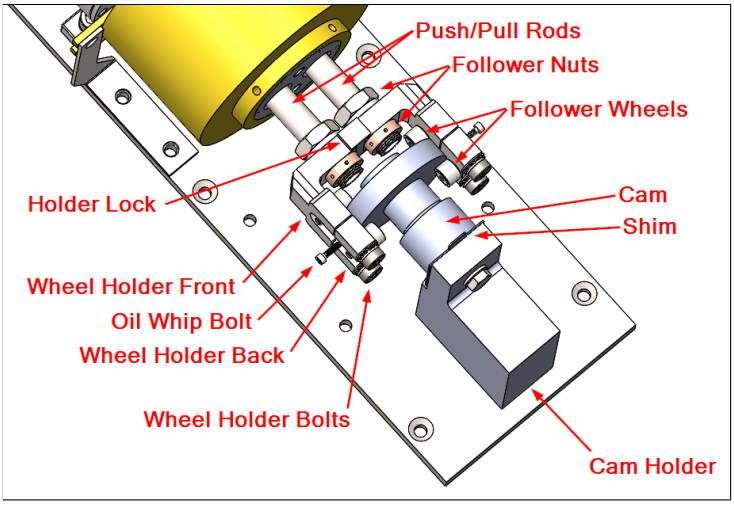

Figure 4.10: The cyclical pitch mechanism.

The cam surface is shaped according to the desired pitch trajectory and its center is aligned with the propeller shaft's center by mounting the cam on the cam holder. On each side of the cam surface is a pair of follower wheels (a pair for each propeller blade), which follow the surface of the cam. Each pair of wheels is mounted on a wheel holder which ensures that the wheels clamp around the cam by tightening the wheel holder bolts. The front wheel holder was mounted onto the push/pull rod by the two follower nuts. The follower nuts were used to adjust the length of the push/pull rods individually thus determining the propeller blades pitch. The shim between the cam and the cam holder is used to change the pitch of both propeller blades. The wheel holders were kept from rotating about the push/pull rod by using a holder lock made of nylon. Depending on how the cam surface was shaped, the follower wheels, holders and push/pull rods are pushed/pulled back and forth as the shaft rotates. The push/pull rods extend through the hollow shaft into the propeller hub, as shown in Figure 4.11. The whole cam mechanism was enclosed in an oil chamber, as shown in Figure 4.9 and Figure 4.11. This enclosure was partially filled with lubrication oil for the cam and the oil whip bolt's function is to spread the oil in the enclosure to lubricate the cam.

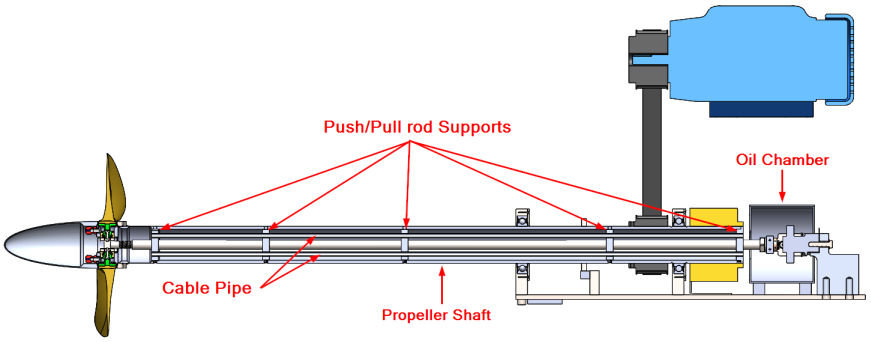

Figure 4.11: Cut-through view of the dynamomemeter.

Through the propeller shaft there are five supports for the push/pull rods which each support the push/pull rods radially through a Teflon sliding bearing. The support for the push/pull rods was made in order to reduce buckling and to ensure the correct alignment of the rods. Through the propeller shaft there are two pipes to keep two cables in place. The cables go from the slip ring to the sensors in the propeller. A cut-view of the propeller is shown in Figure 4.12.

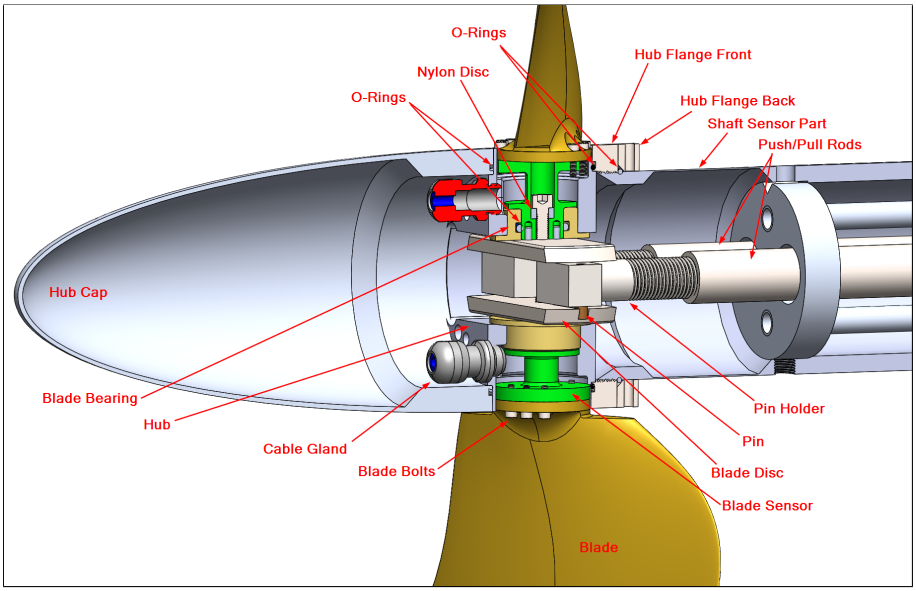

Figure 4.12: Cut-through view of the propeller assembly.

At the end of the push/pull rods, in the propeller, a pin holder is mounted. The pin holder holds a pin which extends from the pin holder into a groove in the blade disc. The blade disc is mounted to the blade sensor through a bolt and two pins, and the blade is mounted on the blade sensor through six bolts. When the push/pull rods move, the motion results in a change of the blade pitch.

The hub assembly consists of four parts, two flanges (front and back), the hub and the hub cap. The back flange has four radially threaded holes for four flat point screws to lock the flange from rotating. The front flange is screwed onto the shaft to transfer the axial thrust and ensure that the flanges are aligned correctly. The whole hub assembly was assembled with twelve bolts.

The measurements of the forces and the torques were made by using strain gauges in a full bridge configuration. The strain gauges were placed on the blade sensors and the sensing part of the shaft. The strain gauges on one of the blade sensors was set up to measure the forces along the x- and y-axes in the propeller coordinate system, i.e. the thrust and the side force which are perpendicular to the thrust. The other blade sensor was set up to measure the blade spindle torque. On the shaft, the strain gauges are set up to measure the shaft torque. All of the strain gauges and soldering points are coated with polyurethane lacquer and silicone rubber to protect them from the water. To acquire the signals from the blade sensors, the cables from the blade sensors are wired through a cable gland to ensure that water does not enter the propeller. To keep water out of the propeller a number of o-rings are used at all the assembly joints of the propeller, and the nylon disc was used for the same purpose. It is important to keep water out from the propeller such that the electronics in the hub cap are not exposed to it. Also, if the propeller is flooded, the water can flow through the hollow propeller shaft and cause trouble for the rest of the dynamometer. In the hub cap a printed circuit board was located which distributed the signals for the data acquisition.

4.1.4 Open-Water Carriage

For the open-water tests the dynamometer was enclosed in the open-water carriage such that the dynamometer was not flooded during the test. The open-water carriage is shown in Figure 4.13.

The main components of the open-water carriage are the carriage house, tower and holder. The carriage house is the cylinder enclosing the dynamometer. The carriage tower is welded onto the carriage house and forms the open-water carriage enclosure. The cross section of the carriage tower is formed as foil to streamline the tower. The open-water carriage enclosure was mounted on the towing tank carriage through the carriage holder and

some clamps. The motor was mounted on the carriage holder. The motor holder was used to adjust the height of the motor above the carriage holder and thereby tightening or loosening the belt driving the propeller. The internal details of the carriage and the mounting of the propeller dynamometer are shown in Figure 4.14.

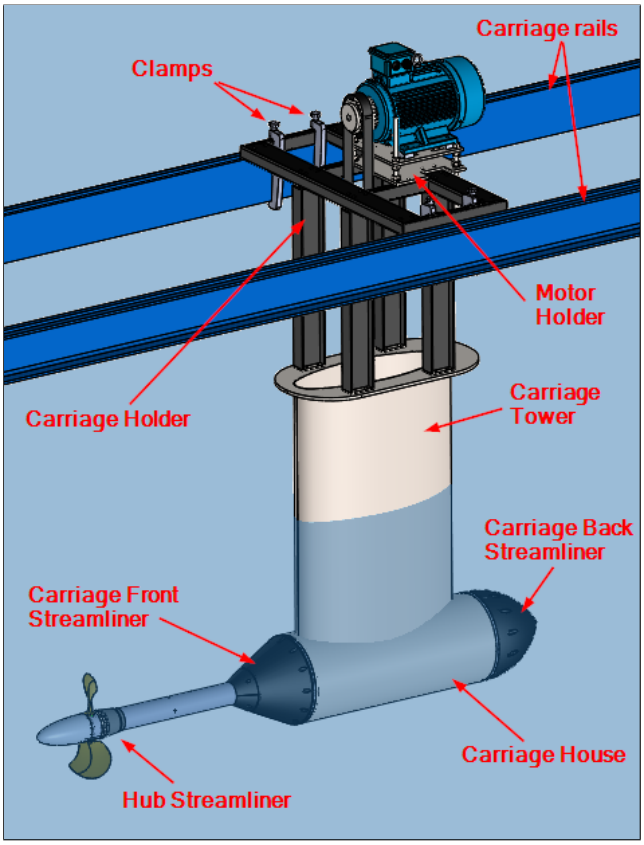

Figure 4.13: The open-water carriage containing the dynamometer for the open-water tests.

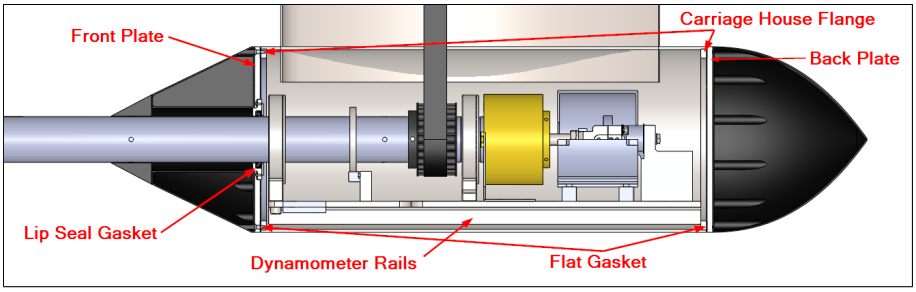

Figure 4.14: The insides of the open-water carriage housing.

Figure 4.15: The build open-water carriage and propeller dynamometer.

The propeller dynamometer was mounted through a set of bolts onto the dynamometer rails which were welded onto the carriage housing. The propeller shaft goes through a lip seal gasket to ensure that no water comes into the carriage housing. The cylinder carriage housing was sealed at each end by a plate which is mounted on the flanges of the carriage housing with a flat gasket seal in-between. The open-water carriage with the dynamometer installed is shown in Figure 4.15.

For the self-propulsion test, the propeller dynamometer was mounted in the ship hull as shown in Figure 4.16. This mounting re-uses the top part of the carriage holder with some adapter pieces on the sides to make it wide enough to be mounted on the ship. The dynamometer shaft extends through the ship hull through a stern tube with a sliding bearing inside. No seals were used at the stern tube other than the sliding bearing. A pump was therefore required to pump the water out of the ship during the self-propulsion tests.

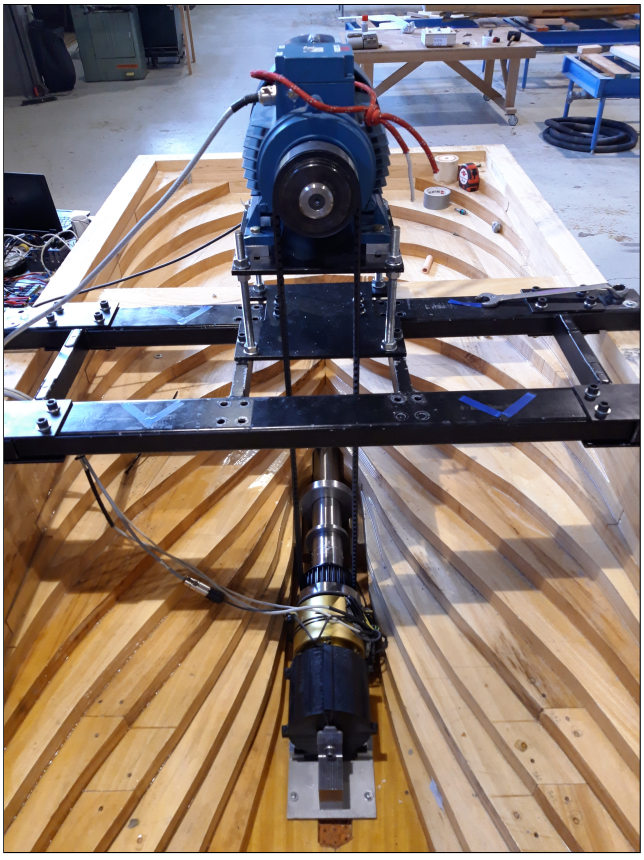

Figure 4.16: Mounting of the propeller dynamometer in the ship hull for the self-propulsion tests.

4.1.5 Sensors and Data Acquisition

To make the tests and be able to make some conclusion from them, it was necessary to be able to log the signals from the different sensors. The signals logged during the tests were:

- Blade thrust sensor signal
- Blade side force sensor signal
- Blade spindle torque sensor signal
- Propeller shaft torque sensor signal
- Propeller encoder signals
- Carriage speed signal
- Towing force signal
- Heave fore and aft signals

The four sensors; blade thrust, blade side force, blade spindle torque and propeller shaft torque were all custom built sensors using strain gauges. The strain gauges for the blade thrust and blade side force were mounted on the same blade sensor. The strain gauges for the blade spindle torque were mounted on the other blade sensor. The strain gauges for the propeller shaft torque were mounted on the inner side of the sensor part of the propeller shaft shown in Figure 4.12.

To evaluate the unsteady loads acting on the propeller and its blades, it was necessary to know the positions of the blades in the wake field. A radial magnetic encoder was therefore mounted on the propeller shaft. The radial mounted encoder was used since an axial mounted encoder could not be mounted at the end of the propeller shaft since the cam mechanism was placed here. The magnetic encoder was a HEIDENHAIN AR-ERM-2480-900 encoder which contained 900 pole pairs, giving a high resolution of the blade's position.

The pitch of the blades was measured during the test setup. The pitch sensor was made by using two displacement sensors of the type OMEGA LD630-100 with a ball tip. The two sensors were mounted onto the hub through a sensor holder as shown in Figure 4.17. The location of the pitch sensors was such that the sensors measured at the same radial section of the blade at two points where the surface of the blade crosses the chord line, as shown in Figure 4.18. The difference in the two signals was then used to determine the pitch of the blade as in Eq. 4.4. The pitch sensor was mounted onto the propeller such that it rotated with the propeller and measured the pitch trajectory over a complete propeller revolution.

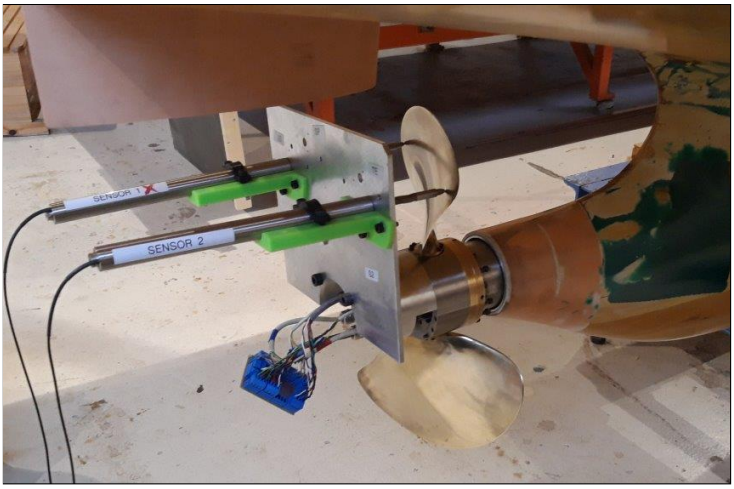

Figure 4.17: Setup for measuring the blade pitch.

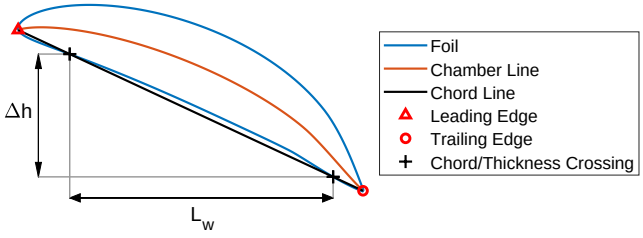

Figure 4.18: Principle for measuring the pitch of the blade.

$$\alpha_p = \text{atan}\left(\frac{\Delta h}{L_w}\right) \tag{4.4}$$

For the carriage speed, towing force and heave measurements, the sensors on the towing tank at FORCE Technology, Lyngby, were used. The signals were not logged with the data acquisition equipment on the towing tank due to the custom sensors used in the test setup. The test setup had its own data acquisition equipment which logged the strain gauge signals, carriage speed, towing force and heave in order to have all the signals synchronised.

The data acquisition was made using LabVIEW2018 together with a NI-cRIO9068 with I/O modules. The I/O modules used for the data acquisition were the NI9237 for logging the signals from the strain gauges and the NI9215 for logging the rest of the analog signals.

The data acquisition was made with different logging frequencies for the signals. The strain gauge signals were logged with a frequency of 2 kHz and were filtered by an integrated filter in the NI9237 module with a break frequency of about half the sampling frequency to prevent aliasing. The signals from the encoder were sampled at 66.6 kHz. The high sampling frequency for the encoder was necessary to resolve the signal because it consisted of 900 sine pulses during one rotation. This gives about 8-9 measurement points per sine wave of the encoder at a propeller speed of 500 rpm. The signals from the carriage were sampled at 5 kHz. In retrospect, this sampling rate could be reduced because the dynamics of these signals was significantly lower than those of the strain gauges.

4.2 Pitch Trajectories

Three different pitch trajectories were used for the CVP propeller tests. One of the pitch trajectories was the variable pitch trajectory used in the blade design in Section 4.1.2. Another pitch trajectory was where the blades are fixed. The last pitch trajectory was a cosine varying pitch trajectory. These pitch trajectories are shown in Figure 4.19. Due to the time constraints, only the CP propeller was tested with the constant pitch trajectory (i.e. fixed blades) in the self-propulsion test. In the open-water test, the constant, cosine and variable pitch trajectories were used for both propellers.

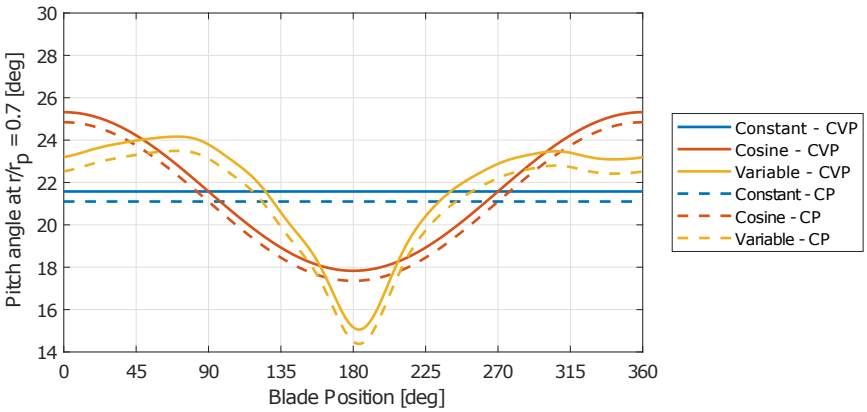

Figure 4.19: Pitch trajectories used in the CP and CVP propeller tests.

The variable pitch trajectory shown in Figure 4.19 is a Fourier series approximation of the non-smooth point defined pitch trajectory in Section 4.1.2. For all the pitch trajectories it is necessary to define them in a continuous differentiable manner such that the jerk is finite and reduces the possibility of

an unexpected breakdown. A Fourier series satisfies this requirement. Furthermore, it is seen that the pitch trajectories for the CP propeller are offset relative to the CVP propeller. This offset was to ensure equivalent thrust for the CP and CVP propeller which was used as a requirement during the blade design.

4.3 Sensor Calibration and Data Treatment Procedure

The test setup had three different types of sensors which had to be calibrated. These sensors were:

- Strain gauge sensors
  - The measurements of the forces and torques were made by using strain gauges in a full bridge configuration. Over each of the bridges there was a voltage difference which was proportional to the loading of the sensor. To determine the relation between the measured voltage and the load, the strain gauge sensors were calibrated by applying known loads to them.
- Encoder index location
  - Due to slack in the hub assembly, the relative position between the encoder's index position and the propeller blade's position could differ for each assembly of the propeller. The index position was therefore measured for each assembly of the propeller.
- Pitch sensor
  - For each assembly of the pitch measuring sensor there could be a difference in how the displacement sensors were placed relative to the mounting plate. The displacement sensors therefore had to be calibrated to determine the new offset for the sensors.

To determine the offset and proportional gain for the strain gauge sensors, the sensors were calibrated by applying known loads on the sensors and measuring the voltage difference. From these measurements a regression model was made for each of the sensors. This regression model was used to determine, the loads acting on the sensors from the measured voltages during the experiments, and the uncertainty of the sensor.

From the calibration it was found that the offset of the strain gauges drifted over time. This was compensated for during the experiments. The regression model for the blade loads included the coupling between the loads.

The regression models used for the blade loads and the shaft torques were:

$$\begin{bmatrix} u_x \\ u_y \\ u_z \end{bmatrix} = \begin{bmatrix} a_{xx} & a_{xy} & a_{xz} \\ a_{yx} & a_{yy} & a_{yz} \\ a_{zx} & a_{zy} & a_{zz} \end{bmatrix} \begin{bmatrix} F_x \\ F_y \\ M_z \end{bmatrix} + \begin{bmatrix} u_{0,x} \\ u_{0,y} \\ u_{0,z} \end{bmatrix} \rightarrow \boldsymbol{u} = \boldsymbol{A}\boldsymbol{F} + \boldsymbol{u_0} \tag{4.5}$$

$$u_p = a_p\, M_x + u_{0,p} \tag{4.6}$$

u_x, u_y, u_z and u_p are the voltages measured for the strain gauge sensors for the blade thrust, blade side force, blade spindle torque and propeller shaft torque, respectively. a_x is the gain coefficients for the regression model. F_x, F_y, M_z and M_x are the blade thrust, blade side force, blade spindle torque and propeller shaft torque, respectively. $u_{0,x}$, $u_{0,y}$, $u_{0,z}$ and $u_{0,p}$ are the offset voltage for the strain gauge sensor. The uncertainty of the regression models was two times the standard deviation of the regression model. The standard deviations for u_x, u_y, u_z and u_p were σ_x, σ_y, σ_z and σ_p, respectively. Furthermore, there was also the uncertainty of the analog to digital convertion in the strain gauge modules which is noted as u_v. The loads and their uncertainties were determined using the regression model as:

$$\boldsymbol{F} = \boldsymbol{A}^{-1}\,\boldsymbol{u} \mp \boldsymbol{A}^{-1} \begin{bmatrix} \sqrt{4\,\sigma_x^2 + u_v^2} \\ \sqrt{4\,\sigma_y^2 + u_v^2} \\ \sqrt{4\,\sigma_z^2 + u_v^2} \end{bmatrix} \tag{4.7}$$

$$M_x = \frac{1}{a_p}\,u_p \mp \frac{1}{a_p}\,\sqrt{4\,\sigma_p^2 + u_v^2} \tag{4.8}$$

In Eq. 4.7 and Eq. 4.8 the offset voltage was not included because the offset was compensated for during the test. The collected uncertainties were determined under the assumption that the uncertainties for the regression model and analog to digital conversion are independent of each other. The uncertainties for each of the sensors are listed in Table 4.6.

Table 4.6: Uncertainty of the strain gauge sensors. * SP = self-propulsion test. + OW = open-water test.

Sensor	Uncertainty
Blade Thrust Sensor	26.979 mN
Blade Side Force Sensor	28.599 mN
Blade Spindle Torque Sensor	0.325 mNm
Propeller Shaft Torque (SP*)	0.297 Nm
Propeller Shaft Torque (OW+)	0.573 Nm

From Table 4.6 it is seen that there are two uncertainties for the propeller shaft torque. One for the self-propulsion test and one for the open-water test. The reason for this is because the characteristics of the sensor change depended on how much the flat point screws holding the hub flange were tightened. Since the hub was dismounted from the shaft when changing from the open-water test to the self-propulsion test it was necessary to recalibrate the sensor. The recalibration of the sensor may change its uncertainty because the flat point screws were tightened differently.

The offset of the strain gauge signals and the possible drift in it over time was compensated for by adapting the test procedures. This test procedure consisted of making a reference measurement with the propeller before each tow through the tank. The reference measurement was made by rotating the propeller at 5 rpm with the tank carriage at rest. The strain gauge signal was determined as:

$$u_x(\theta_b) = u_{test}(\theta_b) - u_{ref}(\theta_b) \tag{4.9}$$

u_x is the strain gauge signal used to determine the load. u_{test} is the measured strain gauge signal during the test. u_{ref} is the measured strain gauge signal during the reference measurement. It was assumed that the strain gauge offset did not drift over the time period from the reference measurement to the end of the test measurement at the end of the tank. This was a time period of about ten minutes. Both of the signals u_{test} and u_{ref} contain the offset which, by subtracting the signals from each other, is cancelled. This also canceled the load due to gravity and buoyancy.

The signals subtracted from each other in Eq. 4.9 were done at their corresponding blade positions. This was done by making a Fourier series approximation of the signals as a function of the blade's position. The number of harmonics used in the Fourier series approximation was the same number used to estimate the pitch trajectory from the pitch measurements. The standard deviation of the Fourier series was included in the uncertainty by assuming that it was independent of the other uncertainty sources. The measurement uncertainty thereby becomes:

$$\boldsymbol{U} = \begin{bmatrix} U_{Fx} \\ U_{Fy} \\ U_{Mz} \end{bmatrix} = \boldsymbol{A}^{-1} \begin{bmatrix} \sqrt{4\,\sigma_x^2 + u_v^2 + 4\,\sigma_{F,Fx}^2 + 4\,\sigma_{0,Fx}^2} \\ \sqrt{4\,\sigma_y^2 + u_v^2 + 4\,\sigma_{F,Fy}^2 + 4\,\sigma_{0,Fy}^2} \\ \sqrt{4\,\sigma_z^2 + u_v^2 + 4\,\sigma_{F,Mz}^2 + 4\,\sigma_{0,Mz}^2} \end{bmatrix} \tag{4.10}$$

$$U_{Mx} = \frac{1}{a_p} \sqrt{4\,\sigma_p^2 + u_v^2 + 4\,\sigma_{F,Mx}^2 + 4\,\sigma_{0,Mx}^2} \tag{4.11}$$

U_{Fx}, U_{Fy}, U_{Mz} and U_{Mx} are the uncertainties of the measurements for the blade thrust, side force, spindle torque and propeller shaft torque, respec-

tively. $\sigma_{F,Fx}$, $\sigma_{F,Fy}$, $\sigma_{F,Mz}$ and $\sigma_{F,Mx}$ are the standard deviations of the Fourier series approximation of the voltage signals measured during the test for the blade thrust, side force, spindle torque and propeller shaft torque, respectively. $\sigma_{0,Fx}$, $\sigma_{0,Fy}$, $\sigma_{0,Mz}$ and $\sigma_{0,Mx}$ are the standard deviations of the Fourier series approximation of the voltage signal during the reference measurement for the blade thrust, side force, spindle torque and propeller shaft torque, respectively. The results presented for the open-water tests and the self-propulsion tests present some of the results for the 0th harmonic. In this case the standard deviation for the 0th harmonic coefficient was used instead of the standard deviations of the Fourier series approximation of the measurement and reference signal.

4.4 Open-Water Test

The open-water tests were made with the dynamometer mounted in the open-water carriage which was mounted onto the towing tank carriage, as shown in Figure 4.20.

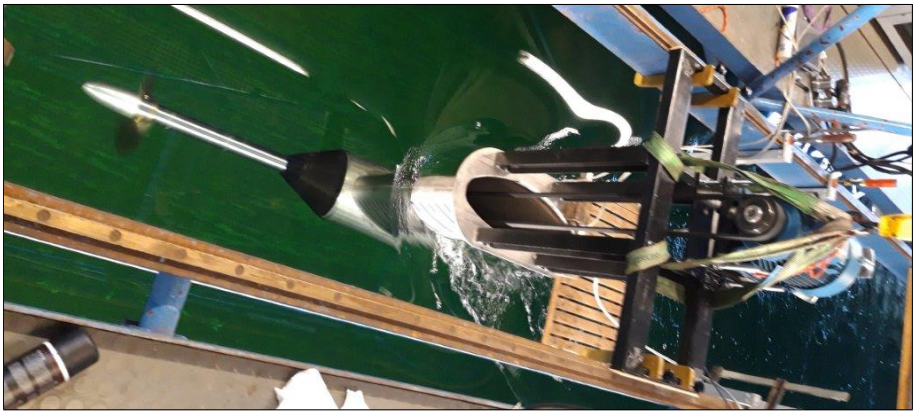

Figure 4.20: open-water carriage mounted on the towing tank carriage.

Before each open-water test, the pitch of the propeller blades was set. The pitch was set by adjusting the shimming of the cam and adjusting the cam follower nuts. When adjusting the pitch it was the mean measured pitch that was used to adjust the pitch. After the open-water tests was made, it was found that this resulted in an error in the pitch for the open-water test. This was because the shaft did not rotate with a constant speed during the pitch measurement. The 0th harmonic of a Fourier series approximation of the measured pitch should be used instead. This was corrected for in the self-propulsion tests. The measured pitch, desired pitch and the pitch error for the open-water tests are shown in Table 4.7.

Table 4.7: The measured pitch and the error with respect to the desired pitch for each propeller configuration used in the open-water tests.

Propeller Configuration		Desired	Measured	Error
CP - Constant at $r/r_p = 0.825$	Thrust Blade Sensor	17.74°	17.73°	0.01°±0.02°
	Spindle Torque Blade Sensor	17.74°	17.73°	0.01°±0.02°
CP - Cosine at $r/r_p = 0.825$	Thrust Blade Sensor	17.75°	17.58°	0.17°±0.06°
	Spindle Torque Blade Sensor	17.75°	17.91°	-0.16°±0.04°
CP - Variable at $r/r_p = 0.825$	Thrust Blade Sensor	17.68°	17.39°	0.29°±0.06°
	Spindle Torque Blade Sensor	17.68°	17.53°	0.15°±0.05°
CVP - Constant at $r/r_p = 0.9$	Thrust Blade Sensor	16.30°	16.31°	-0.01°±0.02°
	Spindle Torque Blade Sensor	16.30°	16.36°	-0.06°±0.01°
CVP - Cosine at $r/r_p = 0.9$	Thrust Blade Sensor	16.31°	16.41°	-0.10°±0.06°
	Spindle Torque Blade Sensor	16.31°	16.38°	-0.07°±0.04°
CVP - Variable at $r/r_p = 0.9$	Thrust Blade Sensor	16.64°	16.54°	0.10°±0.05°
	Spindle Torque Blade Sensor	16.64°	16.60°	0.04°±0.06°

When setting the blade pitch it was desired to get a pitch within $\pm 0.1^{\circ}$ of the desired pitch. From Table 4.7 it is seen that this was not successful for all the setups. This was due to the error of using the mean value instead of the 0th harmonic of the Fourier series. The measured pitch displacement trajectories are shown in Figure 4.21 and Figure 4.22 for the CP and CVP propeller blades, respectively. The measured pitch displacement was used instead of the measured pitch because of the error in the 0th harmonic of the pitch. Furthermore, the measured pitch displacement is shown for both of the blades using the same colour.

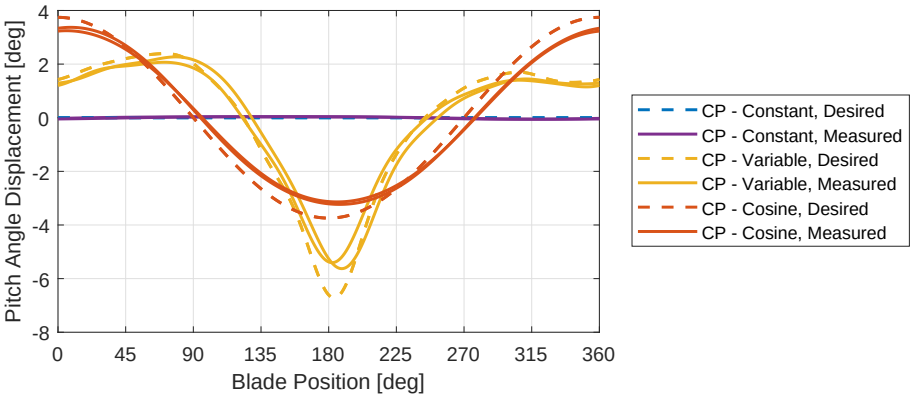

Figure 4.21: Measured pitch displacement for the test setup with the CP propeller for the open-water tests.

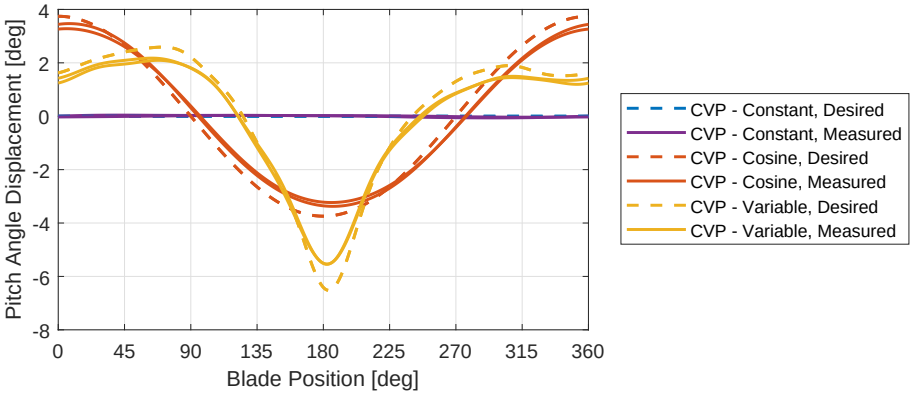

Figure 4.22: Measured pitch displacement for the test setup with the CVP propeller for the open-water tests.

From Figure 4.21 and Figure 4.22 it is seen that the pitch trajectory has, in general, the desired shape. But the amplitudes of the pitch trajectories are smaller than the desired amplitudes and there are some phase differences. This may either be due to the cams not being fabricated as specified or the cams have been designed incorrectly. The fabricated cams can be verified by measuring the cam surface and comparing it to the designed surface. This was not done and is left as further work with the test setup. Furthermore, for the CP propeller blades there is some difference in the variable pitch trajectory. It is thought that this difference may be due to either the follower nuts or the wheel holder bolts not being tightened sufficiently. This could have resulted in the push/pull rods not following the cam as desired. Other measurements of the variable pitch displacement for the CP propeller blades

have been made where the shape of the pitch displacement for the two blades corresponds to the shape of the variable pitch displacement trajectory for the CVP propeller blades shown in Figure 4.22.

The test procedure for the open-water test was:

- If no runs through the tank had been made for 30 minutes, a dummy run was made with constant speed of the ship and propeller. If it had been more than 60 minutes then two dummy runs were made.
- Drive the tank carriage into the starting position in the towing tank.
- Make reference measurement where the propeller rotates with 5 rpm and the tank carriage is fixed. The data logging was made over 60 seconds.
- Accelerate the carriage and propeller up to the desired speed and log the data for 10 seconds. Repeat this until the end of the tank was reached. The propeller speed used for the open-water tests was 250 rpm.
- Stop the carriage and the propeller.
- Drive the carriage back to the starting position in the towing tank.
- Wait 15 minutes between the start of each run.

The open-water curves were determined using the 0th harmonic of the Fourier series approximations of the measurements. The open-water curves as their measured loads are shown in Figure 4.23 for each of the two propellers' three pitch trajectories. The results for quasi-steady RANS CFD simulations of the propellers with fixed pitch are shown for comparison in Figure 4.23. The CFD simulations were made similarly as in Appendix D but with the propeller in model scale and with the viscous sub-layer fully resolved.

From Figure 4.23 it is seen that the measured blade thrust was always smaller than the one determined with the CFD simulation. This difference becomes smaller as the advance coefficient increases. It is seen in the bollard pull tests that two times the blade thrust is not equal to or greater than the propulsion force acting on the ship resistance transducer. It was therefore likely that the measured blade thrust for the open-water tests was smaller than the actual blade thrust. It has to be investigated in the further work why the measured blade thrust was smaller than the actual blade thrust. It is thought that it may be due to the difference between the calibration procedure for the blade thrust sensor and the procedure used for the other strain gauge sensors. The blade thrust sensor was calibrated by using a screw to apply a load to the sensor. A transducer was mounted on the screw so that the load applied with the screw was known. If the screw was not aligned properly during the calibration then this would lead to a smaller load being applied to the sensor than what was measured with the transducer. This lead to the slope for the calibration being smaller than it should be, which would give a smaller measured load. This coincides with the observation from the

experiments. Furthermore, it is seen that the tendencies of the blade thrust do not exhibit any large oscillation in the results and the uncertainty of the measurements is generally small.

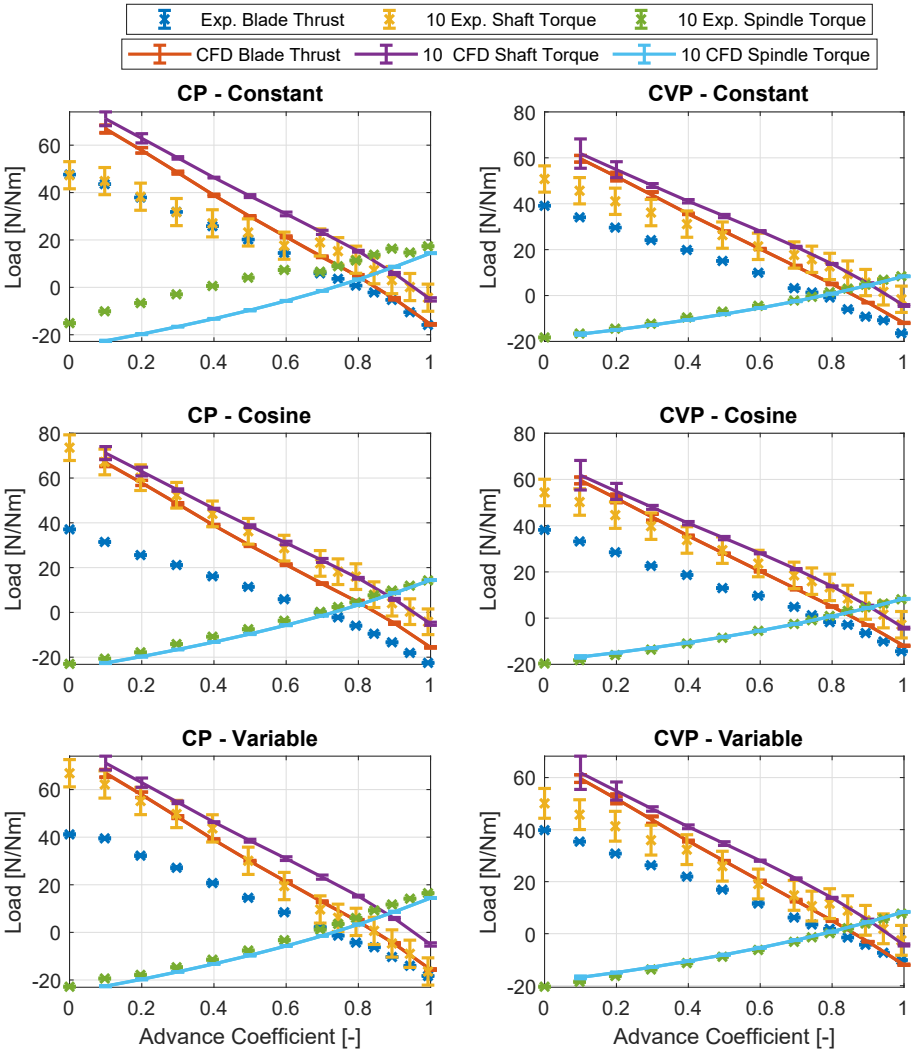

Figure 4.23: open-water loads curves determined as the 0th harmonic of the Fourier series approximation of the measurements.

From Figure 4.23 it is seen that the measurements of the propeller shaft torque is less consistent than the blade thrust. For example, for all the measurements, except for the CP propeller with the cosine pitch trajectories, there is a step change in the propeller shaft torque at about an advance coefficient

of 0.7. This was about where the first tow through the tank was stopped and the secondary tow was made to get the remainder of the measurements. This may have introduced a shift in the offset. This offset change should be compensated for by the reference run, but it is possible that the offset changed during the experiments. This could have been checked by making a reference measurement at the end of the tank. If the two reference measurements at the start and at the end of the tank do not match, then the measurement is invalid and a new one should have been made. This was not done for either the open-water tests or the self-propulsion tests. Instead for some of the propeller configurations the tests were repeated multiple times and it is the most consistent results that are presented in Figure 4.23. The exception to this is for the CP propeller with the constant pitch trajectory for which the measurements are not as consistent as the other measurements. In general, it can be concluded that the propeller torque sensor was not reliable and improving it should be done in the future. One reason for this is that the sensor was relatively insensitive because the sensor was relatively stiff for the magnitude of the propeller torques measured. This means that the sensor was more sensitive to small changes in the offset than the other sensors.

From Figure 4.23 it is seen that the measured blade spindle torque generally fits the simulated blade spindle torque well. The exception to this is for the CP propeller with the constant pitch trajectory. The correspondence between the CFD simulations and the measurements are the worst for the CP propeller and the best for the CVP propeller. The correspondence is not good enough for any of these to validate the CFD simulation within the uncertainty of the experiments and the simulations.

4.5 Self-Propulsion Test

The self-propulsion tests were made with the dynamometer mounted in the ship hull model and the ship hull model was mounted onto the towing tank carriage as shown in Figure 4.24.

Figure 4.24: Setup for the self-propulsion tests.

The self-propulsion tests were made at four different ship speeds given in Table 4.8 in model and full scale. For the self-propulsion test it is the self-propulsion point that is of interest, which is the point where the measured towing force equals the skin friction correctional force. The skin friction correctional force is given in Table 4.8 for the different ship speeds. The skin friction correctional force is used in order to ensure the correct loading of the propeller [43] by accounting for the difference between the skin friction of the model and full scale ship.

Table 4.8: Test conditions used for the self-propulsion tests.

Ship Speed	14 knots	16 knots	18 knots	20 knots
Model Speed	1.590 m/s	1.818 m/s	2.045 m/s	2.271 m/s
Skin Friction Correction Force	23.34 N	29.31 N	35.84 N	42.90 N

The self-propulsion tests were not made for all the configurations used in the open-water tests. This was due to the time available in the tank was limited and because more time had been used for testing the test bench and making the open-water tests, than was planned. It was therefore only possible to test the CP propeller blade design with the constant pitch trajectory and the CVP propeller blade design with the variable, cosine and constant pitch trajectories. It was prioritised to make the self-propulsion test for different pitch trajectories with the CVP propeller, than for the CP propeller. This was because the CP propeller mainly serves as a reference for the possible improvements that could be obtained with the CVP propeller. Note that the pitch setting of the propeller blades for all the CVP propeller trajectory was measured one time when the ship was out of the water. During these measurements the combination of shims for the cams was determined for the three pitch trajectories. Therefore, the cams could easily be changed during the self-propulsion tests without having to take the ship out of the water. This saved a considerable amount of time. The measured pitch of the blades for each self-propulsion test is shown in Figure 4.25 relative to the desired pitch trajectory. From Figure 4.25 it is seen that the amplitudes of the cosine and variable pitch trajectories are not as large as desired which is also the case for the open-water tests.

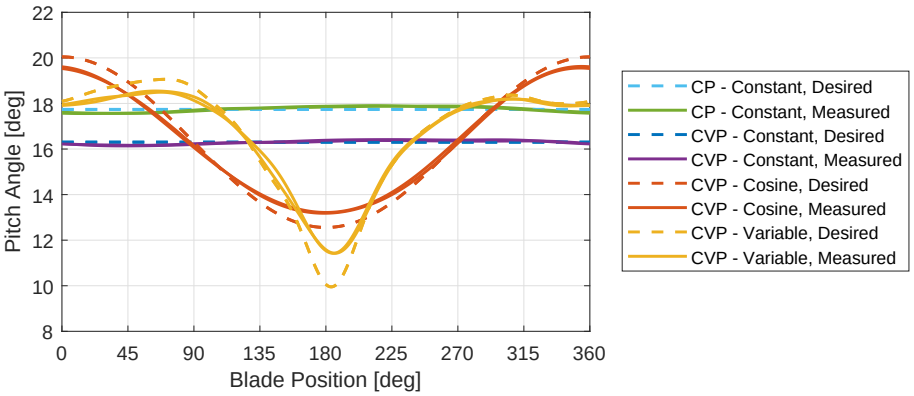

Figure 4.25: Desired and measured pitch trajectories used in the self-propulsion tests for all the propeller configurations.

The pitch of the blades was set such that the 0th harmonic of the measured pitch was within $\pm 0.1^\circ$ of the desired 0th harmonic pitch. The error between the desired and measured 0th harmonic pitch is listed in Table 4.9 for each propeller configuration.

Table 4.9: The measured pitch and the error with respect to the desired pitch for each propeller configuration used in the self-propulsion tests.

Propeller Configuration		Desired	Measured	Error
CP - Constant at r/r_p = 0.825	Thrust Blade Sensor	17.74°	17.75°	-0.01°±0.02°
	Spindle Torque Blade Sensor	17.74°	17.75°	-0.01°±0.02°
CVP - Constant at r/r_p = 0.9	Thrust Blade Sensor	16.30°	16.28°	0.02°±0.03°
	Spindle Torque Blade Sensor	16.30°	16.31°	-0.01°±0.02°
CVP - Cosine at r/r_p = 0.9	Thrust Blade Sensor	16.31°	16.28°	0.03°±0.05°
	Spindle Torque Blade Sensor	16.31°	16.33°	-0.01°±0.06°
CVP - Variable at r/r_p = 0.9	Thrust Blade Sensor	16.64°	16.60°	0.04°±0.06°
	Spindle Torque Blade Sensor	16.64°	16.67°	-0.03°±0.11°

The test procedure for the self-propulsion test was:

- If no runs through the tank had been made for 45 minutes, a dummy run was made with constant speed of the ship and propeller. If it had been more than 60 minutes, two dummy runs were made.
- Drive the tank carriage into the starting position in the towing tank.
- Make reference measurement where the propeller rotates with 5 rpm and the tank carriage is fixed. The data logging was made over 60 seconds.
- (Optional) Make bollard pull with the rate of revolution for the first measurement point for the self-propulsion test of the tow.
- Accelerate the carriage and propeller up to the desired speed and log the data for 10 seconds.
- Accelerate the propeller speed for the second measurement point and log the data for 10 seconds.
- Stop the carriage and propeller.
- Drive the carriage back to the starting position in the towing tank.
- Wait 20 minutes between the start of each tow.

The towing force as a function of the propeller rate of revolution is shown in Figure 4.26 for all of the self-propulsion tests. Four propeller speeds are used for each ship speed and propeller configuration. In Table 4.10, the rate

of revolution of the propeller at the self-propulsion point is given. The point is determined using a linear regression model of the data in Figure 4.26.

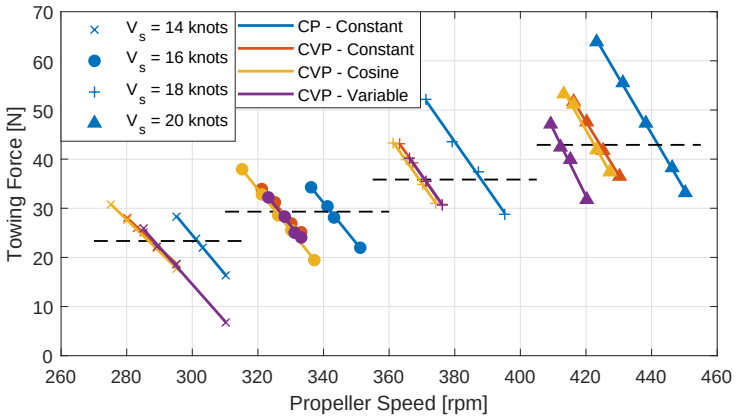

Figure 4.26: The towing force as a function of the propeller revolution for the different propeller configurations and ship speeds. The dashed black line is the skin friction correctional force for the different ship speeds.

Table 4.10: Propeller speed at the self-propulsion point for each ship speed and propeller configuration.

Ship Speed, V_s	14 knots	16 knots	18 knots	20 knots
CP - Constant	301.5 rpm	342.2 rpm	388.1 rpm	442.0 rpm
CVP - Constant	287.7 rpm	327.4 rpm	370.9 rpm	424.3 rpm
CVP - Cosine	286.7 rpm	325.5 rpm	369.2 rpm	422.5 rpm
CVP - Variable	288.3 rpm	326.7 rpm	370.8 rpm	412.3 rpm

From Figure 4.26 and Table 4.10 it is seen that fewer rpms were required for the CVP propeller to obtain the same thrust as the CP propeller. This may have been due to the higher set pitch of the CVP propeller. The required rpms for the CVP propeller was generally the same for all the pitch trajectories except for the variable pitch trajectory at a ship speed of 20 knots. It is thought that this may be due to some non-linear effect of the propeller or an interaction effect between the propeller and ship hull.

During the self-propulsion tests the propeller shaft torque, blade thrust, blade side force and blade spindle torque were measured. Unfortunately, technical problems occurred during the self-propulsion test which could not be fixed during the test without having to further compromise the test program. For some of the tests the blade thrust, blade side force and blade spindle torque were unavailable. The blade thrust was not measured for almost all of the tests with the CVP propeller. Even though the blade thrust was

missing for most of the measurements with the CVP propeller, the propulsion power could still be determined and compared for the CP and CVP propeller because the propeller shaft torque was available. The propeller shaft torque, M_x, measured during the self-propulsion tests is shown in Figure 4.27a and the propulsion power is shown in Figure 4.27b with their uncertainties. The propulsion power was determined as:

$$P_{prop} = M_x \, \omega_p \tag{4.12}$$

ω_p is the propeller speed in $[rad/s]$. The propeller shaft torque shown in Figure 4.27a and the propeller power shown in Figure 4.27b are the 0th harmonic coefficient of the Fourier series approximation of the measurement.

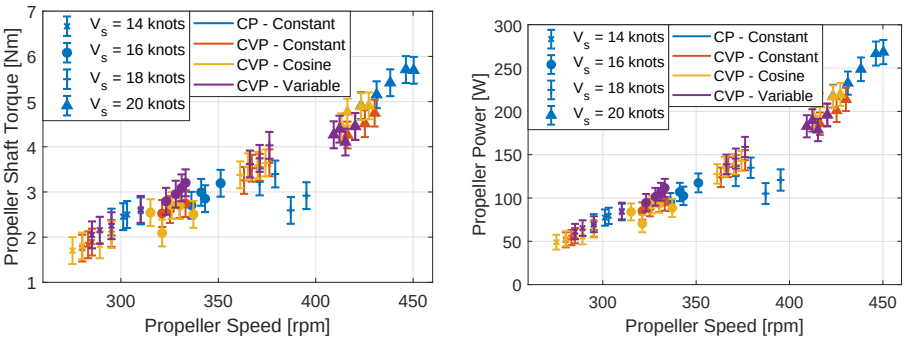

Figure 4.27: (a) Propeller shaft torque and its uncertainty as a function of the rotational speed of the propeller for the different propeller configurations and ship speeds. **(b)** Propeller power and its uncertainty as a function of the rotational speed of the propeller for the different propeller configurations and ship speeds.

From Figure 4.27a and Figure 4.27b it is seen that there was some jitter in the measurements, most significantly for the two highest rates of revolution for the CP propeller at 18 knots. These points were therefore neglected for the further data treatment. The uncertainty of the measurements makes it difficult to distinguish between the different propeller configurations with a high degree of confidence. The propeller power at the self-propulsion point for each of the propeller configuration is given in Table 4.11 and shown in Figure 4.28. The power was determined using a linear regression model for the available data points which followed the general tendency of the measurements. The power uncertainties in Table 4.11 and Figure 4.28 include the uncertainty of the measurement and the uncertainty from the linear regression of the propeller shaft power.

Table 4.11: Propeller power for the different propeller configurations and ship speeds at self-propulsion point.

Ship Speed	14 knots	16 knots	18 knots	20 knots
CP - Constant	77.4 ± 9.5 W	104.4 ± 13.0 W	$146.1 \pm Inf$ W	254.8 ± 14.9 W
CVP - Constant	58.1 ± 9.0 W	90.8 ± 10.3 W	137.2 ± 13.3 W	201.5 ± 14.0 W
CVP - Cosine	57.3 ± 8.9 W	89.9 ± 12.0 W	138.0 ± 12.3 W	213.6 ± 17.4 W
CVP - Variable	64.0 ± 9.1 W	99.8 ± 10.4 W	146.8 ± 12.7 W	187.6 ± 13.9 W

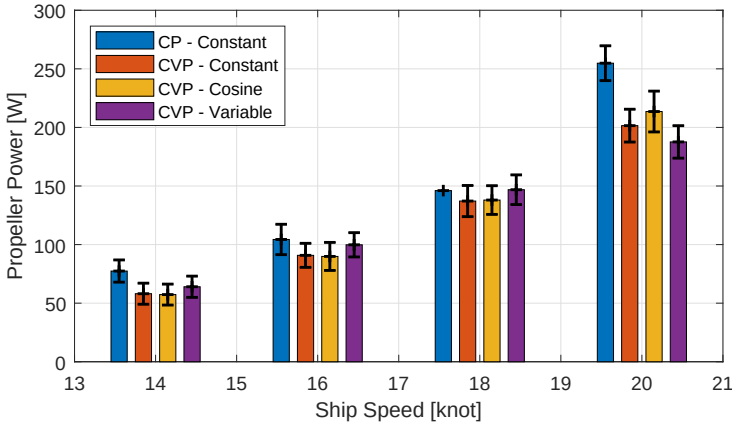

Figure 4.28: Propeller power for the different propeller configurations and ship speeds at self-propulsion point.

From Table 4.11 and Figure 4.28 it is seen that the general tendency is that the CVP propeller uses less power than the CP propeller, but due to the uncertainties in the measurements it is only at some conditions that this is certain. This is at a ship speed of 20 knots for all the pitch trajectories and at a ship speed of 14 knots for the constant and cosine pitch trajectories. At the other conditions the uncertainties overlap each other and therefore it cannot be concluded, with certainty, that a power saving was obtained. If a clearer conclusion is sought, then it requires a new method to determine the propeller shaft torque which has smaller uncertainty bounds.

Having determined the propulsion power, the propulsion efficiency, η_D, for the tests was determined as:

$$\eta_D = \frac{F_D \, V_m}{M_x \, \omega_p} \tag{4.13}$$

F_D is the skin friction correctional force. V_m is the model ship speed. The propulsion efficiency and its uncertainty is given in Table 4.12 and the relative gain in propulsion efficiency for the CVP propeller relative to the CP propeller is given in Table 4.13.

Table 4.12: Propulsion efficiency for the different propeller configurations and ship speeds at self-propulsion point.

Ship Speed	14 knots	16 knots	18 knots	20 knots
CP - Constant	0.49 ± 0.06	0.52 ± 0.06	$0.51 \pm \infty$	0.39 ± 0.02
CVP - Constant	0.65 ± 0.10	0.59 ± 0.07	0.54 ± 0.05	0.49 ± 0.03
CVP - Cosine	0.66 ± 0.10	0.60 ± 0.08	0.54 ± 0.05	0.46 ± 0.04
CVP - Variable	0.59 ± 0.08	0.54 ± 0.06	0.51 ± 0.04	0.53 ± 0.04

Table 4.13: Relative gain in propulsion efficiency for the different CVP propeller configurations and ship speeds at the self-propulsion point. Note that the uncertainty used in the table is the absolute uncertainty of the relative gain in efficiency and not relative.

Ship Speed	14 knots	16 knots	18 knots	20 knots
CP - Constant	-	-	-	-
CVP - Constant	$33 \pm 37\%$	$15 \pm 27\%$	$6 \pm \infty\%$	$26 \pm 16\%$
CVP - Cosine	$35 \pm 38\%$	$16 \pm 30\%$	$6 \pm \infty\%$	$19 \pm 17\%$
CVP - Variable	$21 \pm 32\%$	$5 \pm 24\%$	$-1 \pm \infty\%$	$36 \pm 18\%$

The results in Table 4.12 and Table 4.13 show that it is only at a ship speed of 20 knots that it is certain that an efficiency improvement was obtained.

The above results from the self-propulsion tests do not describe the sub-components of the propeller performance such as; the effective wake coefficient, rotational efficiency and thrust deduction factor. The effective wake coefficient and rotational efficiency are determined through the thrust identity method described in Appendix **??** and [46]. The thrust deduction factor can be determined as described in [46] from the self-propulsion tests or as in [43] from the bollard pull tests. The results from the bollard pull tests are shown in Figure 4.29, which shows the measured blade thrust times two and the measured towing force.

From Figure 4.29 it is seen that the measured thrust was always significantly lower than the measured towing force. This is odd, since the thrust should be larger than the towing force in bollard pull due to the thrust deduction factor. It has to be investigated in the future what is wrong with the thrust sensor which is discussed in Section 4.4.

Due to the thrust not being accurate and that there is almost no thrust measurements for the CVP propeller, the performances of the CP and CVP propeller are not compared for the thrust deduction, effective wake and rotational efficiency.

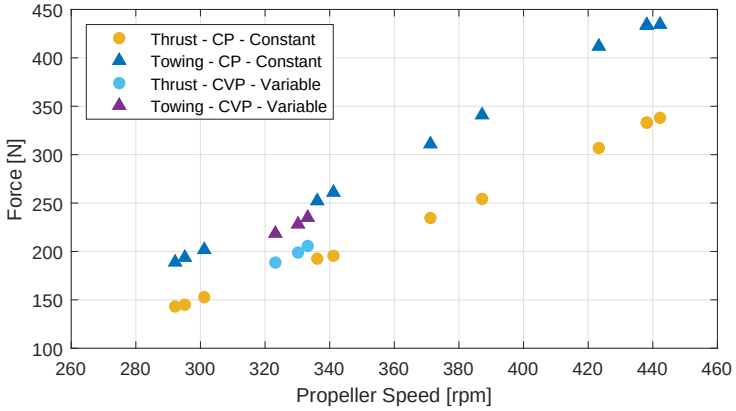

Figure 4.29: Bollard pull test results.

The last results from the self-propulsion test used to compare the performance of the CP propeller and the CVP propeller are the variations in the forces and torques. The CVP propeller with a pitch trajectory should reduce the variations in the forces and torques acting on the propeller and its blades. The difference between the maximum and minimum loads during a revolution is shown in Figure 4.30.

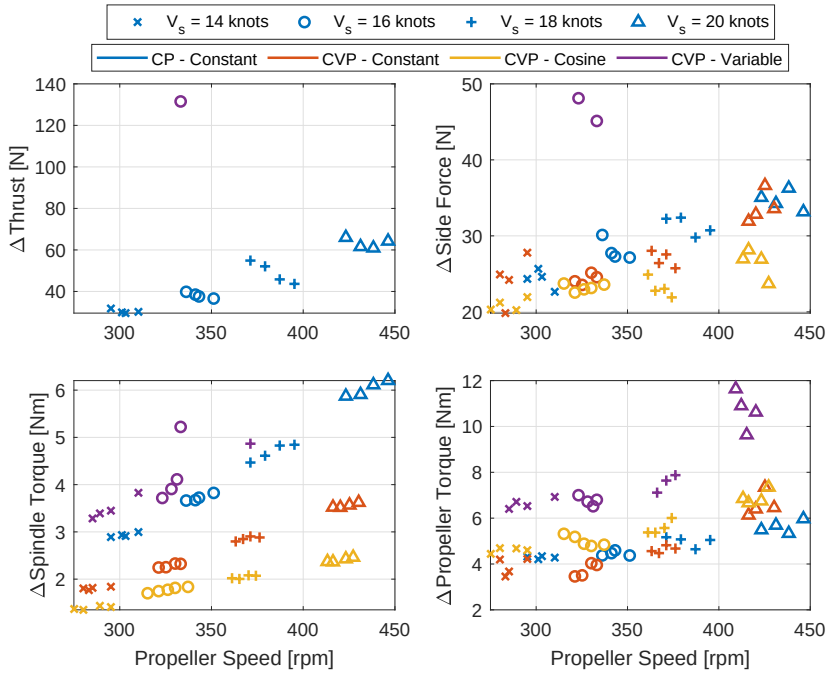

Figure 4.30: Difference between the maximum and minimum of loads during a propeller revolution during the self-propulsion tests.

From Figure 4.30 it is generally seen that the CVP propeller with the constant and cosine pitch trajectory reduces the load variation or it is approximately the same as the CP propeller. For the variable pitch trajectory with the CVP propeller it is seen that the load variation is always larger than the load variations for the CP propeller. This corresponds to the analysis made in Chapter 2, but in the analysis used for the blade design this is not the case.

4.6 Partial Conclusion, Discussion and Future Work

Making experimental tests with the CVP propeller serves two purposes. One is to validate the gain in propulsion efficiency by using the CVP propeller instead of the CP propeller. The second purpose was to get experimental data to be able to validate the model for the hydrodynamical loads acting on the CVP propeller and its blades. To fulfil both of these purposes, both open-water and self-propulsion tests were made with the CVP and CP propellers. One challenge with these tests was that a commonly available test setup did not exist to make these tests with the CVP propeller. A CVP propeller test system was therefore designed and constructed. The test setup was able to pitch the blades cyclically through a cam mechanism and it could measure the three load components, thrust, side force and spindle torque acting on the propeller blade and the propeller shaft torque. The data acquisition was fast enough to capture the unsteadiness of the loads such that these components could be validated. Furthermore, the test setup was made for a two bladed propeller for which two sets of propeller blades were designed for the tests. One set of propeller blades was designed for a CP propeller whilst the other set was designed for a CVP propeller. The blade designs were made for a ship hull model of a container feeder made for the project.

The open-water tests were carried out with three different pitch trajectories for each of the two sets of propeller blades. The pitch of the blades was set before each test according to the desired mean pitch of the pitch trajectory. The pitch measuring procedure used resulted in a small error in the set pitch because the pitch should have been set according to the 0th harmonic Fourier series approximation of the measured pitch trajectory. Furthermore, the measured pitch trajectory did not match the design pitch trajectory. It is unclear if it is because the cams were not fabricated according to the specification, or if the design procedure for the cam surface was wrong, which should be investigated in the future. The quality of the results for the open-water tests is questionable. From the open-water tests and the self-propulsion tests it is seen that the measured blade thrust is smaller than the actual blade thrust. This may be caused by a misalignment during the calibration but the exact cause has to be investigated in further work with the test setup. For the open-water test, the propeller shaft torque was not reliable. The mea-

sured propeller shaft torque at high advance coefficients generally matched the propeller shaft torque determined using quasi-steady open-water CFD simulations of the propellers. At lower advance coefficients, the agreement is generally poorer. Generally, there is a shift in the measured propeller shaft torque at an advance coefficient of about 0.7. This shift may be caused by drift in the offset of the strain gauges. It is typically at about an advance coefficient of 0.7 that the carriage reaches the end of the tank and has to be reset to make the remaining tests. Furthermore, the propeller shaft torque was relatively insensitive in the measurement range and a small shift in the offset could therefore result in a large change in the measured torque. The assembly method used to attach the propeller to the propeller shaft may also be a cause for the shift in the offset. This is because the assembly may not have been the best method to transfer the torque due to lash in the assembly. A better method would perhaps be to use pins in the assembly instead, which should transfer the torque better with reduced lash in the assembly. It is therefore necessary in the future to reconsider how the propeller shaft torque sensor can be improved. The blade spindle torque measured generally corresponds well with the CFD simulations but the difference is larger than the uncertainty in the measurements and the simulations, whereby it cannot be valid at this level.

The self-propulsion tests was made at four ship speeds with the CP propeller blades fixed and with the CVP propeller blades for three different pitch trajectories. For each test the propeller power was determined at the self-propulsion point for each ship speed and propeller configuration. These results generally show that the propulsion efficiency was improved with the CVP propeller, relative to the CP propeller. But the uncertainty of the measurements is generally too large to make this conclusion with certainty. The exception to this is for the highest ship speed test where, with confidence, it can be concluded that an efficiency improvement was obtained.

To make explicit conclusions with respect to the efficiency improvement with the CVP propeller and to get accurate experimental data for model validation, the test setup should be modified. The accuracy and precision of the sensors was not good enough to make a precise conclusion. This is especially the case for the propeller shaft torque sensor. An alternative method is to use the existing shaft as a pipe/support and to place the drive shaft inside the shaft, which can have a significantly smaller diameter and thereby increase the sensitivity of the sensor. This solution may result in the encoder having to be moved closer to the propeller due to the twist of the shaft becoming more prominent. Furthermore, it is also desirable to get the propeller thrust measurement instead of just the blade thrust. This may be possible by placing strain gauges on the propeller shaft and the push/pull rods. Alternatively, the cam can be moved closer to the propeller, as in [51], and then measure the thrust on the shaft between the cam and the carriage housing. The thrust

is thereby not influenced by the push/pull rods but the cyclical pitch mechanism will instead influence the propeller shaft torque. Alternatively, the cyclical pitch mechanism should be changed to be an actuator in the propeller hub, whereby the propeller thrust and shaft torque can be measured on the drive shaft. The challenges with this are to design a system which can pitch the blades fast, accurately and reliably enough.

For the further work the URANS CFD simulation of the CVP propeller should be made with the blades making the cyclic pitching motion according to the pitch trajectories tested. The agreement between the variations in the hydrodynamical loads from the experiments and the variations in the hydrodynamical loads for the simulations can thereby be investigated and the simulation may be validated.

Chapter 5

Conclusion and Future Work

Through a review of the state of the art literature associated with the CVP propeller, four challenges in realising the CVP propeller were identified. These challenges were: design of an optimum propeller blade for the CVP propeller, determination of the optimum pitch trajectory for the CVP propeller, design of an individual cyclical pitching mechanism for the propeller blades and the reliability of the CVP propeller. The main contributions of this dissertation are associated with these challenges, but none of the challenges have been fully resolved through the work presented in this dissertation.

One of the contributions, from this dissertation, is the development of a modelling approach which is able to determine the loads (i.e. forces and torques) acting on the CVP propeller blades during the cyclical pitching of the propeller blades. The loads accounted for are: inertia, hydrodynamic, gravitation, buoyancy, friction, reactive and the actuator loads. This model can be used to determine the requirements for the actuator system that makes the cyclical pitching of the propeller blades. These requirements are with respect to the required power and torque to make the cyclical pitching of the propeller blade. The model established requires that the propeller geometry, operating conditions and pitch trajectory for the CVP propeller are known. Being able to evaluate the requirements for the actuator system is a necessity before a feasibility study can be made for different topological designs of the individual pitch mechanism for the CVP propeller.

Another contribution from this dissertation is the investigation of alternative models to determine the hydrodynamic loads acting on the CVP propeller blades. Common for these alternative models is that they require fewer computational resources to evaluate the hydrodynamic loads for a new pitch trajectory, than an unsteady CFD simulation of the CVP propeller. These models may therefore be more suitable to determine the optimum pitch trajectory for the CVP propeller, than using unsteady CFD simulations. This is

because it may be necessary to make several evaluations to determine the optimum pitch trajectory for the CVP propeller if it is determined in an iterative manner. A series of optimum pitch trajectory candidates are determined for the CVP propeller which minimise the variation in the hydrodynamic loads. The validation of these pitch trajectories is part of the future work for the CVP propeller.

The last contribution from this dissertation is the design and construction of a model scale test setup for the CVP propeller. The test setup was fabricated for the project, and was used to make tank tests with the CVP propeller together with a ship hull model design. To determine if the CVP propeller can be used to improve the propulsion efficiency, the tank tests were made using two different sets of propeller blades. One set designed for a CP propeller and the other set designed for a CVP propeller whereby a relative comparison could be made. The results showed that the CVP propeller has a tendency to improve the propulsion efficiency but the uncertainties are generally too large to make conclusions with certainty. The exception to this is for the highest ship speed tested where there is an efficiency improvement greater than the uncertainty of the measurements. This does not account for the required power to pitch the propeller blades cyclically. In order to make more accurate conclusions about the efficiency improvement with the CVP propeller, the design of the test setup should be reconsidered as part of future work. Furthermore, the test setup was made such that it was able to measure some of the blade loads which, in the future, can be used to validate the models for the CVP propeller.

5.1 Future work

None of the identified challenges in realising the CVP propeller have been fully resolved in this dissertation. Resolving these challenges is therefore part of future work. The future work can also be related more specifically to the contribution of this dissertation as:

- The adaptation of the propeller blade design from the CP propeller to the CVP propeller has, in this dissertation, been determined through a quasi-steady approach. It has, in this dissertation, been shown that the quasi-steady approach is not suitable to determine the pitch trajectory for the CVP propeller. It is therefore likely that the quasi-steady approach is not appropriate to determine the adapted propeller blade geometry for the CVP propeller. It has to be investigated, in the future, if it is an appropriate approach to use for the design of the CVP propeller blades. If it is not, then an approach has to be found which is more appropriate to design the propeller blade for the CVP propeller.

- The design of the propeller blades for the CVP propeller should also be considered as part of an optimisation scheme for the design of the complete CVP propeller system. The optimisation scheme should also consider the pitch trajectory and the individual pitch mechanism as design variables. The objective of the optimisation scheme should include the performance of the propeller such as: thrust, efficiency, shaft vibrations, cavitation, pressure pulses, noise and reliability over the range of operation of the vessel. Using such an optimisation scheme would ensure an optimum design for the CVP propeller. It is part of the future work to make such an optimisation scheme.

- The modelling approach developed to determine the loads acting on the CVP propeller blades is based on a number of assumptions. Future work should investigate whether these assumptions are appropriate. One of the assumptions is the load distribution in the blade bearing which is used to determine the frictional loads. Different assumptions have been made for these load distributions which yield significant differences in the frictional loads. Therefore, it should be investigated which approach is best suited or conservative enough to model the frictional loads. This can be investigated through experiments and elastic simulations of the blade bearing.

- To determine the topological design of the individual cyclic pitch mechanism of the CVP propeller, a morphological analysis should be made. The morphological analysis considers a number of different topological designs for the individual cyclical pitch mechanism and evaluates if these designs can satisfy the requirements for the mechanism. These requirements are determined by using the approach presented in this dissertation for the range of operating conditions for the vessel.

References

[1] 23th ITTC, "Propulsion Committee: Final Report and Recommendations to the 23th ITTC," 2002.

[2] 24th ITTC, "Propulsion Committee: Final Report and Recommendations to the 24th ITTC," 2005.

[3] 25th ITTC, "Propulsion Committee: Final Report and Recommendations to the 25th ITTC," 2008.

[4] 25th ITTC, "The Specialist Committee on Wake Fields: Final Report and Recommendations to the 25th ITTC," 2008.

[5] 26th ITTC, "Propulsion Committee: Final Report and Recommendations to the 26th ITTC," 2011.

[6] 26th ITTC, "The Specialist Committee Scaling of Wake Field: Final Report and Recommendations to the 26th ITTC," 2011.

[7] 27th ITTC, "Propulsion Committee: Final Report and Recommendations to the 27th ITTC," 2014.

[8] 27th ITTC, "Specialist Committee on CFD in Marine Hydrodynamics," 2014.

[9] 28th ITTC, "Propulsion Committee: Final Report and Recommendations to the 28th ITTC," 2017.

[10] 28th ITTC, "Specialist Committee on Energy Saving Methods - Presentation and Discussion at the 28th ITTC Conference," 2017.

[11] ABB, "Podded Propulsion," http://www.abb.com/cawp/seitp202/91ab6289fa6ca6d6c1256dad0054ac5a.aspx, 2018.

[12] Airfoil Tools, "NACA 6412 (naca6412-il) Xfoil prediction polar at RE=1,000,000 Ncrit=9," http://airfoiltools.com/polar/details?polar=xf-naca6412-il-1000000, 2018.

[13] J. C. Bakker, H. T. Grimmelius, and A. Wesselink, "The use of non linear model in the analysis of cpp actuator behaviour," *World Maritime Technology Conference*, 2006.

[14] S. Bindel, "Oscillating-Bladed Propellers," Seventh Symposium Naval Hydrodynamics, August 1968.

[15] R. L. Bisplinghoff, H. Ashley, and R. L. Halfman, *Aeroelasticity*. Dover Publications Inc., 1955, ISBN: 0-486-69189-6.

[16] R. J. Boswell, S. D. Jessup, and K.-H. Kim, "Periodic Single Blade Loads on Propellers in tangential and longitudinal wakes," SNAME Propellers '81 Symposium, June 1981.

[17] R. J. Boswell and M. L. Miller, "Unsteady Propeller Loading-Measurement, Correlation with Theory, and Parametric Study," Department of the Navy Naval Ship Research and Development Center, 1968, Report 2625.

[18] R. J. Boswell, J. J. Nelka, and R. D. Kader, "Experimental Spindle Torque and Open-Water Performance of Two Skewed Controllable-Pitch Propellers," *David W. Taylor Naval Ship Research and Development Center Report No. 4753*, 1975.

[19] B. J. Cantwell, "AA200 Applied Aerodynamics - Course Notes," Stanford University, http://web.stanford.edu/ cantwell/, 2014.

[20] J. Carlton, *Marine Propellers and Propulsion*, 2nd ed. Elsevier Ltd., 2007, ISBN: 978-07506-8150-6.

[21] J. Carlton, *Marine Propellers and Propulsion*, 3rd ed. Elsevier Ltd., 2012, ISBN: 978-0-08-097123-0.

[22] J. Clark and E. Grover, "Assessing convergence in predictions of periodic-unsteady flowfields," *Journal of Turbomachinery*, vol. 129, no. 4, pp. 740–749, 2007.

[23] J. Dang, J. Brouwer, R. Bosman, and C. Pouw, "Quasi-Steady Two-Quadrant Open Water Tests for the Wageningen Propeller C- and D-Series," *Twenty-Ninth Symposium on Naval Hydrodynamics*, August 2012.

[24] J. A. Drischler, "Calculation and compilation of the unsteady-lift functions for a rigid wing subjected to sinusoidal gusts and to sinusoidal sinking oscillations," National Advisory Committee for Aeronautics Technical Note 3748, 1956.

[25] C. C. Dubbs, "Propeller," 1939, US Patent 2,231,464.

[26] L. Eca, M. Hoekstra, and G. Vaz, "Verification of Solutions in Unsteady Flows," 2015. [Online]. Available: http://www.refresco.org/?p=1422

[27] L. Eça and M. Hoekstra, "On the Influence of the Iterative Error in the Numerical Uncertainty of Ship Viscous Flow Calculations," *26th Symposium on Naval Hydrodynamics*, 2006.

[28] L. Eça and M. Hoekstra, "Code Verification of Unsteady Flow Solvers with the Method of Manufactured Solutions," *The Seventeenth International Offshore and Polar Engineering Conference*, 2007.

[29] L. Eça and M. Hoekstra, "A procedure for the estimation of the numerical uncertainty of cfd ccalculation based on grid refinement studies," *Journal of Computaional Physics*, 2014.

[30] U. S. Freiberg, T. O. Andersen, and J. R. Nielsen, "Hydrodynamic Modelling and Performance Evaluation of Cycling Varying Pitch Propeller in Non-Uniform Wake Field Using Open-Water RANS CFD Simulations," *Proceedings of the ASME 2018 37th International Conference on Ocean, Offshore and Arctic Engineering*, vol. Volume 7A: Ocean Engineering, 09 2018. [Online]. Available: https://doi.org/10.1115/OMAE2018-78041

[31] U. S. Freiberg, T. O. Andersen, and J. R. Nielsen, "Review of Cyclic Varying Pitch Propeller for Commercial Vessels," *Proceedings of the Sixth International Symposium on Marine Propulsors*, 2019.

[32] I. Funeno, C. Pouw, and R. Bosman, "Measurments and computations for Blade Spindle Torque of Controllable Pitch Propellers in Open Water," *Proceedings of the Third International Symposium on Marine Propulsors*, pp. 381–388, May 2013.

[33] R. Gabriel and M. Atlar, "Calculation of the performance of a ship propeller with cyclic blade pitch control," *International shipbuilding progress*, vol. 45, no. 443, pp. 201–223, 1998.

[34] M. Godjevac, T. van Beek, H. T. Grimmelius, T. Tinga, and D. Stapersma, "Prediction of fretting motion in a controllable pitch propeller during service," *Proc. IMechE Vol. 223 Part M: J. Engineering for the Maritime Environment*, 2008.

[35] M. Godjevac, "Wear and Friction in a Controllable Pitch Propeller," Delft University of Technology, Department of Marine and Transport Technology, 2009, ISBN: 978-90-8891-136-1.

[36] A. N. Hayati, S. M. Hashemi, and M. Shams, "A study on the behind-hull performance of marine propellers astern autonomous underwater vehicles at diverse angles of attack," *Ocean Engineering*, vol. 59, pp. 152 – 163, 2013.

[37] N. Hiroshi and F. Ryosuke, "Screw propeller," Patent JPS6243394, 1987.

[38] D. H. Hodges and G. A. Pierce, *Introduction to Structual Dynamics and Aeroelasticity*. Cambridge University Press, 2002, ISBN: 0-521-80698-4.

[39] I. Hutchings, J. Williams, M. Sutcliffe, G. Roper, G. Plint, S. Kukureka, and N. Randall, "Cambridge Tribology Course - Friction, Wear and Lubrication," University of Cambridge - Department of Engineering, 2017.

[40] K. Hyuk, "Propeller for Ship Method to Adjust Pitch of Propeller," Patent KR20100061167 20100628, 2012.

[41] International Maritime Organisation, "IMO Train the Trainer (TTT) Course on Energy Efficient Ship Operation Module 2 - Ship Energy Efficiency Regularions and Related Guidelines," 2016.

[42] International Maritime Organization, "Guidelines for the reduction of underwater noise from commercial shipping to address adverse impacts on marine life," MEPC. 1/Circ 833, 2014.

[43] ITTC, "ITTC - Recommended Procedures and Guidelines: Testing and Extrapolation Methods Propulsion, Performance Propulsion Test," 2002.

[44] ITTC, "ITTC - Recommended Procedures and Guidelines: Testing and Extrapolation Methods Propulsion, Propulsor Open Water Test," 2008.

[45] ITTC, "ITTC - Recommended Procedures and Guidelines: Uncertainty Analysis in CFD Verification and Validation Methodology and Procedures - 7.5-03-01-01," 2008.

[46] ITTC, "ITTC - Recommended Procedures and Guidelines: Performance, Propulsion 1978 ITTC Performance Prediction Method," 2011.

[47] ITTC, "ITTC - Recommended Procedures and Guidelines: Resistance Test 7.5-02-02-01," 2011.

[48] Japan Marine United Corporation, "Technology Development - Hydrodynamic Engineering - Energy Saving Devices," https://www.jmuc.co.jp/en/rd/development/hydrodynamics/energy-saving/, 2018.

[49] S. Jessup, M. Donnelly, I. McClintock, and S. Carpenter, "Measurments of Controllable Pitch Propeller Blade loads Under Cavitating Conditions," *Proceedings of the First International Symposium on Marine Propulsors*, June 2009.

[50] S. D. Jessup and R. J. Boswell, "The Effects of Hull Pitch Motions and Waves on Periodic Propeller Blade Loads," *Fourteenth Symposium on Naval Hydrodynamics*, 1982.

[51] S. D. Jessup, "Reduction of propeller vibration and cavitation by cyclic variation of blade pitch," 1976, Massachusetts Institute of Technology - Deparment of Ocean Engineering, Thesis.

[52] S. D. Jessup, "Measurement of Multiple Blade Rate Unsteady Propeller Forces," David Taylor Research Center, DTRC-90/015, 1990.

[53] B. Ji, X. wu Luo, S. hong Liu, H. yuan Xu, and A. Oshima, "Numerical Investigation of Unsteady Cavitating Turbulent Flow Around a Full Scale Marine Propeller," *9th International Conference on Hydrodynamics*, 2010.

[54] R. T. Jones, "The unsteady lift of a wing of finite aspect ratio," National Advisory Committee for Aeronautics Report No. 681, 1940.

[55] K. Kazuyuki, "Variable-Pitch Propeller," Patent JP19840241542, 1986.

[56] J. E. Kewin and J. B. Hadler, *The Principles of Naval Architecture Series: Propulsion*, J. R. Paulling, Ed. The Society of Naval Architects and Marine Engineers, 2010, ISBN: 978-0-939773-83-1.

[57] K. Kimura, T. Kawamura, A. Fujii, T. Taketani, and Z. Huang, "Study on Unsteady Cavitating Flow Simulation Around Marine Propeller Using a RANS CFD Code," *Proceedings of the 7th International Sympsosium on Cavitation*, 2009.

[58] C. M. Klaij, G. Vaz, and L. Eça, "Numerical Uncertainty Estimation in Maritime CFD Applications," *6th European Conference on Computational Fluid Dynamics (ECFD VI)*, 2014.

[59] K. Koushan, S. Spence, and L. Savio, "Ventilated Propeller Blade Loadings and Spindle Moment of a Thruster in Calm Water and Waves," *Proceedings of the Second International Symposium on Marine Propulsors*, June 2011.

[60] H. Kwun and J.-N. Kim, "Variable-Pitch-Propeller Drive Device and Pitch-Angle Control Method, and Boat Having Same," US Patent 2015/0166157, 2015.

[61] P. S. K. Lai, R. C. McGregor, and N. Bose, "On the development and application of oscillating foil propellers," *Transactions on the Built Environment*, vol. 1, 1993, ISSN: 1743-3509.

[62] J. G. Leishman, *Principles of Helicopter Aerodynamics*, 2nd ed. Cambridge University Press, 2005.

[63] C. A. Lindahl, "Marine Propeller with Periodically Adjustable Blades," 1967, US Patent 3,323,598.

[64] L. Ljung, *System Identification: Theory for the User*, 2nd ed. Upper Saddle River, NJ, USA: Prentice-Hall, Inc., 1986, ISBN: 0-138-81640-9.

[65] MAN Diesel & Turbo, "EEDI - Energy Efficiency Design Index," https://marine.man.eu/docs/librariesprovider6/4-Stroke-Engines/eedi-energy-efficiency-design-index.pdf?sfvrsn=6, booklet.

[66] MAN Diesel & Turbo, "Variable Pitch Setting During one Rotation," Internal Report at MAN Diesel & Turbo Frederikshavn, 2011.

[67] MAN Energy Solutions, "Internal database," 2018.

[68] MARIN, "Report No. 20558-1-DT - Calm water model tests for a 1000 TEU container vessel," 2006.

[69] M. Martelli, M. Figari, M. Altosole, and S. Vignolo, "Controllable pitch propeller actuating mechanism, modelling and simulation," *Proceedings of the Institution of Mechanical Engineers, Part M: Journal of Engineering for the Maritime Environment*, vol. Vol 228, pp. 29–43, 2013.

[70] R. Mikkelsen, P. Andersen, and J. N. Sørensen, "Modelling of behind condition wake flow in RANS computation on a conventional and high skew propeller," *10th Numerical Towing Tank Symposium*, 2007.

[71] D. Montgomery, *Design and Analysis of Experiments*, 8th ed. John Wiley & Sons Incorporated, 2012, ISBN: 978-1-118-09793-9.

[72] J. R. Nielsen, K. W. Shin, E. Lundgren, and F. Faghani, "Combined Kappel propeller and rubber bulb system for improved propulsion efficiency," *The 34th the Motor Ship Propulsion & Emissions Conference*, 2012.

[73] P. Niyomka, N. Boss, J. Binns, and H. Nguyen, "Experimental Characterization of Collective and Cyclic Pitch Propulsion for Underwater Vehicle," *Third International Symposium on Marine Propulsors*, 2013.

[74] H. Olsson, K. Åström, C. C. de Wit, M. Gäfvert, and P. Lischinsky, "Friction Model and Friction Compensation," *European Journal of Control*, no. 4, pp. 176–195, 1998.

[75] F. Orbeck, "Propeller," 2002, UK Patent BG 2.345.732B.

[76] C. Pronk, "Blade spindle torque and off-design behaviour of controllable pitch propellers," Delft University of Technology, Doctoral Thesis, 1980.

[77] W. J. Richardson, J. Charles R. Greene, C. I. Malme, and D. H. Thomson, *Marine Mammals and Noise*. Academic Press, 1998, ISBN: 0-12-588441-9.

[78] Rolls Royce, "Propulsion," Brochure, 2012.

[79] F. Salvatore, H. Streckwall, and T. van Terwisga, "Propeller Cavitation Modelling by CFD - Result from the VIRTUE 2008 Rome Workshop," *First International Symposium on Marine Propulsors*, 2009.

[80] K. E. Schoenherr, "Feathering controllable pitch propeller," 1966, US patent 3,249,161.

[81] W. R. Sears, "Some Aspects of Non-Stationary Airfoil Theory and Its Practical Application," *Journal of Aeronautical Sciences*, 1941.

[82] K. W. Shin, "Cavitation simulation on marine propellers," Technical University of Denmark, Ph.D. Thesis, 2010.

[83] K. W. Shin, P. B. Regener, and P. Andersen, "Methods for Cavitation Prediction on Tip-Modified Propellers in Ship Wake Fields," *Fourth International Symposium on Marine Propulsors*, 2015.

[84] P. Simonsson, "The pinnate propeller - a cavitation and noise-free propeller," *Propeller '81 Symposium*, 1981.

[85] P. Simonsson, "The Pinnate Propeller," Royal Institute of Technology, Department of Mechanics, 1983, Doctor Thesis.

[86] P. Simonsson, "Report on Full-Scale Tests With Pinnate Propellers in a Swedish Navy Patrol Boat," *Propeller '84 Symposium*, 1984.

[87] F. Stern, R. V. Wilson, H. W. Coleman, and E. G. Paterson, "VERIFICATION AND VALIDATION OF CFD SIMULATIONS," University of Iowa College of Engineering Institute of Hydraulic Reseach, IIHR Report No. 407, 1999.

[88] A. C. Takinaci and M. Atlar, "Performance assesment of a concept propulsor: the thrust-balanced propeller," *Ocean Engineering*, 2002.

[89] S. Tarbiat, H. Ghassemi, and M. Fadavie, "Numerical Prediction of Hydromechanical Behaviour of Controllable Pitch Propeller," *International Journal of Rotating Machinery*, vol. 2014, 04 2014.

[90] J. S. Thomsen and U. Freiberg, "Design of shadow pitpitch system for controllable pitch propellers," Master thesis, Aalborg University, 2015.

[91] Turkey SeaNews International Shipping Magazine, "Germany: Voith to Present New Development at SMM," https://www.seanews.com.tr/germany-voith-to-present-new-developments-at-smm/84511/, 2012.

[92] Ülgen Gülçat, *Fundamentals of Modern Unsteady Aerodynamics*, 2nd ed. Springer, 2016.

[93] UNCTAD, "Review of Maritime Transport 2016," United Nations Conference on Trade and Development, 2016.

[94] T. Watanabe, T. Kawamura, Y. Takekoshi, M. Maeda, and S. H. Rhee, "Simulation of Steady and Unsteady Cavitation on a Marine Propeller Using a RANS CFD Code," *Fifth International Symposium on Cavitation*, 2003.

[95] Wenham Museum, "Paddle Wheel," http://www.wenhammuseum.org/programs/paddle-wheel/, 2018.

[96] A. F. Wesselink, D. Stapersma, D. van den Bosch, and P. C. Teerhuis, "Non-linear aspects of propeller pitch control," *World Maritime Technology Conference*, 2006.

[97] J. Wind, "Principles of mechanisms used in controllable pitch propellers," *1st Propeller symposium*, 1971.

[98] W. Wührer, "Adjustable Propeller for Marine Vessel Drive," 1985, US Patent 4,540,341.

Appendix A

Hydrodynamic Modelling of CVP Propeller Through URANS CFD Simulations

This appendix presents an approach to performing an URANS (Unsteady Reynolds-Averaged Navier-Stokes) CFD simulation of the CP and CVP propellers in a non-uniform wake field incorporating all three velocity components. The purpose of the URANS CFD simulation is to determine the forces and torques acting on the propeller and its blades for the CP and CVP propellers when they operate in a non-uniform wake field. An efficiency comparison between the CP and CVP propeller can therefore be made. The non-uniform wake field is implemented into the simulation without including the ship hull. This is done because the ship hull design is not always available to the propeller designer and excluding the ship hull from the simulation saves computational resources. The URANS CFD simulations are made for the case presented in Chapter 2, which is a single screw CP propeller for a 1,000 TEU container vessel.

This appendix is divided into five sections, which are:

- Section A.1 contains a discussion regarding the uncertainties in using the measured wake field from a scaled ship hull in the simulation of a full scale propeller operating in the wake of the ship. The section discusses different existing methods to compensate for these uncertainties in the measured wake field. One of these methods is selected and is used to incorporate the wake field into the CFD simulation of the full scale propeller

- Section A.2 presents how the wake field is incorporated into the CFD simulation by using an iterative approach to achieve the best correspondence between the simulated wake field and the desired wake field.
- Section A.3 presents the method used to simulate the CP propeller in a non-uniform wake field using URANS CFD. Furthermore, the section also presents the simulation results when it has achieved periodic convergence. The results are presented with their uncertainty bounds determined using the method described in Appendix C.
- Section A.4 presents the method used to simulate the individual pitching of the CVP propeller blades in the URANS CFD simulation and the results of the simulations. The results presented are for the two pitch trajectories for the CVP propeller, determined in Section 2.2, after a periodic convergence has been achieved and with their uncertainty bounds.
- Section A.5 compares and discusses the simulation results for the CP and CVP propeller with respect to their efficiency and the dynamics of the forces and torques acting on the propeller and its blades.

A.1 Uncertainty and Compensation of Measured Wake Field

In this section the uncertainties arising from the use of the wake field measured on a scaled ship hull model to determine the performance of the full scale propeller, are discussed. Different methods to compensate for the uncertainties are presented and one is selected and used for the case considered. The better, the wake field for the full scale ship hull is predicted, the better, the performance of the propeller can be determined. It is therefore necessary to consider the uncertainties of the measured wake field relative to the wake field of the full scale ship hull. Model scale tests are used instead of full scale tests due to the high costs associated with full scale tests.

The main contributors to the uncertainties of the measured wake field relative to the full scale wake field are; the disparity in the flow condition for model scale and full scale flow around the ship hull and the intrusiveness of the wake field measuring sensor on the wake field.

This disparity in the flow around the model scale and full scale ship hull is due to inequalities in the non-dimensional flow quantities. The wake field is commonly measured using a scaled model of the ship hull, typically in a towing tank. The ship hull is towed through the towing tank such that the Froude number is equal for the model scale ship hull and the full scale ship hull. Having the same Froude number ensures the same wave pattern over

the ship hull for the model scale ship hull and the full scale ship hull [20]. The Froude condition equality is described as:

$$Fr_m = Fr_s \qquad \rightarrow \qquad \frac{V_m}{\sqrt{g\, l_m}} = \frac{V_s}{\sqrt{g\, l_s}} \tag{A.1}$$

Fr_m and Fr_s are the Froude numbers for the model scale and the full scale ship hull, respectively. V_m and V_s are the ship speeds in model and full scale, respectively. l_m and l_s are the lengths of the water lines in the model and full scale, respectively. g is the gravitational acceleration constant. The scaled model of the ship hull is generally made by scaling all the dimensions of the ship hull with the factor λ according to $l_m = l_s/\lambda$. To satisfy the Froude number equality, the velocity ratio becomes:

$$\frac{V_m}{V_s} = \frac{\sqrt{g\, l_m}}{\sqrt{g\, l_s}} = \sqrt{\frac{l_s}{l_m}} = \frac{1}{\sqrt{\lambda}} \tag{A.2}$$

Satisfying the Froude number equality makes the Reynolds number between the model and full scale differ. If the model is to have the same Reynolds number as the full scale ship hull, then the velocity ratio becomes (note it is assumed that the viscosity, v, of the fluid is the same in model and full scale):

$$Re_m = Re_s \qquad \rightarrow \qquad \frac{V_m\, l_m}{v} = \frac{V_s\, l_s}{v} \qquad \rightarrow \qquad \frac{V_m}{V_s} = \frac{l_s}{l_m} = \lambda \tag{A.3}$$

It is seen that the velocity ratios cannot be satisfied for both the equal Froude number and the equal Reynolds number condition in Eq. A.2 and Eq. A.3, respectively. When measuring the wake field in model scale the Reynolds number is not the same as it is in full scale. The Reynolds number influences the viscous boundary layer over the ship hull. For the scaled ship hull model the boundary layer becomes larger relative to the hull than the boundary layer for the full scale ship hull would be. This means that the velocity distribution of the measured wake field on the scaled model is not the same, as the velocity distribution of the wake field in full scale.

The other uncertainty source is due to the intrusiveness of the pitot tube used to measure the velocities in the wake field. When measuring the fluid velocities, pitot tubes are placed in the position where the propeller would be placed. The measurement of the velocity distribution in the wake field therefore does not account for the presence of the propeller operating behind the ship hull. The acceleration of the water into the propeller and the interaction between the propeller and the ship hull is therefore not accounted for in wake field measurements.

The measured wake field without the presence of the propeller is called the nominal wake field [6,21]. The wake field which accounts for the acceler-

ation of the water into the propeller is called the effective wake field [21] and this is of interest for a propeller designer [6, 21] and also the one desired to be implemented into the CFD simulation as a substitute for the ship hull.

The effective wake field is obtained from the nominal wake field through the thrust identity method which uses the results from the self-propulsion test and the open-water curves. The difference between the wake field for the model scale and the full scale is due to the viscous boundary and can be accounted for by wake scaling. Wake scaling is done on the measured nominal wake field from which a nominal wake field for the full scale ship hull is obtained.

The International Towing Tank Conference (ITTC) has, over the recent couple of conferences, had a special committee on wake fields [4, 6] and a special committee in hydrodynamics including wake fields [8]. The focus of these committees has been to review and make guidelines for measuring, scaling and predicting the wake field in both model and full scale.

In [6] three scaling methods are reviewed to determine the full scale wake field. One method uses a single scaling factor on all the measuring points for the nominal wake field to obtain the effective wake field. This scaling factor is typically found by using the thrust identity method. This method does not account for the smaller wake peak in full scale due to the smaller boundary layer in full scale. Another method is to make a contraction of the wake peak using some boundary layer considerations. Several of these contraction methods exist but [6] recommends the use Sasajima-Tanaka after having compared a number of these different methods. It should be noted that the accuracy of the Sasajima-Tanaka method depends on the type of ship hull considered. To use the Sasajima-Tanaka method it is necessary to determine the potential wake field which is found by towing the ship hull astern. Since these tests have not been made for the case considered the Sasajima-Tanaka method is not considered for further use. Another method is to determine the nominal wake field in full scale through CFD simulations. To validate the CFD simulation, the measured nominal wake field should be compared by a CFD simulation of the nominal wake field in model scale. If the CFD simulation of the wake field in model scale corresponds with the measured wake field, then the CFD simulation can be used to determine the wake field in full scale. For the case considered the geometry of the ship hull is not available. CFD simulations of the ship hull, to determine the wake field, cannot therefore be used and are therefore not considered further. That leaves only the thrust identity method to scale the nominal wake field to the effective wake field. The thrust identity method does not include a contraction of the wake peak when determining the effective wake field for full scale.

For the case considered the wake field is measured using the measuring grid shown in Figure A.1a which assumes that the wake field is symmetric.

The measured velocity ratio distribution is shown in Figure A.1b which gives the velocity distribution in Figure A.1c. The wake fields in Figure A.1 are viewed from behind the ship hull.

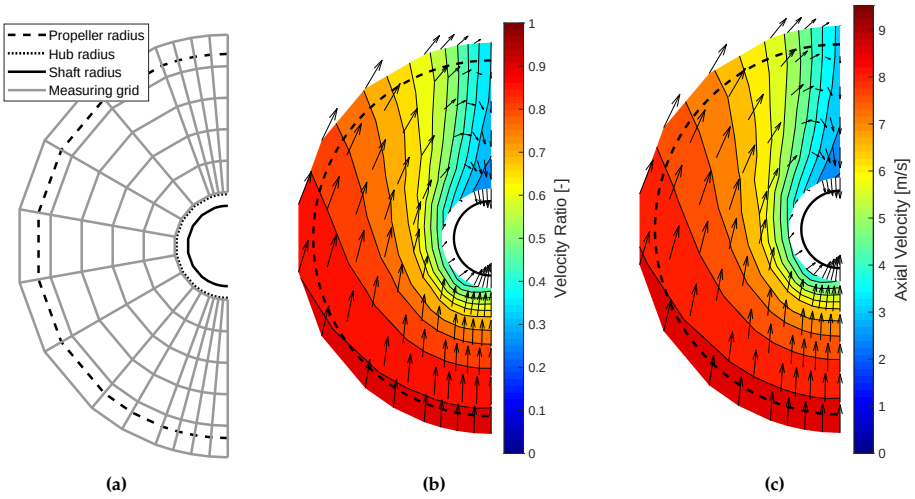

Figure A.1: (a) Wake field measuring grid. **(b)** Measured nominal wake field as velocity ratio (v_a/V_s). **(c)** Measured nominal wake field at the ship speed $V_s = 18.5$ [knots] ≈ 9.52 [m/s].

The nominal wake coefficient, w_{nom}, is determined as a non-dimensional coefficient for the average fluid velocity through the propeller and is calculated as:

$$w_{nom} = 1 - \underbrace{\frac{2}{\pi \left(r_p^2 - r_h^2\right)} \int_{r_h}^{r_p} \int_0^{\pi} v_a(\theta_b, r) d\theta_b \, r \, dr}_{V_a} \frac{1}{V_s} = 1 - \frac{V_a}{V_s} \tag{A.4}$$

r_p and r_h are the propeller and hub radius respectively. v_a is the local measured axial velocity in the wake field which varies with the circumferential and the radial position. θ_b is the angular position in the wake field with respect to the 6 o'clock position and increasing in the clockwise direction when viewing the wake field from behind. V_a is the average advance velocity of the water into the propeller. V_s is the ship speed. To evaluate the integrals in Eq. A.4, the lower limit for the radius is the smallest radius used in the measuring grid and the velocity value at the propeller radius is found through linear interpolation. The resulting nominal wake coefficient is $w_{nom} = 0.278$.

Using the thrust identity as described in [46] and the results from the open-water curve of the stock propeller and the self-propulsion test with the stock propeller from [68], the effective wake coefficient, w_{eff}, is determined to be ≈ 0.266 at a ship speed of 16.55 [knots] and ≈ 0.264 at a ship speed

of 18.5 [knots]. The effective wake field is obtained by scaling the nominal wake field by, λ_w, the ratio between the effective wake coefficient w_{eff} and the nominal wake coefficient w_{nom} as:

$$V_{a,eff}\left(\theta_b, r\right) = \underbrace{\frac{w_{eff}}{w_{nom}}}_{\lambda_w} V_{a,nom}\left(\theta_b, r\right) \tag{A.5}$$

$\lambda_w \approx 0.9554$ at $V_s = 16.55$ [knots] and ≈ 0.9584 at $V_s = 18.5$ [knots]. Applying the scaling to the nominal wake field in Figure A.2a yields the effective wake fields in Figure A.2b and Figure A.2c. This scaling is in correspondence with the scaling made in [68]. The transverse velocities are the same for the nominal and effective wake field.

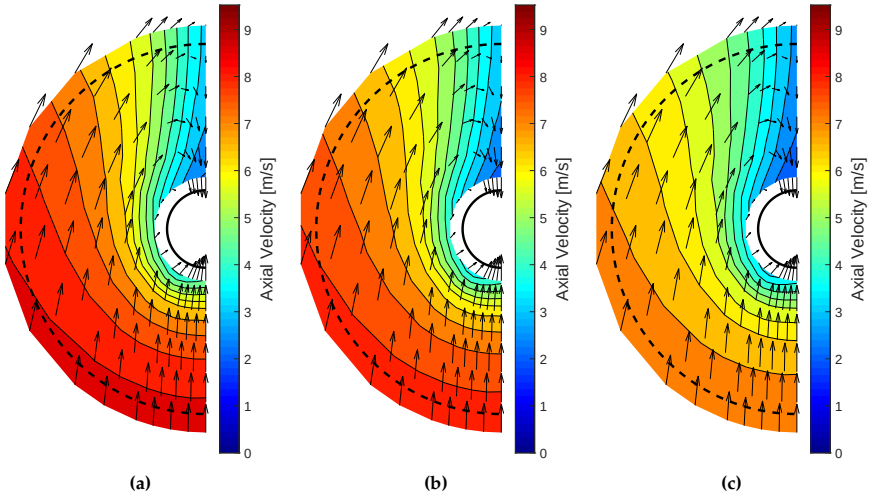

Figure A.2: (a) Measured nominal wake field at the ship speed $V_s = 18.5$ [knots] ≈ 9.52 [m/s]. **(b)** Effective wake field at the ship speed $V_s = 18.5$ [knots] ≈ 9.52 [m/s]. **(c)** Effective wake field at the ship speed $V_s = 16.55$ [knots] $V_s \approx 8.51$ [m/s].

A.2 Implementation of Wake Field in CFD Simulation

The effective wake field is only defined for a small area covering the propeller. In the CFD simulations of the CP and CVP propellers a region significantly larger than the one defined by the effective wake field is used. This is to ensure that the boundary conditions do not affect the simulation results. It is therefore necessary to extrapolate the effective wake field to cover the entire region of the CFD simulation. Furthermore, the transverse velocities cannot be imposed on the boundaries of the CFD simulation and are therefore implemented using momentum sources. This section describes how the effective wake field is implemented into the CFD simulation of the CP and CVP propellers and the required extrapolation of the effective wake field.

To simulate a propeller operating in a non-uniform wake field the whole propeller has to be included in the simulation. The domain therefore becomes a cylinder with the propeller in the center, as shown in Figure A.3.

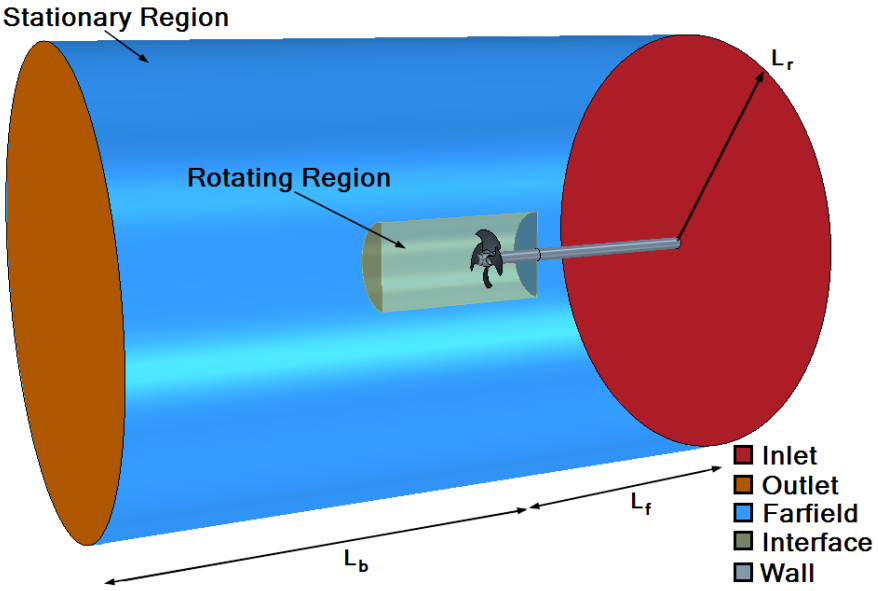

Figure A.3: The domain used in the CFD simulation of the propeller in a non-uniform wake field.

Including the ship's non-uniform wake field into a CFD simulation has previously been made by applying the measured axial velocity to the inlet of the simulation [53, 57, 79, 94]. This approach does not include the transverse velocity components.

A method to account for the transverse velocity in the CFD simulation is to apply momentum sources between the inlet and the propeller to accelerate the water in order to obtain the desired velocity distribution at the propeller plane. This has been used in [83] for an unstructured mesh and in [70, 82] for structured meshes. The same principle of using momentum sources to achieve the transverse velocities is applied to these simulations.

The measured wake field only covers a small part of the domain used in the CFD simulation. It is therefore necessary to extrapolate the wake field velocities to cover the entire domain. The extrapolation of the wake field consists of two parts. One part is to extrapolate the velocities from the outermost radial wake field measurement to the radius of the domain. The second part is to extrapolate the velocities from the innermost radial wake field measurement to the shaft radius.

The radial outward extrapolation of the axial velocity is limited to the ship speed. The extrapolation from the outermost radial measurement to the radial boundary is made for each angular position using a linear function. The slope of the linear function is the same as the slope of the outermost radial measurements. The extrapolation is made for each angular position starting from the 12 o'clock position and made in the anticlockwise direction towards the 6 o'clock position. The slope of the linear function used for the extrapolation can only increase from the 12 o'clock position towards the 6 o'clock position.

The extrapolation from the innermost radial section of the measured wake field, towards the shaft is linear. The linear extrapolation is made by assuming the velocity to be zero at the shaft due to the non-slip condition. The extrapolation of the effective wake field is shown in Figure A.4 at a ship speed of 16.55 [knots] $\approx$ 8.51 [m/s] for the angular positions used when measuring the nominal wake field.

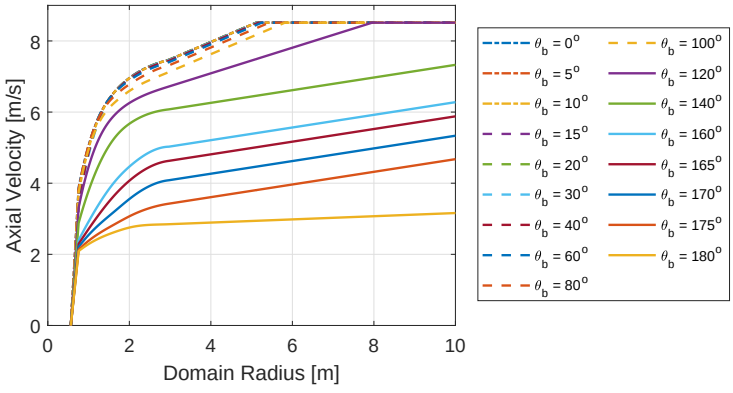

Figure A.4: Extrapolation of the axial velocity of the wake field.

The transverse velocities will be zero far away from the ship hull. The extrapolation of the transverse velocities is made with an exponentially decaying function. The decay function is made such that it has decayed ≈96% at the radius equal to two times the propeller diameter. The extrapolated wake field is shown in Figure A.5a and Figure A.5b.

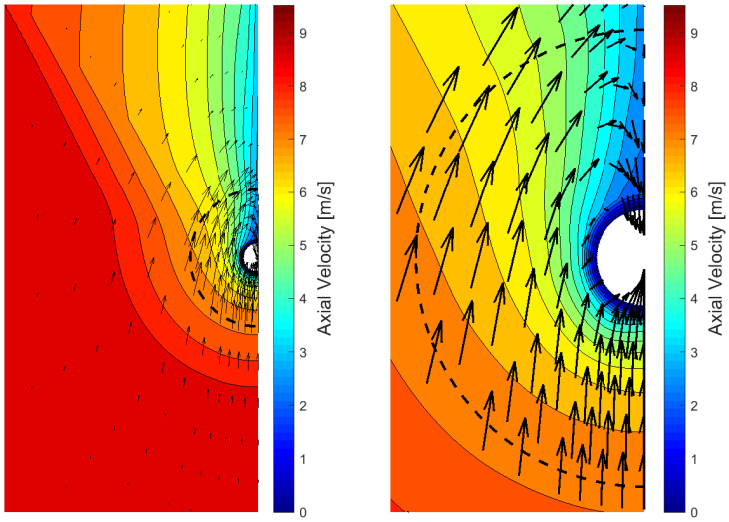

(a) **(b)**

Figure A.5: **(a)** Extrapolated effective wake field for $V_s = 16.55$ [knots]. **(b)** Close-up of the extrapolated effective wake field for $V_s = 16.55$ [knots].

The dashed lines in Figure A.5a and Figure A.5b are the outline of the propeller radius. To obtain the whole wake field, the wake field in Figure A.5a is mirrored about the vertical plane. The axial velocity component of this wake field is applied at the inlet of the CFD simulation. To obtain the transverse velocities at the propeller, momentum sources are defined in a region between the inlet and the propeller. To determine the momentum source strength for the unstructured mesh, an iterative approach is used, as in [83]. The CFD software package used uses the Cartesian coordinate system. The velocities therefore have to be defined in the Cartesian coordinate system instead of the cylindrical coordinate system used until now. The Cartesian coordinate system is shown in Figure A.6a and the cylindrical coordinate system is shown in Figure A.6b.

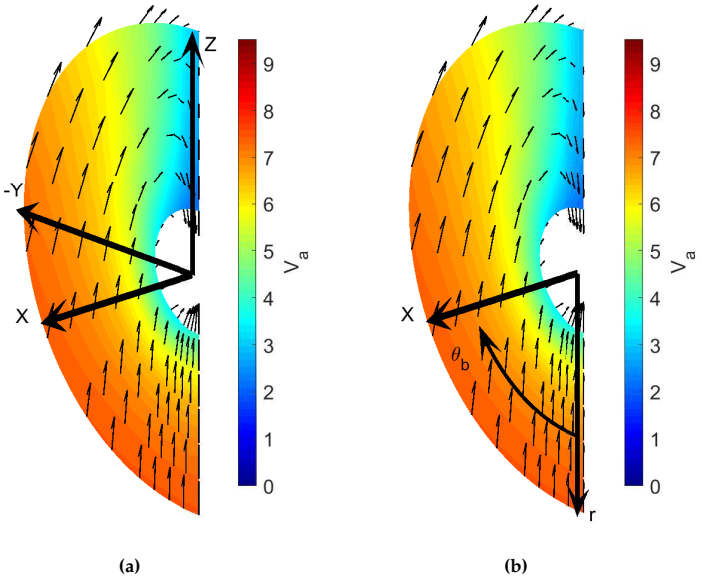

Figure A.6: **(a)** Effective wake field with the Cartesian coordinate system. **(b)** Effective wake field with the cylindrical coordinate system.

The transverse velocities are reformulated as velocities in the Cartesian coordinate system as functions of the y- and z-coordinates as:

$$\begin{aligned} V_y &= -V_r(\theta_b, r)\ \sin\theta_b - V_t(\theta_b, r)\ \cos\theta_b \\ V_z &= -V_r(\theta_b, r)\ \cos\theta_b + V_t(\theta_b, r)\ \sin\theta_b \\ y &= -r\ \sin\theta_b \\ z &= -r\ \cos\theta_b \end{aligned} \tag{A.6}$$

The momentum sources (S) are found through a linear relationship with the velocities V_y and V_z as:

$$\begin{aligned} S_x(y,z) &= 0 \\ S_y(y,z) &= msf\ V_y(y,z) \\ S_z(y,z) &= msf\ V_z(y,z) \end{aligned} \tag{A.7}$$

msf is the momentum strength factor which is a constant to be determined. The momentum sources are applied to a volume upstream of the propeller as shown in Figure A.7. Figure A.7 shows the momentum source strength in the z-direction with $msf = 550\ [kg\,s/m^3]$.

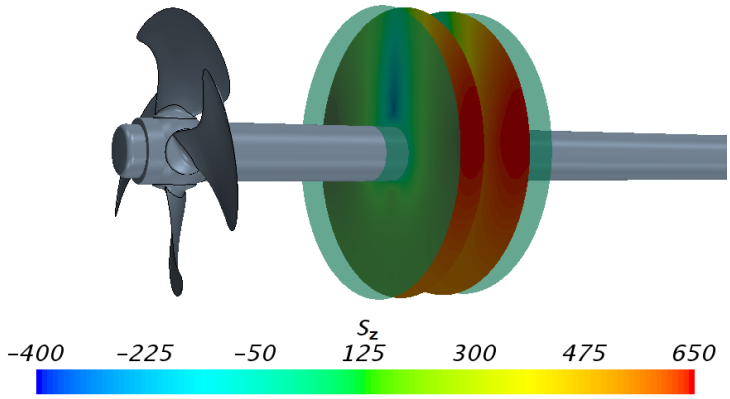

Figure A.7: The momentum source S_z applied to a volume of the CFD simulation with a $msf = 550$.

To determine the momentum strength factor (msf), a series of steady CFD simulations are made without the propeller blades included in the simulation. The domain is therefore a cylinder containing the shaft and the hub only. A series of CFD simulations were made for various lengths between the propeller plane and the inlet and for various sizes of the momentum strength factors. For each of these simulations a least-squares cumulative wake velocity error was determined as in Eq. A.8. The least-squares cumulative wake velocity error is the square of the sum of the three normalized velocity error components in the wake field. The grid points used to evaluate the error are the same as the ones used to measure the wake field shown in Figure A.1a on page 157.

$$e_w = \sqrt{\sum_{i=x,y,z} \left[\left(\frac{1}{N} \sum_{n=1}^{N} \left| \frac{v_i(n) - v_{i,CFD}(n)}{v_i(n)} \right| \right)^2 \right]} \tag{A.8}$$

e_w is the least-squares cumulative wake velocity error. i is the subscript index for the velocity components in the x-, y- and z-directions. n is the measurement index where N is the total number of measurement points. v_i is the measured velocity component for the effective wake field. $v_{i,CFD}$ is the velocity component from the CFD simulation. The least-squares cumulative wake velocity error for the CFD simulations is shown in Figure A.8. The CFD simulations were made using the domain size defined in Section A.3 and the finest grid settings.

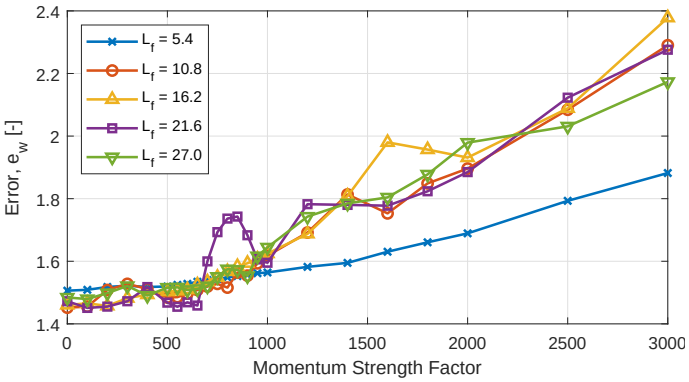

Figure A.8: The least-squares cumulative wake velocity error for varies momentum strength factors and distances between the inlet and the propeller plane L_f.

The choice of wake field and the resulting momentum strength factor and length between the inlet and the propeller plane are made partly based on Figure A.8. Many of the simulated wake fields are close to the minimum error. The five simulated wake fields with the lowest error are shown in Figure A.9 together with the measured wake field. The five simulated wake fields in Figure A.9 are compared and an engineering judgement is made with respect to which wake field is the most appropriate one to use. The transverse velocities for the two simulated wake fields with the smallest error (Figure A.9b and Figure A.9c) do not match the measured transverse velocities in Figure A.9a well. The simulated wake field with the third smallest error is used instead because the transverse velocities match the measured velocities better. This results in a momentum strength factor of 550 and the distance between the inlet and the propeller plane is $L_f = 4\,D_p = 21.6$ [m]. General for all the simulated wake fields are that they do not obtain the same low velocity in the wake peak as the measured wake field. This is due to the viscosity of the fluid which makes it difficult to have large velocity gradients in the fluid without the fluid interacting with a wall, such as the ship hull. The velocity error in the simulated wake field, with respect to the measured wake field, is shown in Figure A.10 for all three velocity components.

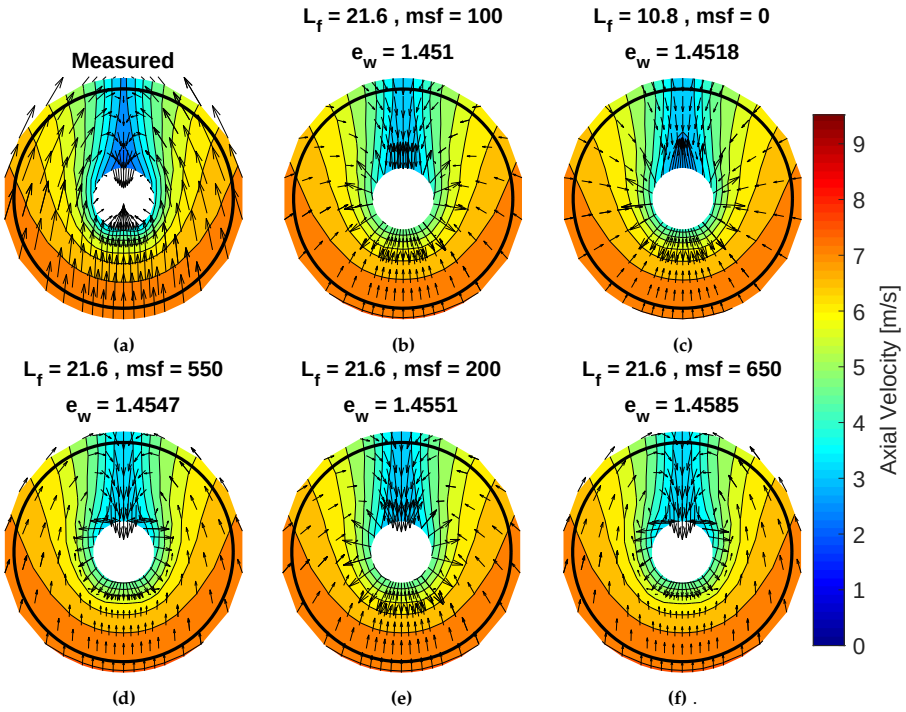

Figure A.9: **(a)** Measured effective wake field. **(b-f)** Simulated wake fields. **(b)** Smallest error. **(c)** Second smallest error. **(d)** Third smallest error. **(e)** Fourth smallest error. **(f)** Fifth smallest error.

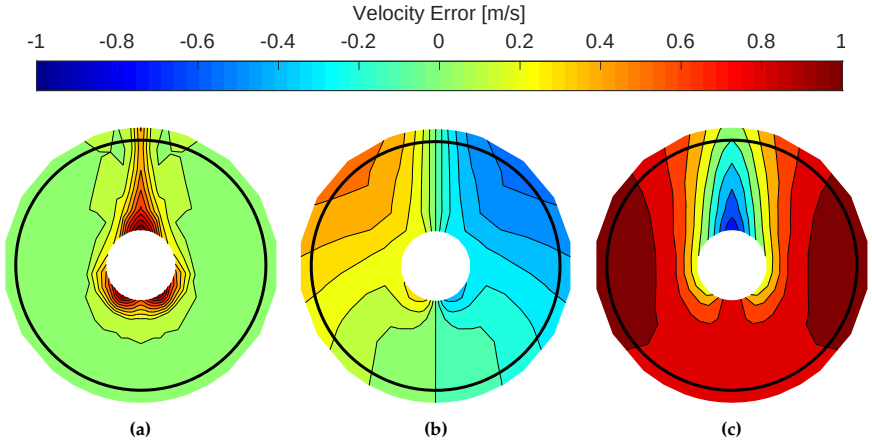

Figure A.10: **(a)** Axial velocity error. **(b)** y-component velocity error. **(c)** z-component velocity error.

A.3 CFD Simulation of CP Propeller

This section describes the setup and results of the URANS CFD simulation of the CP propeller in a non-uniform wake field. The non-uniform wake field was implemented in the CFD simulation in the previous section.

The commercial CFD package STAR-CCM+ 12.02.010 was used for the mesh generating and solving the fluid problem. The physics solver used for the simulations is the unsteady, single phase, incompressible flow solver with gravity included. The turbulence is modelled using the SST $k\omega$ turbulence model without a transition model. The flow is solved using the segregated flow solver by second-order discretization in both space and time.

The spatial discretization of the domain is made using STAR-CCM+'s unstructured polyhedral mesher generator with prism layer cells near the walls to refine the mesh in the boundary layer. The prism layer settings are such that the y^+-value is ≈ 100 for the first prism layer. The y^+-value of 100 is chosen such that the first cell is in the log-law region and thereby avoiding it being in the buffer layer region. This also means that the viscous sub-layer is not resolved which is an active choice since the viscous sub-layer is relatively thin compared to the overall geometry due to the high Reynolds number. Resolving the viscous sublayer would entail a large computational cost. Because the viscous sublayer is not resolved, STAR-CCM+'s all y^+ wall function is used.

The domain for the URANS CFD simulations of the CP propeller in a non-uniform wake field is shown in Figure A.3. The simulation consists of two regions, a large outer region defining the boundaries of the simulation and a cylindrical region enclosing the propeller, shown as the yellow region in Figure A.3. The rotation of the propeller is made using a sliding mesh between the stationary region and the rotating propeller region. The length from the propeller plane to the inlet is determined in Appendix A.2 to be $L_f = 4D_p = 21.6$ [m]. The radius of the domain L_R and the distance from the propeller plane to the outlet L_b are determined in Appendix G.2. These domain parameters are $L_R = 10.5D_p = 56.7$ [m] and $L_b = 12.7D_p = 68.6$ [m].

The URANS CFD simulation is discretized in both time and space. Both of these discretizations contribute to the uncertainty of the simulation. To determine the discretization uncertainty of the simulation a number of different simulations are made with different spatial and temporal discretizations. From these simulations the discretization uncertainty is determined for the simulations using the method described in Section C.3. The simulations are made with five different spatial discretizations and four different temporal discretizations. The number of cells and the time step sizes used for each simulation are given in Table A.1. A total of eight simulations with different discretizations are made to determine the uncertainty.

Table A.1: Discretizations of the URANS CFD simulations made for the CP propeller in a non-uniform wake field. $[MC]$ is million cells. The X in the table marks the discretizations used for the CFD simulations. The "-" in the table marks the discretizations not used in the CFD simulations.

Temporal discretization		Spatial discretization				
		$n = 0$	$n = 1$	$n = 2$	$n = 3$	$n = 4$
$d\theta_b$	dt	13.6 $[MC]$	6.5 $[MC]$	3.7 $[MC]$	2.3 $[MC]$	1.5 $[MC]$
1°	$\approx 1.4\,[ms]$	X	X	X	X	X
2°	$\approx 2.8\,[ms]$	X	-	-	-	-
4°	$\approx 5.5\,[ms]$	X	-	-	-	-
8°	$\approx 11\,[ms]$	X	-	-	-	-

The meshes for the spatial discretization of the domain are defined relative to a base size. This base size varies for each mesh with the factor $\sqrt{2}^n$ where n is equal to 0, 1, 2, 3 and 4 for each of the five meshes. The notation of $n = x$ is therefore used to indicate the spatial discretization henceforth.

The results that are used for each simulation are the last complete revolution of the propeller when the simulation has obtained a periodic converged solution. Periodic converged solution means that the solution does not change significantly for each rotation of the propeller. To evaluate if a periodic converged solution has been obtained, the method described in Section C.4 is used, which is based on [22]. The method is based on calculating a fuzzy convergence level for each period of the simulation. This fuzzy convergence level should be larger than 0.95 for at least two evaluation points. Each evaluation considers the solution for two rotations of the propeller to calculate the fuzzy convergence level. The fuzzy convergence level considers; the mean of the signal, the phases and the amplitudes of the signals discrete Fourier transform, the signals cross-correlation and the power spectral density for each of the forces and torques acting on the propeller blades. A total of 24 signals (six forces and torques for each of the four blades) for each revolution is considered when determining the fuzzy convergence level.

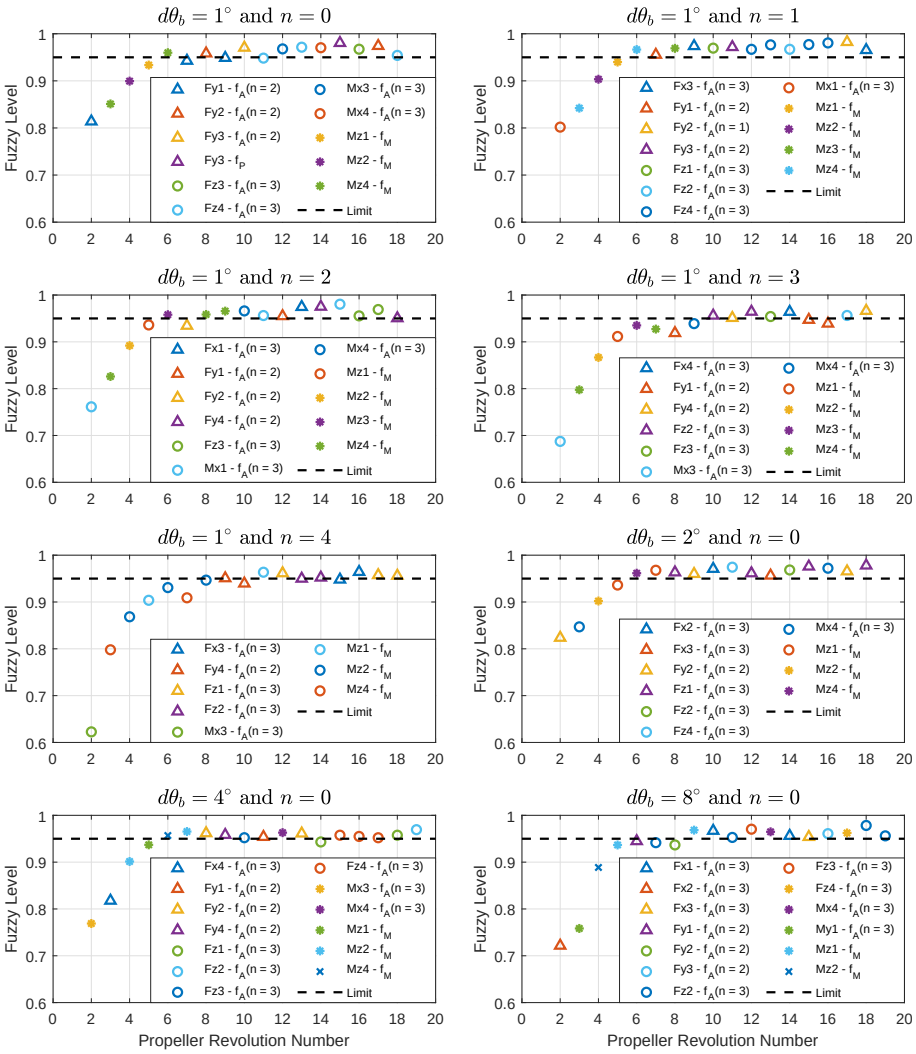

Figure A.11: The fuzzy convergence level of the URANS CFD simulation of the CP propeller in a non-uniform wake field at different temporal and spatial discretizations.

The fuzzy convergence level for each of the simulations is shown in Figure A.11. The legend in Figure A.11 shows which signal and convergence parameter that sets the lowest limit for the fuzzy convergence level for each evaluation. The dashed line shows the limit for having obtained periodic convergence. The notation in the legend before the dash indicates the force/torque and blade number which sets the minimum limit for the fuzzy convergence level. The blade number is determined from the blade's initial position in the wake field at the start of the simulation. The blade, which at the start of the

simulation is in the wake peak i.e. 12 o'clock position, has the blade number 1. The following blade numbers are assigned following the clockwise direction and counting upwards. The blade initially towards the starboard side is blade number 2, the blade initially in the bottom of the wake field is blade number 3 and the blade towards the port side is blade number 4. The notation after the dash, indicates the convergence parameter that sets the minimum convergence levels. f_A is the fuzzy convergence set of the amplitude of the n'th harmonic of the discrete Fourier transform. f_M is the fuzzy convergence set of the mean value of the signal. f_P is the fuzzy convergence set of the power spectrum density. For all the simulations made these are the ones setting the minimum level of the fuzzy convergence level. The limit is not seen in the phases of the discrete Fourier transform or in the cross-correlation of the signal.

From Figure A.11 it is seen that all the simulations obtain periodic convergence. The periodic convergence of the simulations are obtained between the seventh to the thirteenth rotations of the propeller. Some computational resource could have been saved if the periodic convergence study was made online during the simulations. The number of propeller revolutions, before periodic convergence is obtained for each of the discretizations, is given in Table A.2.

Table A.2: Number of propeller revolutions in the URANS CFD simulation before periodic convergence is obtained.

$d\theta_b$	$n=0$	$n=1$	$n=2$	$n=3$	$n=4$
1°	13	7	9	11	12
2°	7	-	-	-	-
4°	7	-	-	-	-
8°	10	-	-	-	-

The results for the forces and torques acting on the third propeller blade are shown in Figure A.12. Figure A.12 shows the results for the last rotation of the propeller, for all the different discretizations of the simulation. The forces and torques are defined in the propeller coordinate system, see Section 2.1 on page 33.

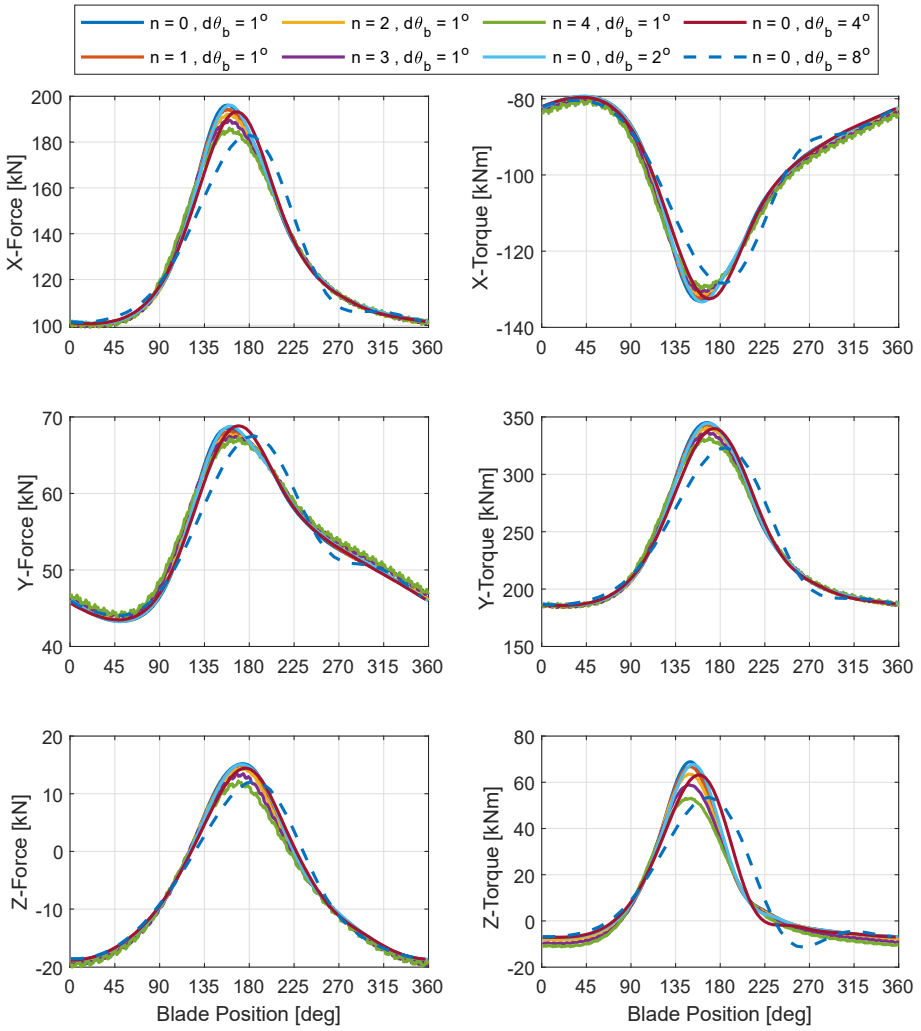

Figure A.12: The forces and torques acting on the third propeller blade when periodic convergence has been obtained for all the diferent used discretizations. The 12 o'clock position in the wake field is equal to a blade position on 180°.

From Figure A.12 it is seen that as the spatial discretization coarsens the amplitude of the variation tends to be reduced. For the coarser spatial discretizations the solution tends to have small fluctuations. The coarsening of the temporal discretization tends to reduce the amplitude of the variation and introduces some phase-shift. All the simulations show the same expected tendency that the load increases when the blade is in the wake peak at blade position 180°. In Figure A.12 the simulation with the temporal discretization $d\theta_b = 8°$ does not have the same tendency as the other simulations. The si-

mulation with the temporal discretization on $d\theta_b = 8^\circ$ is therefore presumed to not be in the asymptotic range and is therefore not included in the numerical uncertainty study.

The numerical uncertainty due to the discretization of the simulation is determined using the method described in Section C.3. The method is based on making a least-squares fit of the dataset to the truncated power series expansion. The least-squares fit is made for each time instance of the simulation with the largest time step. These time instances are used because the solutions for the simulations with smaller time steps are also evaluated at these instances. The simulation results and uncertainty of the simulation with the finest discretization are shown in Figure A.13 for the three forces and torques acting on the propeller blades and the propeller. The forces and torques in Figure A.13 are plotted as a function of the third blade's position in the wake field. The propeller forces and torques are determined from the forces and torques acting on the blades and the forces and torques acting on the hub and shaft in the rotating region. The forces and torques acting on the propeller are defined with respect to the ship coordinate system, see Section 2.1 on page 33.

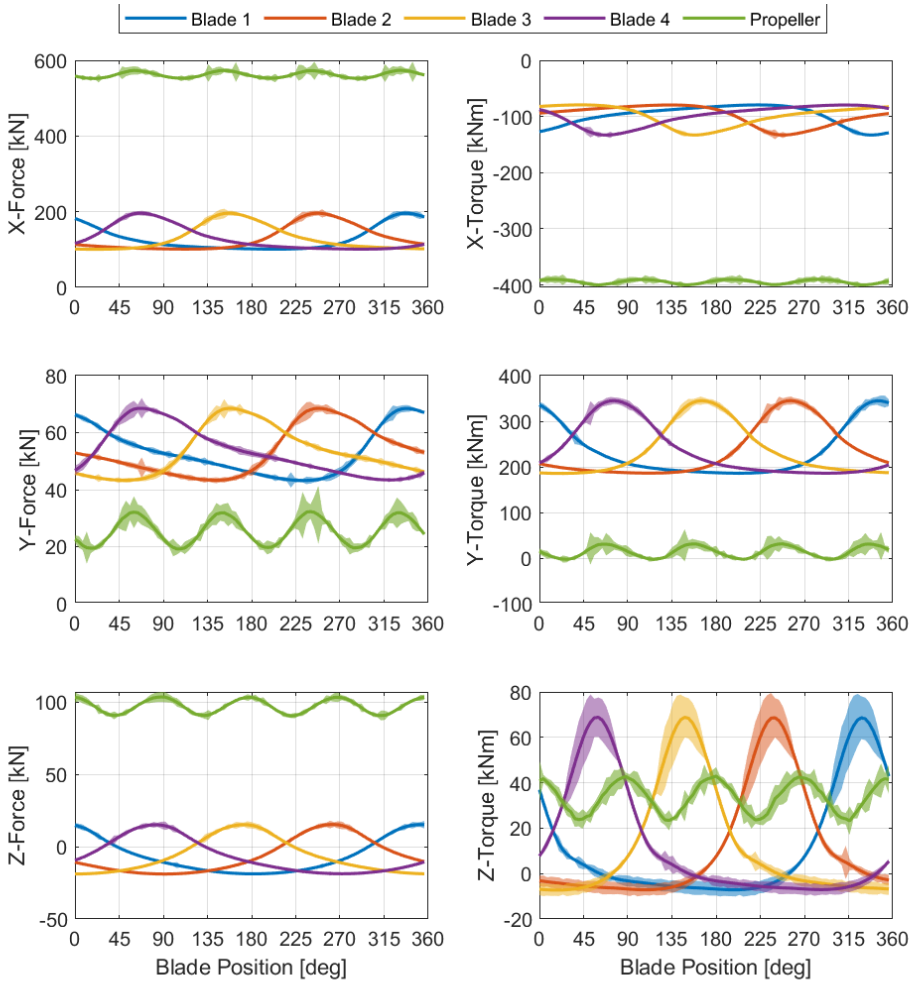

Figure A.13: The forces and torques acting on the CP propeller and its blades for the finest discretization with the discretization uncertainty shown as the shaded areas.

It is seen in Figure A.13 that the uncertainties of the blade forces and torques are generally the greatest in the wake peak. It is in the wake peak that the simulation results differ the most between the different discretization settings, as seen from Figure A.12. The average, minimum and maximum forces and torques and their uncertainties are shown in Table A.3 for all the propeller blades and the propeller as a whole.

Table A.3: Average, minimum and maximum forces and torques and their absolute and relative uncertainties for the propeller blades and the propeller for the URANS CFD simulation of the CP propeller in a non-uniform wake field.

		Blade 1	Blade 2	Blade 3	Blade 4	Propeller
F_x [kN]	Avg.	$129.1 \pm 2.3 \pm 1.8\%$	$129.5 \pm 2.2 \pm 1.7\%$	$129.2 \pm 2.3 \pm 1.8\%$	$129.3 \pm 2.3 \pm 1.8\%$	$562.0 \pm 7.3 \pm 1.3\%$
	Min.	$100.9 \pm 2.0 \pm 1.9\%$	$101.2 \pm 1.3 \pm 1.3\%$	$100.7 \pm 1.9 \pm 1.9\%$	$101.0 \pm 3.6 \pm 3.5\%$	$552.1 \pm 10.6 \pm 1.9\%$
	Max.	$195.9 \pm 6.4 \pm 3.3\%$	$196.0 \pm 10.0 \pm 5.1\%$	$196.0 \pm 11.7 \pm 6.0\%$	$196.0 \pm 6.5 \pm 3.3\%$	$573.6 \pm 23.0 \pm 4.0\%$
M_x [kNm]	Avg.	$-98.4 \pm 1.7 \pm 1.7\%$	$-98.5 \pm 1.8 \pm 1.8\%$	$-98.4 \pm 1.6 \pm 1.7\%$	$-98.5 \pm 1.6 \pm 1.7\%$	$-394.5 \pm 4.0 \pm 1.0\%$
	Min.	$-133.0 \pm 2.4 \pm 1.8\%$	$-133.0 \pm 7.4 \pm 5.6\%$	$-133.0 \pm 2.7 \pm 2.0\%$	$-133.1 \pm 5.5 \pm 4.1\%$	$-400.1 \pm 4.3 \pm 1.1\%$
	Max.	$-79.5 \pm 2.3 \pm 3.0\%$	$-79.5 \pm 1.9 \pm 2.4\%$	$-79.4 \pm 1.8 \pm 2.3\%$	$-79.6 \pm 1.2 \pm 1.5\%$	$-390.1 \pm 8.5 \pm 2.2\%$
F_y [kN]	Avg.	$53.3 \pm 1.0 \pm 1.8\%$	$53.4 \pm 1.0 \pm 1.9\%$	$53.3 \pm 0.9 \pm 1.7\%$	$53.4 \pm 0.9 \pm 1.7\%$	$25.6 \pm 2.2 \pm 8.7\%$
	Min.	$43.2 \pm 2.5 \pm 5.7\%$	$43.3 \pm 1.0 \pm 2.4\%$	$43.3 \pm 0.9 \pm 2.1\%$	$43.4 \pm 0.8 \pm 1.8\%$	$19.2 \pm 5.2 \pm 27.1\%$
	Max.	$68.5 \pm 1.2 \pm 1.8\%$	$68.5 \pm 2.3 \pm 3.3\%$	$68.5 \pm 3.3 \pm 4.8\%$	$68.5 \pm 3.6 \pm 5.3\%$	$32.3 \pm 9.0 \pm 28.0\%$
M_y [kNm]	Avg.	$233.5 \pm 3.8 \pm 1.6\%$	$233.9 \pm 3.5 \pm 1.5\%$	$233.6 \pm 3.4 \pm 1.4\%$	$233.7 \pm 3.8 \pm 1.6\%$	$13.8 \pm 9.2 \pm 66.5\%$
	Min.	$186.0 \pm 3.9 \pm 2.1\%$	$186.2 \pm 2.5 \pm 1.3\%$	$185.7 \pm 4.1 \pm 2.2\%$	$186.0 \pm 3.1 \pm 1.7\%$	$-2.9 \pm 11.3 \pm 391.2\%$
	Max.	$344.9 \pm 11.6 \pm 3.4\%$	$345.3 \pm 9.0 \pm 2.6\%$	$345.0 \pm 9.1 \pm 2.6\%$	$345.2 \pm 8.0 \pm 2.3\%$	$31.1 \pm 32.2 \pm 103.5\%$
F_z [kN]	Avg.	$-6.5 \pm 0.9 \pm 13.2\%$	$-6.5 \pm 0.8 \pm 11.6\%$	$-6.5 \pm 0.8 \pm 12.8\%$	$-6.5 \pm 0.8 \pm 12.9\%$	$97.1 \pm 1.8 \pm 1.8\%$
	Min.	$-18.8 \pm 0.6 \pm 3.3\%$	$-18.9 \pm 0.8 \pm 4.5\%$	$-18.9 \pm 0.7 \pm 3.7\%$	$-18.7 \pm 1.2 \pm 6.6\%$	$90.3 \pm 3.2 \pm 3.5\%$
	Max.	$15.2 \pm 2.5 \pm 16.7\%$	$15.3 \pm 2.6 \pm 17.3\%$	$15.2 \pm 2.3 \pm 15.5\%$	$15.1 \pm 2.2 \pm 14.8\%$	$103.4 \pm 3.5 \pm 3.3\%$
M_z [kNm]	Avg.	$10.7 \pm 3.4 \pm 31.4\%$	$10.8 \pm 3.2 \pm 29.9\%$	$10.8 \pm 3.1 \pm 29.2\%$	$10.8 \pm 3.1 \pm 28.9\%$	$33.6 \pm 3.6 \pm 10.7\%$
	Min.	$-7.2 \pm 3.0 \pm 41.8\%$	$-7.2 \pm 2.8 \pm 39.3\%$	$-7.3 \pm 2.7 \pm 36.9\%$	$-7.1 \pm 2.7 \pm 38.0\%$	$23.2 \pm 6.4 \pm 27.4\%$
	Max.	$68.7 \pm 10.5 \pm 15.3\%$	$68.6 \pm 10.9 \pm 15.8\%$	$68.8 \pm 10.0 \pm 14.5\%$	$68.9 \pm 10.0 \pm 14.6\%$	$42.9 \pm 6.8 \pm 15.7\%$

From Table A.3 it is seen that there are small variations in the results between the blades. These variations are relatively small and are within the determined uncertainty bounds of each other. The variations in the results between the blades are therefore acceptable.

The propeller efficiency for the simulation is determined as:

$$\overline{\eta_p} = \frac{V_a \, \overline{F_{x,p}}}{\omega_p \, \overline{M_{x,p}}} = 0.6464 \; \begin{matrix} \pm 0.0150 \\ \pm 2.3134\% \end{matrix} \tag{A.9}$$

$\overline{F_x}$ and $\overline{M_x}$ are the average propeller thrust and torque, respectively. ω_p is the rotational speed of the propeller. V_a is the average velocity through the propeller disc which is determined from the wake field simulations in Section A.2.

A.4 CFD Simulation of CVP Propeller

This section describes how the URANS CFD simulation of the CP propeller is changed to simulate the CVP propeller instead. The simulations of the CVP propeller are made using the pitch trajectories determined in Section 2.2 on page 36.

The setup of the URANS CFD simulation of the CVP propeller in a non-uniform wake field is the same as for the CP propeller in a non-uniform wake field, with one exception. This exception is that the grid in the rotational region is updated for each time step, to simulate the pitching motion of the blades. In STAR-CCM+ 12.02.010 there are four methods which can be utilized to simulate the motion of the propeller blades, which are:

- **Sliding mesh**
  - The sliding mesh is the principle used to simulate the rotation of the propeller. Using the sliding mesh to simulate the individual pitching motion of the propeller blades requires that an axisymmetric domain around the blades spindle axis can be made for each individual blade. These domains must not overlap each other. For the case considered it is not possible to define an axisymmetric domain for each blade that does not overlap with another domain. This is due to the large skew and area of each blade.
- **Remeshing**
  - The remeshing strategy is to change the underlying geometry, used to make the mesh for the simulation, between each time step and then make a new mesh. Remeshing is computationally expensive and another solution is therefore desired. The remeshing strategy has also shown to be unstable with respect to the solution of the pressure.
- **Overset meshing**
  - In the overset mesh strategy, a domain is made for each part in the simulation and the remaining stationary domain. Each domain is meshed independently and independent rigid motion can be made for each of the domains. For each time step a hole is cut out in the stationary domain where the individual domains fit. The domains are thereafter assembled into one mesh which can be used for the simulations of the CVP propeller.

- **Morphing meshing**
  - The morphing mesh strategy is made by displacing the cell vertices at the blade surface. The remaining cell vertices in the domain of the mesh are then displaced to accommodate the displacement of the cell vertices at the blade surface. The CVP propeller can be simulated with the morphing mesh by using the setup in Section A.3 and define the displacement of the cell vertices of the blades in the propeller region for each time instance. The remaining volume mesh of the propeller region will then deform to accompany this displacement of the blades.

Of the four methods described above to simulate the motion of the CVP propeller, only the overset and morphing meshing strategies are considered for use. Both the overset and morphing meshing strategy have been implemented in STAR-CCM 12.02.010. The morphing meshing strategy has been the most successful implementation for simulating the CVP propeller. The experience when using the overset mesh strategy has been associated with difficulties in obtaining convergence at the surfaces where the blades have contact with the hub. The URANS CFD simulation of the CVP propeller is therefore made using the morphing meshing strategy to model the individual pitching motion of the propeller blades. A disadvantage by using the morphing meshing instead of the overset meshing is that the morphing of the mesh degrades the quality of the mesh. If the quality of the mesh degrades too much it can influence the results and in the worst case it can result in the simulation diverging or terminating abruptly. The amount of degradation of the mesh quality is closely related to the amount of deformation of the mesh relative to the mesh size. The quality of a fine mesh will degrade faster than a coarse mesh given the same deformation. For a specific pitch trajectory there is a limit on how fine the mesh can be without the mesh quality degrading too much during the simulation.

When using the morphing mesh strategy for a region in the CFD simulation it is necessary to define all the surface meshes' morphing properties. There are four morphing properties that can be set for the surfaces of the region and they are:

- **Fixed**
  - The cell vertices are fixed and can therefore not be displaced.
- **Floating**
  - The cell vertices can freely move in order to accompany the motion of the surfaces that move.
- **Displacement**

  - The cell vertices can be displaced according to some predetermined motion or be displaced according to a fluid-structure interaction.

- **Constraint**
  - The cell vertices can be displaced as with the displacement surface property. The constraint property allows the user to make constrains on the displacement of the cell vertices, thereby ensuring the cell vertices stay within a desired space.

For the simulation of the CVP propeller the two surface properties, floating and displacement are used. These surface properties are only used for the rotating region which encloses the propeller. The sliding mesh interface is therefore still used to simulate the rotation of the propeller. The morphing properties of the surfaces of the propeller are shown in Figure A.14.

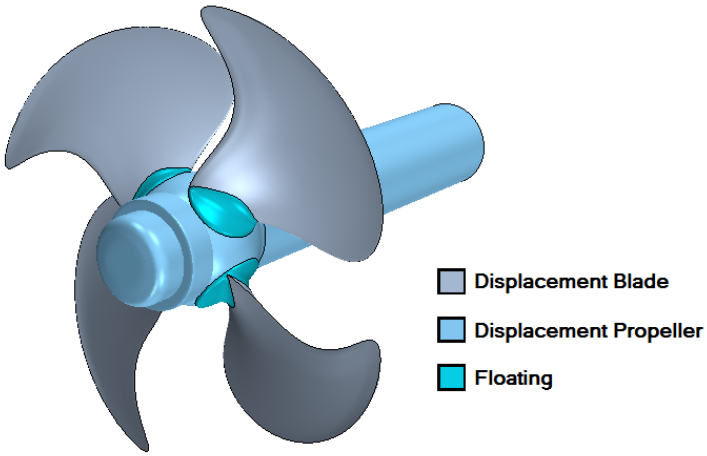

Figure A.14: Morphing surface properties for the propeller.

In Figure A.14 two different surface displacements are defined: the displacement for the blades and the displacement for the shaft and hub. The displacement for the blade makes the blade rotate about the shaft center and about the blade's spindle axis according to the desired pitch trajectory. The propeller displacement makes the surface rotate around the shaft center only. The outer surface of the rotating region is not shown in Figure A.14 but its morphing surface property is also the displacement for the propeller. The blade foot surfaces are set as the floating surface property in order to accompany the relative motion between the blade and the hub. An example of how the mesh morphs for the blade foot surface is shown in Figure A.15 for different positions of the blade in the wake field.

The floating surface property for the blade foot is chosen to not over-constrain the morphing of the mesh for larger deformations. If the morphing property of the blade foot was set to either the blade or propeller displacement, then the simulation would quickly terminate, due to the cells collapsing in on themselves.

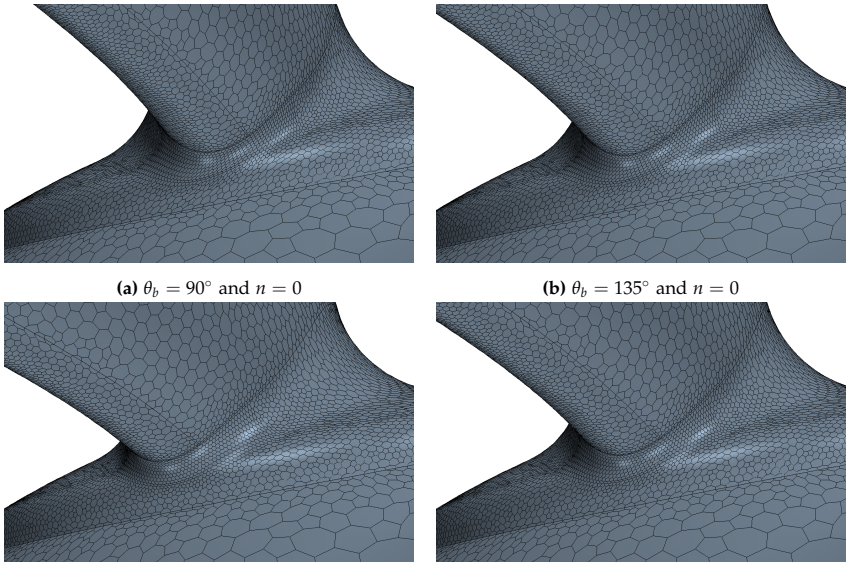

(a) $\theta_b = 90^\circ$ and $n = 0$ **(b)** $\theta_b = 135^\circ$ and $n = 0$

(c) $\theta_b = 180^\circ$ and $n = 0$ **(d)** $\theta_b = 225^\circ$ and $n = 0$

Figure A.15: Example on the deformation of the surface mesh of the blade foot at the leading edge of the blade. The example is for the CVP simulation using the variable pitch trajectory in [66] and the finest mesh ($n = 0$). The example is for blade 1 in the simulation which is the blade that is initialized in the wake peak i.e. 12 o'clock position. The initial mesh is therefore made with the blade in its low pitch position in the wake field. The deformation of the mesh is therefore the largest outside the wake peak.

The URANS CFD simulation of the CVP propeller is made using the cosine and variable pitch trajectory determined in Section 2.2 on page 36. These pitch trajectories are shown in Figure A.16.

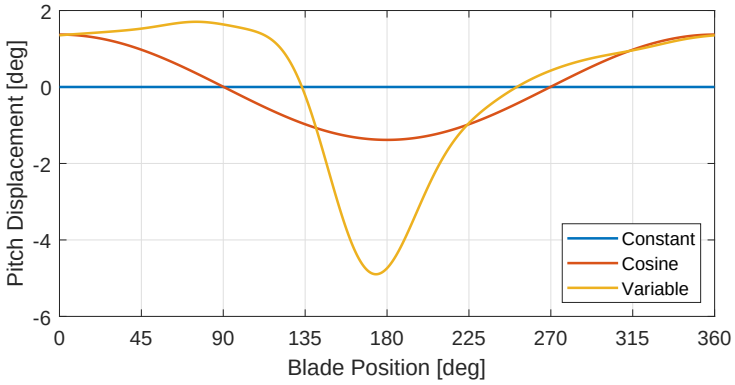

Figure A.16: Pitch displacement trajectories for the CVP propeller determined in Section 2.2.

The simulations are made for different spatial and temporal discretizations. The spatial and temporal discretization used were the same as those used for the CP propeller simulations (see Table A.1 on page 167), except for the coarsest spatial and temporal discretizations. These discretizations are excluded for the CVP simulations to save computational resources. The coarsest temporal discretization is excluded because it was not included in the uncertainty study for the CP propeller simulations. The simulations are initially set to make 14 propeller rotations, since this is the largest number of rotations that the CP propeller simulations require to obtain periodic convergence. If the CVP propeller simulations have not obtained periodic convergence after 14 propeller rotations, the simulation is continued to make additional propeller rotations until periodic convergence is achieved. Some of the simulations are stopped early because periodic convergence has been achieved. The periodic convergence is determined using the same procedure as used for the CP propeller simulations given in Appendix C.4. The minimum fuzzy convergence level for each propeller revolution is shown in Figure A.17 and Figure A.18 for the cosine and variable pitch trajectories, respectively.

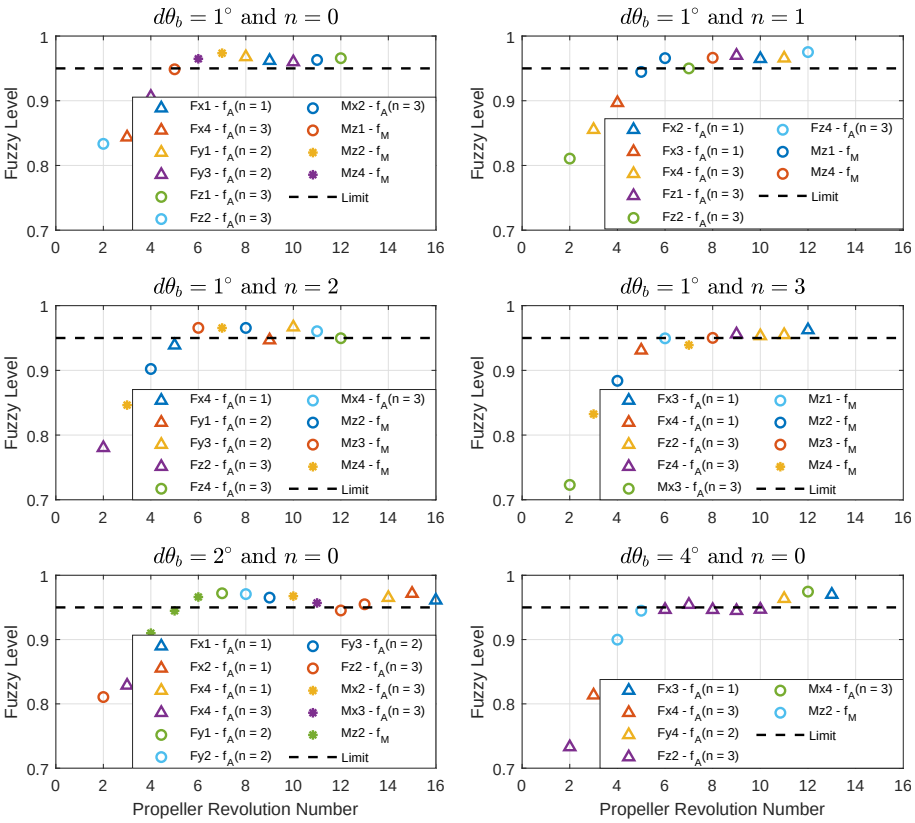

Figure A.17: The fuzzy convergence level of URANS simulation of the CVP propeller in a non-uniform wake field with the cosine pitch trajectory.

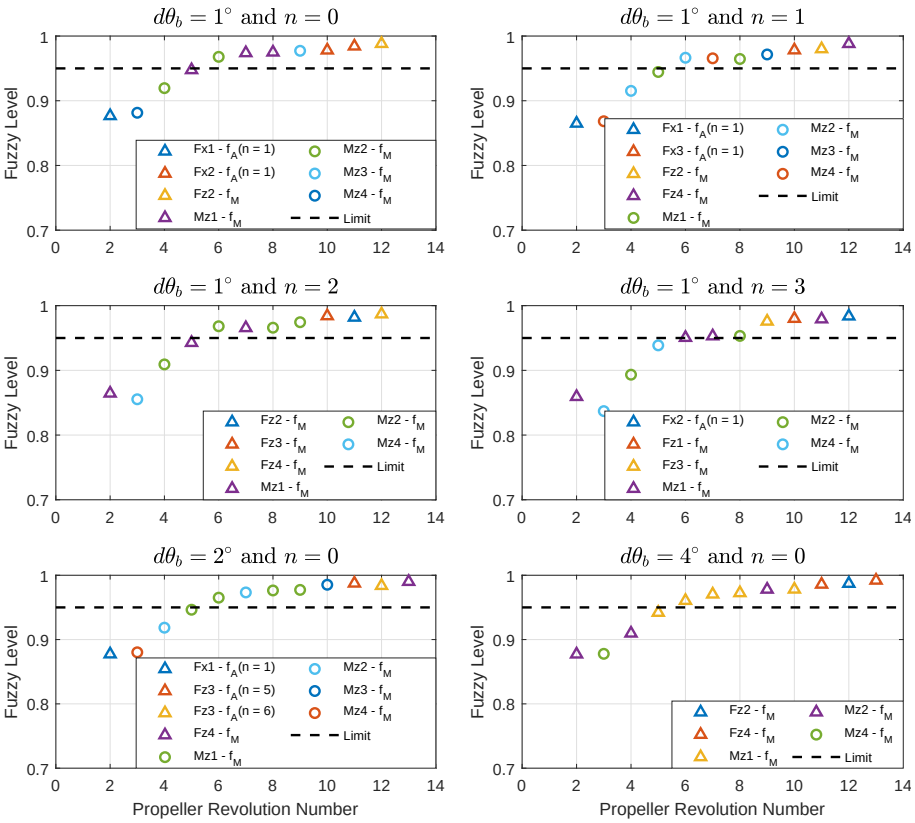

Figure A.18: The fuzzy convergence level of URANS simulation of the CVP propeller in a non-uniform wake field with the variable pitch trajectory.

From Figure A.18, it is seen that the minimum convergence level crosses the lower limit after approximately six rotations of the propeller for most of the simulations. From Figure A.17 it is seen that all the simulations of the CVP propeller obtain periodic convergence.

With all the simulations having obtained period convergence, the results can be used to determine the discretization uncertainty. The forces and torques acting on the CVP propeller and its blades are shown in Figure A.19 and Figure A.20 for the cosine and the variable pitch trajectory, respectively. The forces and torques in Figure A.19 and Figure A.20 are for the simulation with the finest discretization ($n = 0$ and $d\theta_b = 1^\circ$) and their corresponding uncertainties. The uncertainties are determined using the method described in Appendix C.3. The simulation results are summarized for the average, minimum and maximum forces and torques and their uncertainties in Table A.4 and Table A.5 for the cosine and variable pitch trajectory, respectively.

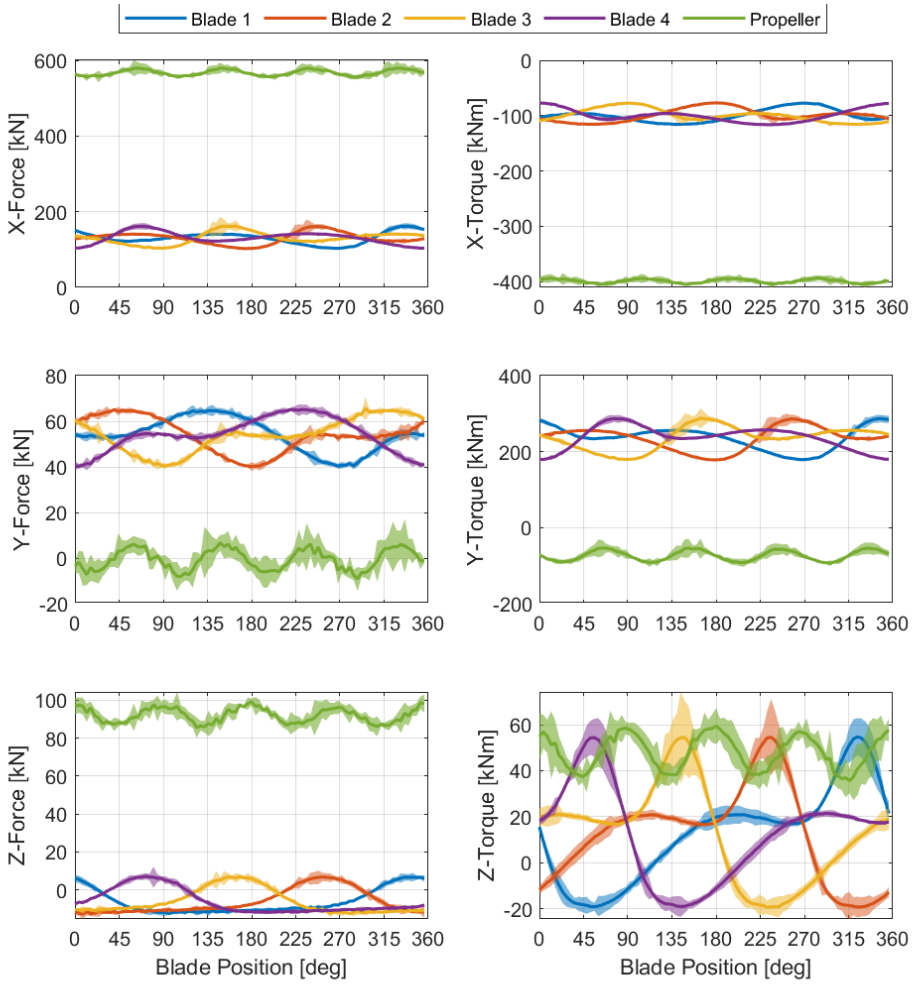

Figure A.19: The forces and torques acting on the CVP propeller and its blades with the cosine pitch trajectory for the finest discretization with the discretization uncertainty shown as the shaded areas.

Table A.4: Average, minimum and maximum forces and torques and their absolute and relative uncertainties for the propeller and its blades for the URANS CFD simulation of the CVP propeller with the cosine pitch trajectory in a non-uniform wake field.

		Blade 1	**Blade 2**	**Blade 3**	**Blade 4**	**Propeller**
F_x [kN]	Avg.	$130.6\ ^{\pm 3.2}_{\pm 2.5\%}$	$130.4\ ^{\pm 3.5}_{\pm 2.7\%}$	$130.7\ ^{\pm 3.7}_{\pm 2.8\%}$	$131.1\ ^{\pm 2.9}_{\pm 2.2\%}$	$567.9\ ^{\pm 8.2}_{\pm 1.4\%}$
	Min.	$103.3\ ^{\pm 2.9}_{\pm 2.9\%}$	$102.9\ ^{\pm 1.6}_{\pm 1.5\%}$	$103.5\ ^{\pm 2.6}_{\pm 2.6\%}$	$103.5\ ^{\pm 3.0}_{\pm 2.9\%}$	$555.8\ ^{\pm 13.3}_{\pm 2.4\%}$
	Max.	$161.8\ ^{\pm 8.2}_{\pm 5.1\%}$	$161.0\ ^{\pm 18.7}_{\pm 11.6\%}$	$162.1\ ^{\pm 24.4}_{\pm 15.1\%}$	$161.7\ ^{\pm 8.7}_{\pm 5.4\%}$	$580.2\ ^{\pm 20.3}_{\pm 3.5\%}$
M_x [kNm]	Avg.	$-99.5\ ^{\pm 2.1}_{\pm 2.1\%}$	$-99.3\ ^{\pm 2.0}_{\pm 2.1\%}$	$-99.5\ ^{\pm 2.2}_{\pm 2.2\%}$	$-99.8\ ^{\pm 2.1}_{\pm 2.1\%}$	$-398.9\ ^{\pm 4.6}_{\pm 1.2\%}$
	Min.	$-115.7\ ^{\pm 3.2}_{\pm 2.7\%}$	$-115.5\ ^{\pm 2.0}_{\pm 1.7\%}$	$-115.6\ ^{\pm 4.2}_{\pm 3.7\%}$	$-116.3\ ^{\pm 3.1}_{\pm 2.7\%}$	$-404.9\ ^{\pm 5.4}_{\pm 1.3\%}$
	Max.	$-77.3\ ^{\pm 2.3}_{\pm 2.9\%}$	$-76.9\ ^{\pm 1.5}_{\pm 2.0\%}$	$-77.4\ ^{\pm 1.9}_{\pm 2.4\%}$	$-77.3\ ^{\pm 2.3}_{\pm 3.0\%}$	$-393.1\ ^{\pm 8.8}_{\pm 2.2\%}$
F_y [kN]	Avg.	$53.9\ ^{\pm 1.5}_{\pm 2.9\%}$	$53.9\ ^{\pm 1.4}_{\pm 2.7\%}$	$54.0\ ^{\pm 1.6}_{\pm 2.9\%}$	$54.2\ ^{\pm 1.5}_{\pm 2.7\%}$	$-0.6\ ^{\pm 4.6}_{\pm 735.6\%}$
	Min.	$40.4\ ^{\pm 1.4}_{\pm 3.6\%}$	$40.1\ ^{\pm 1.9}_{\pm 4.8\%}$	$40.4\ ^{\pm 1.4}_{\pm 3.5\%}$	$40.3\ ^{\pm 1.7}_{\pm 4.3\%}$	$-9.2\ ^{\pm 5.3}_{\pm 57.4\%}$
	Max.	$64.7\ ^{\pm 2.5}_{\pm 3.9\%}$	$65.0\ ^{\pm 1.4}_{\pm 2.2\%}$	$65.6\ ^{\pm 5.0}_{\pm 7.7\%}$	$65.2\ ^{\pm 2.2}_{\pm 3.4\%}$	$6.7\ ^{\pm 10.4}_{\pm 156.2\%}$
M_y [kNm]	Avg.	$235.9\ ^{\pm 4.0}_{\pm 1.7\%}$	$235.4\ ^{\pm 4.7}_{\pm 2.0\%}$	$235.9\ ^{\pm 5.2}_{\pm 2.2\%}$	$236.6\ ^{\pm 4.0}_{\pm 1.7\%}$	$-73.4\ ^{\pm 9.7}_{\pm 13.3\%}$
	Min.	$178.9\ ^{\pm 3.1}_{\pm 1.8\%}$	$178.4\ ^{\pm 3.8}_{\pm 2.1\%}$	$179.2\ ^{\pm 3.2}_{\pm 1.8\%}$	$179.5\ ^{\pm 3.6}_{\pm 2.0\%}$	$-93.5\ ^{\pm 9.5}_{\pm 10.2\%}$
	Max.	$287.0\ ^{\pm 9.6}_{\pm 3.4\%}$	$285.9\ ^{\pm 14.1}_{\pm 4.9\%}$	$287.9\ ^{\pm 26.5}_{\pm 9.2\%}$	$286.8\ ^{\pm 9.8}_{\pm 3.4\%}$	$-53.8\ ^{\pm 25.3}_{\pm 47.1\%}$
F_z [kN]	Avg.	$-6.3\ ^{\pm 1.1}_{\pm 17.6\%}$	$-6.4\ ^{\pm 1.3}_{\pm 20.5\%}$	$-6.3\ ^{\pm 1.2}_{\pm 19.7\%}$	$-6.2\ ^{\pm 1.1}_{\pm 17.4\%}$	$92.0\ ^{\pm 3.6}_{\pm 3.9\%}$
	Min.	$-12.5\ ^{\pm 1.4}_{\pm 11.0\%}$	$-12.8\ ^{\pm 2.6}_{\pm 20.4\%}$	$-12.5\ ^{\pm 1.9}_{\pm 14.9\%}$	$-11.8\ ^{\pm 1.1}_{\pm 8.9\%}$	$85.5\ ^{\pm 5.3}_{\pm 6.2\%}$
	Max.	$6.7\ ^{\pm 2.3}_{\pm 34.2\%}$	$6.8\ ^{\pm 3.3}_{\pm 49.4\%}$	$6.8\ ^{\pm 2.9}_{\pm 42.6\%}$	$7.1\ ^{\pm 5.1}_{\pm 71.3\%}$	$99.0\ ^{\pm 5.3}_{\pm 5.4\%}$
M_z [kNm]	Avg.	$12.4\ ^{\pm 3.3}_{\pm 26.4\%}$	$12.1\ ^{\pm 3.3}_{\pm 27.1\%}$	$12.3\ ^{\pm 3.6}_{\pm 29.2\%}$	$12.6\ ^{\pm 2.8}_{\pm 22.2\%}$	$48.0\ ^{\pm 6.1}_{\pm 12.7\%}$
	Min.	$-19.2\ ^{\pm 4.2}_{\pm 21.6\%}$	$-19.4\ ^{\pm 5.2}_{\pm 26.6\%}$	$-19.4\ ^{\pm 4.3}_{\pm 22.2\%}$	$-19.1\ ^{\pm 4.5}_{\pm 23.8\%}$	$35.6\ ^{\pm 8.4}_{\pm 23.6\%}$
	Max.	$54.7\ ^{\pm 8.1}_{\pm 14.7\%}$	$54.6\ ^{\pm 16.7}_{\pm 30.5\%}$	$54.5\ ^{\pm 19.8}_{\pm 36.3\%}$	$54.3\ ^{\pm 8.6}_{\pm 15.7\%}$	$59.4\ ^{\pm 7.8}_{\pm 13.2\%}$

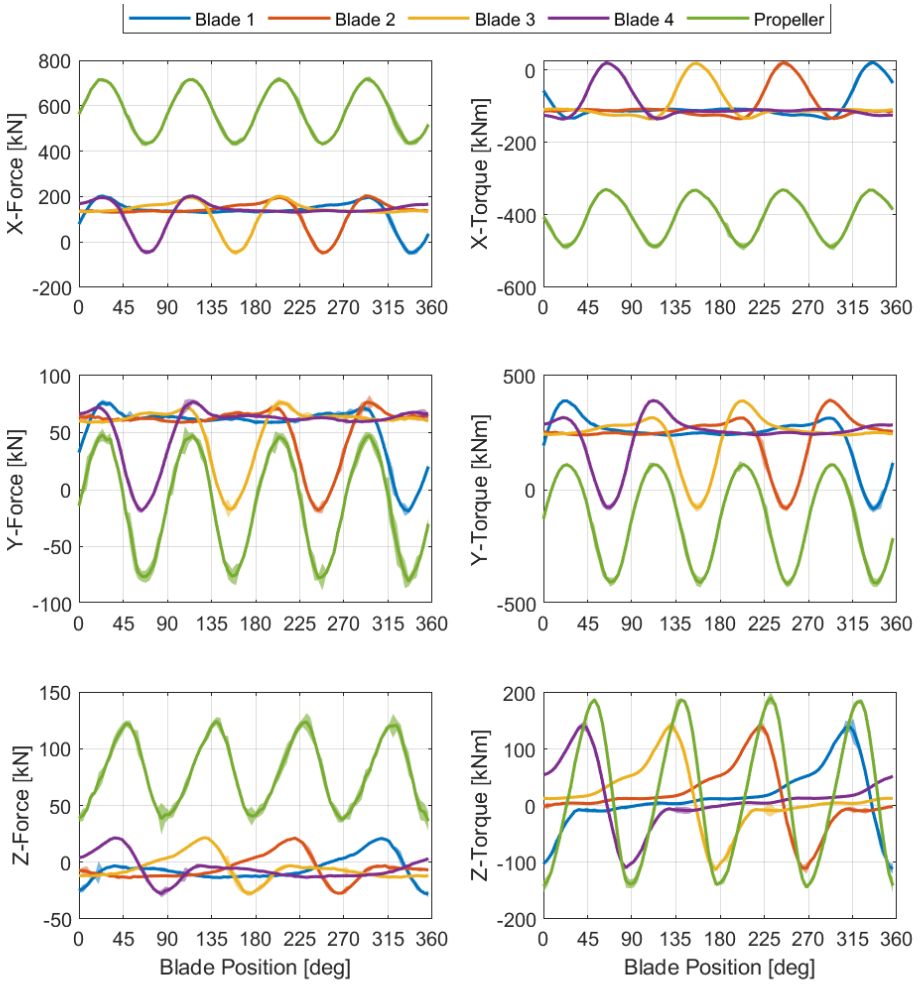

Figure A.20: The forces and torques acting on the propeller and its blades with the variable pitch trajectory for the finest discretization with the discretization uncertainty shown as the shaded areas.

Table A.5: Average, minimum and maximum forces and torques and their absolute and relative uncertainties for the propeller and its blades for the URANS CFD simulation of the CVP propeller with the variable pitch trajectory in a non-uniform wake field.

		Blade 1	**Blade 2**	**Blade 3**	**Blade 4**	**Propeller**
F_x [kN]	Avg.	$131.9 \pm 4.1 \pm 3.1\%$	$132.7 \pm 4.2 \pm 3.2\%$	$132.7 \pm 3.7 \pm 2.8\%$	$133.4 \pm 3.9 \pm 2.9\%$	$575.8 \pm 10.9 \pm 1.9\%$
	Min.	$-47.4 \pm 9.4 \pm 19.9\%$	$-47.7 \pm 9.8 \pm 20.6\%$	$-46.5 \pm 12.6 \pm 27.1\%$	$-45.1 \pm 11.6 \pm 25.8\%$	$431.7 \pm 10.5 \pm 2.4\%$
	Max.	$202.3 \pm 2.7 \pm 1.3\%$	$203.3 \pm 4.9 \pm 2.4\%$	$201.9 \pm 1.9 \pm 1.0\%$	$202.4 \pm 7.0 \pm 3.5\%$	$716.7 \pm 13.1 \pm 1.8\%$
M_x [kNm]	Avg.	$-100.8 \pm 2.5 \pm 2.5\%$	$-101.3 \pm 2.9 \pm 2.9\%$	$-101.3 \pm 2.5 \pm 2.5\%$	$-101.8 \pm 2.8 \pm 2.8\%$	$-406.0 \pm 5.6 \pm 1.4\%$
	Min.	$-134.6 \pm 1.7 \pm 1.2\%$	$-134.6 \pm 5.0 \pm 3.7\%$	$-135.2 \pm 3.7 \pm 2.7\%$	$-135.8 \pm 5.7 \pm 4.2\%$	$-488.2 \pm 10.0 \pm 2.0\%$
	Max.	$20.6 \pm 4.2 \pm 20.5\%$	$19.2 \pm 7.2 \pm 37.5\%$	$18.3 \pm 2.7 \pm 14.9\%$	$19.4 \pm 5.8 \pm 30.0\%$	$-329.8 \pm 3.4 \pm 1.0\%$
F_y [kN]	Avg.	$54.8 \pm 1.8 \pm 3.4\%$	$55.1 \pm 2.1 \pm 3.8\%$	$55.2 \pm 1.8 \pm 3.2\%$	$55.4 \pm 1.7 \pm 3.1\%$	$-12.7 \pm 6.2 \pm 48.4\%$
	Min.	$-18.8 \pm 4.2 \pm 22.5\%$	$-18.2 \pm 2.5 \pm 13.7\%$	$-17.0 \pm 7.8 \pm 45.5\%$	$-18.5 \pm 2.0 \pm 10.9\%$	$-80.5 \pm 7.9 \pm 9.9\%$
	Max.	$76.5 \pm 2.5 \pm 3.3\%$	$76.5 \pm 6.5 \pm 8.5\%$	$76.2 \pm 3.1 \pm 4.0\%$	$77.1 \pm 2.5 \pm 3.2\%$	$48.1 \pm 7.6 \pm 15.7\%$
M_y [kNm]	Avg.	$238.2 \pm 5.7 \pm 2.4\%$	$239.2 \pm 6.2 \pm 2.6\%$	$239.3 \pm 5.4 \pm 2.2\%$	$240.3 \pm 5.2 \pm 2.2\%$	$-127.8 \pm 16.0 \pm 12.5\%$
	Min.	$-84.9 \pm 14.6 \pm 17.2\%$	$-81.9 \pm 14.2 \pm 17.3\%$	$-79.0 \pm 17.7 \pm 22.4\%$	$-77.7 \pm 13.7 \pm 17.6\%$	$-414.4 \pm 14.5 \pm 3.5\%$
	Max.	$389.1 \pm 3.6 \pm 0.9\%$	$392.8 \pm 7.3 \pm 1.8\%$	$389.0 \pm 3.8 \pm 1.0\%$	$390.5 \pm 8.9 \pm 2.3\%$	$110.6 \pm 15.1 \pm 13.6\%$
F_z [kN]	Avg.	$-6.2 \pm 1.4 \pm 22.2\%$	$-6.0 \pm 1.3 \pm 21.4\%$	$-5.9 \pm 1.4 \pm 23.4\%$	$-5.9 \pm 1.2 \pm 20.5\%$	$78.9 \pm 4.9 \pm 6.2\%$
	Min.	$-27.9 \pm 2.7 \pm 9.6\%$	$-27.4 \pm 1.0 \pm 3.8\%$	$-27.4 \pm 2.5 \pm 9.1\%$	$-27.6 \pm 3.2 \pm 11.7\%$	$36.2 \pm 11.9 \pm 32.9\%$
	Max.	$21.0 \pm 0.6 \pm 2.8\%$	$21.3 \pm 1.0 \pm 4.5\%$	$21.6 \pm 1.2 \pm 5.6\%$	$21.4 \pm 0.7 \pm 3.1\%$	$124.2 \pm 7.1 \pm 5.7\%$
M_z [kNm]	Avg.	$12.9 \pm 3.8 \pm 29.3\%$	$13.2 \pm 3.0 \pm 22.8\%$	$13.3 \pm 3.2 \pm 23.7\%$	$13.7 \pm 2.8 \pm 20.5\%$	$20.2 \pm 6.7 \pm 33.1\%$
	Min.	$-111.1 \pm 9.2 \pm 8.3\%$	$-110.3 \pm 9.7 \pm 8.8\%$	$-112.4 \pm 5.5 \pm 4.9\%$	$-109.4 \pm 2.3 \pm 2.1\%$	$-144.1 \pm 10.7 \pm 7.4\%$
	Max.	$139.5 \pm 14.2 \pm 10.2\%$	$141.0 \pm 7.1 \pm 5.1\%$	$140.3 \pm 8.9 \pm 6.3\%$	$141.3 \pm 6.8 \pm 4.8\%$	$190.6 \pm 10.7 \pm 5.6\%$

The simulations for the CVP propeller have some variation in the results between the blades, and these are acceptable since the variation is relatively small and the variations are within the uncertainty bounds. The variations in the results between the propeller blades are therefore considered as acceptable.

The efficiency of the CVP propeller is calculated using Eq. A.9. The efficiency of the CVP propeller for the cosine pitch trajectory is given in Eq. A.10 and for the variable pitch trajectory in Eq. A.11.

$$\eta_p = 0.6460 \begin{matrix} \pm 0.0168 \\ \pm 2.5941\% \end{matrix} \tag{A.10}$$

$$\eta_p = 0.6436 \begin{matrix} \pm 0.0211 \\ \pm 3.2829\% \end{matrix} \tag{A.11}$$

A.5 Comparision of CP and CVP Propeller Simulations

Having simulated the CP and CVP propeller in a non-uniform wake field, a comparison of the performances of the two propellers can be made. The comparison is made for the whole propeller and the individual blades.

The propeller efficiency is calculated for each of the simulations by using Eq. A.9 and is summarized in Table A.6.

Table A.6: The propeller efficiency for the CP and CVP propeller simulations.

	CP Propeller	**CVP Propeller Cosine Pitch Trajectory**	**CVP Propeller Variable Pitch Trajectory**
η_p	$0.6464 \begin{matrix} \pm 0.0150 \\ \pm 2.3134\% \end{matrix}$	$0.6460 \begin{matrix} \pm 0.0168 \\ \pm 2.5941\% \end{matrix}$	$0.6436 \begin{matrix} \pm 0.0211 \\ \pm 3.2829\% \end{matrix}$

From Table A.6 it is seen that there are only small differences in the propeller efficiency between the CP and the CVP propeller, and these are well within the uncertainty bounds. The results shown in Table A.6 do not coincide with the results in [66] where the pitch trajectories are determined. The likely cause for this is that the same blade design is used for all the simulations. In [66] the blade design is changed for each of the pitch trajectories to obtain the best trade-off between the cavitation performance and the efficiency. This change in blade design results in the area ratio of the propeller changing from 0.64 for the CP propeller to 0.57 for the CVP propeller with the cosine pitch trajectory and 0.5 for the variable pitch trajectory. This reduction in the area ratio is obtained because a better cavitation performance is obtained with the CVP propeller and the loading of the blade can therefore be increased. With the decreased area ratio for the CVP propeller, the viscous effects should be reduced and thereby increase the efficiency of the propeller. The results for the comparison of the propeller efficiency between the CP and CVP propeller correspond well with previous research such as in [84, 85].

The other aspect with respect to the propeller performance, that is obtained from the simulations, is the variation in the forces and torques acting on the propeller, i.e. shaft vibrations, and are shown in Figure A.21 and the average and the difference between the minimum and maximum are given in Table A.7.

Table A.7: Comparison of the average propeller forces and torques for the CP and CVP propeller simulations. $\hat{\Delta}$ is the maximum variation in the forces or torques during one revolution of the propeller.

		CP Propeller	**CVP Propeller Cosine Pitch Trajectory**	**CVP Propeller Variable Pitch Trajectory**
F_x [kN]	Avg.	562.0 ± 7.3 $\pm 1.3\%$	567.9 ± 8.2 $\pm 1.4\%$	575.8 ± 10.9 $\pm 1.9\%$
	$\hat{\Delta}$	21.5 ± 33.6 $\pm 156.1\%$	24.4 ± 33.5 $\pm 137.4\%$	285.0 ± 23.6 $\pm 8.3\%$
M_x [kNm]	Avg.	-394.5 ± 4.0 $\pm 1.0\%$	-398.9 ± 4.6 $\pm 1.2\%$	-406.0 ± 5.6 $\pm 1.4\%$
	$\hat{\Delta}$	9.9 ± 12.9 $\pm 129.7\%$	11.8 ± 14.2 $\pm 119.9\%$	158.4 ± 13.4 $\pm 8.4\%$
F_y [kN]	Avg.	25.6 ± 2.2 $\pm 8.7\%$	-0.6 ± 4.6 $\pm 735.6\%$	-12.7 ± 6.2 $\pm 48.4\%$
	$\hat{\Delta}$	13.1 ± 14.2 $\pm 108.7\%$	15.9 ± 15.7 $\pm 99.0\%$	128.6 ± 15.5 $\pm 12.1\%$
M_y [kNm]	Avg.	13.8 ± 9.2 $\pm 66.5\%$	-73.4 ± 9.7 $\pm 13.3\%$	-127.8 ± 16.0 $\pm 12.5\%$
	$\hat{\Delta}$	34.0 ± 43.5 $\pm 127.9\%$	39.8 ± 34.8 $\pm 87.6\%$	525.0 ± 29.6 $\pm 5.6\%$
F_z [kN]	Avg.	97.1 ± 1.8 $\pm 1.8\%$	92.0 ± 3.6 $\pm 3.9\%$	78.9 ± 4.9 $\pm 6.2\%$
	$\hat{\Delta}$	13.1 ± 6.6 $\pm 50.4\%$	13.5 ± 10.6 $\pm 78.8\%$	88.0 ± 19.0 $\pm 21.6\%$
M_z [kNm]	Avg.	33.6 ± 3.6 $\pm 10.7\%$	48.0 ± 6.1 $\pm 12.7\%$	20.2 ± 6.7 $\pm 33.1\%$
	$\hat{\Delta}$	19.7 ± 13.1 $\pm 66.6\%$	23.8 ± 16.2 $\pm 68.1\%$	334.7 ± 21.3 $\pm 6.4\%$

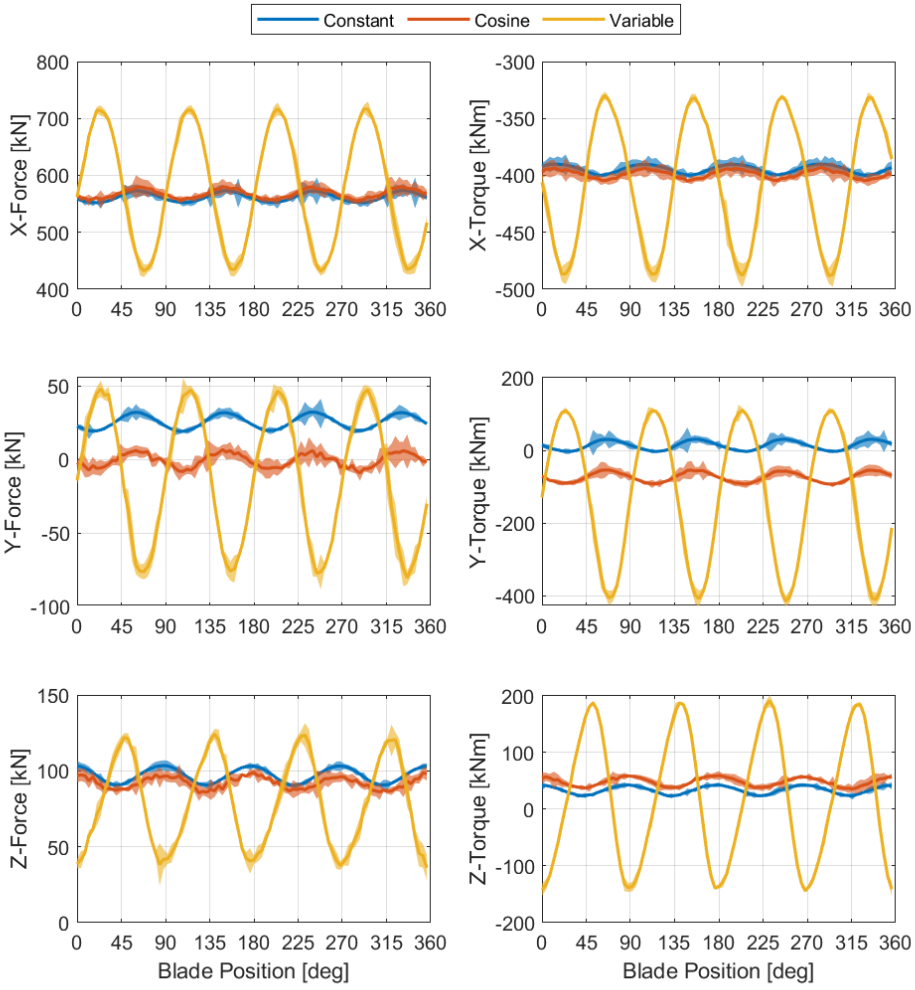

Figure A.21: Comparison of the forces and torques acting on the propeller during one revolution for the CP and CVP simulations for the finest discretization. The uncertainty is shown as the shaded areas.

From Table A.7 and Figure A.21 it is seen that the variation in the forces and torques is the most severe for the CVP propeller with the variable pitch trajectory. The variations in the forces and torques for the CP propeller and CVP propeller with the cosine pitch trajectory are almost identical and the differences in the variation are within the uncertainty bounds. The reason for this is that the CVP propeller with the cosine pitch trajectory does not have a fourth harmonic component. Only the zeroth, fourth, eighth, sixteenth etc. harmonics of the blade forces and torques influence the forces and torques acting on the whole propeller. This is because the other harmonics for the

blades cancel each other and only the harmonics equal to the number of blades on the propeller times an integer influences the propeller's response.

If the CVP propeller is to reduce the vibration level of the propeller then the pitch trajectory should include the $n\,Z$ harmonics. The CVP propeller with the variable pitch trajectory has a fourth-order harmonic component since it is defined using a seventh-order harmonics Fourier series. This is seen in the variation in the forces and torques for the CVP propeller with the variable pitch trajectory. These variations are significantly larger than the variation in the forces and torques for the CP propeller. This shows that the fourth-order harmonic for the variable pitch trajectory is not the appropriate choice, to minimise the shaft vibrations. It can therefore be concluded that the variable pitch trajectory determined in [66] is not the optimum pitch trajectory to minimise the vibration level of the propeller. That the variable pitch trajectory is not the optimum pitch trajectory is also seen from the forces and torques acting on the individual blades of the propeller, and these are shown in Figure A.22 as a function of its position in the wake field. The figure is the average response for the four blades. The average and maximum difference for each of the forces and torques are given in Table A.8.

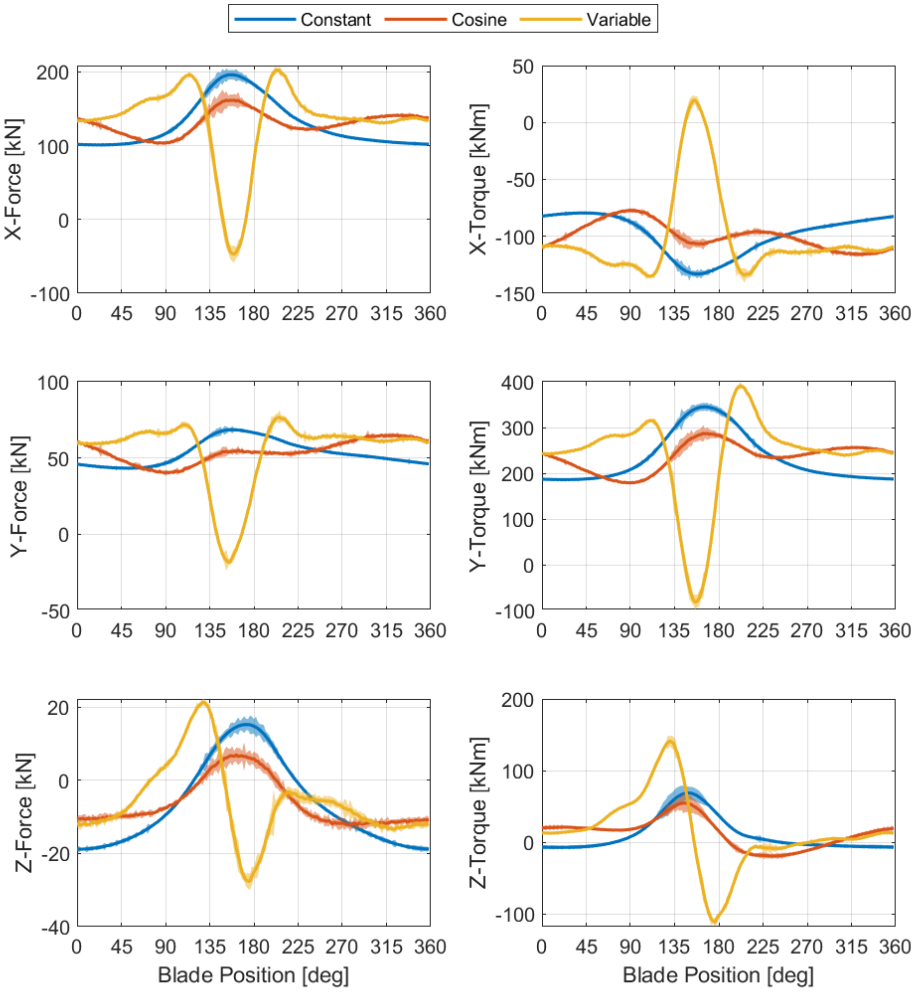

Figure A.22: Comparison of the forces and torques acting on the propeller blade during one revolution for the CP and CVP simulations for the finest discretization. The uncertainty is shown as the shaded areas.

Table A.8: Comparison of the average and maximum variation blade forces and torques for the CP and CVP propeller simulations. $\hat{\Delta}$ is the maximum variation in the forces or torques during one revolution of the propeller.

		CP Propeller	**CVP Propeller Cosine Pitch Trajectory**	**CVP Propeller Variable Pitch Trajectory**
F_x [kN]	Avg.	129.3 ± 2.3 $\pm 1.8\%$	130.7 ± 3.3 $\pm 2.5\%$	132.7 ± 4.0 $\pm 3.0\%$
	$\hat{\Delta}$	95.2 ± 10.8 $\pm 11.4\%$	58.3 ± 17.5 $\pm 30.0\%$	249.1 ± 15.0 $\pm 6.0\%$
M_x [kNm]	Avg.	-98.4 ± 1.7 $\pm -1.7\%$	-99.5 ± 2.1 $\pm -2.1\%$	-101.3 ± 2.7 $\pm -2.7\%$
	$\hat{\Delta}$	53.6 ± 6.3 $\pm 11.8\%$	38.6 ± 5.1 $\pm 13.3\%$	154.6 ± 9.0 $\pm 5.8\%$
F_y [kN]	Avg.	53.4 ± 1.0 $\pm 1.8\%$	54.0 ± 1.5 $\pm 2.8\%$	55.1 ± 1.9 $\pm 3.4\%$
	$\hat{\Delta}$	25.3 ± 3.9 $\pm 15.4\%$	24.8 ± 4.4 $\pm 17.9\%$	95.2 ± 7.7 $\pm 8.1\%$
M_y [kNm]	Avg.	233.7 ± 3.6 $\pm 1.5\%$	236.0 ± 4.5 $\pm 1.9\%$	239.2 ± 5.6 $\pm 2.4\%$
	$\hat{\Delta}$	159.4 ± 12.8 $\pm 8.0\%$	108.0 ± 18.4 $\pm 17.1\%$	473.6 ± 20.9 $\pm 4.4\%$
F_z [kN]	Avg.	-6.5 ± 0.8 $\pm -12.6\%$	-6.3 ± 1.2 $\pm -18.8\%$	-6.0 ± 1.3 $\pm -21.9\%$
	$\hat{\Delta}$	34.1 ± 3.3 $\pm 9.7\%$	19.2 ± 5.1 $\pm 26.7\%$	49.0 ± 3.2 $\pm 6.6\%$
M_z [kNm]	Avg.	10.8 ± 3.2 $\pm 29.8\%$	12.4 ± 3.2 $\pm 26.2\%$	13.3 ± 3.2 $\pm 24.0\%$
	$\hat{\Delta}$	76.0 ± 13.1 $\pm 17.3\%$	73.8 ± 17.8 $\pm 24.1\%$	252.9 ± 15.9 $\pm 6.3\%$

From Figure A.22 and Table A.8 it is seen that the variations in the forces and torques are generally smallest for the CVP propeller with the cosine pitch trajectory. The variations in the forces and torques are largest for the CVP propeller with the variable pitch trajectory. The forces and torques along/around the x- and y-axis have a shape similar to the pitch acceleration of the trajectory. This shows that the response of the CVP propeller with the variable pitch trajectory strongly depends on the dynamics and a quasi-steady analysis would be a poor method to use. The variable pitch trajectory is determined using a quasi-steady analysis method in [66] and this explains why the variable pitch trajectory is not an optimum pitch trajectory for the CVP propeller. The response along/around the z-axis for the CVP propeller with the variable pitch trajectory has a shape similar to the pitch rate of the pitch trajectory. This means that the response along/around the z-axis also strongly depends on the pitch dynamics. The same strong dependency on the pitch dynamics cannot be seen from the response for the CVP propeller with the cosine pitch trajectory. The change in the response for the CVP propeller

with the cosine pitch trajectory compared to the CP propeller matches well by adding a cosine signal to the response. The exception to this may be for the torque about the z-axis. A quasi-steady analysis method may only be appropriate to analyse the CVP propeller if the variations in the pitch trajectory are limited.

Appendix A. Hydrodynamic Modelling of CVP Propeller Through URANS CFD Simulations

Appendix B

Modelling of Coulomb Friction in Blade Bearing

This appendix concerns the derivation of the Coulomb friction in the blade bearing for the different load models presented in Section 2.8. The loads models are shown again in Figure B.1 for convenience.

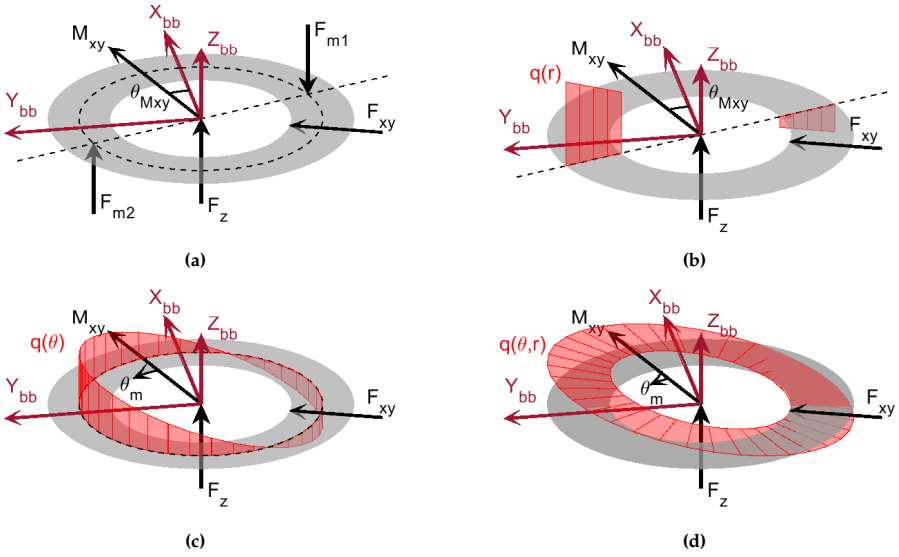

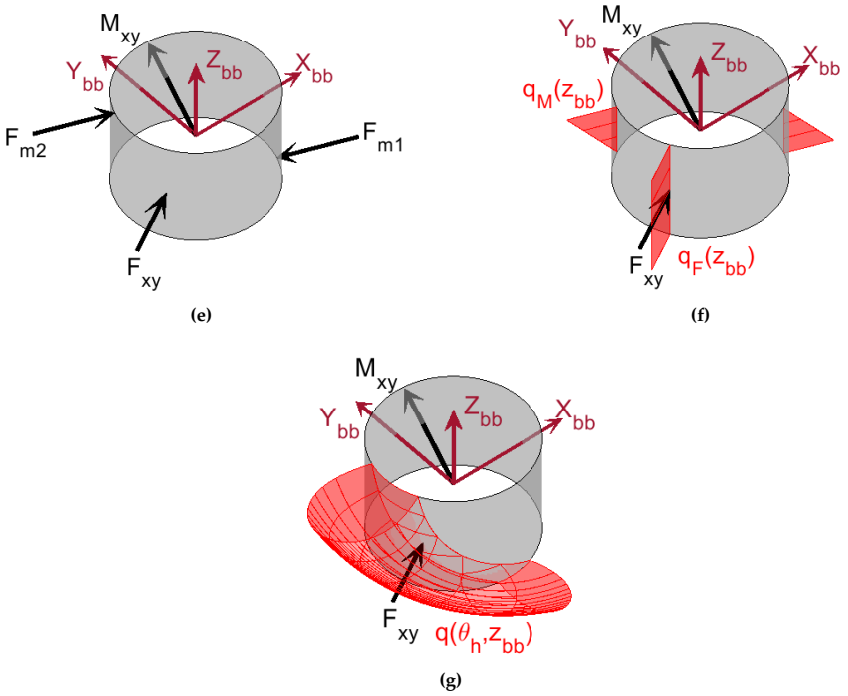

Figure B.1: The different load distributions assumed for the blade bearing.

The force and torque vectors F_{xy} and M_{xy} in Figure B.1 are the force and torque due to the resulting reactive force $F_{reac,xy,bb}$ and torque $M_{reac,xy,bb}$. The red shaded areas are the assumed shapes of the load distribution, q, for the model. The models without the red shaded areas consider the loads acting in points.

The models in Figure B.1 can be divided into two types, one where the resulting reactive torque $M_{reac,xy,bb}$ acts upon the axial surface (models A-D) and the others where the resulting reactive torque $M_{reac,xy,bb}$ acts upon the radial surface (models E-G). For the models A-D, it is assumed that the surfaces can be viewed as a disc in the xy-plane of the blade bearing coordinate system.

In the following two sections the Coulomb friction is derived for the models A-D in Section B.1 and for the models E-G in Section B.2. The derived Coulomb frictional loads are $F_{c,x,bb}$, $F_{c,y,bb}$ and $M_{c,z,bb}$ and the other loads $F_{c,z,bb}$, $M_{c,x,bb}$ and $M_{c,y,bb}$ are zero. The Coulomb friction models are derived such that the friction is correctly aligned when the pitch rate is positive. The derived Coulomb friction models are used in Section 2.8 to determine the frictional loads.

B.1 Axial Coulomb Friction Models

In the axial Coulomb friction models the reactive torques $M_{reac,x}$ and $M_{reac,y}$ act upon the axial surfaces of the blade bearing. Four different models (models A-D) are proposed for modelling the Coulomb friction in the axial part of the blade bearing. These models only consider the axial part of the bearing but the Coulomb friction in the radial part of the bearing still has to be included in the model. Before describing the models (models A-D), the modelling of the Coulomb friction in the radial part of the bearing is considered.

B.1.1 Radial Coulomb Friction Models

Two options are considered for modelling the Coulomb friction in the radial bearing for the models A-D. The two options are shown in Figure B.2a and Figure B.2b. In Figure B.2a the reactive force $F_{reac,xy,bb}$ is considered to act in a point. In Figure B.2b it is assumed that the reactive load in the blade bearing is distributed over a part of the bearing according to Hertzian contact mechanics. The assumption that the reactive load is distributed over a part of the bearing is made to account for the elastic deformation of the materials under loading and the clearance between the bodies.

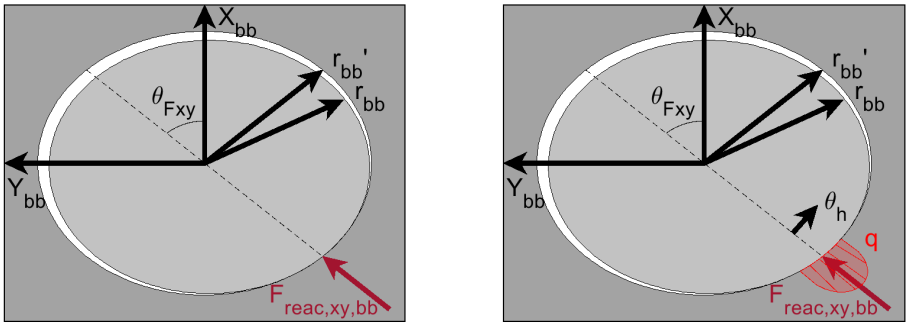

Figure B.2: (a) Radial bearing with point load. **(b)** Radial bearing with distributed load.

For both of the models in Figure B.2a and Figure B.2b the parameters $F_{reac,xy,bb}$ and θ_{Fxy} are determined as:

$$F_{reac,xy,bb} = \sqrt{F_{reac,x,bb}^2 + F_{reac,y,bb}^2} \tag{B.1}$$

$$\theta_{Fxy} = \text{atan2}\left(F_{reac,y,bb}\ ,\ F_{reac,x,bb}\right) \tag{B.2}$$

For the point load model, the friction is determined as:

$$\begin{bmatrix} F_{c,x,bb} \\ F_{c,y,bb} \\ M_{c,z,bb} \end{bmatrix} = \begin{bmatrix} -\mu_c \, F_{reac,y,bb} \\ \mu_c \, F_{reac,x,bb} \\ -\mu_c \, F_{reac,xy,bb} \, r_{bb} \end{bmatrix} \tag{B.3}$$

The results for the Coulomb friction modelling are not shown here, since the model has to be combined with one of the models for the Coulomb friction in the axial blade bearing.

The load distribution in Figure B.2b is assumed to be a Hertzian contact between the two cylindrical bodies. For Hertzian contact the load distribution is elliptical as shown in Figure B.3.

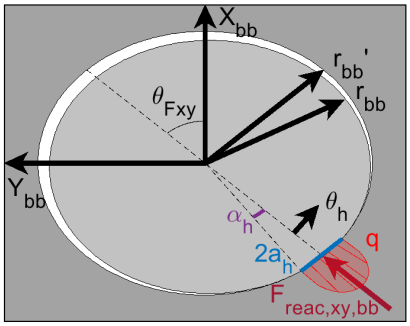

Figure B.3: Radial bearing with Hertzian contact.

The elliptical load distribution, defined in Eq. B.4 [39] is rewritten to use the angle, α_h instead, as shown in Eq. B.5.

$$q(x_h) = q_0 \sqrt{1 - \frac{x_h^2}{a_h^2}} \tag{B.4}$$

As, $a_h = r'_{bb} \, \sin \alpha_h$ and $x = r'_{bb} \, \sin \theta_h$

$$q(\theta) = q_0 \sqrt{1 - \frac{\left(r'_{bb} \, \sin \theta_h\right)^2}{\left(r'_{bb} \, \sin \alpha_h\right)^2}} = q_0 \sqrt{1 - \frac{\sin\left(\theta_h\right)^2}{\sin\left(\alpha_h\right)^2}} \tag{B.5}$$

For Eq. B.5 there are two unknown parameters, q_0 and α_h. q_0 is the peak load of the elliptical load distribution. α_h is half of the contact angle, the load distribution spans over. These two parameters depend on the elastic properties of the materials, the loading and the geometry. The parameters are determined as [39]:

$$q_0 = \sqrt{\frac{F_{reac,xy,bb}}{h_{bb}} \frac{E^*}{\pi\, r^*}} \tag{B.6}$$

$$2a_h = 4\sqrt{\frac{F_{reac,xy,bb}}{h_{bb}} \frac{r^*}{\pi\, E^*}} \tag{B.7}$$

$$\alpha_h = \arcsin\left(\frac{a_h}{r'_{bb}}\right) = \arcsin\left(\frac{2}{r'_{bb}}\sqrt{\frac{F_{reac,xy,bb}}{h_{bb}} \frac{r^*}{\pi\, E^*}}\right) \tag{B.8}$$

Where,

$$E^* = \frac{1}{\frac{1-v_1^2}{E_1} + \frac{1-v_2^2}{E_2}} \quad , \quad r^* = \frac{1}{\frac{1}{r_{bb}} + \frac{1}{-r'_{bb}}} \tag{B.9}$$

E^* is the effective modulus of elasticity. E_1 and E_2 are the modulus of elasticity of two bearing materials. v_1 and v_2 are the Poisson ratios of the two bearing materials. r^* is the effective radius of curvature. For the elliptical loading of the bearing, the friction model is determined as:

$$\begin{bmatrix} F_{c,x,bb} \\ F_{c,y,bb} \\ M_{c,z,bb} \end{bmatrix} = \begin{bmatrix} -\mu_c\, F_{reac,y,bb} \\ \mu_c\, F_{reac,x,bb} \\ -\mu_c\, r_{bb}\, h_{bb} \int_{-\alpha}^{\alpha} q(\theta)\, r'_{bb}\, d\theta \end{bmatrix} \tag{B.10}$$

The evaluation of the integration of the elliptical load distribution is made numerically. The results for the friction modelling are not shown here, since the model has to be combined with one of the models for the friction in the axial blade bearing.

B.1.2 Model A - Point Loads

In the Coulomb friction model A, it is assumed that the reactive loads act in points as shown in Figure B.4. This model uses the point load model for the radial bearing since using the load distributed model would contradict the assumption of the point load model.

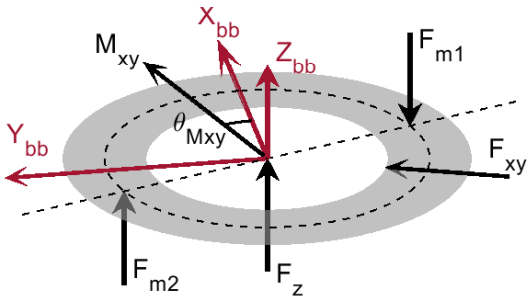

Figure B.4: Axial bearing with loads acting in points.

The reactive torque $M_{reac,xy,bb}$ and angle θ_{Mxy} are determined as:

$$M_{reac,xy,bb} = \sqrt{M_{reac,x,bb}^2 + M_{reac,y,bb}^2} \tag{B.11}$$

$$\theta_{Mxy} = \text{atan2}\left(M_{reac,y,bb}\ ,\ M_{reac,x,bb}\right) \tag{B.12}$$

The torque $M_{reac,xy,bb}$ is assumed to act as a force F_m in two points perpendicular to the vector $M_{reac,xy,bb}$ at a radius r_a which is $r_{bb} \leq r_a \leq R_{bb}$. The forces F_{m1} and F_{m2} are determined as:

$$F_{m,1} = -\frac{M_{reac,xy,bb}}{2\,r_a} \quad , \quad F_{m,2} = \frac{M_{reac,xy,bb}}{2\,r_a} \tag{B.13}$$

The reactive force $F_{reac,z,bb}$ is assumed to act equally in each of these two points with the forces $F_{reac,z,bb}/2$. The Coulomb friction model therefore becomes:

$$F_{c,x,bb} = \mu_c \begin{pmatrix} -F_{reac,y,bb} \\ -\left|F_{m,1} + \frac{F_{reac,z,bb}}{2}\right| \cos\left(\theta_{Mxy}\right) \\ +\left|F_{m,2} + \frac{F_{reac,z,bb}}{2}\right| \cos\left(\theta_{Mxy}\right) \end{pmatrix} \tag{B.14}$$

$$F_{c,y,bb} = \mu_c \begin{pmatrix} F_{reac,x,bb} \\ -\left|F_{m,1} + \frac{F_{reac,z,bb}}{2}\right| \sin\left(\theta_{Mxy}\right) \\ +\left|F_{m,2} + \frac{F_{reac,z,bb}}{2}\right| \sin\left(\theta_{Mxy}\right) \end{pmatrix} \tag{B.15}$$

$$M_{c,z,bb} = -\mu_c \begin{pmatrix} F_{reac,xy,bb}\, r_{bb} \\ +\left|F_{m,1} + \frac{F_z}{2}\right| r_a \\ +\left|F_{m,2} + \frac{F_z}{2}\right| r_a \end{pmatrix} \tag{B.16}$$

B.1.3 Model B - Radially Varying Load

In the Coulomb friction model B, it is assumed that the reactive loads are distributed radially on a line perpendicular on the vector $M_{reac,xy,bb}$ as shown in Figure B.5.

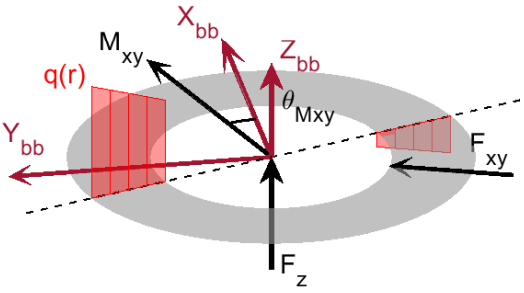

Figure B.5: Axial bearing with radial varying load distribution.

The load distribution $q(r)$ is assumed to be a linear function as:

$$q(r) = a\,r + b \tag{B.17}$$

The load distribution has two unknown parameters that have to be determined. The load distribution can, in principle, be any function consisting of two parameters but it has to satisfy the following two conditions:

$$F_{reac,z,bb} = \int_{r_{bb}}^{R_{bb}} q(r)\,dr + \int_{-R_{bb}}^{-r_{bb}} q(r)\,dr \tag{B.18}$$

$$M_{reac,xy,bb} = \int_{r_{bb}}^{R_{bb}} q(r)\,r\,dr + \int_{-R_{bb}}^{-r_{bb}} q(r)\,r\,dr \tag{B.19}$$

From these conditions the unknown parameters in the load distribution are determined as:

$$a = \frac{3\,M_{reac,xy,bb}}{2\,\left(R_{bb}^3 - r_{bb}^3\right)} \quad , \quad b = \frac{F_{reac,z,bb}}{2\,\left(R_{bb} - r_{bb}\right)} \tag{B.20}$$

Using this load distribution the Coulomb friction model is determined as:

$$F_{c,x,bb} = \mu_c \left(\begin{array}{l} \int_{r_{bb}}^{R_{bb}} |q(r)| \cos\left(\theta_{Mxy}\right) dr \\ -\int_{-R_{bb}}^{-r_{bb}} |q(r)| \cos\left(\theta_{Mxy}\right) dr \end{array} \right) \tag{B.21}$$

$$F_{c,y,bb} = \mu_c \left(\begin{array}{l} \int_{r_{bb}}^{R_{bb}} |q(r)| \sin\left(\theta_{Mxy}\right) dr \\ -\int_{-R_{bb}}^{-r_b b} |q(r)| \sin\left(\theta_{Mxy}\right) dr \end{array} \right) \tag{B.22}$$

$$M_{c,z,bb} = -\mu_c \left(\int_{r_{bb}}^{R_{bb}} |q(r)| \ |r| \ dr + \int_{-R_{bb}}^{-r_{bb}} |q(r)| \ |r| \ dr \right) \tag{B.23}$$

The above model does not include the Coulomb friction contribution from the radial part of the bearing. Both models for the radial bearing can be used together with this model.

B.1.4 Model C - Circumferentially Varying Load

In the Coulomb friction model C, it is assumed that the reactive loads are circumferentially distributed over the disc at the radius r_a, as shown in Figure B.6.

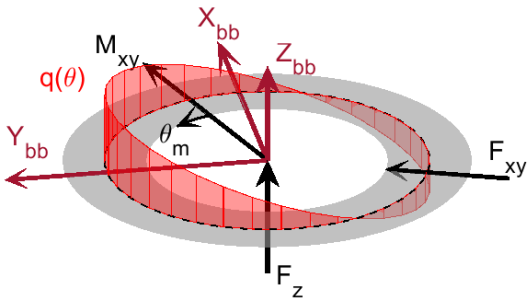

Figure B.6: Axial bearing with circumferentially varying load distribution.

The load distribution is assumed to be a sine function as:

$$q(\theta_m) = a \sin\left(\theta_m\right) + b \tag{B.24}$$

The load distribution has two unknown parameters that have to be determined. The load distribution can, in principle, be any function consisting of

two parameters but it has to satisfy the following two conditions:

$$F_{reac,z,bb} = \int_0^{2\,\pi} q(\theta_m)\, d\theta_m \tag{B.25}$$

$$M_{reac,xy,bb} = \int_0^{2\,\pi} q(\theta_m)\, r_a\, \sin(\theta_m)\, d\theta_m \tag{B.26}$$

From these conditions the unknown parameters in the load distribution are determined as:

$$a = \frac{M_{reac,xy,bb}}{\pi\, r_a} \quad , \quad b = \frac{F_{reac,z,bb}}{2\,\pi} \tag{B.27}$$

Using this load distribution the Coulomb friction model is determined as:

$$F_{c,x,bb} = \mu \int_0^{2\,\pi} |q(\theta_m)|\, \sin\left(\theta_{Mxy} + \theta_m\right) d\theta_m \tag{B.28}$$

$$F_{c,y,bb} = -\mu \int_0^{2\,\pi} |q(\theta_m)|\, \cos\left(\theta_{Mxy} + \theta_m\right) d\theta_m \tag{B.29}$$

$$M_{c,z,bb} = -\mu \int_0^{2\,\pi} |q(\theta_m)|\, r_a\, d\theta_m \tag{B.30}$$

The above model does not include the Coulomb friction contribution from the radial part of the bearing. Both models for the radial bearing can be used together with this model.

B.1.5 Model D - Radially and Circumferentially Varying Load

In the Coulomb friction model D, it is assumed that the reactive loads are distributed radially and circumferentially over the whole disc as shown in Figure B.7.

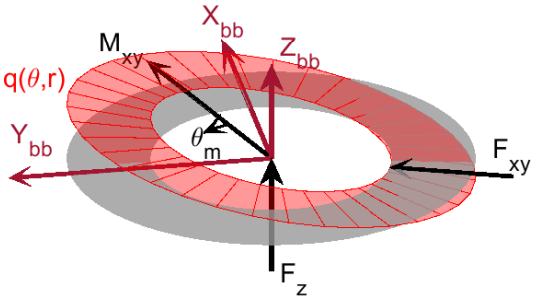

Figure B.7: Axial bearing with radial and circumferentially varying load distribution.

The load distribution $q(r, \theta_m)$ is assumed to be a combined linear and sine function as:

$$q(r, \theta_m) = a\, r\, \sin(\theta_m) + b \tag{B.31}$$

The load distribution has two unknown parameters that have to be determined. The load distribution can, in principle, be any function consisting of two parameters but it has to satisfy the following two conditions:

$$F_{reac,z,bb} = \int_0^{2\pi} \int_{r_{bb}}^{R_{bb}} q(r, \theta_m)\, dr\, d\theta_m \tag{B.32}$$

$$M_{reac,xy,bb} = \int_0^{2\pi} \int_{r_{bb}}^{R_{bb}} q(r, \theta_m)\, r\, \sin(\theta_m)\, dr\, d\theta_m \tag{B.33}$$

From these conditions the unknown parameters in the load distribution are determined as:

$$a = \frac{3\, M_{reac,xy,bb}}{\pi\, \left(R_{bb}^3 - r_{bb}^3\right)} \quad , \quad b = \frac{F_{reac,z,bb}}{2\,\pi\, \left(R_{bb} - r_{bb}\right)} \tag{B.34}$$

Using this load distribution the Coulomb friction model is determined as:

$$F_{c,x,bb} = \mu \int_0^{2\pi} \int_{r_{bb}}^{R_{bb}} |q(r, \theta_m)|\, \sin\left(\theta_{Mxy} + \theta_m\right) dr\, d\theta_m \tag{B.35}$$

$$F_{c,y,bb} = -\mu \int_0^{2\pi} \int_{r_{bb}}^{R_{bb}} |q(r, \theta_m)|\, \cos\left(\theta_{Mxy} + \theta_m\right) dr\, d\theta_m \tag{B.36}$$

$$M_{c,z,bb} = -\mu \int_0^{2\pi} \int_{r_{bb}}^{R_{bb}} |q(r, \theta_m)|\, r\, dr\, d\theta_m \tag{B.37}$$

The above model does not include the Coulomb friction contribution from the radial part of the bearing. Both models for the radial bearing can be used together with this model.

B.2 Radial Coulomb Friction Models

In the radial Coulomb friction models the reactive torques $M_{reac,x}$ and $M_{reac,y}$ are assumed to act upon the radial surface of the blade bearing. Three different models (models E-G) are proposed for modelling the Coulomb friction in the radial part of the blade bearing. These models only consider the radial part of the bearing but the Coulomb friction in the axial part of the bearing still has to be included in the model. Before describing the models (models E-G), the modelling of the Coulomb friction in the radial part of the bearing is considered.

B.2.1 Axial Coulomb Friction Models

Two options are considered for modelling the Coulomb friction in the axial bearing. The two options are shown in Figure B.8a and Figure B.8b. In Figure B.8a the load is uniformly distributed circumferentially at the radius r_a. In Figure B.8b the load is uniformly distributed over the whole disc.

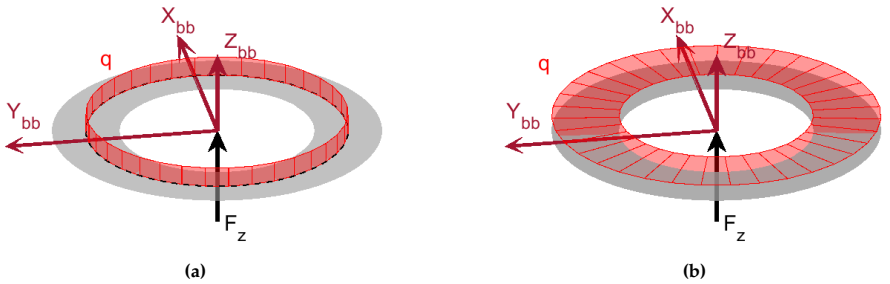

Figure B.8: (a) Axial bearing with circumferential load distribution. **(b)** Axial bearing with the load distribution over the whole disc.

The load distributions for Figure B.8a and Figure B.8b are respectively:

$$q(\theta_m) = a \quad , \quad q(r, \theta_m) = a \tag{B.38}$$

The two load distributions have to satisfy the following respective conditions:

$$F_{reac,z,bb} = \int_0^{2\,\pi} q(\theta_m)\, d\theta_m \tag{B.39}$$

$$F_{reac,z,bb} = \int_0^{2\,\pi} \int_{r_{bb}}^{R_{bb}} q(r, \theta_m)\, dr\, d\theta_m \tag{B.40}$$

The uniform load distribution amplitude, a, becomes:

$$a = \frac{F_{reac,z,bb}}{2\,\pi} \quad , \quad a = \frac{F_{reac,z,bb}}{2\,\pi\,\left(R_{bb} - r_{bb}\right)} \tag{B.41}$$

Due to the axis symmetry in the load distribution around the z-axis, there are no Coulomb friction components along the x- and y-axis. There is only a Coulomb friction contribution to the torque about the z-axis. This contribution is determined as:

$$M_{c,z,bb} = -\mu_c \int_0^{2\pi} |q(\theta_m)| \; r_a \, d\theta_m$$
$$= -\mu_c \; |F_{reac,z,bb}| \; r_a \tag{B.42}$$
$$M_{c,z,bb} = -\mu_c \int_0^{2\pi} \int_{r_{bb}}^{R_{bb}} |q(r,\theta_m)| \; r \, dr \, d\theta_m$$
$$= -\mu_c \; |F_{reac,z,bb}| \; \frac{R_{bb} + r_{bb}}{2} \tag{B.43}$$

The two Coulomb friction models are equal if r_a is taken as the average radius of the axial bearing. The Coulomb friction torque for the circumferential loading will be larger than the surface loaded model, if r_a is assumed to be larger than the average radius of the axial bearing, and smaller if r_a is assumed to be smaller than the average radius of the axial blade bearing. The results for the friction modelling are not shown here, since the model has to be combined with one of the models for the friction in the radial part of the bearing.

B.2.2 Model E - Point Load

In the Coulomb friction model E, it is assumed that the reactive loads act in points on the radial part of the blade bearing as shown in Figure B.4.

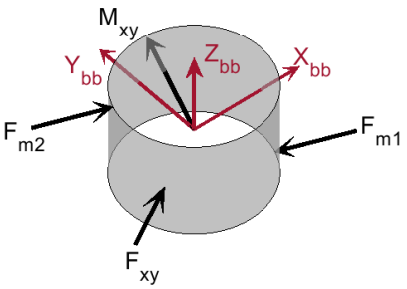

Figure B.9: Radial bearing with loads acting in points.

To derive the Coulomb friction it is assumed that the reactive torque $M_{reac,xy,bb}$ can be split into the two forces F_{m1} and F_{m2} as shown in Figure B.9. Each of these forces has an amplitude of $M_{reac,xy,bb}/h_{bb}$ where h_{bb} is the height of the bearing. From Figure B.9, the Coulomb friction model is determined as:

$$F_{c,x,bb} = \mu_c \, F_{reac,y,bb} \tag{B.44}$$

$$F_{c,y,bb} = -\mu_c \, F_{reac,x,bb} \tag{B.45}$$

$$M_{c,z,bb} = -\mu_c \left(F_{reac,xy,bb} + 2 \, \frac{M_{reac,xy}}{h_{bb}} \right) r_{bb} \tag{B.46}$$

B.2.3 Model F - Height Varying Load

In the Coulomb friction model F, it is assumed that the reactive loads vary along the height of the radial bearing as shown in Figure B.10.

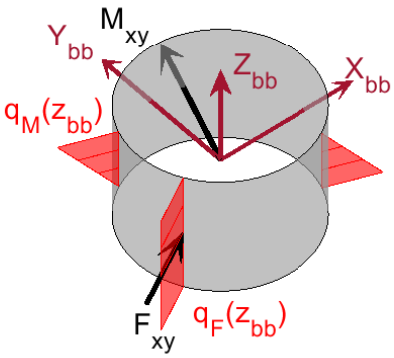

Figure B.10: Radial bearing with a height varying load distribution.

In Figure B.10 it is seen that the load distribution from the reactive force and torque may not be aligned. It is therefore necessary to define two load distributions, each with one unknown parameter. The two load distributions are defined as:

$$q_F(z_{bb}) = b \tag{B.47}$$

$$q_M(z_{bb}) = a \, z_{bb} \tag{B.48}$$

The two conditions used to determine the unknown parameters in the load distributions are:

$$F_{reac,xy,bb} = \int_{-\frac{h_{bb}}{2}}^{\frac{h_{bb}}{2}} q_F(z_{bb}) \, dz_{bb} \tag{B.49}$$

$$M_{reac,xy,bb} = \int_{-\frac{h_{bb}}{2}}^{\frac{h_{bb}}{2}} q_M(z_{bb}) \, z_{bb} \, dz_{bb} \tag{B.50}$$

Using the above conditions the parameters for the load distribution are determined as:

$$a = \frac{12\, M_{reac,xy,bb}}{h_{bb}^3} \quad , \quad b = \frac{F_{reac,xy,bb}}{h_{bb}} \tag{B.51}$$

The two load distributions are combined into a single load distribution (as shown in Figure A.15d) as:

$$q_{FM}(z_{bb}) = \sqrt{\left(q_{F,x} + q_{M,x}\right)^2 + \left(q_{F,y} + q_{M,y}\right)^2} \tag{B.52}$$

$$\theta_{FM}(z_{bb}) = \text{atan2}\left(q_{F,y} + q_{M,y}\ ,\ q_{F,x} + q_{M,x}\right) \tag{B.53}$$

Where,

$$q_{F,x}(z_{bb}) = q_F\ \cos\theta_{F_{xy}} \quad , \quad q_{F,y}(z_{bb}) = q_F\ \sin\theta_{F_{xy}} \tag{B.54}$$

$$q_{M,x}(z_{bb}) = q_M\ \sin\theta_{M_{xy}} \quad , \quad q_{M,y}(z_{bb}) = -q_M\ \cos\theta_{M_{xy}} \tag{B.55}$$

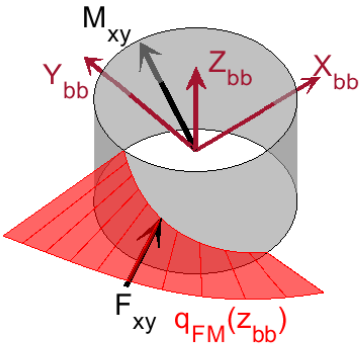

Figure B.11: Radial bearing with a height varying load distribution.

The friction model is determined as:

$$F_{c,x,bb} = \mu_c \int_{-\frac{h_{bb}}{2}}^{\frac{h_{bb}}{2}} q_{FM}(z_{bb})\ \sin\left(\theta_{FM}(z_{bb})\right) dz_{bb} \tag{B.56}$$

$$F_{c,y,bb} = -\mu_c \int_{-\frac{h_{bb}}{2}}^{\frac{h_{bb}}{2}} q_{FM}(z_{bb})\ \cos\left(\theta_{FM}(z_{bb})\right) dz_{bb} \tag{B.57}$$

$$M_{c,z,bb} = -\mu_c\, r_{bb} \int_{-\frac{h_{bb}}{2}}^{\frac{h_{bb}}{2}} q_{FM}(z_{bb})\, dz_{bb} \tag{B.58}$$

B.2.4 Model G - Height and Circumferential Varying Load

In the Coulomb friction model H, it is assumed that the reactive loads are distributed over the whole surface of the radial part of the blade bearing as shown in Figure B.12.

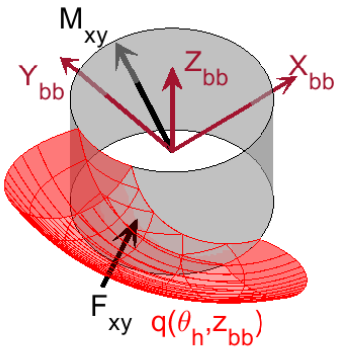

Figure B.12: Radial bearing with height and circumferential varying load distribution.

The load distribution in Figure B.12 is an extension of model F by including a circumferential load distribution based on Hertzian contact. The load distribution is determined as:

$$q(\theta_h, z_{bb}) = q_0(z_{bb}) \sqrt{1 - \frac{\sin(\theta_h)^2}{\sin(\alpha_h(z_{bb}))^2}} \tag{B.59}$$

Where,

$$q_0(z_{bb}) = \sqrt{\frac{q_{FM}(z_{bb})\, E^*}{\pi\, r^*}} \tag{B.60}$$

$$\alpha_h(z_{bb}) = \arcsin\left(\frac{2}{r'_{bb}} \sqrt{\frac{q_{FM}(z_{bb})\, r^*}{\pi\, E^*}}\right) \tag{B.61}$$

Using this load distribution the friction is determined as:

$$F_{c,x,bb} = \mu_c \int_{-\frac{h_{bb}}{2}}^{\frac{h_{bb}}{2}} \int_{-\alpha_h}^{\alpha_h} q(\theta_h, z_{bb}) \sin(\theta_{FM}(z_{bb}) + \theta_h)\, r'_{bb}\, d\theta_h\, dz_{bb} \tag{B.62}$$

$$F_{c,y,bb} = -\mu_c \int_{-\frac{h_{bb}}{2}}^{\frac{h_{bb}}{2}} \int_{-\alpha_h}^{\alpha_h} q(\theta_h, z_{bb}) \cos(\theta_{FM}(z_{bb}) + \theta_h)\, r'_{bb}\, d\theta_h\, dz_{bb} \tag{B.63}$$

$$M_{c,z,bb} = -\mu_c\, r_{bb} \int_{-\frac{h_{bb}}{2}}^{\frac{h_{bb}}{2}} \int_{-\alpha_h}^{\alpha_h} q(\theta_h, z_{bb})\, r'_{bb}\, d\theta_h\, dz_{bb} \tag{B.64}$$

Appendix C

Uncertainty and Periodic Convergence of CFD Simulations

CFD simulations are used to compute the physical behaviour of fluids and their interaction with solid bodies. In this project CFD simulations are used to compute the flow around marine propellers and determine the forces and torques the fluid exerts on the propeller under different flow conditions. In CFD it is the Navier-Stokes momentum equations and the continuity equation that are solved. The Navier-Stokes equations are solved iteratively by discretization of the equations. The discretization and the iterative solver give an approximated solution to the Navier-Stokes equations and the continuity equation. Due to the solution being an approximation, there typically is a simulation error (e_s) which is the difference between the simulated value and the true physical value. The simulation error is typically decomposed into a numerical error (e_n) and a modelling error (e_m) [45] as in Eq. C.1.

$$e_s = e_n + e_m = \text{simulated value} - \text{true value} \tag{C.1}$$

The decomposition of the simulation error into a numerical error and a modelling error is related to the concept of verification and validation respectively.

Verification is the process of determining the numerical error or if that is not possible, then to determine the numerical uncertainty. The numerical error is due to the discretization, iterative solver and the round-off error due to the finite number of bits used to represent a number in the computer.
Validation is the process of determining if the right model has been solved. This is with respect to the assumptions and approximations used in the modelling such as; the domain size for external flows, choice of turbulence model,

boundary conditions, unsteady or steady flow solver etc. To make the validation assessment of a CFD simulation, the simulation results must be compared with experimental results for the same application.

When the numerical error has been determined, one can choose to correct the simulation results with the error. The uncertainty for the error estimate is then the numerical uncertainty for the simulation. In some cases it is not possible to determine the numerical error. In these cases only the numerical uncertainty is determined. The numerical uncertainty defines a 95 % confidence band for the simulation results by which the true/exact value (ϕ_{excact}) is within as:

$$\phi_i - U_{num} \leq \phi_{excact} \leq \phi_i + U_{num} \tag{C.2}$$

ϕ_i is the simulated value. U_{num} is the numerical uncertainty.

The focus of this appendix is on how to determine the numerical uncertainty of the CFD simulations made in this dissertation. This is with respect to the discretization and the iterative solver. The round-off error is considered as negligible. For the time varying CFD simulations of the propeller in Appendix A the periodic convergence of the simulation is also considered. With periodic convergence it is meant that the solutions for the two latest revolutions of the propeller are the same, or that the difference in the solutions is insignificant.

The iterative error and uncertainty are considered in Section C.1. The spatial discretization error and uncertainty are considered in Section C.2. The temporal discretization error and uncertainty are considered in Section C.3 and the periodic convergence is considered in Section C.4.

C.1 Iterative Convergence Error and Uncertainty

The iterative convergence error and uncertainty are due to the iterative solver being stopped before the solution has converged to the machine accuracy of the computer. The iterative solver may not get to converge to the machine accuracy due to limited computational resources and that an acceptable level of error and uncertainty is obtained before the machine accuracy is obtained. It is also possible that the solution may not be able to reach the level of machine accuracy for example due to complex turbulent flows [27].

The determination of the iterative error and uncertainty is made according to [87]. The convergence of the iterative solver is divided into four cases. These four cases are; asymptotic convergent, oscillatory, mixed oscillatory/asymptotic and diverging. Examples of the four cases are shown in Figure C.1. Figure C.1 is made considering a steady simulation but the same applies for each time step of an unsteady simulation. In unsteady simulation

the iterative error and uncertainty are determined for each time step, but the number of iterations used for one time step is about 5-30 iterations instead of a thousand or more iterations used in a steady simulation. Because of the lower number of iterations it can be difficult to determine which case each time step belongs to, but typically it belongs to the asymptotic convergent case.

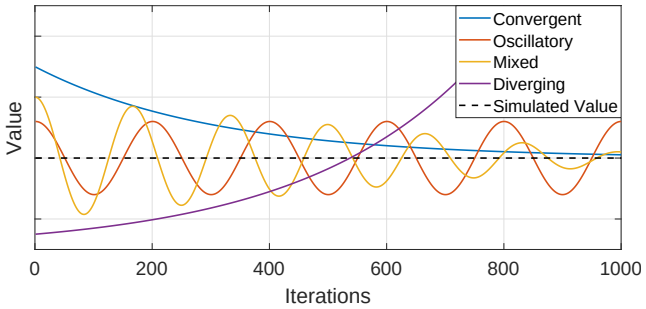

Figure C.1: Example of the four categories/types of classifying the iterative convergence.

The iterative error (e_I) and uncertainty (U_I) for the four cases are given in Table C.1.

Table C.1: Iterative error and uncertainty depending on the convergence case.

Case	**Error**, e_I	**Uncertainty**, U_I
Convergent	$\phi_i - \phi_\infty$	$\lvert\phi_i - \phi_{i,\infty}\rvert$
Oscillatory	-	$\frac{1}{2}\ \lvert\phi_{i,U} - \phi_{i,L}\rvert$
Mixed	-	$\frac{1}{2}\ \lvert\phi_{i,U} - \phi_{i,L}\rvert$
Diverging	∞	∞

ϕ_i is the simulated value at the last iteration for the CFD simulation for the asymptotic convergent case. For the oscillatory and mixed case ϕ_i is found as an average over the last X iterations. The number of iterations used to determine ϕ_i varies from simulation to simulation. $\phi_{i,\infty}$ are the value at infinite iterations when making a curve fit using an exponential function to the simulation data. $\phi_{i,U}$ and $\phi_{i,L}$ are the upper and lower simulation values, respectively. The upper and lower limits are taken over an appropriate interval for the last iteration and X iterations back. For the example shown in Figure C.1 the interval would likely be from iteration number 700-800 to 1000. The error terms for the oscillatory and mixed are not defined. For the diverging case the error and uncertainty are infinite because the simulation results are unusable.

The general procedure that is used to determine the iterative uncertainty is the oscillatory, and the iterative error is therefore not determined. The oscillatory convergence is used for all the steady simulations because most of the simulations exhibit oscillation in their results. An example of this is shown in Figure C.2, which is the iterative solution for the blade thrust for the open-water simulation in Appendix D at the finest mesh at $J = 0.6$.

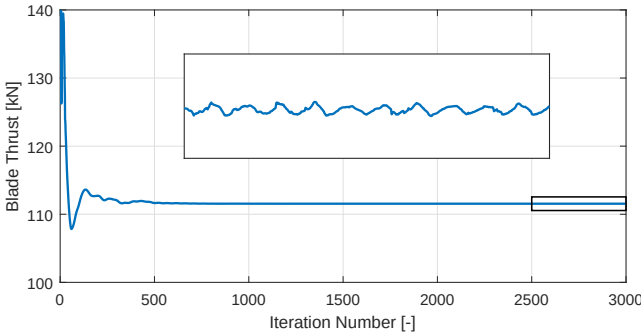

Figure C.2: The iterative solution of the blade thrust for the open-water CFD simulation in Appendix D at the finest mesh at $J = 0.6$. A close up of the last 500 iteration is shown in the box.

In Figure C.2 it is seen that the thrust has converged to an approximately constant value. A close-up of the approximate constant value is shown in the box. It is seen that the solution oscillates. This is for a case that is close to the design point of the propeller. For off-design conditions the amplitude of the oscillation usually becomes larger. Because of these oscillations the general procedure used to determine the iterative uncertainty is the one for oscillatory convergence.

All steady simulation results are considered individually, to determine the appropriate iterative interval to determine whether the general oscillatory procedure is appropriate to use or if the converging procedure is to be used. If nothing else is stated then the oscillatory procedure has been applied to determine the iterative uncertainty for the steady simulations.

C.2 Spatial Discretization Error and Uncertainty

The spatial discretization error and uncertainty are due to the finite cell size used for the mesh in the CFD simulations. The spatial discretization error and uncertainty are determined by making the simulation using different refinements of the mesh. It is typical to assume that the discretization error is described by a truncated power series. The truncated power series neglects the higher orders. It is therefore assumed that the discretization er-

ror is in the asymptotic range. The order of the power series depends on the discretization scheme used. The spatial discretization scheme used in this project is second-order unless otherwise specified. The theoretical order of convergence for the spatial discretization error should therefore also be second-order in the asymptotic range. In practice this second-order convergence of the spatial discretization error may not be observed. This is due to complex problems, such as complex geometries and turbulent flow. There may even be scatter/noise in the results relative to the truncated power series. The scatter may be due to flux limiters, damping functions, switching or a lack in geometric similarity between the meshes for example due to using unstructured meshing [29]. Scatter has been observed for the simulations made and the method proposed in [29] is used to account for the scatter and determine the discretization error and uncertainty. The discretization error is approximated with the truncated power series as:

$$\epsilon_{\phi_i} \approx \delta_x = \phi_i - \phi_0 = \alpha_x \, h_i^{p_x} \tag{C.3}$$

ϵ_{ϕ_i} is the spatial discretization error for the i'th simulation. ρ_x is the approximation of the discretization error. ϕ_i is the i'th simulation value of interest which can be a point value or an integrated value. In this project ϕ_i is usually either a force or torque. ϕ_0 is the estimate of the true value of the value of interest with an infinitely fine mesh. α_x is the error term gain. h_i is the mesh metric which is a metric for the cell size of the i'th mesh. p_x is the observed order of convergence. The mesh metric h_i is determined relative to the finest mesh, where $h_1 = 1$. The other mesh metrics are determined as [58]:

$$\frac{h_i}{h_1} = \sqrt[3]{\frac{N_1}{N_i}} \tag{C.4}$$

N_i is the number of cells in the i'th mesh. In [29] the coefficients ϕ_0, α_x and p_x in Eq. C.3 are estimated through a least-squares fit of the simulation results for the different meshes. The least-squares fit of the three coefficients requires simulation results for at least four different meshes [29] to also get an estimate on the scatter/noise.

The observed order of convergence estimated by the least-squares fit may be unrealistic. An unrealistic observed order of convergence is if the observed order of convergence is larger than the theoretical order of convergence or if it is significantly lower than the theoretical order of convergence. If the observed order of convergence is larger than the theoretical order of convergence, then the spatial discretization error will tend to be underestimated. If the observed order of convergence is too small, then the spatial discretization error tends to be overestimated. To deal with this problem [29] suggests some

alternative approximations for the spatial discretization error, which are:

$$\epsilon_{\phi_i} \approx \delta_1 = \phi_i - \phi_0 = \alpha_x \, h_i \tag{C.5}$$

$$\epsilon_{\phi_i} \approx \delta_2 = \phi_i - \phi_0 = \alpha_x \, h_i^2 \tag{C.6}$$

$$\epsilon_{\phi_i} \approx \delta_{12} = \phi_i - \phi_0 = \alpha_{x,1} \, h_i + \alpha_{x,2} \, h_i^2 \tag{C.7}$$

Common for the three alternative formulation of the spatial discretization error is that the observed order of convergence is fixed. The alternative formulation of the spatial discretization error are only used if the observed order of convergence from the least-squares fit of Eq. C.3 is unrealistic. The alternative formulation of the spatial discretization error in Eq. C.7 is for when the simulation results are not in the asymptotic range. The assumption of truncated the power series is therefore not appropriate for the spatial discretization error.

All the coefficients in the alternative formulations of the spatial discretization error are approximated by a least-squares fit. The least-squares estimates are made with and without weighting of the simulation results. The weighting is made such that the simulation results for the finer meshes are weighted more than the simulation results for the coarser meshes. The estimates of the discretization error with weights are noted with an additional subscript w as; $\delta_{x,w}$, $\delta_{1,w}$, $\delta_{2,w}$ and $\delta_{12,w}$. The selection of which discretization error to use is determined as:

$$\epsilon_{\phi_i} \approx \begin{cases} \delta_x & \text{if} \quad (\ 0.5 \leq \tilde{p}_x \leq 2 \quad \wedge \quad \sigma_x \leq \sigma_{x,w}\ ) \\ & \vee \quad (\ 0.5 \leq \tilde{p}_x \leq 2 \quad \wedge \quad (\tilde{p}_{x,w} < 0.5 \ \vee \ \tilde{p}_{x,w} > 2)\ ) \\ \delta_{x,w} & \text{if} \quad (\ 0.5 \leq \tilde{p}_{x,w} \leq 2 \quad \wedge \quad \sigma_{x,w} \leq \sigma_x\ ) \\ & \vee \quad (\ 0.5 \leq \tilde{p}_{x,w} \leq 2 \quad \wedge \quad (\tilde{p}_x < 0.5 \ \vee \ \tilde{p}_x > 2)\ ) \\ \delta_1 & \text{if} \quad (\ \tilde{p}_{x,\check{\sigma}} > 2 \quad \wedge \quad \min \boldsymbol{\Omega}_1 = \sigma_1\ ) \\ & \vee \quad (\ \tilde{p}_{x,\check{\sigma}} < 0.5 \quad \wedge \quad \min \boldsymbol{\Omega}_2 = \sigma_1\ ) \\ \delta_{1,w} & \text{if} \quad (\ \tilde{p}_{x,\check{\sigma}} > 2 \quad \wedge \quad \min \boldsymbol{\Omega}_1 = \sigma_{1,w}\ ) \\ & \vee \quad (\ \tilde{p}_{x,\check{\sigma}} < 0.5 \quad \wedge \quad \min \boldsymbol{\Omega}_2 = \sigma_{1,w}\ ) \\ \delta_2 & \text{if} \quad (\ \tilde{p}_{x,\check{\sigma}} > 2 \quad \wedge \quad \min \boldsymbol{\Omega}_1 = \sigma_2\ ) \\ & \vee \quad (\ \tilde{p}_{x,\check{\sigma}} < 0.5 \quad \wedge \quad \min \boldsymbol{\Omega}_2 = \sigma_2\ ) \\ \delta_{2,w} & \text{if} \quad (\ \tilde{p}_{x,\check{\sigma}} > 2 \quad \wedge \quad \min \boldsymbol{\Omega}_1 = \sigma_{2,w}\ ) \\ & \vee \quad (\ \tilde{p}_{x,\check{\sigma}} < 0.5 \quad \wedge \quad \min \boldsymbol{\Omega}_2 = \sigma_{2,w}\ ) \\ \delta_{12} & \text{if} \quad (\ \tilde{p}_{x,\check{\sigma}} < 0.5 \quad \wedge \quad \min \boldsymbol{\Omega}_2 = \sigma_{12}\ ) \\ \delta_{12,w} & \text{if} \quad (\ \tilde{p}_{x,\check{\sigma}} < 0.5 \quad \wedge \quad \min \boldsymbol{\Omega}_2 = \sigma_{12,w}\ ) \end{cases} \tag{C.8}$$

Where,

$$\boldsymbol{\Omega}_1 = \begin{bmatrix} \sigma_1 & \sigma_{1,w} & \sigma_2 & \sigma_{2,w} \end{bmatrix}$$
$$\boldsymbol{\Omega}_2 = \begin{bmatrix} \sigma_1 & \sigma_{1,w} & \sigma_2 & \sigma_{2,w} & \sigma_{12} & \sigma_{12,w} \end{bmatrix}$$

$\tilde{p}_x$ and $\tilde{p}_{x,w}$ are the observed order of convergence for the non-weighted and weighted least-squares fits of Eq. C.3. σ is the standard deviation of the least-squares fit. $\tilde{p}_{x,\check{\sigma}}$ is the observed order of convergence for the discretization error with the lowest standard deviation of δ_x and $\delta_{x,w}$.

The discretization uncertainty is determined using the discretization error. In [58] the discretization uncertainty for the i'th simulation is determined as:

$$U_{disc}\left(\phi_i\right) = \begin{cases} 1.25\,\epsilon_{\phi_i} + \sigma + \left|\phi_i - \phi_{fit}\right| & \text{for } \sigma < \Delta_\phi \\ 3\,\frac{\sigma}{\Delta_\phi}\,\left(\epsilon_\phi + \sigma + \left|\phi_i - \phi_{fit}\right|\right) & \text{for } \sigma \geq \Delta_\phi \end{cases} \tag{C.9}$$

Where,

$$\phi_{fit} = \phi_0 + \epsilon_{\phi_i}$$
$$\Delta_\phi = \frac{\max(\phi_i) - \min(\phi_i)}{n_g - 1}$$

U_{disc} is the spatial discretization uncertainty. ϕ_{fit} is the value of the least-squares fit evaluated at h_i. Δ_ϕ is the data range of ϕ_i. n_g is the number of meshes used to determine the discretization uncertainty. If there is no scatter/noise in the mesh independency study, then the uncertainty determined Eq. C.9 becomes the same as the well-known Grid Convergence Index procedure also known as the GCI procedure proposed by Roache [58]. Two different expressions are used to determine the spatial discretization uncertainty depending on the ratio between the standard deviation and the data range and this is to separate the fits into good and bad fits. The good fits use a low safety factor of 1.25 and the bad fits uses a high safety factor of 3. It can be discussed if this is an appropriate method to judge whether a fit is good or bad but this approach will nonetheless be used.
The inclusion of the standard deviation (σ) and value difference with the fitted values $\left(\left|\phi_i - \phi_{fit}\right|\right)$ in Eq. C.9 are to account for the uncertainty due to scatter in the discretization study. Instead of using these two terms to account for the scatter, it is proposed to use $2\,\sigma$ instead. The $2\,\sigma$ is equivalent to a 95.4 % confidence interval under the assumption that the scatter is normally distributed. This corresponds well with the desire for the spatial discretization uncertainty to be the 95 % confidence interval. The modified expression for the discretization uncertainty becomes:

$$U_{disc}(\phi_i) = \begin{cases} 1.25\ \left|\epsilon_{\phi_i}\right| + 2\,\sigma & \text{for } \sigma < \Delta_\phi \\ 3\ \frac{\sigma}{\Delta_\phi}\ \left(\left|\epsilon_{\phi_i}\right| + 2\,\sigma\right) & \text{for } \sigma \geq \Delta_\phi \end{cases} \tag{C.10}$$

The number of meshes that must be used to determine the discretization uncertainty is a trade-off between the amount of information and the amount of computational resources required. The minimum required number of meshes used is four when using the above described approach. In this project four or five meshes are used to determine the spatial discretization uncertainty.

If the data point for the coarsest mesh does not follow the trend then it can be omitted. This practice follows the one used in [58]. The application of this procedure is shown in Figure C.3a and Figure C.3b. The examples shown in Figure C.3a and Figure C.3b are both from the steady state simulations presented in Appendix G.

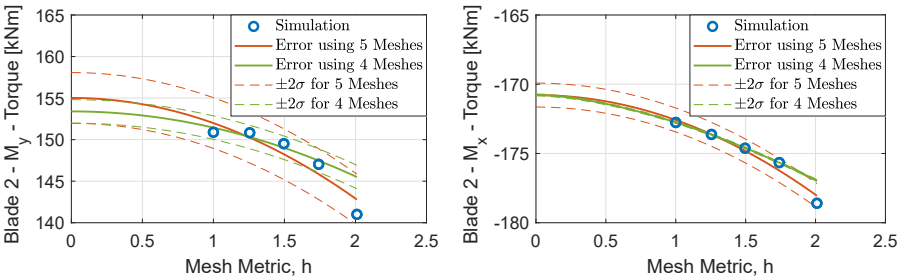

Figure C.3: (a,b) Example for where it is assessed that the coarsest mesh point are not within the asymptotic range.

From both Figure C.3a and Figure C.3b it can be seen that the error estimator is improved and the standard deviation for the least-squares estimation is reduced. The improvement is more significant for the example in Figure C.3b than the example in Figure C.3a. Common for both of the two examples, shown in Figure C.3, is that the standard deviation of the least-squares error estimation is reduced. It has been found that when the ratio between the standard deviation using the five meshes and the standard deviation using four meshes is greater than two, then it should be considered if the coarsest mesh should be removed from the error estimation.

C.3 Temporal Discretization Error and Uncertainty

The procedure described above is used to determine the spatial discretization uncertainty for steady CFD simulations. For unsteady CFD simulations the uncertainty due to the temporal discretization also has to be considered. According to [28] the discretization error for an unsteady problem is defined as in Eq. C.11, where it is assumed that the discretization error due to spatial discretization and temporal discretization are independent of each other.

$$\epsilon_{\phi_i} \approx \delta_{xt} = \phi_i - \phi_0 = \alpha_x \, h_i^{p_x} + \alpha_t \, \tau_i^{p_t} \tag{C.11}$$

p_x and p_t are the observed order of convergence for the spatial and temporal part, respectively. α_x and α_t are the error term gains for the spatial and temporal part, respectively. τ_i is the metric for the relative time step used in the i'th simulation and is calculated as:

$$\frac{\tau_i}{\tau_1} = \frac{\Delta t_i}{\Delta t_1} \tag{C.12}$$

Δt_i is the time step for the i'th simulation where Δt_1 is the time step used in the simulation with the smallest time step. As for the mesh metric h_1, τ_1 is equal to unity.

The temporal discretization error in Eq. C.11 is defined as the spatial discretization error with a truncated power series. The parameters ϕ_0, p_x, p_t, α_x and α_t are determined using the same least-squares fit method as used for the spatial discretization error for the steady CFD simulations. To determine the five parameters explicitly at least five simulations are required with three different meshes and three different time steps. If the parameters are to be determined using the least-squares method at least six simulations are required with different spatial and temporal discretizations.

The discretization uncertainty is determined for each time instance where a solution exists for all the simulations with different time steps. This is illustrated in Figure C.4, which shows how a solution could differ when different time steps are used for the simulation.

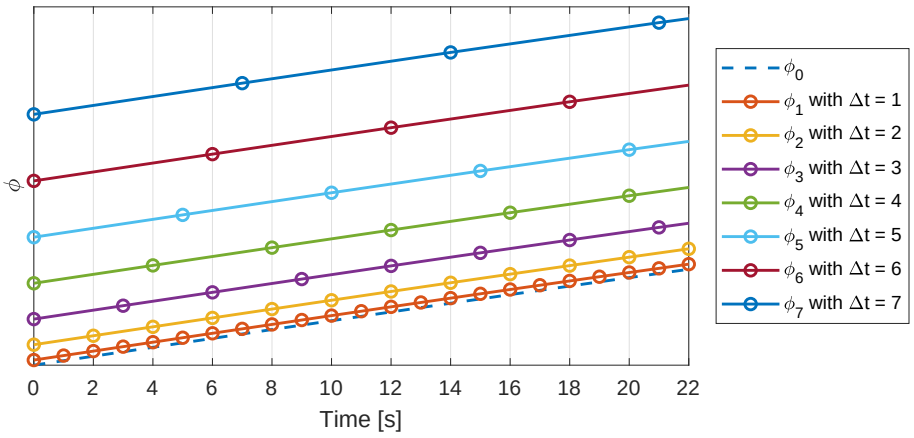

Figure C.4: Example on how the solution could be when using different time steps.

The different time steps used in the simulations should have a common integer denominator relative to the smallest time step used. For example from Figure C.4 it can be seen that if the simulations have been made with the time step on 1, 2 and 4 then the discretization uncertainty can be determined for each time instance of the simulation with a time step of 4. On the other hand, if the simulation had been made with the time step of 1, 3 and 7 then the discretization uncertainty can only be determined for each 21st time step for the simulation with a time step of 1 and for each 7th time step for the simulation with a time step of 3 and for each 3rd time step for the simulation with a time step of 7. One should therefore be careful when choosing the different time steps used to determine the discretization uncertainty. Another

consideration that should be made for the time step for the simulations with a periodic solution is that the ratio between the time period and the time step should be an integer. The solution is thereby obtained at the same instance of the period for each period of the simulation. This makes the data treatment easier and more consistent since the same number of samples is obtained for each period.

For the simulations with a periodic solution only the converged periodic solution is used to determine the discretization uncertainty. Appendix C.4 presents the method used to determine if a periodic converged solution has been obtained. This requires that the time step has been chosen so that the ratio between the period time and the time step is an integer. Otherwise it is not certain that time instances for each periodic solution will match with each other.

The least-squares fit of Eq. C.11 to the simulation data may yield unrealistic observed order of convergence for both the spatial and temporal part of the discretization error. If the observed order of convergence is unrealistic, an alternative discretization error estimator is used as done for the spatial discretization error in Section C.2. The alternative discretization error estimators that are used are given as [26]:

$$\epsilon_{\phi_i} \approx \begin{cases} \delta_{xt} = \phi_i - \phi_0 = \alpha_x \, h_i^{p_x} + \alpha_t \, \tau_i^{p_t} \\ \delta_{x2} = \phi_i - \phi_0 = \alpha_x \, h_i^{p_x} + \alpha_t \, \tau_i^2 \\ \delta_{2t} = \phi_i - \phi_0 = \alpha_x \, h_i^2 + \alpha_t \, \tau_i^{p_t} \\ \delta_{22} = \phi_i - \phi_0 = \alpha_x \, h_i^2 + \alpha_t \, \tau_i^2 \\ \delta_{x1} = \phi_i - \phi_0 = \alpha_x \, h_i^{p_x} + \alpha_t \, \tau_i \\ \delta_{1t} = \phi_i - \phi_0 = \alpha_x \, h_i + \alpha_t \, \tau_i^{p_t} \\ \delta_{21} = \phi_i - \phi_0 = \alpha_x \, h_i^2 + \alpha_t \, \tau_i \\ \delta_{12} = \phi_i - \phi_0 = \alpha_x \, h_i + \alpha_t \, \tau_i^2 \\ \delta_{11} = \phi_i - \phi_0 = \alpha_x \, h_i + \alpha_t \, \tau_i \end{cases} \tag{C.13}$$

The selection of which formulation of the discretization error to use is determined as:

$$\epsilon_{\phi_i} = \begin{cases} \boldsymbol{\delta}_0^{\text{argmin}(\boldsymbol{\Omega}_0)} & \text{if} \quad \begin{pmatrix} \tilde{p}_x \in [0.5,2] & \wedge \\ \tilde{p}_t \in [0.5,2] & \end{pmatrix} \\ & \wedge \quad \begin{pmatrix} \tilde{p}_{x,w} \in [0.5,2] & \wedge \\ \tilde{p}_{t,w} \in [0.5,2] & \end{pmatrix} \\ \delta_{xt} & \text{else if} \quad \begin{pmatrix} \tilde{p}_x \in [0.5,2] & \wedge \\ \tilde{p}_t \in [0.5,2] & \end{pmatrix} \\ & \wedge \quad \begin{pmatrix} \tilde{p}_{x,w} \notin [0.5,2] & \vee \\ \tilde{p}_{t,w} \notin [0.5,2] & \end{pmatrix} \\ \delta_{xt,w} & \text{else if} \quad \begin{pmatrix} \tilde{p}_{x,w} \in [0.5,2] & \wedge \\ \tilde{p}_{t,w} \in [0.5,2] & \end{pmatrix} \\ & \wedge \quad \begin{pmatrix} \tilde{p}_x \notin [0.5,2] & \vee \\ \tilde{p}_t \notin [0.5,2] & \end{pmatrix} \\ \boldsymbol{\delta}_1^{\text{argmin}(\boldsymbol{\Omega}_1)} & \text{else if} \quad \begin{pmatrix} \tilde{p}_{x,\breve{\sigma}} < 0.5 & \wedge \\ \tilde{p}_{t,\breve{\sigma}} \geq 0.5 & \end{pmatrix} \\ \boldsymbol{\delta}_2^{\text{argmin}(\boldsymbol{\Omega}_2)} & \text{else if} \quad \begin{pmatrix} \tilde{p}_{x,\breve{\sigma}} \geq 0.5 & \wedge \\ \tilde{p}_{t,\breve{\sigma}} < 0.5 & \end{pmatrix} \\ \boldsymbol{\delta}_3^{\text{argmin}(\boldsymbol{\Omega}_3)} & \text{else if} \quad \begin{pmatrix} \tilde{p}_{x,\breve{\sigma}} < 0.5 & \wedge \\ \tilde{p}_{t,\breve{\sigma}} < 0.5 & \end{pmatrix} \\ \boldsymbol{\delta}_4^{\text{argmin}(\boldsymbol{\Omega}_4)} & \text{else if} \quad \begin{pmatrix} \tilde{p}_{x,\breve{\sigma}} > 2 & \wedge \\ \tilde{p}_{t,\breve{\sigma}} \in [0.5,2] & \end{pmatrix} \\ & \vee \quad \begin{pmatrix} \tilde{p}_{t,\breve{\sigma}} > 2 & \wedge \\ \tilde{p}_{x,\breve{\sigma}} \in [0.5,2] & \end{pmatrix} \end{cases} \tag{C.14}$$

Where,

$$\boldsymbol{\delta}_0 = \begin{bmatrix} \delta_{xt} \\ \delta_{xt,w} \end{bmatrix} \quad , \quad \boldsymbol{\delta}_1 = \begin{bmatrix} \delta_{2t} \\ \delta_{2t,w} \\ \delta_{1t} \\ \delta_{1t,w} \\ \delta_{x2} \\ \delta_{x2,w} \\ \delta_{22} \\ \delta_{22,w} \\ \delta_{12} \\ \delta_{12,w} \end{bmatrix} \quad , \quad \boldsymbol{\delta}_2 = \begin{bmatrix} \delta_{2t} \\ \delta_{2t,w} \\ \delta_{x2} \\ \delta_{x2,w} \\ \delta_{x1} \\ \delta_{x1,w} \\ \delta_{22} \\ \delta_{22,w} \\ \delta_{21} \\ \delta_{21,w} \end{bmatrix} \quad , \quad \boldsymbol{\delta}_3 = \begin{bmatrix} \delta_{2t} \\ \delta_{2t,w} \\ \delta_{1t} \\ \delta_{1t,w} \\ \delta_{x2} \\ \delta_{x2,w} \\ \delta_{x1} \\ \delta_{x1,w} \\ \delta_{22} \\ \delta_{22,w} \\ \delta_{21} \\ \delta_{21,w} \\ \delta_{12} \\ \delta_{12,w} \\ \delta_{11} \\ \delta_{11,w} \end{bmatrix} \quad , \quad \boldsymbol{\delta}_4 = \begin{bmatrix} \delta_{2t} \\ \delta_{2t,w} \\ \delta_{x2} \\ \delta_{x2,w} \\ \delta_{22} \\ \delta_{22,w} \end{bmatrix}$$

$$\boldsymbol{\Omega}_0 = \begin{bmatrix} \sigma_{xt} \\ \sigma_{xt,w} \end{bmatrix} \quad , \quad \boldsymbol{\Omega}_1 = \begin{bmatrix} \sigma_{2t} \\ \sigma_{2t,w} \\ \sigma_{1t} \\ \sigma_{1t,w} \\ \sigma_{x2} \\ \sigma_{x2,w} \\ \sigma_{22} \\ \sigma_{22,w} \\ \sigma_{12} \\ \sigma_{12,w} \end{bmatrix} \quad , \quad \boldsymbol{\Omega}_2 = \begin{bmatrix} \sigma_{2t} \\ \sigma_{2t,w} \\ \sigma_{x2} \\ \sigma_{x2,w} \\ \sigma_{x1} \\ \sigma_{x1,w} \\ \sigma_{22} \\ \sigma_{22,w} \\ \sigma_{21} \\ \sigma_{21,w} \end{bmatrix} \quad , \quad \boldsymbol{\Omega}_3 = \begin{bmatrix} \sigma_{2t} \\ \sigma_{2t,w} \\ \sigma_{1t} \\ \sigma_{1t,w} \\ \sigma_{x2} \\ \sigma_{x2,w} \\ \sigma_{x1} \\ \sigma_{x1,w} \\ \sigma_{22} \\ \sigma_{22,w} \\ \sigma_{21} \\ \sigma_{21,w} \\ \sigma_{12} \\ \sigma_{12,w} \\ \sigma_{11} \\ \sigma_{11,w} \end{bmatrix} \quad , \quad \boldsymbol{\Omega}_4 = \begin{bmatrix} \sigma_{2t} \\ \sigma_{2t,w} \\ \sigma_{x2} \\ \sigma_{x2,w} \\ \sigma_{22} \\ \sigma_{22,w} \end{bmatrix}$$

$\boldsymbol{\delta}_x$ are the vectors containing different approximations of the discretization error. $\boldsymbol{\Omega}_x$ are the vectors containing the corresponding standard deviation of the discretization error estimation. The subscript w for the discretization errors is when the discretization error is approximated by weighting the observations. The i'th observation is weighted with the weight factor $w(i)$ as:

$$w_i = \frac{\dfrac{1}{\left(\dfrac{h_i}{\max(\boldsymbol{h})}\right)^2 + \left(\dfrac{\tau(i)}{\max(\boldsymbol{\tau})}\right)^2}}{\displaystyle\sum_{i=1}^{i_{tot}} \left(\frac{1}{\left(\dfrac{h_i}{\max(\boldsymbol{h})}\right)^2 + \left(\dfrac{\tau_i}{\max(\boldsymbol{\tau})}\right)^2} \right)} \tag{C.15}$$

$\tilde{p}_{x,\check{\sigma}}$ and $\tilde{p}_{t,\check{\sigma}}$ are the observed order of spatial and temporal convergence respectively with the lowest standard deviation of the approximation of the discretization errors δ_{xt} and $\delta_{xt,w}$. $\delta_x^{\text{argmin}(\boldsymbol{\Omega}_x)}$ is the discretization error at the same vector index as where the minimum value is indexed in the vector $\boldsymbol{\Omega}_x$. For example if $\tilde{p}_{x,\check{\sigma}}$ and $\tilde{p}_{t,\check{\sigma}}$ are less than 0.5, then the approximations for the discretization errors in the vector $\boldsymbol{\delta}_3$ are considered for use to determine the discretization uncertainty. The index of the vector $\boldsymbol{\delta}_3$ to be used is the same index that the minimum of vector $\boldsymbol{\Omega}_3$ has. If σ_{22} is the minimum of $\boldsymbol{\Omega}_3$, then the discretization error δ_{22} of $\boldsymbol{\delta}_3$ are used for determining the discretization uncertainty. The discretization uncertainty is determined using Eq. C.10.

C.4 Periodic Convergence

To evaluate if periodic convergence has been obtained for an unsteady CFD simulation the method proposed in [22] is used. In [22] five metrics are used to access if a periodic solution is obtained. The five metrics are calculated for each period/revolution of the propeller as:

- **Mean value of the signal:** The mean value of the signal, Φ_i, for one period from which the solution oscillates/fluctuates about is given as:

$$\overline{\phi_i} = \frac{1}{N} \sum_{n=0}^{N-1} \Phi_i(n) \tag{C.16}$$

- **Discrete Fourier transform of the signal:** Used to determine the amplitude and phase of each fundamental frequency of the signal. The discrete Fourier transform ($\phi_{i,DFT}$) for the signal ϕ_i is determined using Eq. C.17 which gives a complex number for each fundamental frequency. From the discrete Fourier transform the amplitude, $||\phi_i||_2$, and the phase, $\underline{/\phi_i}$, for each fundamental frequency are determined using Eq. C.18 and Eq. C.19, respectively. ϕ_i is the detrended signal determined in Eq. C.20.

$$\phi_{i,DFT}(n) = \frac{1}{N} \sum_{n=0}^{N-1} \phi_i(n)\ e^{-i\,n\,\omega\,t(n)} \tag{C.17}$$

$$||\phi_{i,DFT}(n)||_2 = \sqrt{\mathbb{R}\mathrm{e}\left(\phi_{i,DFT}(n)\right)^2 + \mathbb{I}\mathrm{m}\left(\phi_{i,DFT}(n)\right)^2} \tag{C.18}$$

$$\underline{/\phi_{i,DFT}(n)} = \mathrm{atan}\left(\frac{\mathbb{I}\mathrm{m}\left(\phi_{i,DFT}(n)\right)}{\mathbb{R}\mathrm{e}\left(\phi_{i,DFT}(n)\right)}\right) \tag{C.19}$$

$$\phi_i = \Phi_i - \overline{\phi_i} \tag{C.20}$$

- **Cross-correlations between the signals:** The cross-correlation is used to evaluate how well the shapes of the signals for two following periods correspond with each other. The cross-correlation (CC) is determined using Eq. C.21. The expression for the cross-correlation in Eq. C.21 is a normalised cross-correlation which results in a cross-correlation of unity at zero lag when the signals for two following periods are equal. This implies that the signals are equal and that the solution has converged.

$$CC(n_L) = \frac{\sum_{n=0}^{N-1} \phi_i(n+n_L)\ \phi_i(n+N)}{\sqrt{\sum_{n=0}^{N-1} \phi_i(n)^2 \sum_{n=0}^{N-1} \phi_i(n+N)^2}} \tag{C.21}$$

- **Power Spectral Density of the signal:** The power spectral density (PSD) is determined using Eq. C.22 and is used to determine the power at each fundamental frequency of the discrete Fourier transform of the signal. The superscript * in Eq. C.22 is the complex conjugate of the discrete Fourier transform.

$$PSD(n) = \phi_{i,DFT}(n)^*\ \phi_{i,DFT}(n) \tag{C.22}$$

Φ_i is the time varying signal of interest which in this case are the forces and torques acting on each of the propeller blades. $\overline{\phi_i}$ is the mean value the signal over one period. n is the sample number, starting from zero. N is the number of samples during one revolution of the propeller. ω is the rotational speed of the propeller. $t(n)$ is the time at sample n. $\mathbb{R}\mathrm{e}$ and $\mathbb{I}\mathrm{m}$ are the real and imaginary parts of the complex number, respectively. n_L is the number of lagged samples in the cross-correlation.

For each of the five convergence metrics a fuzzy set is defined as [22]:

$$f_M = 1 - \left| 1 - \frac{\overline{\phi_{i,N}}}{\overline{\phi_i}} \right| \tag{C.23}$$

$$f_A(n_{exp}) = 1 - \left| 1 - \frac{||\phi_{i,DFT,N}(n_{exp})||_2}{||\phi_{i,DFT}(n_{exp})||_2} \right| \tag{C.24}$$

$$f_\phi(n_{exp}) = 1 - \left| \frac{\angle\phi_{i,DFT,N}(n_{exp}) - \angle\phi_{i,DFT}(n_{exp})}{\pi} \right| \tag{C.25}$$

$$f_S = |CC(0)| \tag{C.26}$$

$$f_P = \frac{\sum_{n_{exp}} PSD(n_{exp})}{\sum_{n=0}^{N-1} PSD(n)} \tag{C.27}$$

f_x are the fuzzy sets. The subscript N is for the signal at the latest period, where the missing subscript N is the previous period. n_{exp} are the expected fundamental frequencies of interest. For the propeller blade forces

and torques the expected fundamental frequencies of interest are $n_{exp} = [1, 2, ..., N_{exp}]$, where N_{exp} is the maximum expected fundamental frequency of interest. If it is the propeller performance that is of interest, then the expected fundamental frequencies of interest is an integer value of the number of blades for the propeller such that $n_{exp} = Z[1, 2, ..., N_{exp}]$, where Z is the number of blades for the propeller. The fuzzy set for the power spectrum density (Eq. C.27) is used to evaluate if a sufficient number of frequencies has been included in the convergence evaluation. If the fuzzy set is not close to one, then there are probably some unexpected unsteadiness at a frequency that has not been considered. This also keeps one from just using one fundamental frequency in order to more easily obtaining convergence for the amplitude and phase for the discrete Fourier transform.

To evaluate if the CFD simulation has converged to a periodic solution, a single fuzzy set is used. This fuzzy set is defined in [22] as:

$$f_C = \min\left(f_M, f_A\left(n_{exp}\right), f_\phi\left(n_{exp}\right), f_S, f_P\right) \tag{C.28}$$

In [22] it is stated that periodic convergence is obtained if $f_C \geq 0.95$ for two following periods for the signals of interest. In this project the signals of interest are the forces and torques acting on the blades. For the four bladed propeller this gives a total of 24 signals that has to converge before a periodic solution has been obtained. Instead of considering each signal individually a common fuzzy set is defined as the minimum of all the signals fuzzy convergences set. If this collected fuzzy convergences set are ≥ 0.95 then the simulation has converged.

The concept of the above procedure is shown through an example. The example considered is from Appendix A which is an unsteady simulation of a CP propeller in a non-uniform wake field. In Figure C.5a and Figure C.5b the time signals and the five metrics are shown. Figure C.5a shows the torque about the z-axis for the 3rd and 4th revolution of the propeller. Figure C.5b shows the torque for the 13th and 14th revolution of the propeller. Figure C.5a is taken for some of the first revolutions of the propeller where periodic convergence has not been obtained and Figure C.5b is for the revolutions where periodic convergence has been obtained.

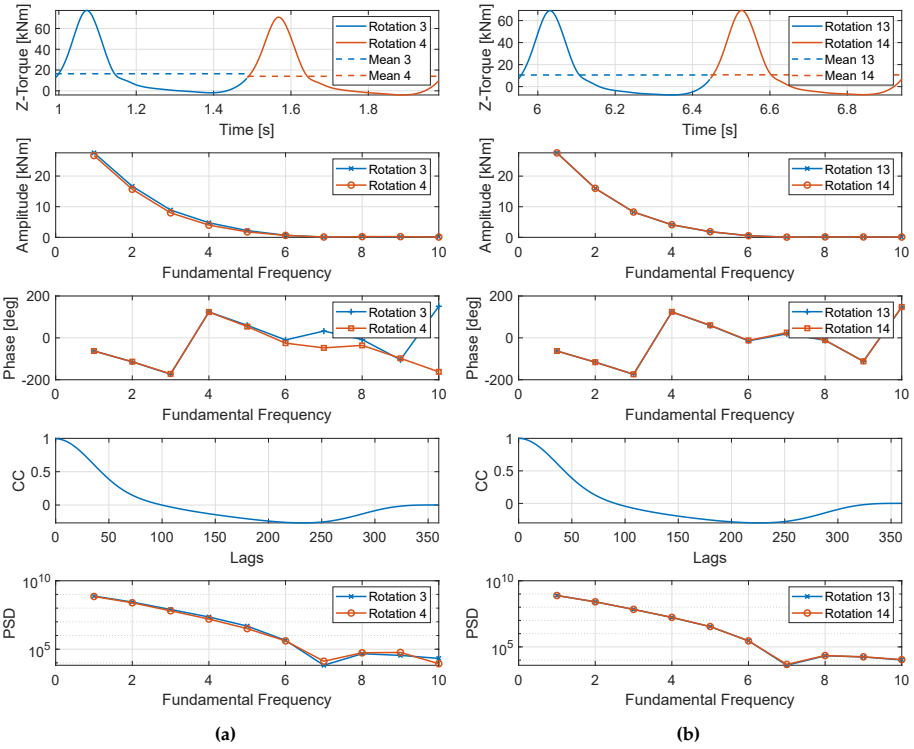

Figure C.5: **(a)** Time series signal and convergence metric for 3th and 4th revolution of the propeller. **(b)** Time series signal and convergence metric for 13th and 14th revolution of the propeller.

From Figure C.5a it is seen that the mean value and the amplitude at low frequencies are different for each period which are the most important frequencies because they contain most of the power. The shape of the signal for the two periods in Figure C.5a does not change significantly which is seen from the cross-correlation (CC). From Figure C.5b it is seen that the metrics for the two periods have a better correspondence to each other than for the periods in Figure C.5a. This is also observed in fuzzy convergence sets which are shown in Figure C.6a and in Figure C.6b for the collected fuzzy convergence set which includes all the convergence metrics for all the signals of interest.

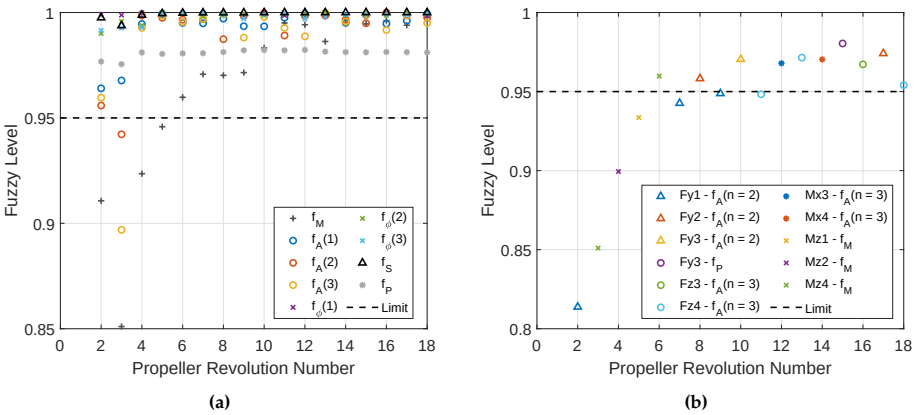

Figure C.6: (a) The fuzzy convergence level for the Z-torque on blade number 4 over the different revolutions of the propeller. **(b)** The minimum fuzzy convergence level over all the signals in the CFD simulations over the different revolutions of the propeller.

From Figure C.6a it is seen that it is the mean value of the signal that sets the limit for convergence for the first 10 cycles. The unsteadiness from the discrete Fourier transform converges after a few cycles and the number of frequencies considered is sufficient as seen from the power spectral density. The shape of the signal does not change much as seen from the high convergence level for the cross-correlation. That the mean value sets the lower limit for the convergence level is not always the case, as seen in Figure C.6b. In Figure C.6b the lowest convergence level for all the signal convergence metrics is shown for each propeller revolution. It is seen generally that it is the amplitude of the discrete Fourier transform or the mean value that sets the lower limit for the convergence. A stable convergence level above the limit is obtained at the 12th revolution and forward. For further work/data treatment of the simulation results the latest revolution with periodic convergence is used. For the case shown in Figure C.6b this means that the solution of the 18th revolution is used.

Appendix D

Hydrodynamic Modelling of CVP Propeller Through Open-Water CFD Simulations

It is typical to describe a propeller's characteristics by its open-water diagram. The open-water diagram for the propeller is made with uniform flow into the propeller. The diagram is usually determined through an open-water test where a scaled model of the propeller is towed through a towing tank. Normally, the open-water diagram includes the thrust coefficient K_T, torque coefficient K_Q, open-water efficiency η_o and sometimes the spindle torque coefficient K_{sh} as a function of the advance coefficient J. These coefficients are non-dimensional and are determined from the propeller thrust, torque, blade spindle torque, carriage velocity and rotational speed of the propeller as:

$$K_T = \frac{T}{\rho\, n^2\, D_p^4} \qquad \text{(D.1)} \qquad K_Q = \frac{Q}{\rho\, n^2\, D_p^5} \qquad \text{(D.2)}$$

$$K_{sh} = \frac{M_z}{\rho\, n^2\, D_p^5} \qquad \text{(D.3)} \qquad J = \frac{V}{n\, D_p} \qquad \text{(D.4)}$$

$$\eta_o = \frac{K_T}{K_Q}\,\frac{J}{2\,\pi} \qquad \text{(D.5)}$$

T and Q are the propeller thrust and torque, respectively. ρ is the density of the water. n is the rate of propeller revolution in [rps]. D_p is the propeller

diameter. M_z is the blade spindle torque. V is the speed of the water flowing into the propeller or the speed at which the propeller is towed through the tank.

To model the CVP propeller all the hydrodynamical forces and torques affecting the propeller blades must be determined. Normally, the blade loads are not determined in an open-water test, but by modifying the test setup it is possible to determine these experimentally. Measurements of the blade loads are made in [16, 50], amongst others, under different operating conditions. For the present case the loads are determined through CFD RANS simulation of the propeller in open-water conditions, as in [30][1]. The simulations are made using the full scale propeller and not the model scale propeller which is usually used to make open-water tests. By doing so, the need to scale the results from model scale to full scale, is removed.

To model the CVP propeller by using open-water CFD simulations the open-water characteristics are determined for a series of pitch settings of the propeller blades, as in [30][1]. The different pitch settings should enclose the desired pitch trajectories used to evaluate the hydrodynamicals loads for the CVP propeller. The simulation results are collected in a table for each of the hydrodynamical loads which depend on the blade pitch and the advance coefficient. The hydrodynamical loads are then determined by interpolating the data in the look-up table depending on the blade pitch and the local advance coefficient [30][1]. The local advance coefficient is determined for each blade position in the wake field to account for the propeller operating in the non-uniform wake field of the ship.

This appendix is divided into three sections:

- Section D.1 presents how the open-water CFD simulations are made and the results of these simulations with their uncertainties. The CFD simulations are made using the propeller and the operating conditions used in Chapter 2. These simulation results are also used in [30][1].
- Section D.2 presents four different methods to determine the local advance coefficient for the blade in the non-uniform wake field. The wake field used is the one used in Appendix A.
- Section D.3 presents the results for applying the derived model for the hydrodynamics of the CVP propeller for the three pitch trajectories considered in Chapter 2.

D.1 Open-Water CFD Simulation

The same setup, as used in Appendix A, is used for the open-water CFD simulations. The commercial CFD package STAR-CCM+ 12.02.010 is used

[1]Paper [30] was produced by the author as part of the research made for this dissertation.

for the mesh generating and solving the fluid problem. The physics used for the simulations are steady, single phase and incompressible flow. The turbulence is modelled using the SST $k\omega$ turbulence model without a transition model because the simulations are made using the full scale propeller. The flow is solved using the segregated flow solver by second-order spatial discretization. The domain for the open-water CFD simulation is shown in Figure D.1.

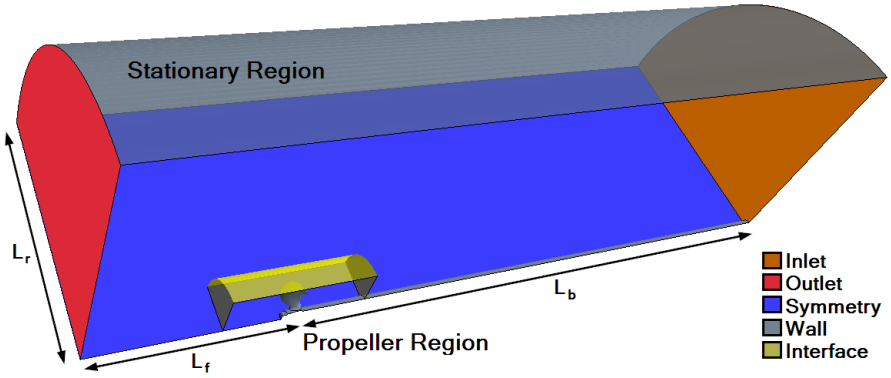

Figure D.1: Domain for open-water CFD simulation.

The domain includes one blade of the propeller and has periodic boundaries conditions on the sides to account for the effect of the other propeller blades. The inlet is located 25 [m] or $\approx 4.6D_p$ upstream of the propeller (L_f), the outlet is located 75 [m] or $\approx 13.9D_p$ downstream of the propeller (L_b) and the radial boundary is located 30 [m] or $\approx 5.6D_p$ from the center of the domain (L_r). The radial boundary condition is a wall with slip. The domain is divided into two regions a stationary region and a propeller region. The propeller region encloses the propeller and is surrounded by the stationary region. The propeller motion is modelled using a moving reference frame applied to the propeller domain. This reference frame rotates about the propeller shaft axis at the same rate as the propeller.

The open-water simulations of the propeller are made for a series of different pitch settings. To evaluate this model, for the pitch trajectories used in Chapter 2, the pitch settings have to cover the span of these pitch trajectories. The pitch displacement trajectories are shown in Figure D.2. The displacement is relative to the design pitch of the propeller blade given in Chapter 2.

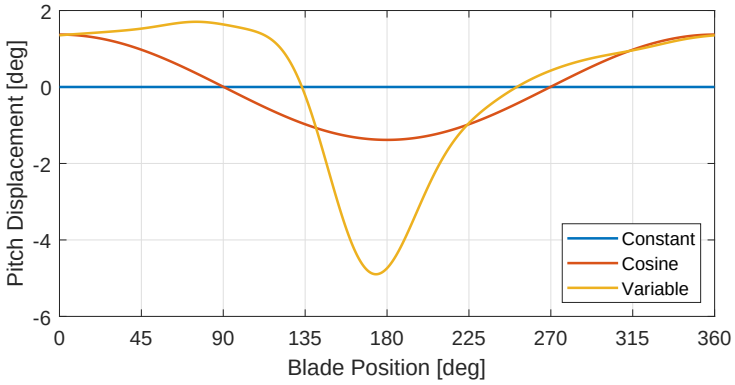

Figure D.2: Pitch displacement trajectories used in Chapter 2.

From Figure D.2 it is seen that the pitch displacement spans from -5° to 2°. The open-water CFD simulations are made covering this span with an increment of 1°. This results in a total of eight open-water characteristics that needs to be made. Each of these open-water characteristics includes 10 different advance coefficients in the interval $0.1 \leq J \leq 0.85$. The simulation results for the open-water simulations are shown in Figure D.3 for the hydrodynamical loads acting on the propeller blades as a function of the relative pitch displacement and advance coefficient. Furthermore, the open-water efficiency is also included in Figure D.3 which is determined from the simulated hydrodynamical loads according to Eq. D.5. The CFD simulation results shown in Figure D.3 are made using the finest mesh used to determine the spatial uncertainty in the following section.

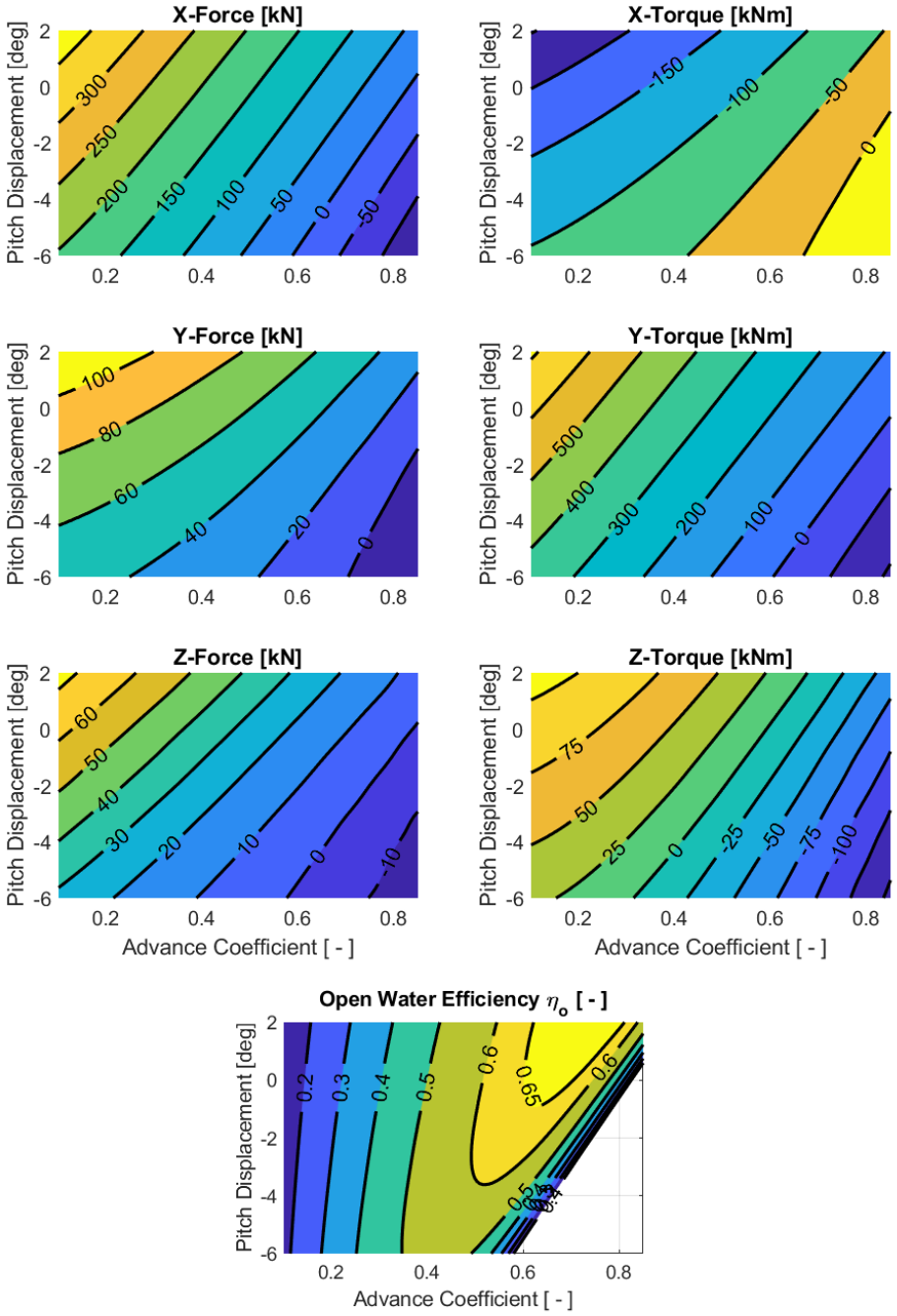

Figure D.3: Open-water CFD simulation results for the hydrodynamical loads and open-water efficiency.

D.1.1 Uncertainty of Open-Water CFD Simulations

The uncertainty of the steady open-water CFD simulations are determined using the approach described in Appendix C. The considered uncertainty sources are the iterative, discretization and domain uncertainties. Determining the discretization and domain uncertainty for each of the evaluation points of the open-water CFD simulations is computationally expensive. Therefore, some assumptions and simplifications are made in order to reduce the computational costs. The iterative uncertainty is determined for each individual simulation. The cause of the iterative uncertainty is due to iterative process having to stop before it has converged to machine accuracy or that the assumption of steady state is not appropriate because the solution is actually unsteady. An example on the iterative uncertainty of an open-water characteristic is shown in Figure D.4 for all the hydrodynamical loads acting on the propeller blades. The iterative uncertainties shown in Figure D.4 are for the zero pitch displacement of the blade and using the finest mesh for the CFD simulation.

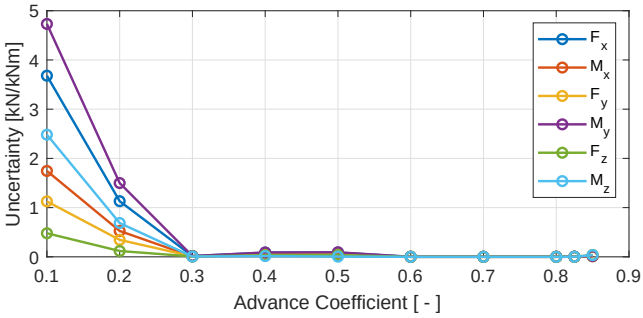

Figure D.4: Iterative uncertainties for the open-water simulation with zero pitch displacement and using the finest mesh for the simulation.

From Figure D.4 it is seen that the iterative uncertainty is the largest at low advance coefficients. This is because inherent unsteady flow is more likely to occur at low advance coefficients, for example, due to periodic flow separations. The steady flow assumption is therefore less appropriate under these operating conditions.

Domain Uncertainty

For external flow the distance from the objective of interest to the boundaries of the domain should be large enough. This is in order to ensure that the boundary conditions do not influence the solution. To assess if appropriate domain dimensions have been chosen, the uncertainty due to the chosen domain dimensions is determined at an advance coefficient of 0.6 and at

zero pitch displacement. The domain uncertainty is determined using the finest mesh used to determine the spatial discretization uncertainty. Three parameters are used to define the domain of the simulations. These three parameters are: the distance from the propeller plane to the inlet (L_f), the distance from the propeller plane to the outlet (L_b) and the radius of the domain (L_r). To determine the domain uncertainty the simulation is made for different domain sizes. The domain parameters are varied one at a time. The other domain parameters are set to the previously mentioned domain sizes. The different domain parameters are varied as:

$$\mathbf{L_x} = D_p \begin{bmatrix} 2 & 3 & 4 & 5 & 5.5 & 6 & 8 & 10 & 12 & 14 & 16 & 20 & 25 & 30 \end{bmatrix} \quad \text{(D.6)}$$

D_p is the propeller diameter which is 5.4 [m] for the case considered. $\mathbf{L_x}$ is the vector containing the dimension lengths used to determine the domain uncertainty. In order to determine the domain uncertainty in a similar manner as the uncertainties determined in Appendix C, a domain error is defined as:

$$\epsilon_{\phi_i} \approx \delta_d = \phi_i - \phi_0 = \alpha\, e^{-p(L_x - \beta_d)} \quad \text{(D.7)}$$

ϵ_{ϕ_i} is the domain error of the i'th simulation. δ_d is the approximation of the domain error. ϕ_i is the i'th simulated value of interest where ϕ_0 is its true/exact value. α is the error gain. p is the domain convergence rate. L_x is the size of the domain parameter considered which can be either L_f, L_b or L_r. β_d is an exponential offset coefficient. The coefficients ϕ_0, α, p and β are determined by a least-squares fit of the exponential function to the simulation data. This least-squares fit is made with and without weighting of the simulation data. The weight vector is made such that simulations with the larger dimensions are weighted more. The weight vector is determined as:

$$\mathbf{w} = \frac{\mathbf{L_x}}{\sum \mathbf{L_x}} \quad \text{(D.8)}$$

$\mathbf{w}$ is the weight vector. The least-squares fit with the lowest standard deviation is used to approximate the domain error. The approximated domain error for the three domain parameters for the hydrodynamical loads are shown in Figure D.5.

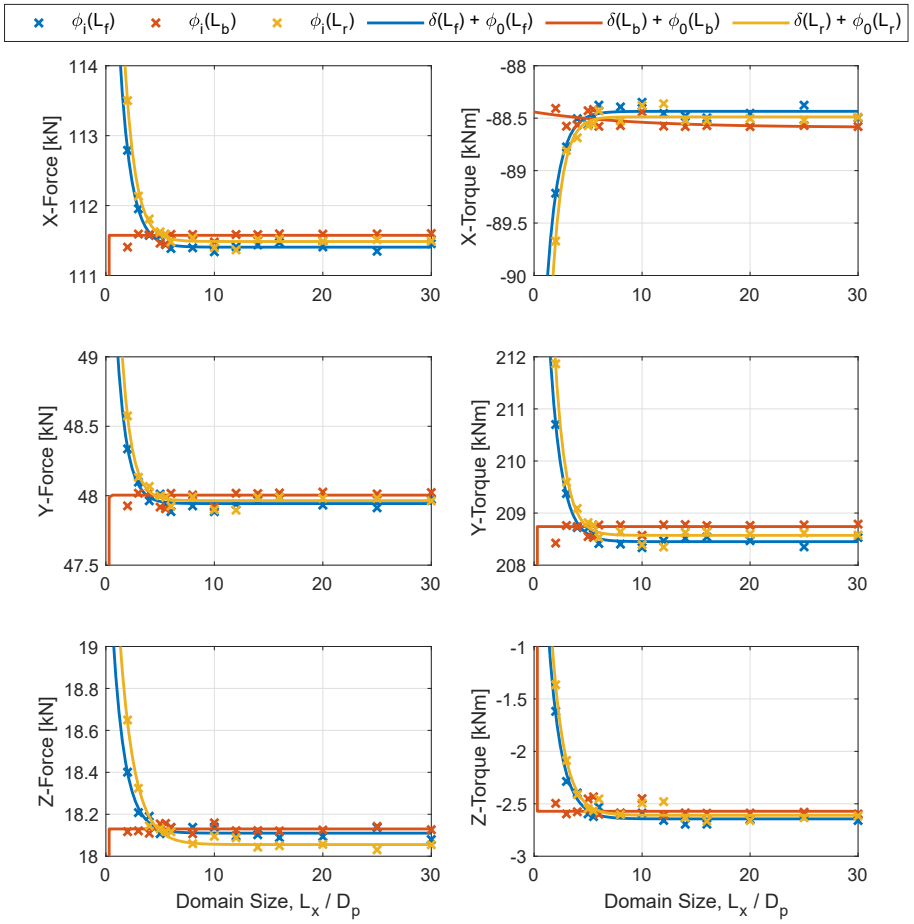

Figure D.5: Domain error approximation for the hydrodynamical loads. The x-axis is defined in relation to D_p as the vector in Eq. D.6. In the legend the simulation values ϕ_i and approximated $\delta + \phi_0$ are shown for each domain variation L_f, L_b and L_r given in the brackets.

From Figure D.5 it is seen that the distance, between the inlet and the propeller plane and the radius of the domain, has the largest influence on the solution at small distances. The distance between the propeller plane and the outlet does not seem to change the results significantly and the changes in the results are due to scatter in the data.

The domain uncertainty due to each of the domain parameters is determined as:

$$U_{dom} = \left|\epsilon_{\phi_i}\right| + 2\,\sigma_i \tag{D.9}$$

U_{dom} is the domain uncertainty and is determined for each of the domain parameters as U_{dom,L_f}, U_{dom,L_b} and U_{dom,L_r}. σ is the standard deviation from the least-squares fit for the corresponding domain parameter. The total domain uncertainty, U_{Dom}, is determined, using Eq. D.10, under the assumption that the uncertainties are independent.

$$U_{Dom} = \sqrt{\sum_{j}^{L_f,L_b,L_r} U_{dom,j}^2} \tag{D.10}$$

Evaluating the total domain uncertainty for the domain used in the open-water simulations gives the uncertainties in Table D.1. The total domain uncertainties in Table D.1 are reasonable, but the relative uncertainty of the torque about the z-axis is large because this torque is close to zero.

Table D.1: Total domain uncertainty for the used domain in the open-water CFD simulations.

	F_x	F_y	F_z	M_x	M_y	M_z
Uncertainty	248 N	219 N	146 N	441 Nm	123 Nm	386 Nm
Relative	0.22 %	0.25 %	0.30 %	0.21 %	0.68 %	15.00 %

Spatial Discretization Uncertainty

The spatial discretization uncertainty is determined for the open-water simulation with zero pitch displacement. The uncertainty is determined according to the procedure described in Appendix C using five different meshes. Each of the meshes are defined relative to a base size which is coarsened with $\sqrt{2}^n$, where n is an integer value between 0 to 4. The value of n is used to note the spatial discretization. The number of cells in each mesh is given in Table D.2 and a section of the different meshes is shown in Figure D.6. The open-water simulation results are shown in Figure D.7 for all the hydrodynamical loads and for all the meshes.

Table D.2: Number of cells in each of the meshes shown in Figure D.6 [30].

n	**Number of cells**
0	$\approx$ 2.355.000
1	$\approx$ 1.350.000
2	$\approx$ 910.000
3	$\approx$ 645.000
4	$\approx$ 475.000

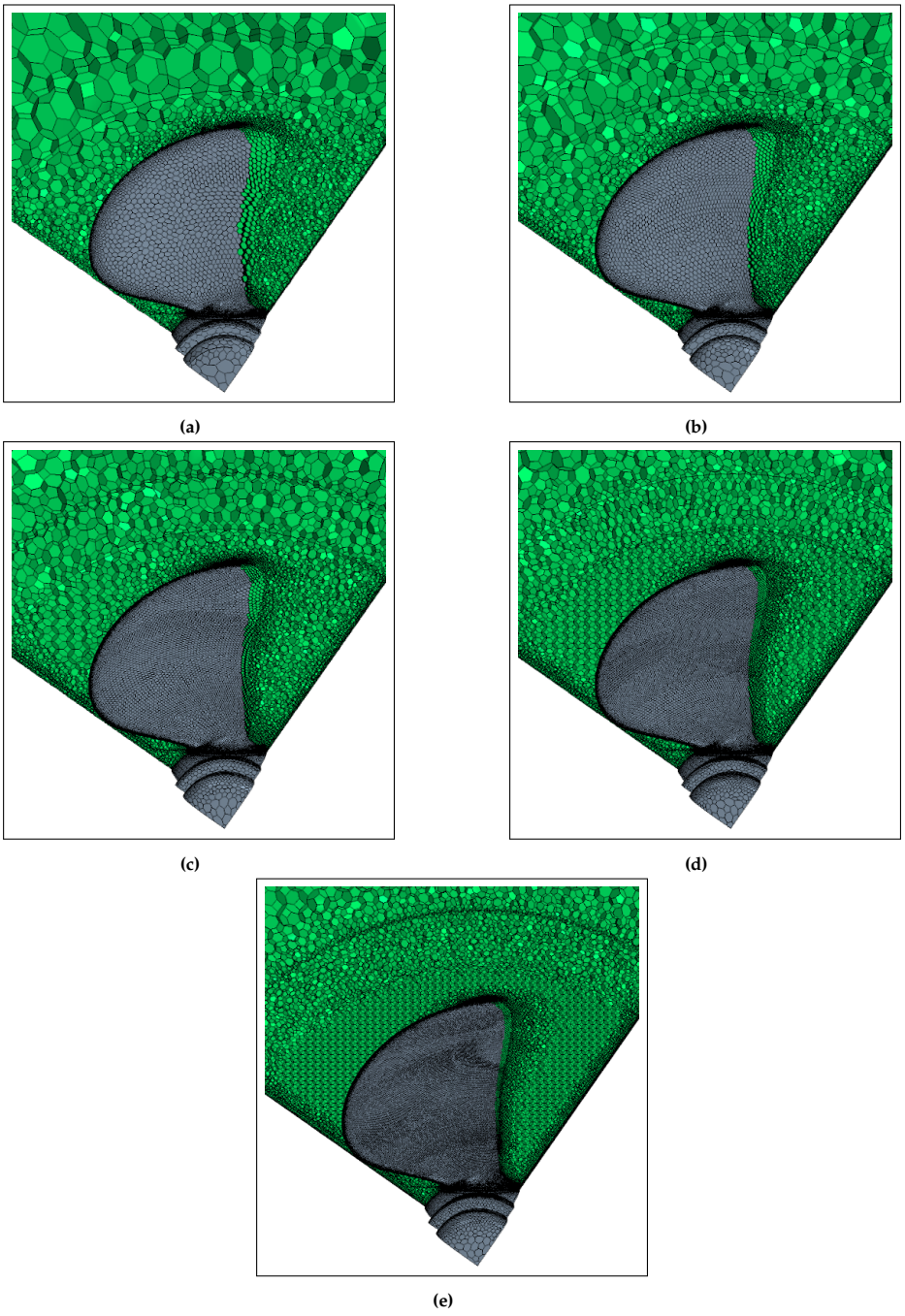

Figure D.6: Mesh at suction side of the propeller. **(a)** $n = 4$. **(b)** $n = 3$. **(c)** $n = 2$. **(d)** $n = 1$. **(e)** $n = 0$.

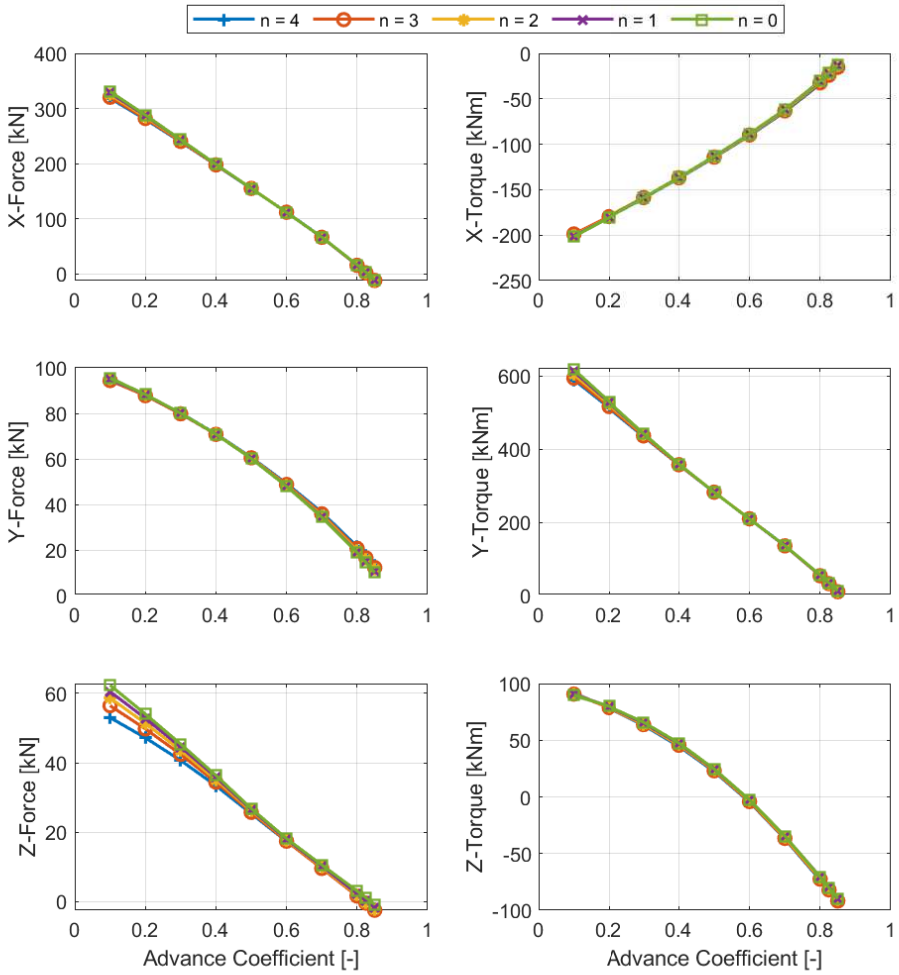

Figure D.7: The open-water hydrodynamical loads acting on the propeller blades at zero pitch displacement for the five different spatial discretizations.

From Figure D.7 it is seen that the hydrodynamical loads acting on the propeller blade do not vary significantly for the different meshes. There is, however, one exception to this, and that is the force along the z-axis. This force deviates for the different meshes as the advance coefficient decreases. Applying the method described in Appendix C.2 to determine the spatial discretization uncertainty for the data in Figure D.7 gives the uncertainty shown in Figure D.8

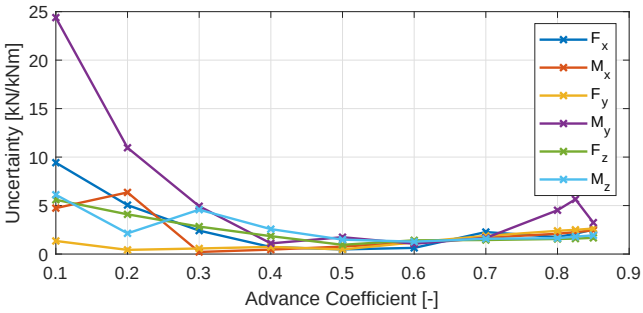

Figure D.8: Spatial discretization uncertainties for the open-water simulations with zero pitch displacement.

From Figure D.8 it is seen that the uncertainty due to spatial discretization is larger than the iterative uncertainty in Figure D.4 and the domain uncertainty. The iterative uncertainty and the spatial discretization uncertainty increases as the advance coefficient decreases. This is probably due to the flow becoming more complex due to, for example, flow separation at the lower advance coefficients.

Total Uncertainty

The iterative uncertainty is determined for each simulation individually. The domain and spatial discretization uncertainty are determined for a limited range of the simulations as described above. This is to reduce the computational costs when determining the uncertainty of the open-water CFD simulations. It is therefore necessary to extrapolate the domain and spatial uncertainty to cover all pitch settings and advance coefficients of the other simulations. The domain and spatial discretization uncertainty are added together, under the assumption that they are independent of each other, as:

$$U_{Dom,spa}(J) = \sqrt{U_{Dom}^2 + U_{spa}(J)^2} \tag{D.11}$$

$U_{Dom,spa}$ is the summed domain and spatial discretization uncertainty. U_{spa} is the spatial discretization uncertainty. Both of these are defined at zero pitch displacement as a function of the advance coefficient. For the extrapolation, the domain and spatial discretization uncertainties are redefined to the relative uncertainty $u_{Dom,spa}(J)$ by normalising with the simulated value. The relative uncertainty is used to avoid unrealistic large or small absolute uncertainties with respect to the exact/true value.

To make the extrapolation, a relative change angle β_c is determined as [30]:

$$\beta_c = \text{atan}\left(\frac{J}{0.7\,\pi}\right) + \Delta P_{rad} \tag{D.12}$$

ΔP_{rad} is the pitch displacement in radians. To make the extrapolation it is assumed that the relative uncertainty only varies with the relative change angle. The relative uncertainty for the simulations at other pitch displacements can thereby be determined by calculating the relative change angle and using linear interpolation to determine the relative uncertainty. If the relative change angle is outside the span determined, then the nearest value is used instead.

The total relative uncertainty is determined by adding the extrapolated relative uncertainty and the relative iterative uncertainty by assuming they are independent and using the L2-norm. For the open-water CFD simulations this gives the uncertainties in Figure D.9. The uncertainty of any of the hydrodynamical loads is determined by interpolating the data in Figure D.9 depending on the blade's pitch displacement and the local advance coefficient.

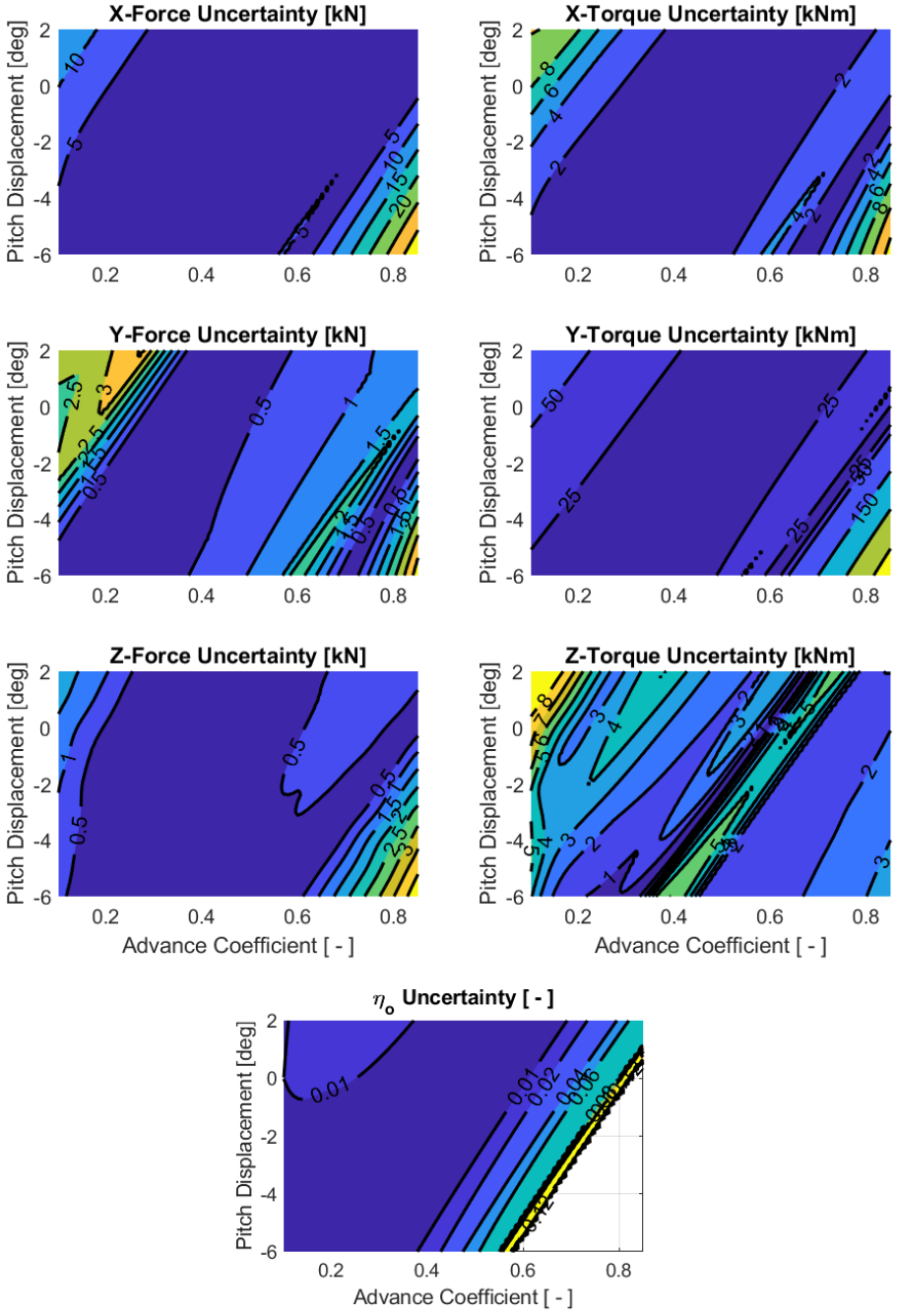

Figure D.9: Uncertainty of the open-water CFD simulations.

D.2 Model for the Local Advance Coefficient

The local advance coefficient is used to interpolate in the open-water simulation results to determine the hydrodynamical loads for the CVP propeller. To determine the local advance coefficient, a local advance velocity for the blade is used. This local advance velocity varies with the blade's position in the wake field, θ_b. Using this local advance velocity the local advance coefficient is determined as [30]:

$$J_{loc}(\theta_b) = \frac{V_{loc}(\theta_b)}{n\, D_p} \tag{D.13}$$

J_{loc} is the local advance coefficient. V_{loc} is the local advance velocity. To determine the local advance velocity, the effective wake field is used which is determined in Section **??** and is shown in Figure D.10.

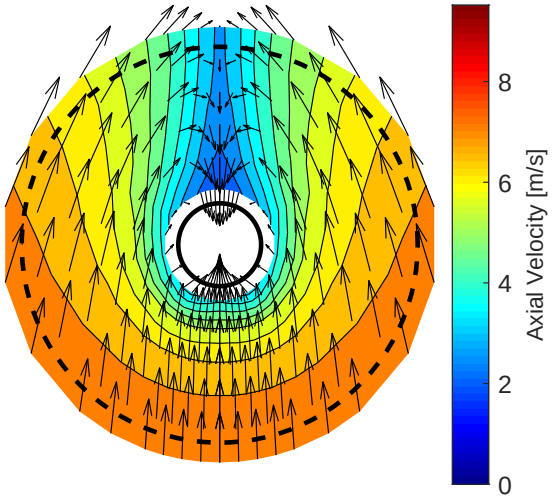

Figure D.10: Effective wake field.

The wake field in Figure D.10 contains the three velocity components but to determine the local advance velocity only the axial velocity component is used. The tangential and radial velocity components are neglected. Four different methods are used to determine the local advance velocity. Later in this report an evaluation is made to determine which one is the most appropriate one to use. The four methods are:

- Average velocity over the blade's spindle axis, $V_{loc,spin}$. Determined as [30]:

$$V_{loc,spin}(\theta_b) = \frac{1}{R_p - r_p} \int_{r_p}^{R_p} v_a(\theta_b, r)\, dr \tag{D.14}$$

- Average velocity over the blade's area, $V_{loc,area}$. Determined as [30]:

$$V_{loc,avg}(\theta_b) = \frac{\int_{r_p}^{R_p} \int_{\theta_{TE}(r)}^{\theta_{LE}(r)} v_a(\theta_b + \theta, r)\, r\, d\theta\, dr}{\int_{r_p}^{R_p} \int_{\theta_{TE}(r)}^{\theta_{LE}(r)} r\, d\theta\, dr} \tag{D.15}$$

- Average velocity over the blade's leading edge, $V_{loc,LE}$. Determined as:

$$V_{loc,LE}(\theta_b) = \frac{1}{R_p - r_p} \int_{r_p}^{R_p} v_a(\theta_b + \theta_{LE}(r), r)\, dr \tag{D.16}$$

- Average velocity over the blade's skew line, $V_{loc,skew}$. Determined as:

$$V_{loc,skew}(\theta_b) = \frac{1}{R_p - r_p} \int_{r_p}^{R_p} v_a(\theta_b + \theta_{skew}(r), r)\, dr \tag{D.17}$$

R_p and r_p are the outer and inner most radius of the propeller blade. $v_a(\theta_b, r)$ is the local axial velocity of the effective wake field shown in Figure D.10. r is the radius. $\theta_{LE}(r)$ and $\theta_{TE}(r)$ are the radial varying angle between the spindle axis and the leading and trailing edge, respectively. $\theta_{skew}(r)$ is the radially varying angle between the spindle axis and the skew line.

The above four methods for determining the local advance coefficient are used in Eq. D.13 to determine the local advance coefficient. The resulting local advance coefficient is shown in Figure D.11. The local advance coefficient is determined using a radially varying Fourier series of the effective wake field.

Three of the four methods depend on the pitch of the blade. These are the blade area, leading edge line and skew line methods. The local advance coefficient shown in Figure D.11 is for the blade at zero pitch displacement, and the variation in the local advance coefficient due to the pitch displacement of the blade is shown as shaded areas. The maximum relative difference in the local advance coefficient due to the pitch displacement is 2.5% for the leading edge model at the blade position equal to 180°. For the blade area and skew line the maximum relative difference is below 1%.

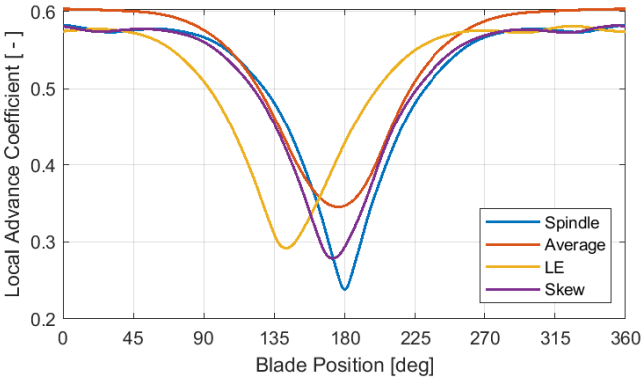

Figure D.11: The local advance coefficient for the blade depending on its position in the wake field.

D.3 Application and Comparison of CVP Propeller Model

The hydrodynamical loads are determined by interpolating the open-water CFD simulation results in Figure D.3 and its uncertainties in Figure D.9 as a function of the blade's pitch displacement in Figure D.2 and the local advance coefficient in Figure D.11. Both the blade pitch displacement and the local advance coefficient depend on the blade's position in the wake field.

To evaluate the performance of using the open-water CFD simulations to model the hydrodynamical loads acting on the CVP propeller blades, the loads are compared to the hydrodynamical loads determined in Appendix A. The comparison is made for each of the three pitch trajectories shown in Figure D.2 and for each of the four local advance coefficient models in Figure D.11. When evaluating the local advance coefficient, the variation due to the blade pitch displacement is included. The hydrodynamical loads for the constant, cosine and variable pitch trajectories are shown in Figure D.12, Figure D.13 and Figure D.14, respectively, for the four local advance coefficient models and the URANS CFD simulations from Appendix A. Note that the open-water CFD simulations do not include the buoyancy load. The buoyancy load from the water determined in Chapter 2 is therefore added to the results presented for the hydrodynamical loads.

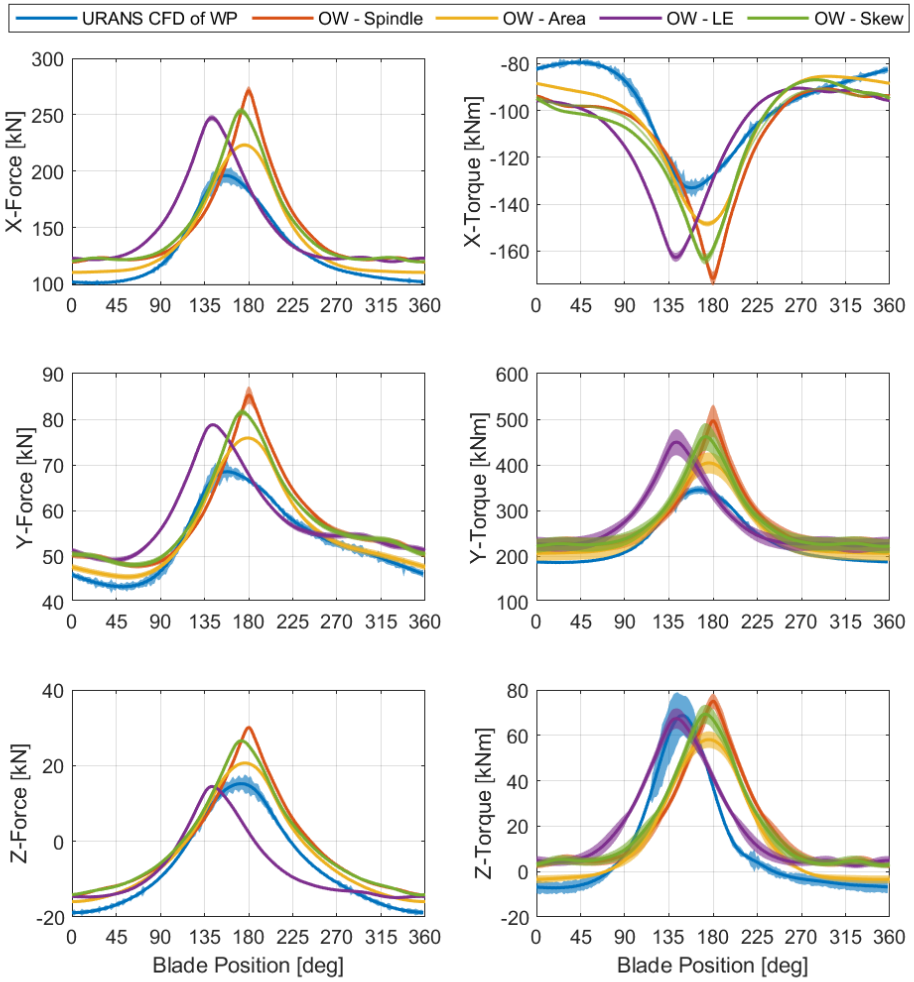

Figure D.12: Comparison of the hydrodynamical loads between the open-water models and the URANS CFD simulation for the constant pitch trajectory. The uncertainty is shown as the shaded areas.

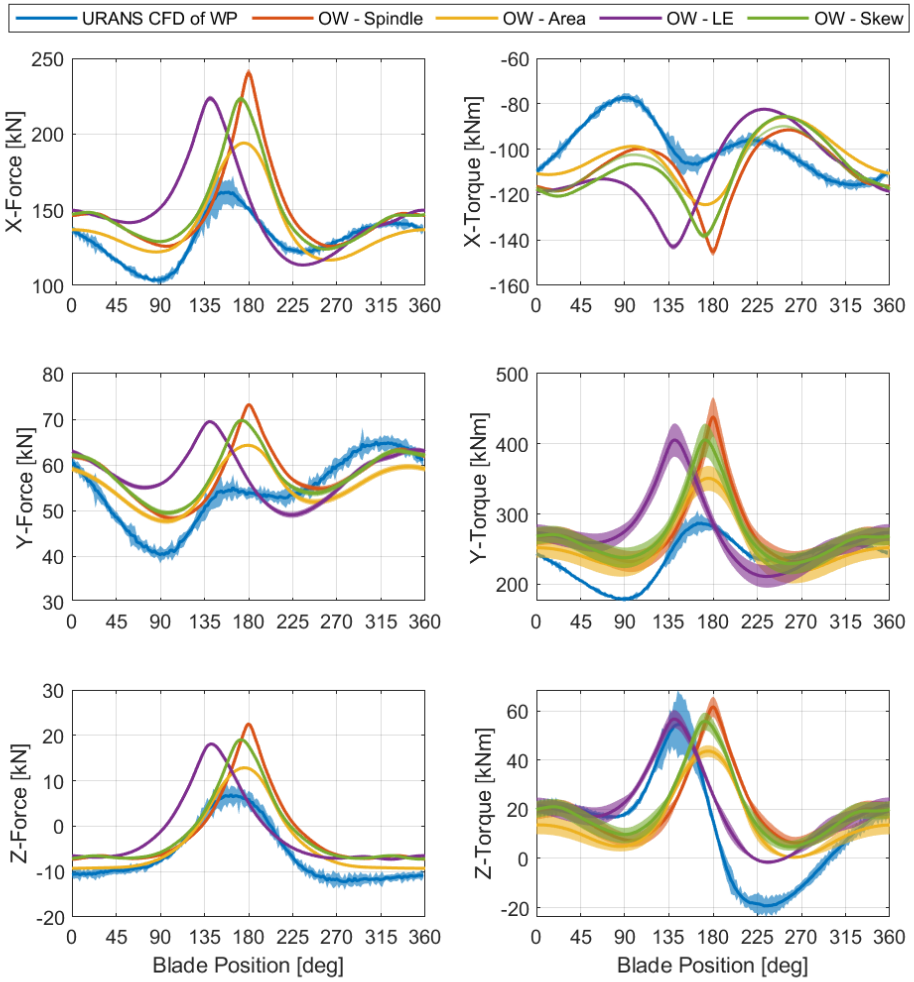

Figure D.13: Comparison of the hydrodynamical loads between the open-water models and the URANS CFD simulation for the cosine pitch trajectory. The uncertainty is shown as the shaded areas.

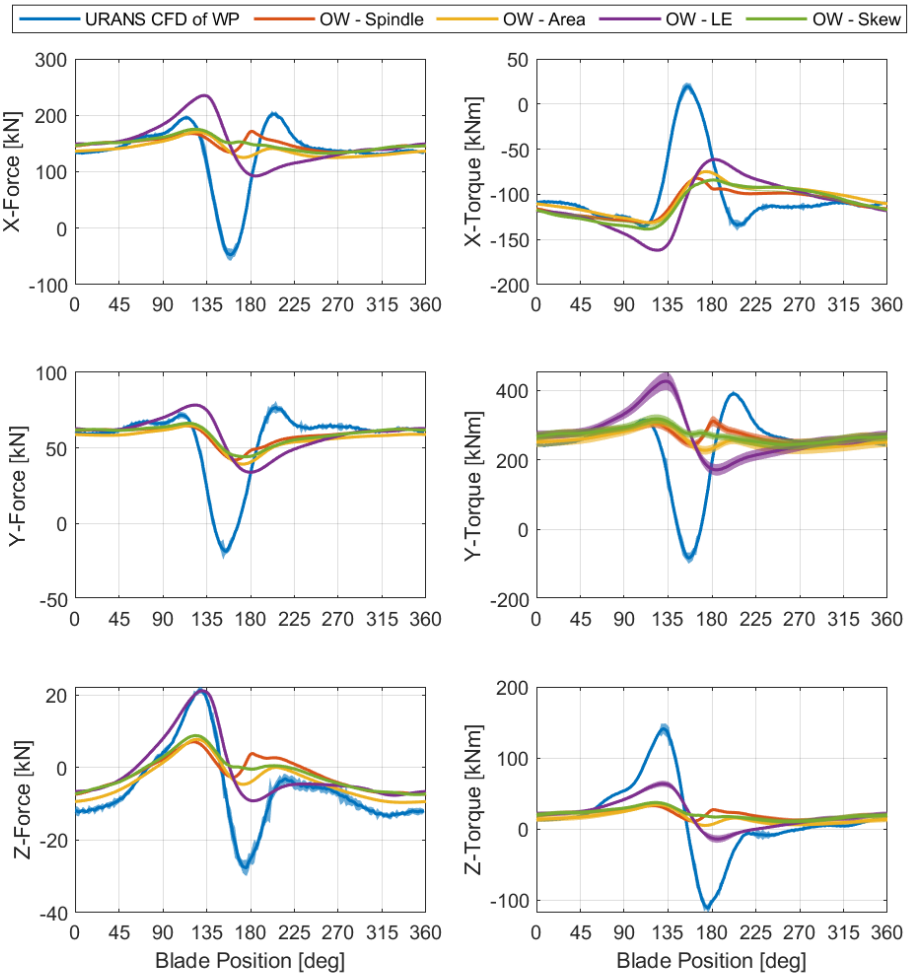

Figure D.14: Comparison of the hydrodynamical loads between the open-water models and the URANS CFD simulation for the variable pitch trajectory. The uncertainty is shown as the shaded areas.

Considering the comparison made for the URANS CFD simulation of the CVP propeller and the open-water models of the CVP propeller in Figure D.12, Figure D.13 and Figure D.14, it is seen that the best correspondence is found for the constant pitch trajectory, followed by the cosine pitch trajectory and then the variable pitch trajectory. This is properly due to the inherent quasi-steady assumption ensuing from the use of the open-water simulation to determine the hydrodynamical loads for the CVP propeller. This assumption does not account for the dynamics due to the pitch trajectory. As the problem becomes more dynamic, with the inclusion of the pitch trajectories,

the correspondence between the open-water models and the URANS CFD simulations decreases.

Another aspect of the poor correspondence could be that different wake fields are used in the two investigations. The modelling of the CVP propeller using the open-water CFD simulations is based on using the measured effective wake field. It is not possible to implement this exact wake field in the URANS CFD simulation of the CVP propeller due to viscous effects. This results in an error in the wake field, as shown in Section A.2. To determine if this is the case, the open-water models of the CVP propeller are carried out again, but where the local advance coefficient is determined using the wake field used in the URANS CFD simulation of the CVP propeller in Appendix A. To compare these different model results the root-mean-square error, e, is determined for each load for the open-water models with respect to the load from the URANS CFD simulation as:

$$e_i = \sqrt{\sum_{\theta_b=0}^{2\pi} \left(L_{i,hydro,OW}(\theta_b) - L_{i,hydro,CFD}(\theta_b) \right)^2} \tag{D.18}$$

$L_{i,hydro,OW}$ is the hydrodynamical load determined using one of the open-water models for the i'th load. $L_{i,hydro,CFD}$ is the corresponding hydrodynamical load determined in the URANS CFD simulation of the CVP propeller. The root-mean-square error determined for each of the open-water models, using the measured and simulated wake field, is shown in Figure D.15 for each of the three pitch trajectories.

From Figure D.15 the general tendency is that the open-water models using the simulated wake field gives a lower root-mean-square error than the open-water models using the measured wake field. This is not surprising since all the open-water models tend to overestimate the variation in the hydrodynamical loads for the constant and cosine pitch trajectory seen in Figure D.12 and Figure D.13. This is also seen from the open-water model that tends to give the lowest root-mean-square error for the constant and cosine pitch trajectory. This is the open-water model that determines the local advance coefficient using the average advance velocity over the whole blade i.e. its area. The exception for this is for the torque about the z-axis where the leading edge model is the best.

For the variable pitch trajectory, the spindle and area open-water models are similar to each other for the loads F_x, M_x, F_y and M_y. But the open-water model using the spindle line generally gives the lowest root-mean-square error except for the loads F_z and M_z where the leading edge model gives the lowest root-mean-square error.

If one open-water model should be chosen to determine the performance of the CVP propeller, then the open-water model that uses the blade area

average advance velocity is the best, especially with respect to predicting the thrust and torque for the propeller and thereby also the efficiency. If the model is to be used to determine the torque about the z-axis then the open-water model using the leading edge is better. It is also possible to use both models to determine the hydrodynamical loads as accurately as possible.

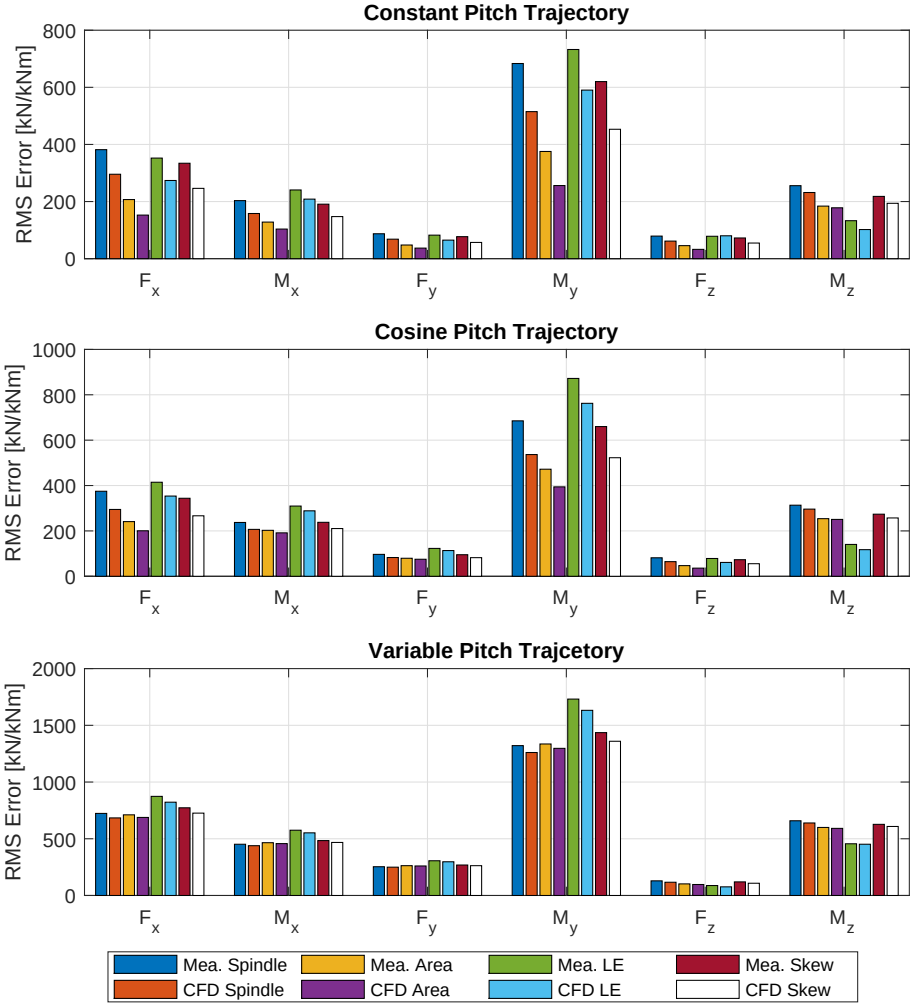

Figure D.15: Root-mean-square error of the different open-water models for each of the hydrodynamical loads and for each pitch trajectory using the measured and CFD simulated wake field.

Considering the predicted hydrodynamical loads of the CVP propeller using the open-water model it is generally seen that the variations in the loads are reduced for the CVP propeller. The mean value and the maximum

variation in the hydrodynamical loads are shown in Table D.3 when the local advance coefficient is determined using the blade area average open-water model for the simulated wake field.

Table D.3: Comparison of the average and maximum variation blade forces and torques for the different pitch trajectories. $\hat{\Delta}$ is the maximum variation in the forces or torques during one revolution of the propeller.

		Constant	**Cosine**	**Variable**
F_x [kN]	Avg.	134.9 ± 0.8 $\pm 0.6\%$	134.6 ± 0.7 $\pm 0.5\%$	134.7 ± 0.6 $\pm 0.5\%$
	$\hat{\Delta}$	106.9 ± 2.3 $\pm 2.1\%$	70.0 ± 1.4 $\pm 2.0\%$	50.9 ± 1.2 $\pm 2.4\%$
M_x [kNm]	Avg.	-101.5 ± 0.6 $\pm 0.6\%$	-101.3 ± 0.6 $\pm 0.6\%$	-102.3 ± 0.6 $\pm 0.6\%$
	$\hat{\Delta}$	59.9 ± 1.3 $\pm 2.2\%$	35.2 ± 1.0 $\pm 2.7\%$	58.6 ± 1.2 $\pm 2.0\%$
F_y [kN]	Avg.	54.2 ± 0.6 $\pm 1.0\%$	54.2 ± 0.6 $\pm 1.0\%$	54.8 ± 0.6 $\pm 1.0\%$
	$\hat{\Delta}$	29.3 ± 0.9 $\pm 3.1\%$	15.3 ± 0.9 $\pm 5.7\%$	26.4 ± 0.9 $\pm 3.2\%$
M_y [kNm]	Avg.	248.8 ± 16.1 $\pm 6.5\%$	247.8 ± 14.7 $\pm 5.9\%$	247.6 ± 13.8 $\pm 5.6\%$
	$\hat{\Delta}$	185.8 ± 38.1 $\pm 20.5\%$	120.0 ± 31.8 $\pm 26.5\%$	91.7 ± 25.6 $\pm 27.9\%$
F_z [kN]	Avg.	-4.3 ± 0.2 $\pm 4.1\%$	-4.6 ± 0.1 $\pm 2.5\%$	-4.5 ± 0.1 $\pm 2.1\%$
	$\hat{\Delta}$	35.3 ± 0.3 $\pm 0.9\%$	20.9 ± 0.1 $\pm 0.4\%$	17.5 ± 0.1 $\pm 0.8\%$
M_z [kNm]	Avg.	11.1 ± 0.1 $\pm 0.7\%$	11.6 ± 2.0 $\pm 17.3\%$	12.1 ± 2.5 $\pm 20.8\%$
	$\hat{\Delta}$	60.4 ± 0.1 $\pm 0.2\%$	40.3 ± 1.5 $\pm 3.6\%$	32.2 ± 1.7 $\pm 5.2\%$

From Table D.3 it is seen that the cosine and variable pitch trajectory reduce the amplitude in the load variations when compared to the constant pitch trajectory. This is one of the benefits of using a CVP propeller. The average loads are generally the same for all the pitch trajectories. The efficiency of the propeller should therefore not change significantly for the different pitch trajectories. The efficiency of the propeller blades using the open-water models is determined as:

$$\eta_p = \frac{T_b \, D_p}{Q_b} \, \frac{J_{loc,avg}}{2 \, \pi} \tag{D.19}$$

T_b is the average blade thrust. Q_b is the average blade torque about the x-axis. $J_{loc,avg}$ is the average local advance coefficient. Using the values in Table D.3 gives the efficiencies in Table D.4 for each pitch trajectory.

Table D.4: The propeller efficiency for different pitch trajectories using the open-water model for the CVP propeller

	Constant	**Cosine**	**Variable**
η_p	$0.6303 \begin{matrix}\pm 0.0070 \\ \pm 1.12\%\end{matrix}$	$0.6300 \begin{matrix}\pm 0.0065 \\ \pm 1.03\%\end{matrix}$	$0.6248 \begin{matrix}\pm 0.0065 \\ \pm 1.04\%\end{matrix}$

From Table D.4 it is seen that the change in efficiency is within the uncertainty bounds. But the efficiency for the variable pitch trajectory is lower than the efficiency for the other pitch trajectories. The relationship between the efficiency for the different pitch trajectories is similar to those found in Appendix A.

In conclusion, it is doubtful how applicable these open-water models are to determine the hydrodynamical loads for the CVP propeller. This is generally due to the inherent quasi-steady nature of the models, and this results in overestimating the load variation for the constant pitch trajectory where the dynamics due to the flow change are not accounted for. For the cosine and variable pitch trajectories this becomes even more prominent where the shape of the hydrodynamical loads diverges even more from the URANS CFD simulation. This is due to the quasi-steady nature of the open-water model which do not account for the pitch motion.

Appendix E

Hydrodynamic Modelling of CVP Propeller Through Unsteady Foil Theory

Instead of using the computationally costly CFD simulation, to determine the hydrodynamical loads acting on the CVP propeller blades, it is desired to make a more computationally efficient model. A number of different methods exist to compute a propeller's quasi-steady performance and unsteady performance in a non-uniform wake field, which has been the primary consideration in propeller analysis so far. In the analysis of the CVP propeller performance it is also necessary to consider the unsteadiness due to the pitch motion of the propeller blades. Many of the existing methods to analyse the propeller performance assume potential flow and may compensate for the viscosity. Potential flow satisfies Laplace's equation, which is a linear partial differential equation and this means that the different solutions can be added together to solve more complex flow problems. This is shown in Figure E.1 for a foil inclined to a flow. The inclined foil can under the assumption of potential flow be decomposed into a thickness, inclined flat plate and a chamber flow problem as shown in Figure E.1 [19].

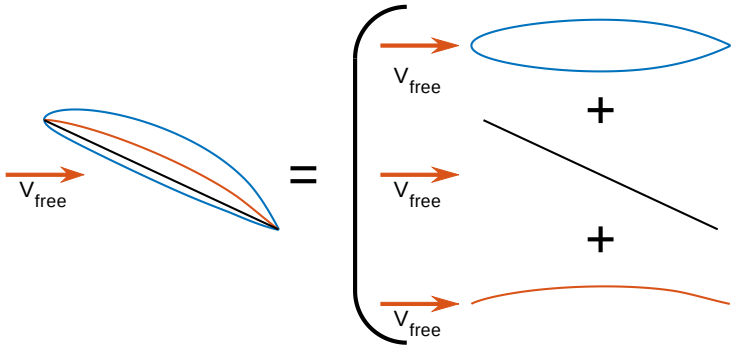

Figure E.1: Decomposition of the potential flow around an inclined foil in a steady flow field.

The same principle can be utilized for an unsteady moving foil operating in a varying flow field. The unsteady foil and the decomposition of the problem is shown in Figure E.2.

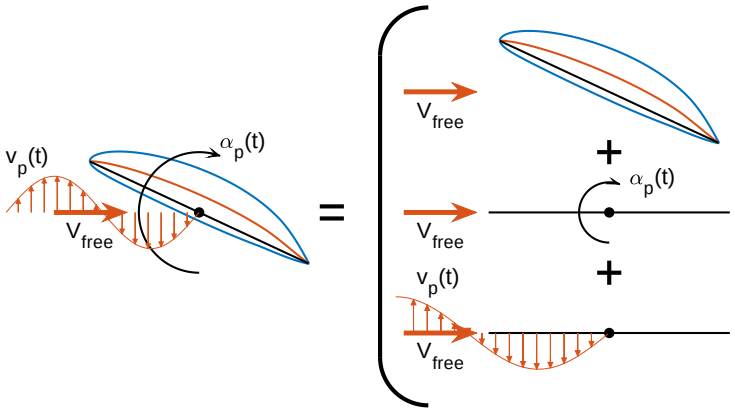

Figure E.2: Decomposition of the potential flow around a foil in unsteady operation.

Figure E.2 shows two sources of unsteadiness. The unsteadiness due to the pitching motion and the unsteadiness due to a varying flow component perpendicular to the free stream velocity, also called a gust. The unsteady response of the foil due to an unsteady pitch motion and unsteady perpendicular gust have been solved analytically by Theodore Theodorsen and William R. Sears in the frequency domain and by Herbert A. Wagner and Hans G. Küssner in the time domain The methods are described in [15, 38, 62, 92], amongst others. For the application of these theories to the CVP propeller, the frequency domain solution is convenient to use when the pitch trajectory and gust are known. It is therefore well suited for the inverse rigid body dynamic modelling made in Chapter 2. The time domain solution is instead

more suited if the system should be modelled using traditional rigid body dynamics.

In the modelling of the hydrodynamical loads acting on the CVP propeller blades in this appendix only the unsteady modelling will be considered. The steady solution is not considered but could be determined by using a lifting line, amongst others. Using a lifting line method would include the induced velocities which are therefore not included in this analysis.

This appendix is divided into three sections:

- Section E.1 presents how the wake field is decomposed into its steady and unsteady components such that the decomposition of the problem can be made, as shown in Figure E.2.
- Section E.2 presents a number of different models to determine the unsteady hydrodynamical loads acting on the CVP propeller blades. Firstly, a model is presented which determines the unsteady loads based on theories assuming an infinite aspect ratio for the propeller blades. Secondly, this model is adapted to compensate for the finite aspect ratio of the propeller blades.
- Section E.3 applies the different derived models in Section E.2 on the case considered in Chapter 2. The hydrodynamical response of the different models is presented for the three pitch trajectories considered in Chapter 2 and it is concluded which model is the most appropriate one to model the hydrodynamicals of the CVP propeller blades.

E.1 Decompositions of Wake Field Velocities

To determine the hydrodynamical loads using unsteady foil theory it is necessary to split the wake field velocities into their steady and unsteady components. It is thereby possible to decompose the flow into a steady and unsteady flow as shown in Figure E.2. The decomposition of the wake field velocities is shown in Figure E.3. The radial velocity component is neglected because the unsteady foil theories, applied later, do not account for it.

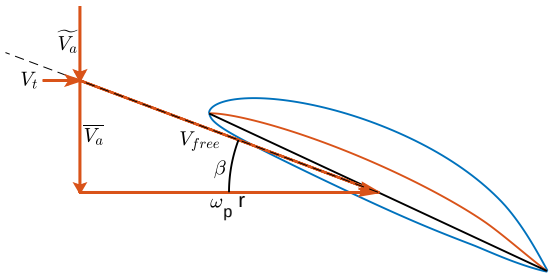

Figure E.3: Decomposition of the wake field velocity components for the flow around the foil.

In Figure E.3 the steady velocity triangle consists of the steady axial velocity component, $\overline{V_a}$, and the steady velocity component due to the propeller rotation $\omega_p\, r$. The resulting steady free stream velocity, V_{free}, formed by these two velocities is inclined at the steady advance angle β to the propeller plane. The unsteady wake field velocity components consist of the unsteady axial velocity, $\widetilde{V_a}$, and the tangential velocity component, V_t. For the wake field of a ship, the steady velocity components only vary with the radius whereas the unsteady velocity components also vary with the position in the wake field, θ_b. To determine these velocity components, the wake field velocities are described with a Fourier series as:

$$v_a(r,\theta_b) = \underbrace{a_a(r,0)}_{\overline{V_a}(r)} + \underbrace{\sum_{n=1}^{N} a_a(r,n)\, \cos\left(n\,\theta_b\right)}_{\widetilde{V_a}(r,\theta_b)} \tag{E.1}$$

$$v_t(r,\theta_b) = \sum_{n=1}^{N} b_t(r,n)\, \sin\left(n\,\theta_b\right) \tag{E.2}$$

$v_a(r,\theta_b)$ is the axial velocity distribution in the wake field. $a_a(r,n)$ is the even Fourier series coefficients for the approximation of the axial velocity distribution. The even Fourier series is used because the wake field considered is assumed to be symmetric for a single screw vessel. $v_t(r,\theta_b)$ is the tangential velocity distribution in the wake field. $b_t(r,n)$ is the odd Fourier series coefficients for the approximation of the tangential velocity distribution. The odd Fourier series is used because the wake field is assumed to be symmetric. The tangential velocity component is therefore zero at $\theta_b = 0$ and π. The Fourier series coefficients are determined by least-squares approximation to the wake field velocities. The wake field used is the effective wake field determined in Section **??** under the operating conditions of the propeller specified in Chapter 2. The resulting decomposition of the wake field velocity components is shown in Figure E.4. The effective wake field used is shown in Figure E.4a. The steady axial velocity is shown in Figure E.4b. The unsteady axial and tangential velocities are shown in Figure E.4c and Figure E.4d, respectively.

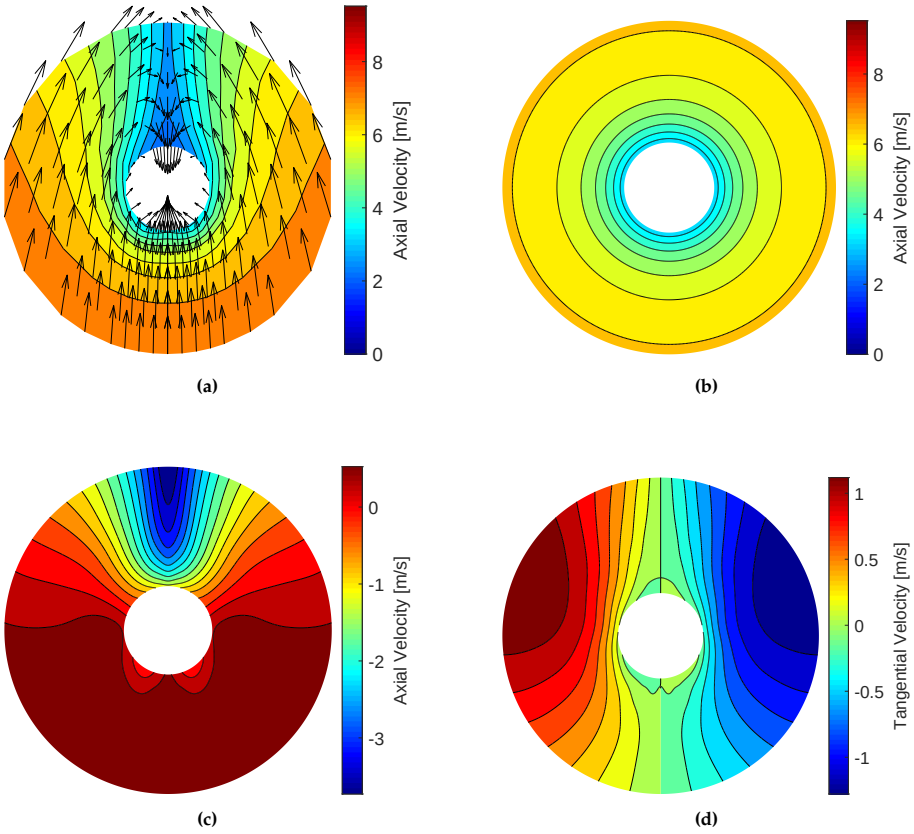

Figure E.4: Decomposition of wake field. **(a)** Effective measured wake field. **(b)** Steady axial wake field velocity, $\overline{V_a}(r)$. **(c)** Unsteady axial wake field velocity, $\widetilde{V_a}(r, \theta_b)$. **(d)** Unsteady tangential wake field velocity, $v_t(r, \theta_b)$.

The unsteady velocities determined from the decomposition of the wake field must be reformulated before they can be used in the models presented later. As shown in Figure E.2 the unsteady velocity must be defined as a perpendicular gust velocity, w_g, with respect to the free stream velocity. This is shown for the velocity decomposition considered in Figure E.5. From Figure E.5 it is seen that this results in another parallel gust velocity, v_g, with respect to the free stream velocity.

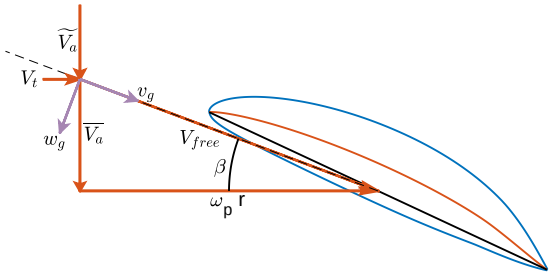

Figure E.5: Unsteady gust velocities parallel and perpendicular to the free stream velocity.

The free stream velocity, perpendicular gust velocity and the parallel gust velocity are determined as:

$$V_{free}(r) = \sqrt{\left(\omega_p\, r\right)^2 + \overline{V_a}(r)^2} \tag{E.3}$$

$$w_g(r,\theta_b) = \widetilde{V_a}(r,\theta_b)\, \cos\left(\beta(r)\right) - v_t(r,\theta_b)\, \sin\left(\beta(r)\right) \tag{E.4}$$

$$v_g(r,\theta_b) = \widetilde{V_a}(r,\theta_b)\, \sin\left(\beta(r)\right) + v_t(r,\theta_b)\, \cos\left(\beta(r)\right) \tag{E.5}$$

Where,

$$\beta(r) = \arctan\left(\frac{\overline{V_a}(r)}{\omega_p\, r}\right) \tag{E.6}$$

The gust velocities can also be represented as a Fourier series by inserting Eq. E.1 and Eq. E.2 into Eq. E.4 and Eq. E.5 as:

$$\begin{aligned} w_g(r,\theta_b) &= \widetilde{V_a}(r,\theta_b)\, \cos\left(\beta(r)\right) - v_t(r,\theta_b)\, \sin\left(\beta(r)\right) \\ &= \cos\left(\beta(r)\right) \sum_{n=1}^{N} \left(a_a(r,n)\, \cos\left(n\,\theta_b\right)\right) \\ &\quad - \sin\left(\beta(r)\right) \sum_{n=1}^{N} \left(b_t(r,n)\, \sin\left(n\,\theta_b\right)\right) \\ &= \sum_{n=1}^{N} \underbrace{a_a(r,n)\, \cos\left(\beta(r)\right)}_{a_w(r,n)} \cos\left(n\,\theta_b\right) + \underbrace{\left(-\sin\left(\beta(r)\right) b_t(r,n)\right)}_{b_w(r,n)} \sin\left(n\,\theta_b\right) \\ &= \sum_{n=1}^{N} a_w(r,n)\, \cos\left(n\,\theta_b\right) + b_w(r,n)\, \sin\left(n\,\theta_b\right) \end{aligned} \tag{E.7}$$

$$
\begin{aligned}
v_g(r,\theta_b) &= \widetilde{V_a}(r,\theta_b)\ \sin\left(\beta(r)\right) + v_t(r,\theta_b)\ \cos\left(\beta(r)\right) \\
&= \sin\left(\beta(r)\right)\ \sum_{n=1}^{N}\left(a_a(r,n)\ \cos\left(n\,\theta_b\right)\right) \\
&\quad + \cos\left(\beta(r)\right)\ \sum_{n=1}^{N}\left(b_t(r,n)\ \sin\left(n\,\theta_b\right)\right) \\
&= \sum_{n=1}^{N} \underbrace{a_a(r,n)\ \sin\left(\beta(r)\right)}_{a_v(r,n)}\ \cos\left(n\,\theta_b\right) + \underbrace{\left(\cos\left(\beta(r)\right)\, b_t(r,n)\right)}_{b_v(r,n)}\ \sin\left(n\,\theta_b\right) \\
&= \sum_{n=1}^{N} a_v(r,n)\ \cos\left(n\,\theta_b\right) + b_v(r,n)\ \sin\left(n\,\theta_b\right) \qquad \text{(E.8)}
\end{aligned}
$$

The resulting decompositions of the wake field into the free stream, perpendicular gust and parallel gust velocities are shown in Figure E.6.

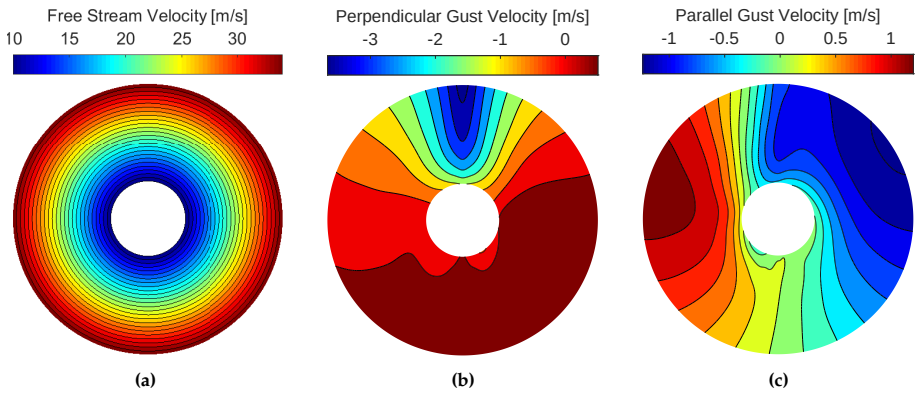

Figure E.6: **(a)** Free stream velocity. **(b)** Perpendicular gust velocity. **(c)** Parallel gust velocity.

From Figure E.6b and Figure E.6c it is seen that the unsteady gust velocities are not symmetric about the vertical plane. This is because the tangential velocity component has opposite signs on each side of the vertical plane.

E.2 Dynamic Modelling of the CVP Propeller Using Unsteady Foil Theory

A number of models are presented in this section which are used to determine the unsteady hydrodynamical loads acting on the CVP propeller blades. The section is divided into four subsections:

- Section E.2.1 describes the modelling of the CVP propeller blades unsteady hydrodynamical loads due to the pitch motion of the blade. The model presented is in the frequency domain and is most appropriately used when the pitch motion is known, as the case considered in Chapter 2.
- Section E.2.2 describes the modelling of the CVP propeller blades unsteady hydrodynamical loads due to the perpendicular gust. The model presented is in the frequency domain and is most appropriately used when the gust variation is known.
- Section E.2.3 presents how the models in Section E.2.1 and Section E.2.2 are adapted to account for the finite aspect ratio of the propeller blades. The models presented in Section E.2.1 and Section E.2.2 are based on the blade having an infinitely large aspect ratio such that the effects due to the third dimension can be neglected. In the adaption of the models the time domain solution is considered because this is what has been considered in most previous literature. The time domain solution is more appropriately used for traditional rigid body dynamic modelling.
- Section E.2.4 discusses the problem with including the parallel gust in the modelling of the CVP propeller blade's hydrodynamical response.

E.2.1 Unsteadiness due to Pitching Motion

The unsteadiness of a moving foil was solved by Theodorsen and Wagner for the frequency and time domain, respectively. For now, only the solution by Theodorsen is considered. The theories assume inviscid, incompressible, two dimensional flow, subjected to small perturbations in the angle of attack and a planar shedded wake extending downstream towards infinity convected at the free stream velocity as shown in Figure E.7.

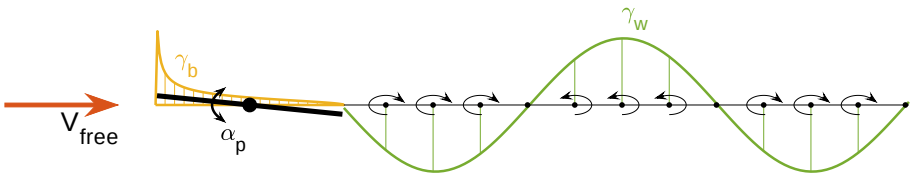

Figure E.7: Principle of Theodorsen and Wagner's assumption for the solution of moving foil in a constant stream. The figure is based on [62].

Theodorsen also includes the response due to a plunging motion of the foil. For the CVP propeller there is no plunge motion of the foil and it is therefore neglected. The frequency solution by Theodorsen gives the lift force, F_L,

and pitch torque about the pitch axis, M_p, per unit span as [15, 62]:

$$F_L = \underbrace{\pi \rho b^2 \left(V_{free} \dot{\alpha} - b\, a\, \ddot{\alpha} \right)}_{\text{Non-circulative}} + \underbrace{2 \pi \rho V_{free} b \left(V_{free} \alpha + b \left(\frac{1}{2} - a \right) \dot{\alpha} \right) C(k)}_{\text{Circulative}} \tag{E.9}$$

$$M_p = \underbrace{\pi \rho b^3 \left(\left(a - \frac{1}{2} \right) V_{free} \dot{\alpha} - b \left(\frac{1}{8} + a^2 \right) \ddot{\alpha} \right)}_{\text{Non-circulative}} + \underbrace{2 \pi \rho V_{free} b^2 \left(\frac{1}{2} + a \right) \left(V_{free} \alpha + b \left(\frac{1}{2} - a \right) \dot{\alpha} \right) C(k)}_{\text{Circulative}} \tag{E.10}$$

ρ is the density of the fluid. b is the half chord ($b = c/2$ where c is the foil chord length). α is the change in angle of attack which for the CVP propeller is equal to the pitch displacement. $\dot{\alpha}$ and $\ddot{\alpha}$ are the rate and acceleration respectively for the angle of attack which for the CVP propeller is equal to the pitch rate and acceleration, respectively. a is the relative position of the pitch axis relative to the mid chord point defined as:

$a = 0$ pitch axis is at the mid chord point
$0 < a < 1$ pitch axis between the mid chord point and the TE
$0 > a > -1$ pitch axis between the mid chord point and the LE

Where,

$$a = \frac{\theta_s\, r}{b} = \frac{l_{skew}}{b} \tag{E.11}$$

θ_s is the skew angle. r is the radial position of the foil section. l_{skew} is the length of the skew along the chord line.

$C(k)$ is Theodorsen's function. Theodorsen's function accounts for the historical effect of the shedded circulation into the wake of the foil as shown in Figure E.7 and is determined as [62]:

$$C(k) = F(k) + iG(k) \tag{E.12}$$

Where,

$$F(k) = \frac{J_1(k)\ (J_1(k) + Y_0) + Y_1\ (Y_1(k) - J_0(k))}{(J_1(k) + Y_0(k))^2 + (J_0(k) - Y_1(k))^2} \tag{E.13}$$

$$G(k) = -\frac{Y_1(k)\, Y_0(k) + J_1(k)\, J_0(k)}{(J_1(k) + Y_0(k))^2 + (J_0(k) - Y_1(k))^2} \tag{E.14}$$

$F(k)$ is the real part of Theodorsen's function. $G(k)$ is the magnitude of the imaginary part of Theodorsen' s function. $J_x(k)$ and $Y_x(k)$ are Bessel functions of the first and second kind, respectively. k is the reduced frequency of the periodic motion and is determined as [62]:

$$k = \frac{\omega_{osc}\, c}{2\, V_{free}} = \frac{n\, \omega_p\, c}{2\, V_{free}} \tag{E.15}$$

ω_{osc} is the frequency of pitch oscillation in $[rad/s]$. If the motion is described by a Fourier series with the fundamental frequency ω_p, then the oscillation frequency for the n'th harmonic is determined as $\omega_{osc} = n\, \omega_p$. The reduced frequency depends on both the geometry of the foil and the flow conditions around it. The reduced frequency is shown in Figure E.8 as a function of the blade radius for each of the harmonics.

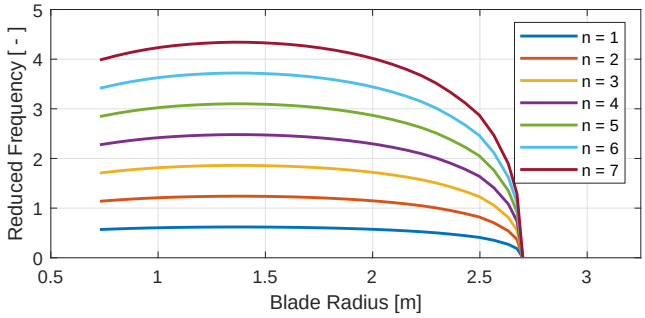

Figure E.8: Reduced frequency of the propeller blade.

The Nyquist and Bode plot of Theodorsen's function are shown in Figure E.9.

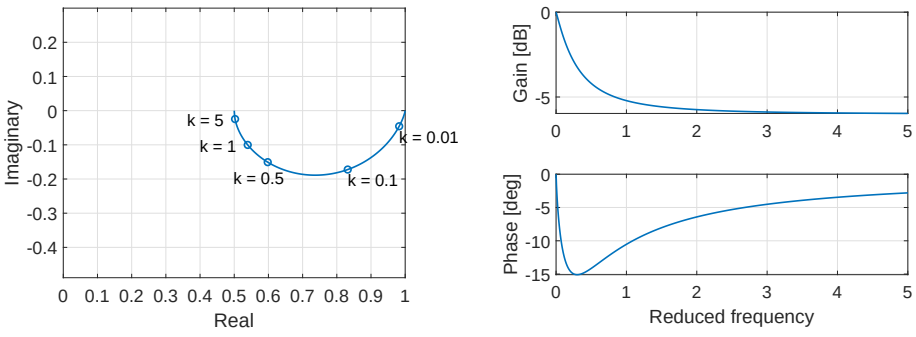

(a) **(b)**

Figure E.9: (a) Nyquist diagram of Theodorsen's function. **(b)** Bode diagram of Theodorsen's function.

From Figure E.9 it is seen that the magnitude of Theodorsen's function decreases as the reduced frequency increases. The magnitude goes toward an asymptote at -6 dB or 0.5 as the reduced frequency goes towards infinity. The phase of Theordorsen's function starts to lag as the reduced frequency increases until it reaches a minimum from which the lag goes towards zero as the reduced frequency goes towards infinite. Considering the reduced frequencies in Figure E.8, which are between 0.5 to 4.5, then it is seen that the gain of Theodorsen's function is between 0.5 to 0.6. This means that the unsteady lift is about 0.5 to 0.6 of the quasi-steady lift.

The expressions for the lift and the pitch torque in Eq. E.9 and Eq. E.10 are divided into two terms, a circulative and a non-circulative term. The circulative term is the one associated with the circulation around the foil and the circulation in the wake. The non-circulative terms are due to the time varying flow creating pressure forces not related to the circulation.

Determining the lift force and pitch torque using Theodorsen's method is only applicable for two-dimensional foils or for infinitely long wings. In the modelling of the CVP propeller Theodorsen's method is applied strip-wise to each radial section of the propeller blade. The parameters that vary radially are the chord length, the skew length and the free stream velocity. The resulting forces and torques acting on the blade are determined by integrating the responses over the whole blade. When integrating the response over all the sections, the forces and torques also needs to be projected to the desired coordinate system. The desired coordinate system is the propeller coordinate system for the blade as described in Section 2.1. The unsteady hydrodynamical forces and torques due to the pitching motion of the propeller blades are

determined as:

$$F_{x,p} = \int_{r_h}^{r_p} F_L(r)\ \cos\left(\beta(r)\right) dr \quad , \quad M_{x,p} = -\int_{r_h}^{r_p} F_L(r)\ \sin\left(\beta(r)\right) r\, dr$$
$$F_{y,p} = \int_{r_h}^{r_p} F_L(r)\ \sin\left(\beta(r)\right) dr \quad , \quad M_{y,p} = \int_{r_h}^{r_p} F_L(r)\ \cos\left(\beta(r)\right) r\, dr$$
$$F_{z,p} = 0 \quad , \quad M_{z,p} = \int_{r_h}^{r_p} M_p(r)\, dr \tag{E.16}$$

The torque about the z-axis determined with Eq. E.16 will overestimate the torque because the equation does not account for the projection of the foil on to the concentric surfaces of the propeller as described in Chapter 1.1.

E.2.2 Unsteadiness due to Perpendicular Gusts

The unsteadiness due to a gust perpendicular to the free stream velocity acting on a flat plate has been solved by Sears and Küssner. Sears and Küssner solved the problem in the frequency and the time domain, respectively. For Sears' solution this means that the perpendicular gust is periodically varying, as shown in Figure E.10. For Küssner the perpendicular gust is a sharp edged gust similar to a step input. Both Sears and Küssner make the same assumption as Theodorson and Wagner made for the solution of the unsteadiness due to a moving flat plate. The assumptions are that the flow is inviscid, incompressible and exposed to small gust disturbances with a planar shedded wake convected at the free stream velocity. The flow problem considered by Sears is sketched in Figure E.10.

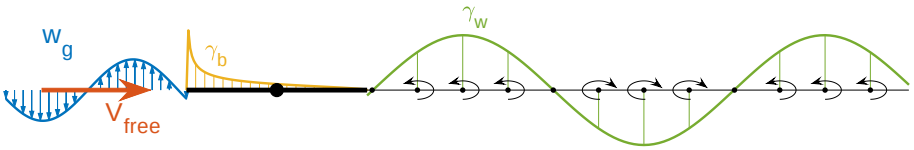

Figure E.10: Principle of the flat plate exposed to a perpendicular oscillating gust considered by Sears. The figure is based on [62].

The lift force and pitch torque per unit span are according to Sears given as [15]:

$$F_L = -2\,\pi\,\rho\,b\,V_{free}\,w_g\,S(k_g) \tag{E.17}$$
$$M_p = F_L\left(\frac{1}{2}+a\right) b$$
$$= -2\,\pi\,\rho\,b^2\,V_{free}\,w_g\left(\frac{1}{2}+a\right) S(k_g) \tag{E.18}$$

w_g is the perpendicular oscillating gust velocity. $S(k_g)$ is Sears' function accounting for the time history due to the shedded circulation into the wake. k_g is the reduced frequency of the gust and is calculated using Eq. E.15. For the CVP propeller k_g is the same as the reduced frequency k used for the oscillating flat plate in Section E.2.1. Sears' function is given as [15, 62]:

$$S(k_g) = \left(J_0(k_g) - i\, J_1(k_g)\right)\, C(k_g) + i\, J_1(k_g) \tag{E.19}$$

$C(k_g)$ is Theodorsen's function evaluated at the reduced frequency of the gust. J_x is the Bessel function of the first kind. Sears' function is applicable when the gust is defined relative to the mid-chord point of the foil. For the propeller the gust is defined relative to the spindle axis instead of the mid-chord line (i.e. skew line). This gives some phase to Sears' function. The phase shifted Sears' functions ($S_s(k_g)$) real and imaginary parts are determine as [62]:

$$\Re\left(S_s(k_g)\right) = \Re\left(S(k_g)\right)\, \cos\left(k_s\right) + \Im\left(S(k_g)\right)\, \sin\left(k_s\right) \tag{E.20}$$

$$\Im\left(S_s(k_g)\right) = -\Re\left(S(k_g)\right)\, \sin\left(k_s\right) + \Im\left(S(k_g)\right)\, \cos\left(k_s\right) \tag{E.21}$$

$\Re\left(S_s\right)$ is the real part of the phase shifted Sears' function. $\Im\left(S_s\right)$ is the imaginary part of the phase shifted Sears' function. S_s is the shifted Sears' function which substitutes $S(k_g)$ in Eq. E.17 and Eq. E.18. k_s is the reduced shift frequency and is determined as:

$$k_s = \frac{\omega_{osc}\, a\, b}{V_{free}} = \frac{n\, \omega_p\, l_{skew}}{V_{free}} \tag{E.22}$$

The Nyquist and Bode plot of Sears' function are shown in Figure E.11a and Figure E.11b, respectively. The plots also include the phase shifted Sears' function, when it is shifted to the leading edge (LE) and the trailing edge (TE).

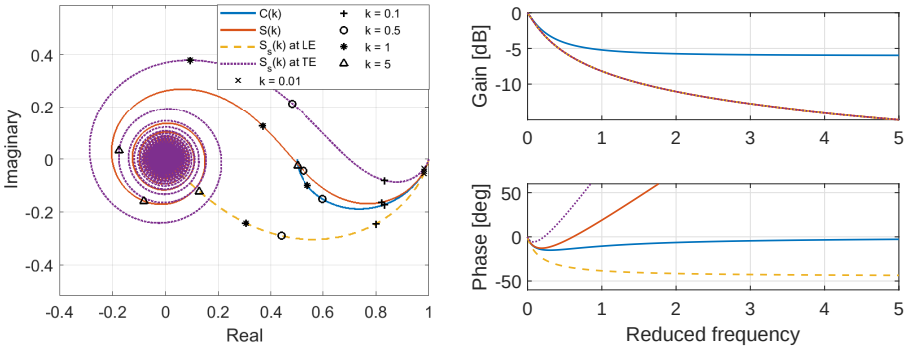

(a) **(b)**

Figure E.11: (a) Nyquist plot of Sears' function for different phase shifts of the function. **(b)** Bode plot of Sears' function for different phase shifts of the function.

Theodorsen's function and Sears' function both lie on the real axis at one when the reduced frequency is zero as the reduced frequency increases, Theodorsen's function goes toward 0.5 on the real axis whilst Sears' function goes toward zero.

Eq. E.17 and Eq. E.18 are the lift and pitch torque for a unit span foil. To get the unsteady forces and torques acting on the whole blade, the lift and torque have to be projected onto the axis of the coordinate system and integrated over the whole span of the blade using Eq. E.16.

E.2.3 Compensation for Three-Dimensional Effects

The response due to the unsteadiness described in the above two sections assumes that the aspect ratio of the blade is infinitely large. This assumption is not appropriate for the propeller blades where the aspect ratio is significantly smaller. For the case considered, the aspect ratio of the blade is approximately 1.06 when the aspect ratio, AR, is determined as:

$$AR = \frac{span^2}{wing\ area} = \frac{\left(r_p - r_h\right)^2}{\int_{r_h}^{r_p} c(r)\, dr} \tag{E.23}$$

For elliptically loaded wings, the lift coefficient for the wing, $C_{L,wing}$, is typically compensated for by its aspect ratio as [15]:

$$C_{L,wing} = \underbrace{2\,\pi\,\alpha}_{C_L} \frac{AR}{AR+2} \tag{E.24}$$

C_L is the lift coefficient for a foil section when only considering two-dimensional flow. This compensation is due to the altered circulation about the wing due to it being finite. If the propeller blade is assumed to be elliptically loaded, then the circulative lift should be compensated for by a gain of 0.347. For the unsteady response of the foil described in the above two sections, the finite aspect ratio of the blade influences both the amplitude and the phase of the circulative terms. The finite aspect ratio compensation for unsteady response has primarily been made for the time domain solution by [54] which is also described in [15, 92]. The time domain equivalent for the circulative terms to Theodorsen and Sears is solved by Wagner and Küssner, respectively. Wagner's and Küssner's solutions are the solution to a step change in the angle of attack and a sharp edged gust, respectively. The dynamics of the circulative terms in the frequency domain in Theodorsen ($\alpha\, C(k)$ and $\dot{\alpha}\, C(k)$) and Sears ($w_g\, S(k)$) can be replaced by an effective angle of attack ($\alpha_e(t)$), effective rate of angle of attack ($\dot{\alpha}_e(t)$) and effective gust ($w_{g,e}(t)$) in the time domain. These effective terms are determined by the convolution integral typically used to evaluate the response of a dynamic system. By using the convolution inte-

gral to evaluate the response, the lift and pitch torque can be determined for any arbitrary input of the angle of attacks and gusts. The effective terms are determined as:

$$\alpha_e(s) = \alpha(0)\,\phi(s) + \int_0^s \frac{d\alpha(\tilde{s})}{dt}\,\phi(s-\tilde{s})\,d\tilde{s} \tag{E.25}$$

$$\dot{\alpha}_e(s) = \dot{\alpha}(0)\,\phi(s) + \int_0^s \frac{d\dot{\alpha}(\tilde{s})}{dt}\,\phi(s-\tilde{s})\,d\tilde{s} \tag{E.26}$$

$$w_{g,e}(s) = w_g(0)\,\psi(s) + \int_0^s \frac{dw_g(\tilde{s})}{dt}\,\psi(s-\tilde{s})\,d\tilde{s} \tag{E.27}$$

ϕ and ψ are Wagner's and Küssner's functions, respectively. $\tilde{s}$ is a dummy variable for time integration. s is the reduced time determined as:

$$s = \frac{2\,V_{free}\,t}{c} \tag{E.28}$$

Wagner's and Küssner's functions can be determined explicitly from Theodorsen's and Sears' functions as [24]:

$$\phi(s) = 1 + \frac{1}{2\,\pi\,i}\int_{-\infty}^{\infty} \frac{C(k)-1}{k}\,e^{i\,k\,s}dk \quad \text{for } s > 0 \tag{E.29}$$

$$\psi(s) = 1 + \frac{1}{2\,\pi\,i}\int_{-\infty}^{\infty} \frac{S(k)-1}{k}\,e^{i\,k\,s}dk \quad \text{for } s > 0 \tag{E.30}$$

In practice Wagner's and Küssner's functions are typically approximated by an exponential function or a fraction function as [62]:

$$\phi(s) \approx 1 - 0.165\,e^{-0.041\,s} - 0.335\,e^{-0.32\,s} \tag{E.31}$$

$$\phi(s) \approx \frac{s+2}{s+4} \tag{E.32}$$

$$\psi(s) \approx 1 - 0.5\,e^{-0.13\,s} - 0.5\,e^{-1\,s} \tag{E.33}$$

$$\psi(s) \approx \frac{s^2+s}{s^2+2.82\,s+0.8} \tag{E.34}$$

Wagner's and Küssner's exponential approximations are shown in Figure E.12.

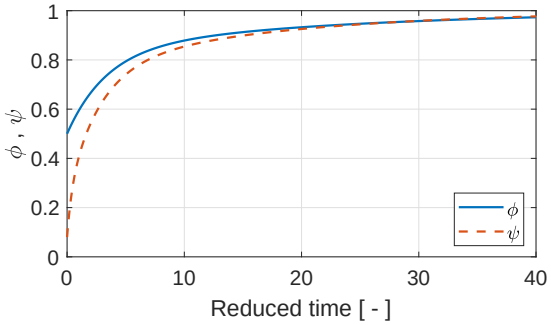

Figure E.12: Wagner's and Küssner's exponential approximations.

From Figure E.12 it is seen that Wagner's function starts initially at 0.5 and then goes towards 1 at infinite reduced time. Küssner's function starts at 0 and goes towards 1 at infinite reduced time. For Wagner's function this means that half the quasi-steady lift and pitch torque are obtained instantly for a step change in the angle of attack which is also seen from the Bode plot of Theodorsen's function in Figure E.9. If the lift and pitch torque response are evaluated for a step change in the angle of attack, then the initial lift and torque will be infinite at the time of the step change due to the non-circulative effects.

The exponential approximation of Wagner's and Küssner's functions are used in [54, 92] to account for the finite aspect ratio. The general expression used for the Wagner's and Küssner's functions are [92]:

$$\left.\begin{matrix}\phi(s)\\ \psi(s)\end{matrix}\right\} = b_0 - b_1\, e^{-\beta_1 s} - b_2\, e^{-\beta_2 s} - b_3\, e^{-\beta_3 s} \tag{E.35}$$

The coefficients b_x and β_x depend on the aspect ratio of the blade and are given in Table E.1.

Table E.1: Coefficient values for Wagner's and Küssner's functions for different aspect ratios according to [92].

Function	Aspect Ratio	b_0	b_1	b_2	b_3	β_1	β_2	β_3
ϕ	3	0.6	0.17	0	0	0.54	-	-
	6	0.74	0.267	0	0	0.381	-	-
	∞	1	0.165	0.335	0	0.0455	0.3	-
ψ	3	0.6	0.407	0.136	0	0.558	3.2	-
	6	0.75	0.336	0.204	0.145	0.290	0.725	3
	∞	1	0.236	0.513	0.171	0.058	0.364	2.42

Wagner's and Küssner's functions are shown in Figure E.13 for different aspect ratios using Eq. E.35 and the coefficients in Table E.1.

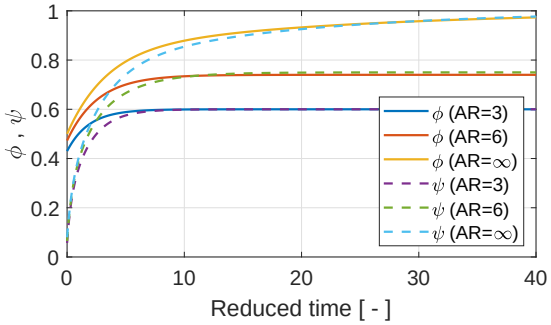

Figure E.13: Wagner's and Küssner's functions compensated for different aspect ratios.

From Table E.1 and Figure E.13 it is seen that the value towards an infinite reduced time for both Wagner's and Küssner's function matches with $AR/(AR+2)$. In [24] Wagner's and Küssner's functions are defined normalised by $AR/(AR+2)$ such that the functions vary from zero to one. The normalized Wagner's and Küssner's functions are defined for a blade with an aspect ratio of zero in [24] as:

$$\phi(s) = \begin{cases} 1 & \text{for } s > 0 \\ 0 & \text{otherwise} \end{cases} \tag{E.36}$$

$$\psi(s) = \begin{cases} s\ (2-s) & \text{for } 0 \leq s \leq 1 \\ 1 & \text{for } s > 1 \\ 0 & \text{otherwise} \end{cases} \tag{E.37}$$

The normalised Wagner's and Küssner's functions are shown in Figure E.14. It is seen that Wagner's function is a step function and Küssner's function is seen to have some transition due to the gust having to travel over the whole length of the foil before being fully developed.

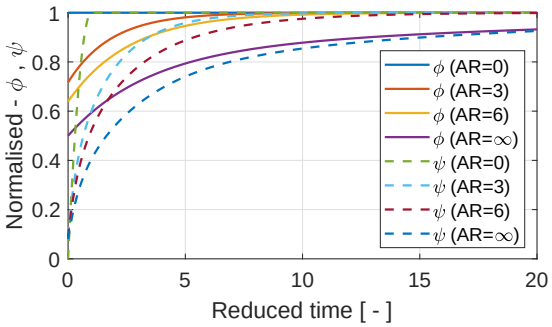

Figure E.14: Normalized Wagner's and Küssner's functions for different aspect ratios.

Wagner's and Küssner's functions for the aspect ratio of the propeller blade are determined through a spline function interpolated from the curves shown in Figure E.14. This interpolated curve is scaled by $AR/(AR+2)$ and fitted to the exponential function in Eq. E.35. The exponential function is determined such that its coefficients are positive. The resulting Wagner's and Küssner's functions for the aspect ratio of the propeller blade are shown in Figure E.15.

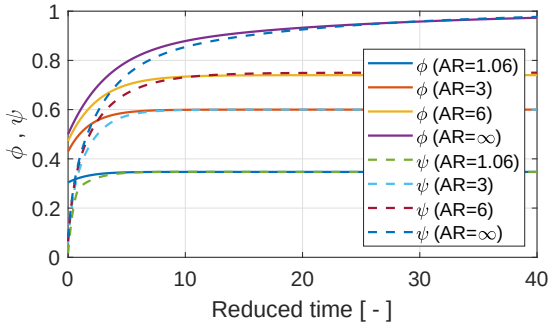

Figure E.15: Wagner's and Küssner's functions for the propeller blade's aspect ratio.

The exponential fitted function of Wagner's and Küssner's functions are re-written into the frequency domain. The same solver can thereby be used to evaluate the unsteady hydrodynamical loads as in Section E.2.1 and Section E.2.2. To determine the frequency representation of Wagner's and Küssner's functions, the method in [24] is used as:

$$C_{AR}(k) = 1 + i\,k \int_0^\infty (\phi(\tilde{s}) - 1)\; e^{-i\,k\,\tilde{s}}\, d\tilde{s} \tag{E.38}$$

$$S_{AR}(k) = 1 + i\,k \int_0^\infty (\psi(\tilde{s}) - 1)\; e^{-i\,k\,\tilde{s}}\, d\tilde{s} \tag{E.39}$$

Because Wagner's and Küssner's functions are defined with an exponential function, the frequency domain solution for both Theodorsen's and Sears' functions can be written as:

$$\left.\begin{matrix} C_{AR}(k) \\ S_{AR}(k) \end{matrix}\right\} = b_0 - \frac{b_1\, k\, i}{\beta_1 + k\, i} - \frac{b_2\, k\, i}{\beta_2 + k\, i} - \frac{b_3\, k\, i}{\beta_3 + k\, i} \tag{E.40}$$

The Sears' function determined from Eq. E.39 is with respect to the leading edge of the blade. To get the Sears' function with respect to the mid-chord point, as it is defined in Section E.2.2, it has to be rewritten by using Eq. E.20 and Eq. E.21 with the reduced shift frequency equal to $-k$. The Nyquist plot of the resulting Theodorsen's and Sears' functions compensated for the finite aspect ratio of the blade is shown in Figure E.16.

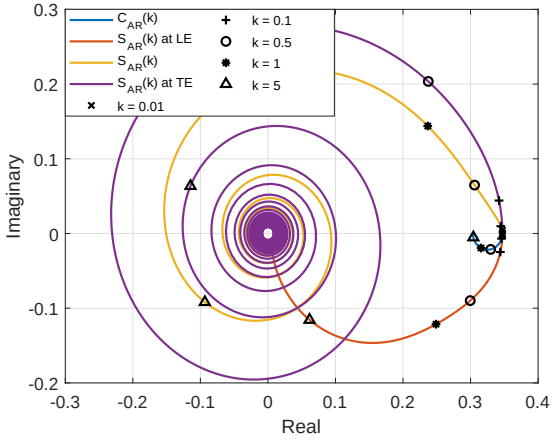

Figure E.16: Nyquist plot of Theodorsen's and Sears' functions for the propeller blade's aspect ratio.

From Figure E.16 it is seen that the variation in Thedorsen's function is reduced significantly. The maximum phase lag is less than 4° and amplitude varies between 0.3 to 0.35. Depending on the required accuracy of the function it could be assumed to be a simple gain. For Sears' function the phase becomes larger faster than for the original Sears' function and the gain is also reduced.

The compensation for the finite aspect ratio so far has only been made with respect to the circulative effects and not the non-circulative effects. This is because the finite aspect ratio of the blade only influences the circulation shedded into the wake and since the non-circulative terms are not affected by the wake, they are not affected by the finite aspect ratio. This is based on a theory for wings of moderate to large aspect ratios and has been shown to

agree well for wings with aspect ratio of two [15, 92]. It may be that this is not the case for the low aspect ratio of the propeller blade.

E.2.4 Response for unsteadiness due to parallel gust

The parallel gust is problematic to incorporate into the models presented in the above sections. This is because the parallel gust violates the assumption made with the shedded vorticity in the wake being conducted at the constant rate of the free stream velocity. The parallel gust results in the shedded vorticity being convected at a varying velocity in the wake. In [62] a review of different methods to account for the parallel gust is made. Common for these methods is that they represent a fore-aft motion of the foil instead of the parallel gust. For helicopter rotors this is an appropriate approximation [62]. This may not be the case for a ship propeller. The parallel gust is therefore not included. This may lead to a difference in the hydrodynamical loads determined with this model but it is expected to be relativelyy small, and this is because the parallel gust is relatively small compared to the free stream velocity, as shown in Figure E.6.

E.3 Application and Comparison of CVP Propeller Model

The above models for the unsteady hydrodynamical loads are applied on the propeller case considered in Chapter 2. Different variations of the models have been derived and the results from these different models are presented in this section. The model results are compared with the hydrodynamical loads determined in Appendix A to assess the models accuracy. To make this comparison, the simulated wake field used in the CFD simulation determined in Section A.2 is used. The mean of the hydrodynamical loads of the CFD simulations are subtracted from the CFD results such that it is only the unsteady components that are compared. Furthermore, the contribution from the hydrostatic pressure determined in Section 2.7 is added to the unsteady hydrodynamical loads determined using the models presented to make the comparison fair.

For the constant pitch trajectory the modelling of the unsteady hydrodynamical loads are made using Sears' gust models. There is no contribution from Theodorsen's model because the propeller blade is fixed. Three different variations of the gust model are used for the comparison with the hydrodynamical loads of the CFD simulation of the CVP propeller. These three variations are:

- Using Sears' model as presented in Section E.2.2 and thereby not account for the finite aspect ratio of the blade. This model is noted in the presented results as *Sears2D*.
- Using Sears' model as presented in Section E.2.2 but scaling the lift and torque by $AR/(AR+2)$ to compensate for the change in slope of the lift coefficient and under the assumption of an elliptically loaded blade. The change in the dynamics of Sears' function is therefore not accounted for. This model is noted in the presented results as *Sears2D-AR*.
- Using Sears' model compensated for the finite aspect ratio of the blade as presented in Section E.2.3 and thereby accounting for the change in Sears' function. This model is noted in the presented results as *Sears3D*.

The results for using these three variations of gust model are presented in Figure E.17 together with the unsteady hydrodynamical loads from the CFD simulation of the propeller with a constant pitch trajectory.

From Figure E.17 it is seen that the shape of the forces and torques along and about the x- and y-axes fit well with the CFD simulation, but with the amplitude diverging. The variation in the force along the z-axis is due to the hydrostatic pressure only and it does not match well with the CFD simulation. For the torque about the z-axis it is seen that there is a significant phase difference between the analytical models and the CFD simulation.

From Figure E.17 it is seen that *Sears2D* has the largest amplitude followed by *Sears3D* and with *Sears2D-AR* having the smallest amplitude. That *Sears2D* has the largest amplitude is not surprising since the lift slope is not compensated for due to the finite aspect ratio of the blade. The amplitude of *Sears3D* is larger than *Sears2D-AR* even though they have the same steady gain. The differences between these two models are due to the difference in the Sears' function used for the models. The amplitude of Sears' function for *Sears2D-AR* decreases faster as a function of the reduced frequency than the amplitude for the Sears' function used for *Sears3D*. For the same reduced frequencies this results in the amplitudes of *Sears3D* being larger than the amplitude of *Sears2D-AR*. The model *Sears2D-AR* generally fits the model the best with the exception for the torque about the z-axis. This indicates that the compensation of Sears' function due to the finite aspect ratio may not be appropriate.

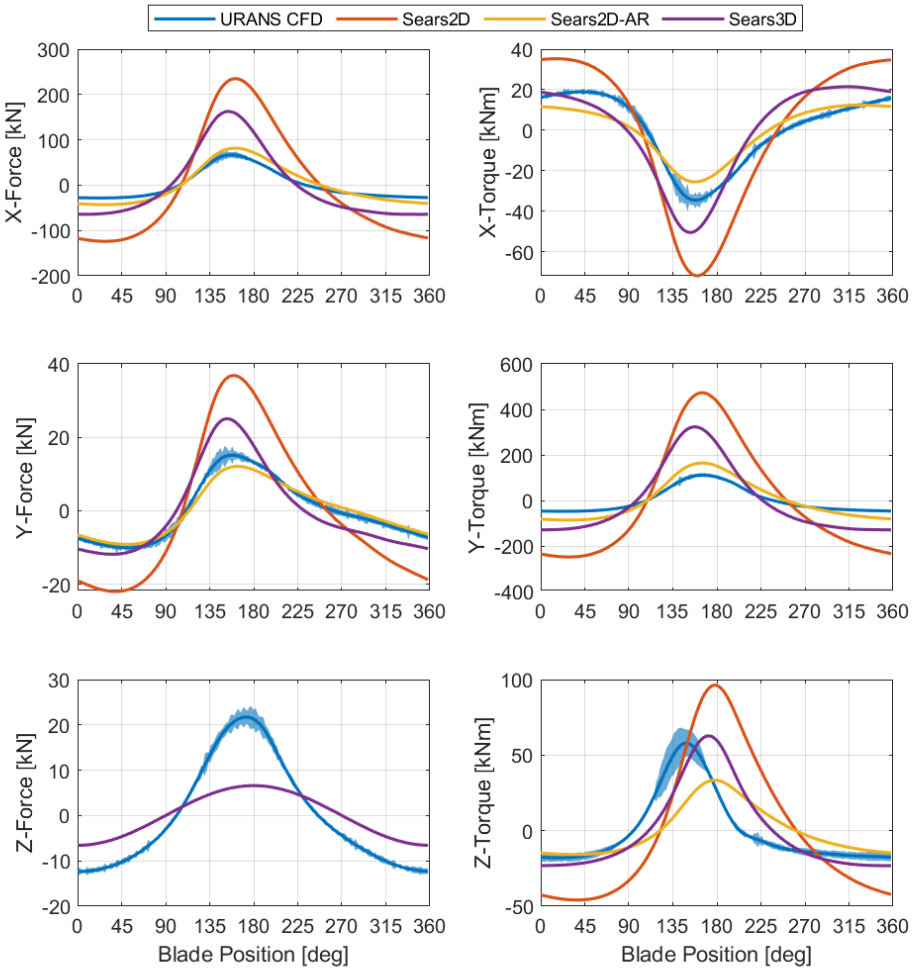

Figure E.17: Comparision of the unsteady hydrodynamical loads between the URANS CFD simulation and the analytical models for the CVP propeller with the constant pitch trajectory.

For *Sears2D-AR* it is seen that the x-force and the y-torque are slightly overestimated and the y-force and x-torque are slightly underestimated. This may be due to the advance angle, β, being used instead of the hydrodynamical pitch angle for the projection of the lift force. The hydrodynamical pitch angle accounts for the induced velocities. If the induced velocities were included, then the angle used for the projection increases which will reduce the x-force and the y-torque and increase the y-force and x-torque. The induced velocities could be included by, for example, using a lifting line to solve the steady flow around the propeller blades.

For the cosine and variable pitch trajectories the analytical models that account for the pitch motion of the blade have to be included. The unsteady hydrodynamical loads due to the pitching motion are modelled with Theodorsen's method and are added to hydrodynamical loads of the gust model to get the resulting unsteady hydrodynamical loads acting on the propeller blade. Different variations of the model for the pitch motion have been presented through the above sections. These different variations are:

- Using Theordorsen's model as presented in Section E.2.1 and thereby not accounting for the finite aspect ratio of the blade. This model is superimposed on the *Sears2D* gust model. This model is noted in the presented results as *Theo2D*.
- Using Theordorsen's model as presented in Section E.2.1 but compensating the circulative terms by $AR/(AR+2)$. This model is superimposed on the *Sears2D-AR* gust model. This model is noted in the presented results as *Theo2D-AR*.
- Using Theordorsen's model as presented in Section E.2.3 compensating for the finite aspect ratio of propeller blade. This model is superimposed on the *Sears3D* gust model. This model is noted in the presented results as *Theo3D*.

The results for the unsteady hydrodynamical loads using the analytical models above are shown in Figure E.18 and Figure E.19 for the cosine and variable pitch trajectory, respectively.

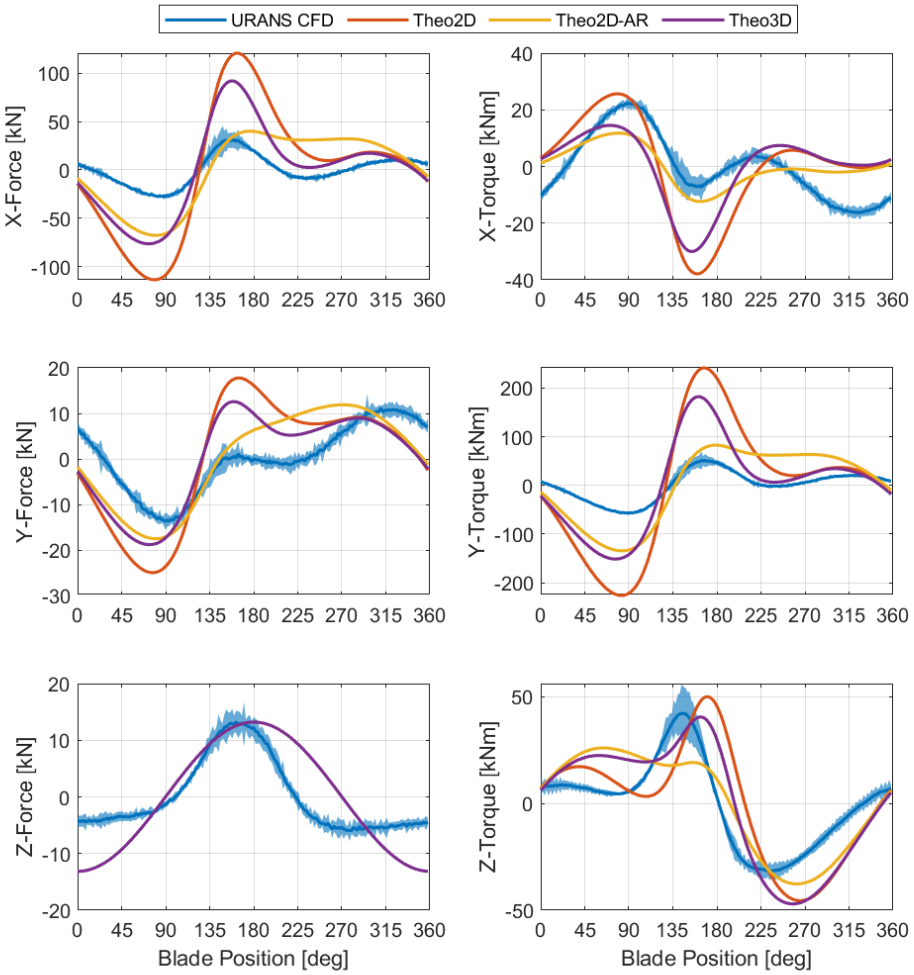

Figure E.18: Comparision of the unsteady hydrodynamical loads between the URANS CFD simulation and the analytical models for the CVP propeller with the cosine pitch trajectory.

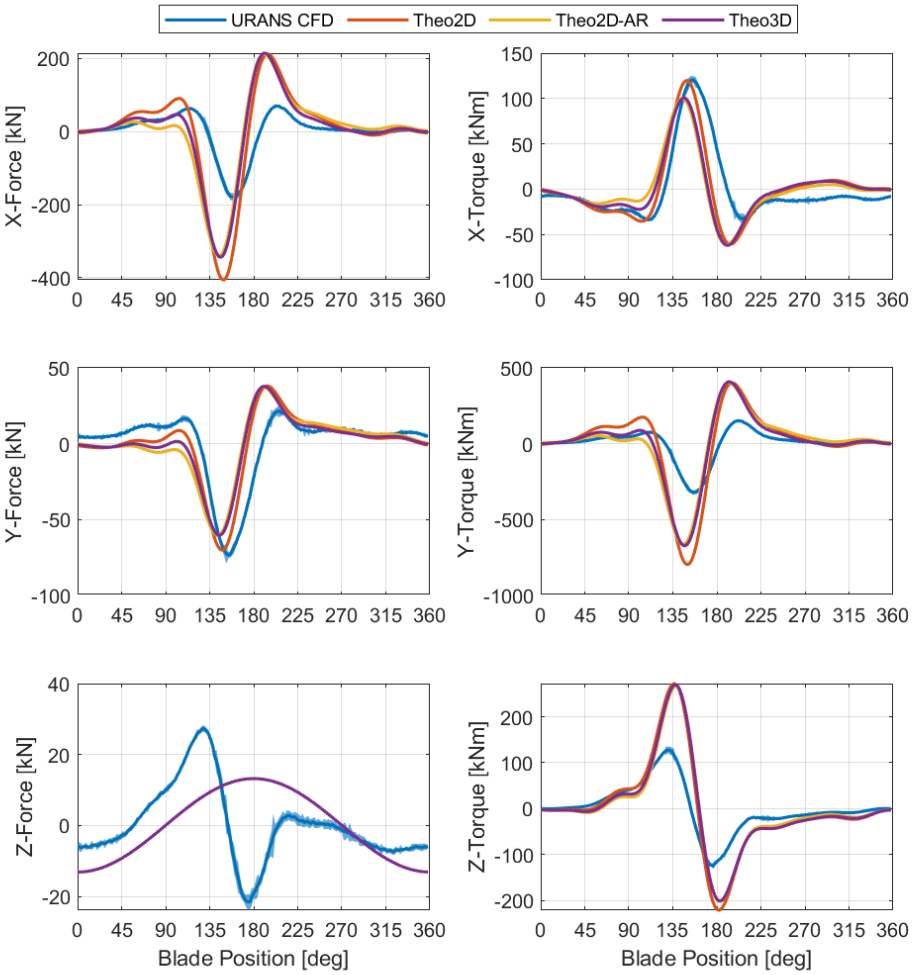

Figure E.19: Comparision of the unsteady hydrodynamical loads between the URANS CFD simulation and the analytical models for the CVP propeller with the variable pitch trajectory.

From Figure E.19, for the variable pitch trajectory, it is seen that all the models have a shape that corresponds with the shape of the loads from the CFD simulation. There is some phase difference between the analytical model and the CFD simulation; the analytical models tend to lead relative to the CFD simulation. It is seen that the x-force, y-torque and z-torque are overestimated and the y-force and x-torque are slightly underestimated. A better overall correspondence may be obtained if the hydrodynamical pitch angle was used instead. This would increase the y-force and x-torque and decrease the x-force and y-torque.

From Figure E.18 for the cosine pitch trajectory it is seen that the shape of the loads for the analytical models do not fit the shape of the CFD simulation as well as for the constant and variable pitch trajectory. The reason for this poorer fit may be due to the variation in the loads being the smallest for the cosine pitch trajectory. If there are any unsteady effects that are not accounted for by the analytical models, then these effects become more prominent for the cosine pitch trajectory than for the other pitch trajectories. This could, amongst others, be due to:

- Not accounting for the unsteadiness due to the parallel gust.
- Not accounting for the helically shaped shedded wake for a propeller. For the analytical models the shedded wake is assumed to be planar.
- Not accounting for the viscous effects.
- Not accounting for the interaction effect between the propeller blades.

To compare the analytical models, the root-mean-square error is determined for each hydrodynamical load for each model and for each pitch trajectory as:

$$e_i = \sqrt{\sum_{\theta_b=0}^{2\pi} \Big(L_{i,hydro,A}(\theta_b) - L_{i,hydro,CFD}(\theta_b) \Big)^2} \tag{E.41}$$

e_i is the root-mean-square error of the i'th hydrodynamical load. $L_{i,hydro,A}$ is the i'th hydrodynamical load determined using one of the analytical models. $L_{hydro,CFD}$ is the corresponding hydrodynamical load from the CFD simulation of the CVP propeller. The determined root-mean-square error for each of the analytical models is shown in Figure E.20 for each of the three pitch trajectories and each of the hydrodynamical loads.

From Figure E.20 it is seen that the analytical models *Sears2D-AR* and *Theo2D-AR* generally yield the lowest root-mean-square error. That these models fit the best for the cosine and variable pitch trajectory may be due to the corresponding gust model having the lowest root-mean-square error.

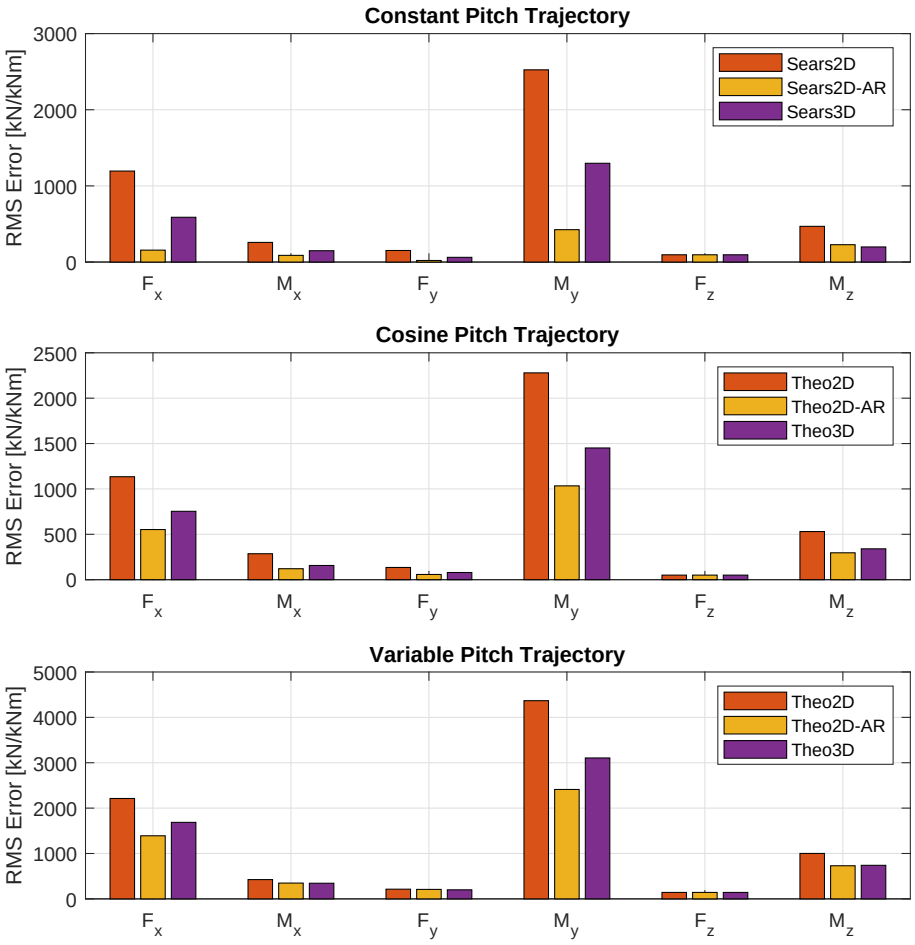

Figure E.20: Root-mean-square error of the different analytical models for each of the hydrodynamical loads and for each of the pitch trajectories.

For the analytical model to be useful for determining the optimum pitch trajectory for the CVP propeller requires that the model accurately predicts the unsteady hydrodynamical loads. It can be discussed if the analytical models presented are good enough in this regard. Alternatively, the analytical model may be used if it generally determines the correct shape of the hydrodynamical loads and it just has to be scaled to get the correct value. Then the analytical model can still be used to determine the optimum pitch trajectory. This is not the case with the models presented due to there being some phase difference and some mismatch in the shape for the cosine pitch trajectory. The analytical model may still be usable as an initial method to determine the optimal pitch trajectory for the CVP propeller due to its low

computational costs. This initial determined optimum pitch trajectory can then be used as an initial pitch trajectory for a more computationally expensive method to determine the optimum pitch trajectory.

Appendix F

Hydrodynamic Modelling of CVP Propeller using Empirical Transfer Function Estimation

In Appendix A three URANS CFD simulations were presented for the CVP propeller for three different pitch trajectories. The unsteadiness of these hydrodynamical loads can be used to determine the dynamics of the CVP propeller through the use of system identification. A number of different methods exist in the field system identification that can be used to determine the dynamics of a system. Both linear and non-linear system identification methods exist but in this appendix a linear system identification method is used. This method is based on the Fourier series of the input and output signal. This Fourier series system identification method is used because both the input pitch trajectory and the output hydrodynamical loads are cyclically varying with the fundamental frequency of the propeller's rate of revolution. The Fourier series based system identification method therefore seems to be an appropriate method to use for the CVP propeller.

F.1 Determining the Empirical Transfer Function Estimation

The principle of the system identification method using Fourier Series is that the system dynamics can be determined as [64]:

$$G(\omega) = \frac{Y(\omega)}{U(\omega)} \tag{F.1}$$

$G(\omega)$ is the empirical transfer function estimate of the system at the frequency ω. $Y(\omega)$ is the complex coefficient of the Fourier series of the output signal at the frequency ω. The output is the hydrodynamical loads acting on the CVP propeller blades. $U(\omega)$ is the complex coefficient of the Fourier series of the input signal at the frequency ω. The input is the pitch of the propeller blade. The empirical transfer function can also alternatively be determined as the amplitude ratio between the output and input and the phase difference between them. The frequencies for which the empirical transfer function can be determined are the frequencies contained in the input signal. For the URANS CFD simulations made in Appendix A of the CVP propeller, the three pitch trajectories include the 0th, 1st and 7th harmonics. This is for the constant, cosine and variable pitch trajectory, respectively. For the constant pitch trajectory it is not possible to determine anything about the system dynamics but the output still varies cyclically. It is therefore assumed that unsteadiness due to the wake field and the unsteadiness of the pitch trajectory are independent of each other and they can be superimposed onto each other to get the response of the CVP propeller. This is similar to the approach used in Appendix E. The hydrodynamical loads from the simulation with constant pitch trajectory are therefore subtracted from the hydrodynamical loads from the cosine and variable pitch trajectory as:

$$\tilde{L}_{traj}(\theta_b) = L_{CFD,traj}(\theta_b) - L_{CFD,const}(\theta_b) \tag{F.2}$$

$\tilde{L}_{traj}$ is the unsteadiness in the hydrodynamical load due to the pitch trajectory $(traj)$ which can either be the cosine or variable pitch trajectory. $L_{CFD,traj}$ is the hydrodynamical load of the URANS CFD simulation of the CVP propeller with either the cosine or variable pitch trajectory. $L_{CFD,const}$ is the hydrodynamical load of the URANS CFD simulation of the CVP propeller with a constant pitch trajectory. The number of harmonics used to determine the Fourier series of the output is the same number of harmonics that is included in the pitch trajectory. The Fourier series approximated for the cosine and variable pitch trajectory are made using least-squares estimation of the Fourier coefficients. The unsteady hydrodynamical loads and the Fourier se-

ries estimation of it are shown in Figure F.1 for both the cosine and variable pitch trajectory.

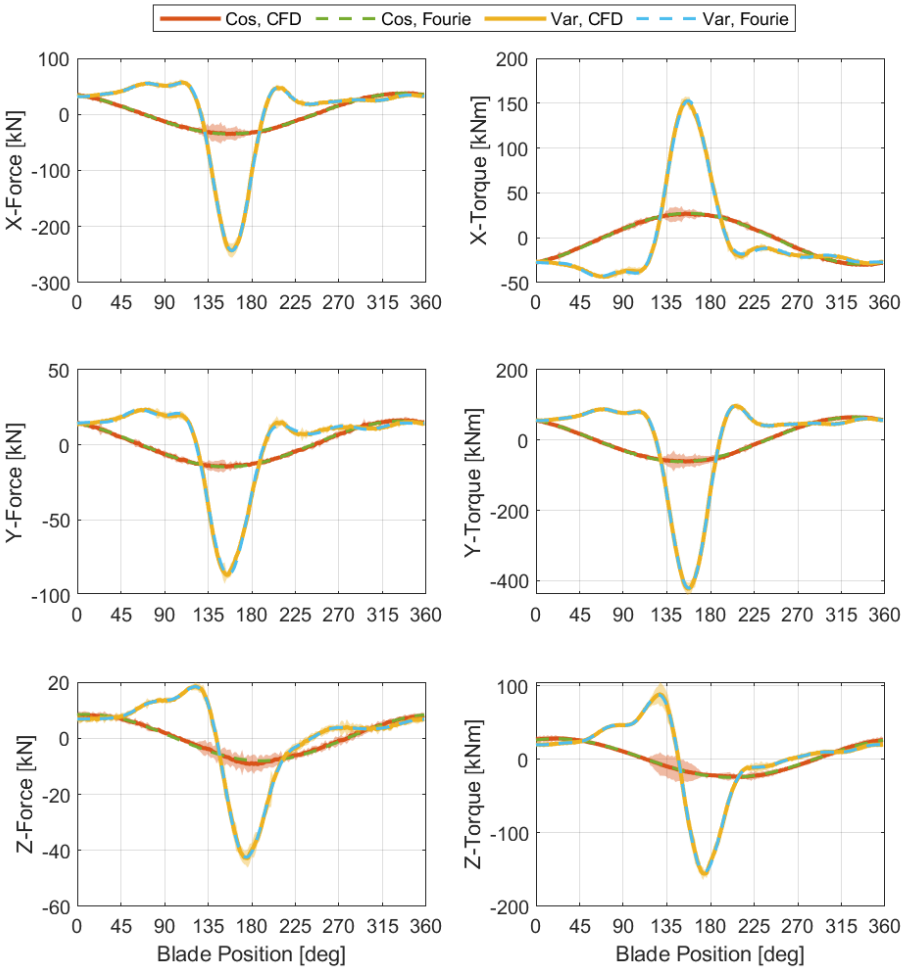

Figure F.1: Comparision of the unsteady hydrodynamical loads due to the pitching motion and the corresponding estimate Fourier series.

From Figure F.1 it is seen that the estimated Fourier series is able to capture the unsteady hydrodynamical loads well. This shows that the unsteadiness in the hydrodynamical loads is generally linear with respect to the pitch motion. The blade positions, where the Fourier series does not match the simulation results exactly, are within the uncertainty bounds of the simulation. From the estimated Fourier series the empirical transfer function is determined for each frequency component of the input signal. The empiri-

cal transfer function is shown in a Nyquist plot in Figure F.2 for each of the hydrodynamical loads, for each of the pitch trajectories.

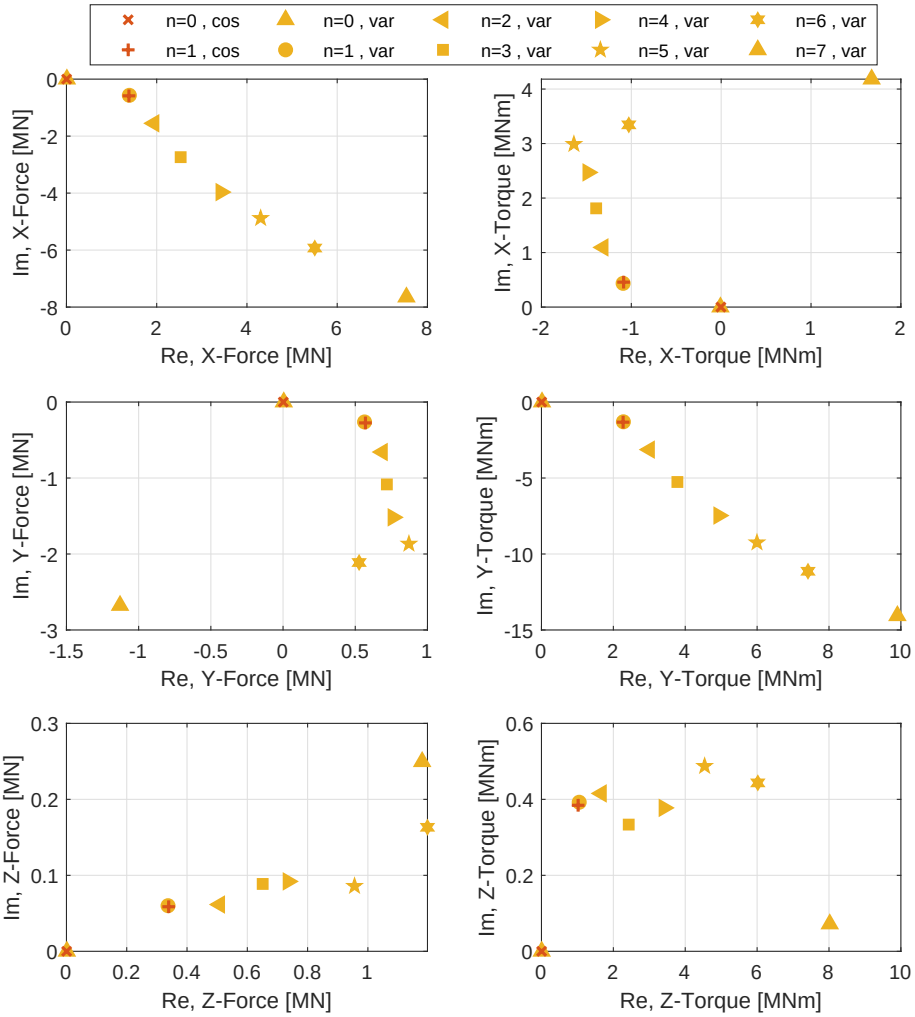

Figure F.2: Nyquist plot of the empirical transfer function.

From Figure F.2 it is seen that the shape of the Nyquist plot is similar for the x-force and y-torque, and similar for the x-torque and the y-force. This shows that the y-torque is highly coupled with the x-force and the x-torque is highly coupled with the y-force. Furthermore, it is also seen that the first harmonic component of the system for the cosine and variable pitch trajectories coincide with each other. This supports the assumption that the

unsteadiness in the hydrodynamical loads has a linear relationship with the pitch trajectory.

The unsteady hydrodynamical loads due to the pitch trajectory can be determined for up to the 7th harmonic of the pitch trajectory for the system considered. The hydrodynamical loads are determined for each harmonic as:

$$Y(\omega) = G(\omega)\, U(\omega) \tag{F.3}$$

The unsteady hydrodynamical loads for each harmonic are superimposed onto each other to get a single signal for the unsteady hydrodynamical load. For the optimal pitch trajectory for the CVP propeller, the unsteady load should be equal to the unsteady load due to the non-uniform wake field, but with a sign change. The sum of unsteady loads due to the pitch motion and the non-uniform wake field thereby equals zero.

Appendix G

Hydrodynamic Modelling of CVP Propeller Through a Reduced Model

The URANS CFD simulation of the CVP propeller in Appendix A has six degrees of freedom for each cell in the mesh. A reduced model for the hydrodynamical loads is a model which has fewer degrees of freedom which gives similar results. The reduced model made in this appendix is inspired by the model made in Appendix E which uses unsteady foil theory to model the hydrodynamical loads acting on the CVP propeller. The model structure used in Appendix E is used for the reduced model, but the model parameters are determined through a number of CFD simulations. The model therefore keeps the physical structure which can be beneficial when analysing the system. The reduced model is also used to account for some of the effects that are neglected in Appendix E, such as the helically structured wake, viscous effects and the blades influence on each other. The reduced model is a grey box modelling approach where the model made in Appendix F is a black box model where the physical understanding is lost. This appendix is divided into five sections which are:

- Section G.1 presents the model structure for the reduced model for modelling the hydrodynamical loads acting on the CVP propeller. The reduced model is divided into three components which have to be determined through CFD simulations. These components are described in the following three sections.
- Section G.2 presents the determination of the reduced model component due to the steady circulative effects. These are determined through a series of quasi-steady CFD simulations of the propeller.

- Section G.3 presents how the dynamic build-up of the circulative effects is determined due to the pitch motion. This is determined through an unsteady CFD simulation where a step change in the pitch is made.
- Section G.4 presents the determination of the reduced model component due to the non-circulative effects. These are determined by fitting the reduced model to the URANS CFD simulation results of the CVP propeller.
- Section G.5 presents the results for the hydrodynamical loads when the reduced model is applied on the propeller considered in Chapter 2 for its three pitch trajectories.

G.1 Reduced Model Structure

The reduced model is made for the ship and the propeller speeds used for the propeller case considered in Chapter 2. The purpose of the model is to determine the unsteady hydrodynamical loads due to the pitch trajectory and is inspired by the model structure in Appendix E. The input to the model is therefore the pitch trajectory of the propeller blades and the output is the hydrodynamical loads. The structure for the reduced model is:

$$L_{x,i} = K_{NC,\ddot{\alpha}}\,\ddot{\alpha}_{p,x} + K_{NC,\dot{\alpha}}\,\dot{\alpha}_{p,x} + K_C(\boldsymbol{\alpha_{p,e}}, \boldsymbol{\dot{\alpha}_{p,e}}) \tag{G.1}$$

$L_{x,i}$ is the i'th hydrodynamical load modelled for the x'th blade of the propeller i.e. 1-4. $K_{NC,\ddot{\alpha}}$ $K_{NC,\ddot{\alpha}}$ are the non-circulative gains for the pitch acceleration ($\ddot{\alpha}_{p,x}$) and pitch rate $\dot{\alpha}_{p,x}$, respectively. K_C is a regression model for the circulative effects which uses the effective pitch displacement and effective pitch rate for all the blades. The effective pitch displacement and pitch rate for all the blades are collected in the vectors $\boldsymbol{\alpha_{p,e}}$ and $\boldsymbol{\dot{\alpha}_{p,e}}$, respectively. The effective pitch displacement and pitch rate are determined through the convolution integral as:

$$\alpha_{p,e,x}(t) = \alpha_{p,x}(0)\,\phi(t) + \int_0^t \dot{\alpha}_{p,x}(\tilde{t})\,\phi(t-\tilde{t})d\tilde{t} = \alpha_{p,x} * \phi \tag{G.2}$$

$$\dot{\alpha}_{p,e,x}(t) = \dot{\alpha}_{p,x}(0)\,\phi(t) + \int_0^t \ddot{\alpha}_{p,x}(\tilde{t})\,\phi(t-\tilde{t})d\tilde{t} = \dot{\alpha}_{p,x} * \phi \tag{G.3}$$

$\alpha_{p,e,x}$ and $\dot{\alpha}_{p,e,x}$ are the effective pitch displacement and pitch rate, respectively, for the x'th blade. ϕ is the step response of the system for the circulative effects similar to Wagner's function in Appendix E.

The parameters that have to be determined for the reduced model are $K_{NC,\ddot{\alpha}}$, $K_{NC,\dot{\alpha}}$, K_C and ϕ. Determining the parameters through CFD simulations ensures that the effects, neglected in Appendix E, are accounted for

such as the helical wake, viscosity and the influence each blade has on the other blades.

G.2 Determination of Circulative Effects

For the reduced model the circulative parts of the hydrodynamical loads are determined through a regression model. This regression model is made through a series of quasi-steady CFD simulations. The CFD simulations are made using the steady axial wake field determined in Appendix E thereby neglecting the unsteady components of the non-uniform wake field. The domain for the quasi-steady CFD simulations is shown in Figure G.1.

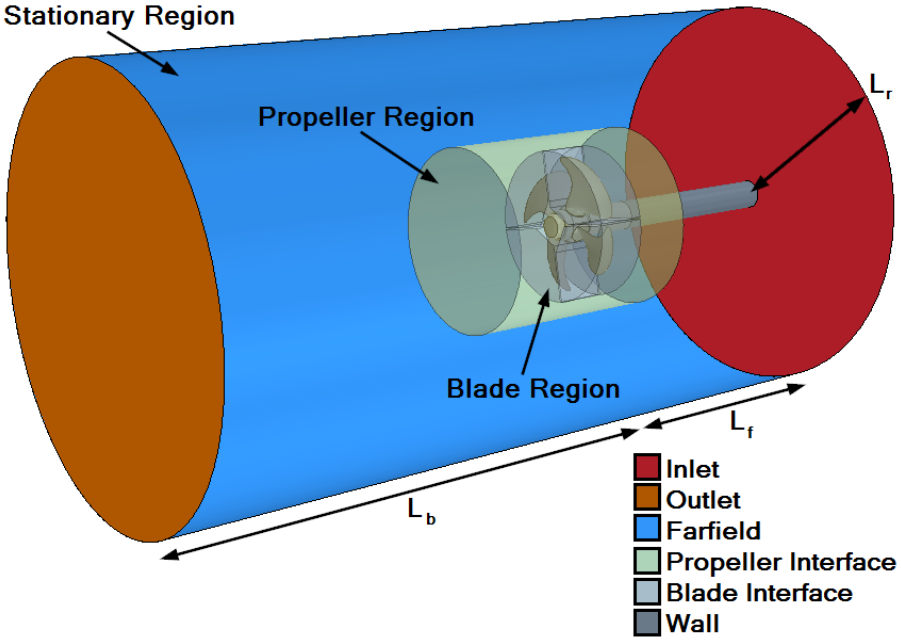

Figure G.1: The domain used for the quasi-steady CFD simulations of the propeller in the steady axial wake field.

From Figure G.1 it is seen that the CFD simulation is divided into six regions as; stationary region, propeller region and four blade regions. The setup is almost identical to the simulation setup in Appendix A but with the exception that the propeller blades are enclosed in their own region. The rotation of the propeller is made by imposing a moving reference frame to the propeller and blade regions about the shaft with the rate of propeller revolutions. The blade regions have an additional motion imposed on them about the blade's spindle axis with the pitch rate of the blade. The pitch and

pitch rate of each blade can therefore be set individually and the hydrodynamical loads due to circulative effects can be determined under quasi-steady conditions.

To determine which pitch displacements and pitch rates the CFD simulations should be made for, it is necessary to consider both the desired regression model to be used, as well as the desired range of the pitch trajectories the reduced model should cover. The considered propeller has four blades which each has an independent pitch displacement and pitch rate. This gives eight states/variables for the regression model. Three different structures for the regression model are considered which are; a first-order model, a first-order model with interactions and a second-order model with interactions. These regression models are defined as, respectively [71]:

$$\hat{y} = \beta_0 + \sum_{i=1}^{k} \beta_i \, x_i \tag{G.4}$$

$$\hat{y} = \beta_0 + \sum_{i=1}^{k} \beta_i \, x_i + \sum_{\substack{i=1 \\ i<j}}^{k} \sum_{j=1}^{k} \beta_{ij} \, x_i \, x_j \tag{G.5}$$

$$\hat{y} = \beta_0 + \sum_{i=1}^{k} \beta_i \, x_i + \sum_{\substack{i=1 \\ i\leq j}}^{k} \sum_{j=1}^{k} \beta_{ij} \, x_i \, x_j \tag{G.6}$$

y is the output variable which in this case is one of the hydrodynamical loads acting on the propeller blade. x_i is the i'th state/variable i.e. effective pitch displacement and effective pitch rate. For the quasi-steady simulation the effective pitch displacement and effective pitch rate are equal to the set pitch displacement and pitch rate, respectively. This is because there is no time history effect in the quasi-steady CFD simulaitons. β_i are model coefficients to be determined. To determine the coefficients of the regression models, a number of quasi-steady CFD simulations is required where the four propeller blades have different pitch displacements and pitch rates. The number of simulations and simulation settings are determined by using the 2^k factorial design approach from [71]. This means that each variable can either be high (1) or low (-1) which results in 256 combinations of the eight variables. These 256 combinations can be used to determine the coefficients of the linear regression model with and without interactions. The 256 simulations can be reduced to 70 simulations due to the symmetry in the setup of the simulation. For example, if all the variables are high except the pitch rate of the blade number 1, then this gives the same results as if it is blade numbers 2, 3 or 4 that have a low pitch rate if the indexing is shifted accordingly.

The second-order regression model requires that the simulations are made at an additional level (0). If all combinations are made for this additional level then this results in 6561 simulations that have to be made which reduces to 1665 simulations if the same symmetry consideration is made. Making 1665 simulations are too computationally expensive to be considered. The alternative is to use the *central composite design* proposed in [71]. This uses a central point and series of axial points such that the second-order term of the regression model can be determined. This results in only 17 additional simulations that have to be made to the 70 simulations and if the symmetry is considered this reduces to 5 additional simulations. All 75 simulation conditions are shown in Figure G.2.

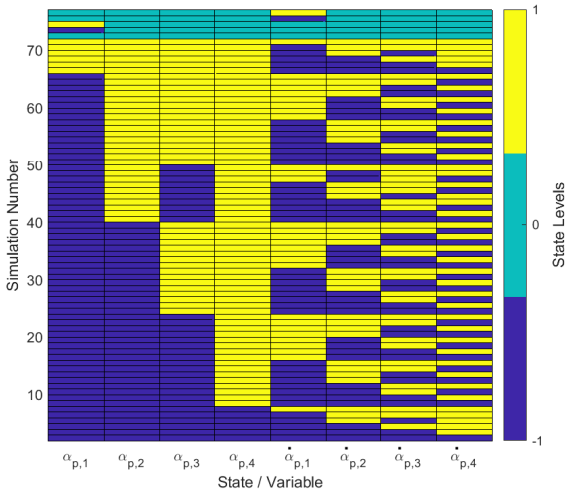

Figure G.2: Levels for the all the variables for the quasi-steady CFD simulations in order to be able to determine the coefficients of the regression model.

To determine the value of the pitch displacement and pitch rate at the levels 1, 0, -1 the pitch trajectories from Section 2.2 are considered. This is in order to be able to compare the reduced model with the URANS CFD simulation for these pitch trajectories. The state trajectories of the pitch trajectories from Section 2.2 are shown in Figure G.3.

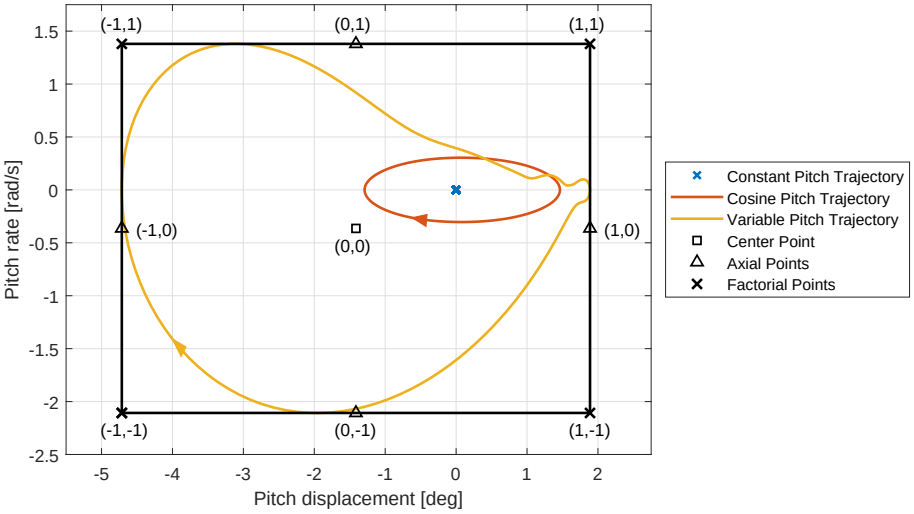

Figure G.3: State trajectories of the different pitch trajectories from Section 2.2 and the evaluation points from the factorial design and the central composite design.

In Figure G.3 the state trajectories are enclosed by a box and the levels of the points are shown in the parenthesis as (pitch displacement, pitch rate). The corners of the box are the levels of the pitch displacement and pitch rate due to the factorial design approach also called the factorial points. The center point is located in the center of the box and the axial points on the sides of the box. The values of the levels -1, 0 and 1 for the pitch displacement and pitch rate are given in Table G.1.

Table G.1: The values for the pitch displacement and pitch rate at the different levels.

Level	Pitch Displacement $[deg]$	Pitch Rate $[rad/s]$
-1	-4.7141	-2.1076
0	-1.4129	-0.3640
1	1.8882	1.3795

Having determined the simulation conditions that the CFD simulations should be made for, the only thing left is to make the CFD simulations. Before the CFD simulations are made, it is necessary to determine the domain size for the CFD simulations and the uncertainty in using this domain size. The domain dimensions are determined using the three parameters L_f, L_b and L_r as shown in Figure G.1. These parameters are respectively the distance between the propeller and the inlet, the distance between the propeller and the outlet and the distance from the shaft center to the radial boundary.

To determine the distance between the inlet and the propeller, the error in the effective wake field velocities at the propeller is considered in a manner

similar to that in Appendix A. The effective wake field imposed on the inlet boundary is the steady axial wake field which is determined as a radial varying zero-order component of the radial varying Fourier series approximation to the non-uniform wake field. This steady axial wake field is determined in Appendix E and is shown in Figure G.4.

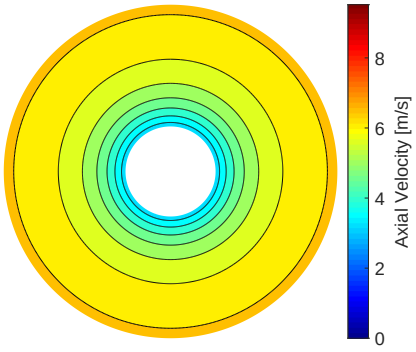

Figure G.4: Steady axial wake field.

The steady wake field in Figure G.4 does not cover the whole domain of the CFD simulation. The wake field is therefore extrapolated to cover the whole domain. The extrapolation is made using the same approach as used for the wake field in Appendix A. The steady wake field does not have any tangential or radial velocity components and it is therefore not necessary to include the momentum sources in the CFD simulations.

The wake field velocity error is determined through a series quasi-steady CFD simulations of the domain without the propeller blades for different distances between the propeller and the inlet. The other domain parameters L_b and L_r are set to 75m and 30m, respectively, which are the same used in Appendix D. For each of the simulations the error in the wake field velocity is determined as:

$$e_w(L_f) = \frac{1}{N} \sum_{n=1}^{N} \left| \frac{v_x(n, L_f) - v_{x,CFD}(n, L_f)}{v_x(n, L_f)} \right| \tag{G.7}$$

N is the number of points used to measure the wake field. v_x is the axial velocity of the measured effective steady wake field and $v_{x,CFD}$ is the axial velocity of the simulated effective steady wake field. The wake error for the simulated values for L_f is given in Table G.2.

Table G.2: Wake field error as a function of the distance between the propeller and the inlet.

L_f	D_p 5.4m	$2\,D_p$ 10.8m	$3\,D_p$ 16.2m	$4\,D_p$ 21.6m	$5\,D_p$ 27m
Error	0.0133	0.0205	0.0250	0.0284	0.0310

From Table G.2 it is seen that the wake field error is the smallest when $L_f = 5.4$m. A distance between the propeller and the inlet of 5.4m is therefore chosen for the following CFD simulations for the reduced model.

To determine the two remaining domain parameters L_b and L_r a series of quasi-steady CFD simulations are made. These simulations are made using only a quarter of the domain similarly to the domain used in Appendix D. Furthermore, the investigation is made for the nine combinations of the three levels for the pitch displacement and pitch rate in Table G.1. For each combination the two parameters are varied between 5.4m ($1\,D_p$) to 162m ($30\,D_p$) whilst the other parameters are fixed at 75m and 30m for L_b and L_r, respectively. The error for the domain parameters is assumed to converge exponentially as:

$$\epsilon_{\phi_i} \approx \delta_d = \phi_i - \phi_0 = \alpha_d\, e^{-p_d\,(L_x - \beta_d)} \tag{G.8}$$

ϵ_{ϕ_i} is the domain error of the i'th simulation. δ_d is the approximation of the domain error. ϕ_i is the simulation value. ϕ_0 is the real/true value. L_x is the length of the domain parameter considered. α_d is the error gain for the domain parameter. p_d is the convergence rate coefficient. β_d is an exponential offset coefficient. The parameters ϕ_0, α_d, p_d and β_d are determined through a least-squares estimation to the simulation data. The least-squares estimation is made with and without weighting of the data, where the data points at large L_x are weighted more. The least-squares estimation with the lowest standard deviation is used to determine the domain uncertainty as:

$$U_{dom,L_x}(L_x) = \left|\epsilon_{\phi_i}(L_x)\right| + 2\,\sigma \tag{G.9}$$

σ is the standard deviation of the least-squares estimation. The limit of the domain parameter is determined for each hydrodynamical load for each of the nine simulation conditions. The limit is determined when the relative uncertainty has increased by 0.15% with respect to the uncertainty at $L_x = 30\,D_p$. This is shown for one of the simulation conditions in Figure G.5, where the limits for the domain parameters are L_b^* and L_r^*.

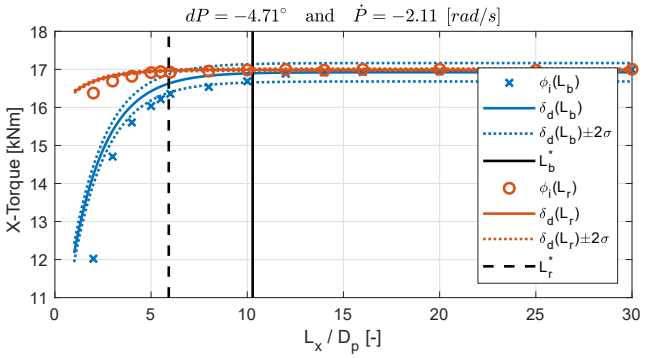

Figure G.5: The least-squares estimation of Eq. G.8 to the simulation data when the pitch displacement is $-4.71°$ and the pitch rate is -2.11 $[rad/s]$ together with the determined limits for the domain parameters.

The limits for all the hydrodynamical loads and all the simulation conditions are shown in Figure G.6.

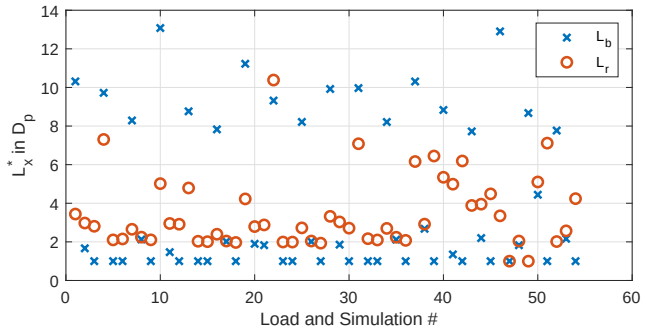

Figure G.6: The domain limits for L_b and L_R for all the hydrodynamical loads and simulation conditions.

The domain parameters used for the following simulations are chosen to be the maximum value for L_b^* and L_r^*. The domain parameters for the CFD simulations are given in Table G.3.

Table G.3: Domain parameters for CFD simulation with steady state wake field.

Domain Parameter	L_f	L_b	L_R
Length	$1\ D_p$	$12.7\ Dp$	$10.5\ Dp$

The domain uncertainty is determined as:

$$U_{dom} = \sqrt{U_{dom,L_b}^2 + U_{dom,L_r}^2} \tag{G.10}$$

The uncertainty due to domain parameters used to determine the domain uncertainty is the maximum uncertainty for all the simulation conditions. This is in order to be conservative when determining the domain uncertainty. The domain uncertainties are given in Table G.4.

Table G.4: Domain uncertainties with the chosen domain parameters.

Uncertainty	U_{dom,L_b}	U_{dom,L_r}	U_{dom}
F_x [N]	689.7	252.9	734.6
M_x [Nm]	343.0	266.5	434.4
F_y [N]	204.0	177.9	270.7
M_y [Nm]	948.7	490.2	1067.9
F_z [N]	267.1	153.7	308.2
M_z [Nm]	511.3	238.4	564.2

Having determined the domain size and the corresponding uncertainty, the quasi-steady CFD simulations can be made for all the test conditions in Figure G.2. The iterative uncertainty and spatial uncertainty are determined for each simulation according to the procedure in Appendix C. The spatial uncertainties are determined using four different spatial discretizations. The simulation results and their uncertainties are shown in Figure G.7 for all 75 simulation conditions. The uncertainty includes the iterative, spatial and domain uncertainty. The simulation numbering correspondence with the numbering shown in Figure G.2. The uncertainty of the simulation results tends to be dominated by the spatial discretization uncertainty.

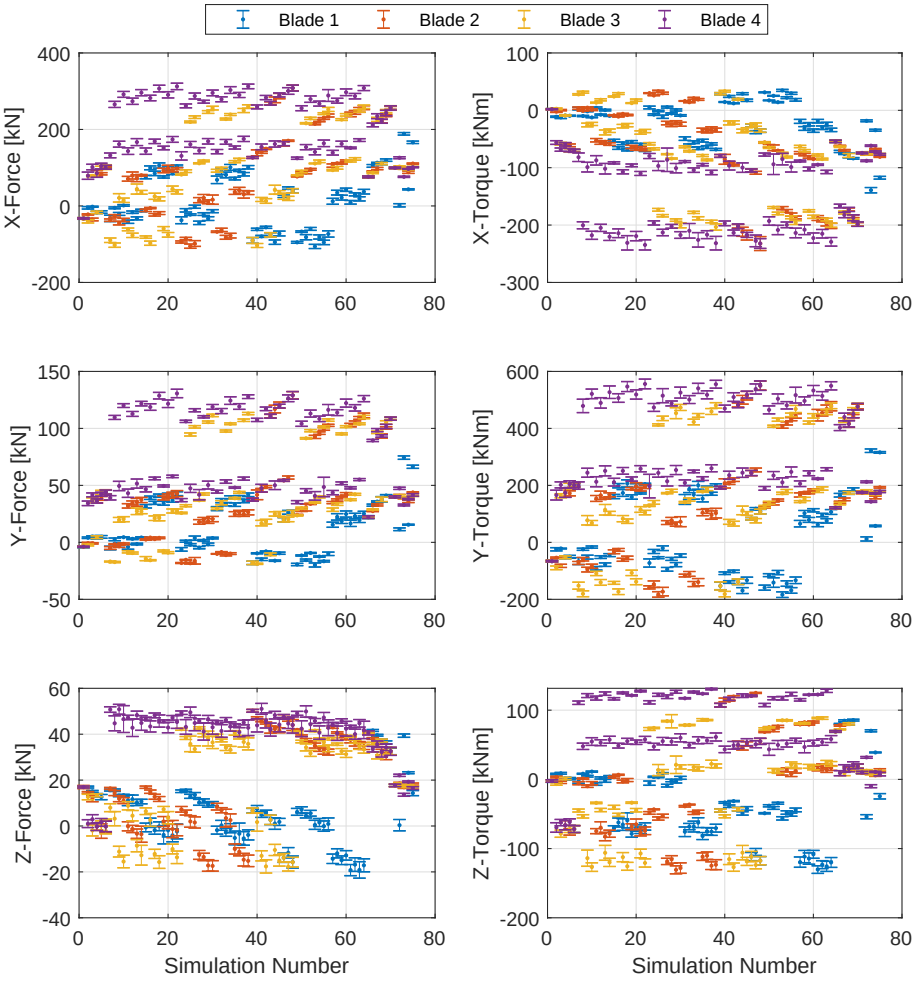

Figure G.7: Simulation results and uncertainties for the simulation conditions in Figure G.2.

The simulation data in Figure G.7 is reformulated such that the solution for all 273 simulation conditions is obtained. These data are used to determine the coefficients for the regression models in Eq. G.4, Eq. G.5 and Eq. G.6. The coefficients are determined through a least-squares estimation. To evaluate the fit of the regression models and to compare them, the standard deviation of the error, σ, is determined as:

$$\sigma = \sqrt{\frac{1}{N - N_p} \sum_{n=1}^{N} (y(i) - \hat{y}(i))} \tag{G.11}$$

N is the number of datasets i.e. simulation conditions. N_p is the number of parameters/coefficients used in the regression model. y is the simulation value used for the regression model. $\hat{y}$ is the estimation of the simulation value using the regression model. The standard deviation of the error for each of the regression models is shown in Figure G.8.

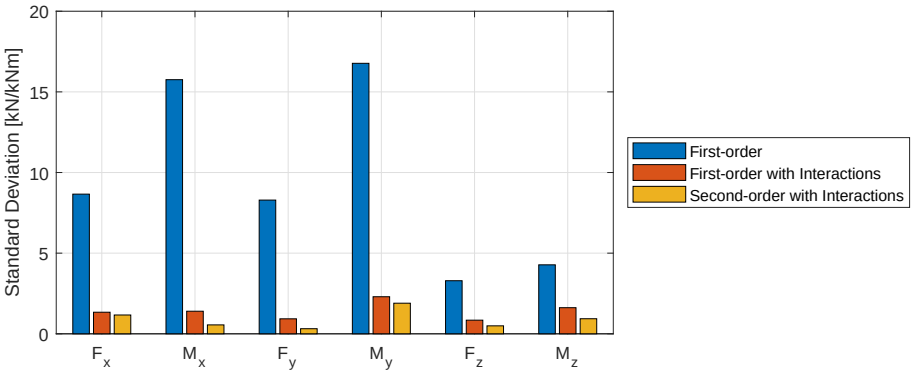

Figure G.8: Standard deviation of the three regression models.

From Figure G.8 it is seen that the standard deviation decreases as the complexity of the regression model increases i.e. including additional coefficients. The standard deviation does not decrease as significantly when going from the first-order regression model with interactions to the second-order regression model with interactions. This may be due to central decomposition approach being used to include the second-order term of the regression model. There is, thereby, not as many data points included where the second-order regression model fits better. The second-order regression model is used in the further work with the reduced model for the CVP propeller.

The second-order regression model uses 45 coefficients which can be reduced by considering the p-value for each coefficient. If the p-value for a coefficient is larger than 0.05 then it is likely that the coefficient does not have a significant influence on the regression model and it can be removed. Using this approach 11-17 coefficients can be removed from the regression model depending on the hydrodynamical load. This is while the standard deviation of the regression model does not change more than 1.4%. This reduction in the number of coefficients in the regression model is not utilized in the further work because the structure of the regression model becomes unique for each hydrodynamical load thus complicating the further work with the reduced model.

G.3 Determination of the Dynamics in the Circulative Effects

The circulation part of the hydrodynamical loads does not follow the forcing from the pitch and pitch rate instantaneously. The circulative effects have a dynamic build-up before they reach a steady state value. This is according to the unsteady foil theory utilized in Appendix E. The dynamic build-up is determined through an unsteady CFD simulation where one blade makes a step change in the pitch. The CFD simulation utilizes the same setup as used in Appendix A, but uses the steady wake field instead of the non-uniform wake field. The step response is made from level 0 to level 1 which is equivalent to the pitch displacement changing from -1.41° to 1.89°. The other blades are, at all times, kept at the 0 level pitch displacement. The simulation is made using the finest spatial discretization and the smallest time step used in Appendix A. The results for the hydrodynamical loads on each of the four propeller blades during the step change are shown in Figure G.9.

In Figure G.9 the step change is made for the blade indexed as one. When this blade is at the top blade position (180°), the blade indexed as two is towards the starboard side, the blade indexed as three is at the bottom and the blade indexed as four is towards the port side. The blade number four is therefore the next blade to go into the top position. From Figure G.9 it is seen that the blade number one is the one mostly effected by the step change followed by blade number four that is the next blade to go into the top position and the same for the following blades. This is due to the following blade being the closest one to the shedded wake from the pitching blade etc. Furthermore, it is seen that the step responses in the hydrodynamical loads are unique for each blade and it requires therefore four step response functions for each hydrodynamical load to model the build-up of the circulative effects. It is also seen that there is a large initial spike in the hydrodynamical loads due to the step change in the pitch. This is in part due to the non-circulative effects and the remeshing of the domain made at the time of the step change in the pitch. After the initial load spike the load has a transition before it settles to a steady value. For the pitching blade the transition in the x-force, y-force, x-torque and y-torque have an overshoot which does not correspond with the unsteady foil theory used in Appendix E. This may be due to some of the assumptions made for the unsteady foil theory not being appropriate for application to the analysis of the CVP propeller. The z-force is almost at the steady value just after the step and the z-torque is initially larger than the steady value. This is also not in agreement with the unsteady foil theory, which may be due to the assumption made when applying the unsteady foil theory to the CVP propeller.

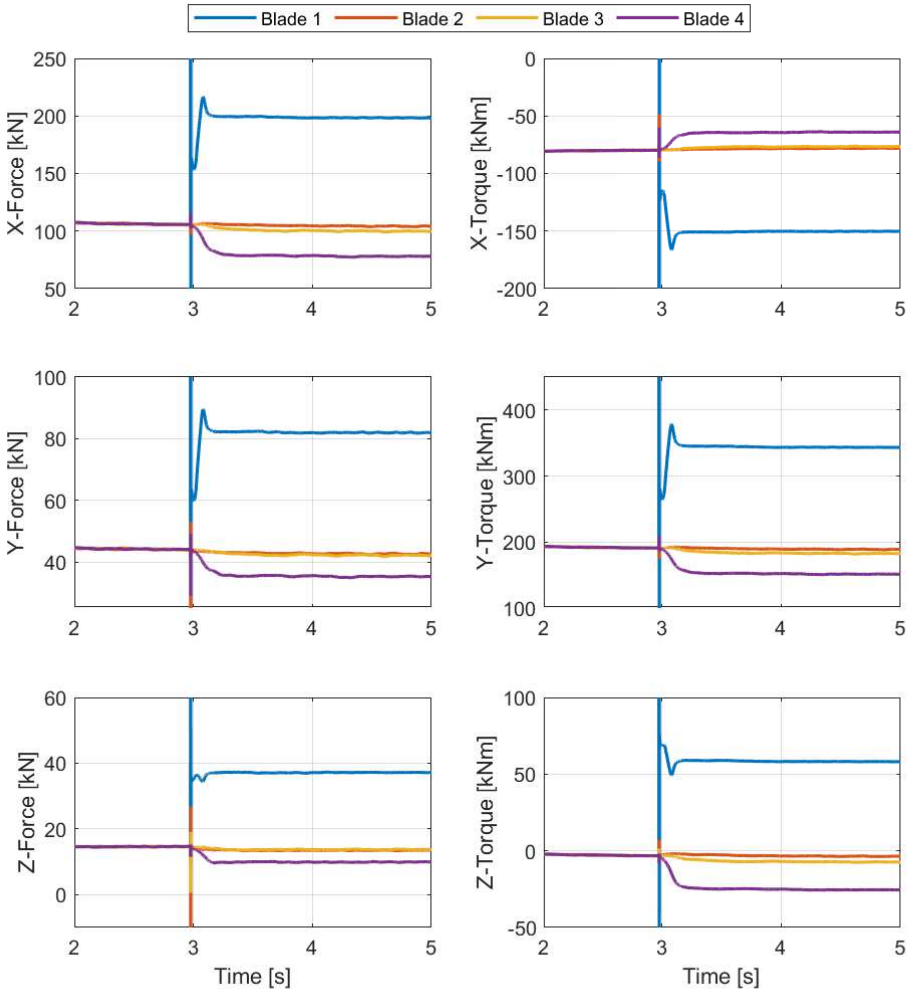

Figure G.9: Hydrodynamical loads on the propeller blades during a step change in the pitch.

To determine the step function for each hydrodynamical load, the following steps are made:

- The hydrodynamical loads are shifted such that the hydrodynamical load equals to zero just before the time step.
- The hydrodynamical loads are normalized with the steady state value at the end of the simulation such that the loads vary between zero and one.
- The hydrodynamical loads are manually fitted using a cubic spline function. This is in order to remove small oscillation in the results.

The step functions determined from the above approach for each of the hydrodynamical loads are shown in Figure G.10.

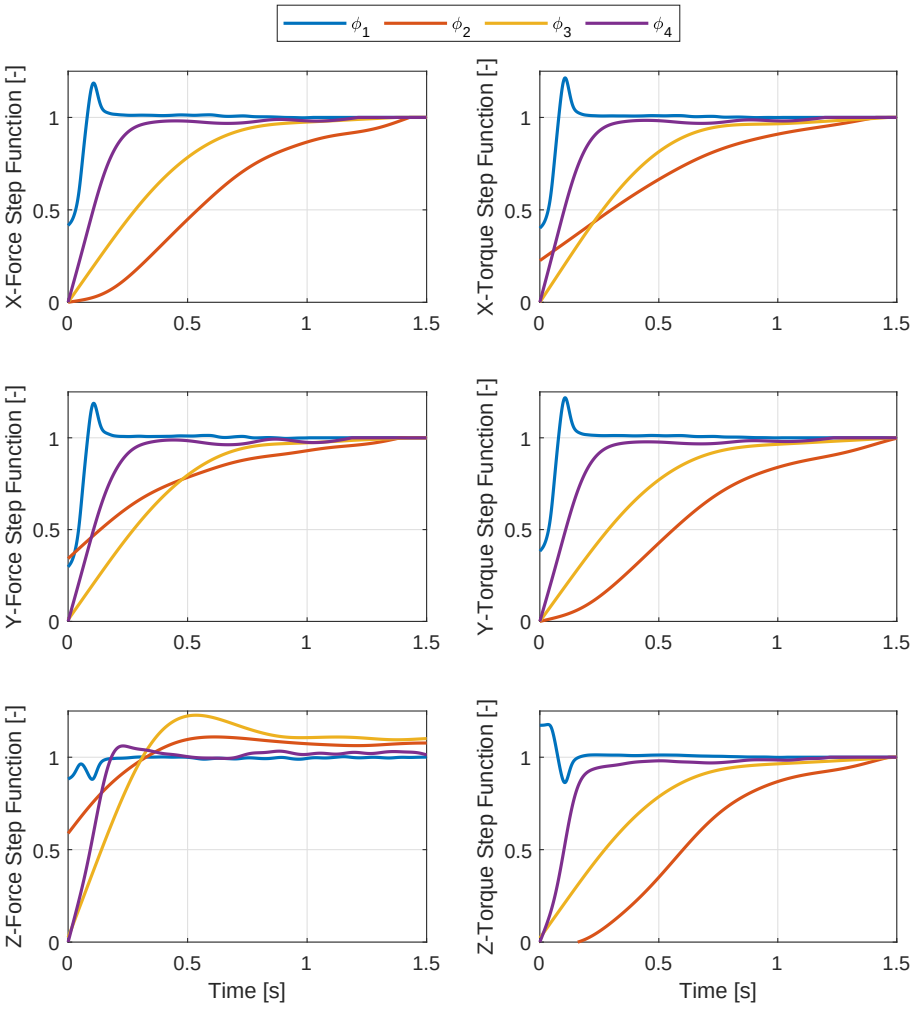

Figure G.10: Step functions for each hydrodynamical load and for each blade of the propeller.

The step function in Figure G.10 for blades 2 and 3 may have an odd shape. This is because the hydrodynamical loads for the second and third blades are relatively unchanged due to the step change in the pitch of blade number one as seen in Figure G.9. This means that these step functions are sensitive to small changes in the results.

The step functions determined in Figure G.10 are used to determine both the effective pitch displacement and the effective pitch rate. This is similar to

how Wagner's and Theodorsen's function are used in Appendix E. To evaluate the hydrodynamical load responses for arbitrary pitch displacements and pitch rates, each of the four step functions are used. For example if it is desired to determine the circulative part for the hydrodynamical x-force acting on blade 1, then the combination of step functions, pitch displacements and pitch rates used are:

$$K_{C,L_{x,i}}(\boldsymbol{\alpha_{p,e}}, \dot{\boldsymbol{\alpha}}_{\boldsymbol{p,e}}) \tag{G.12}$$

Where,

$$\boldsymbol{\alpha_{p,e}} = \begin{bmatrix} \alpha_{p,e,1} \\ \alpha_{p,e,2} \\ \alpha_{p,e,3} \\ \alpha_{p,e,4} \end{bmatrix} = \begin{bmatrix} \alpha_{p,1} * \phi_1 \\ \alpha_{p,2} * \phi_4 \\ \alpha_{p,3} * \phi_3 \\ \alpha_{p,4} * \phi_2 \end{bmatrix} \quad , \quad \dot{\boldsymbol{\alpha}}_{\boldsymbol{p,e}} = \begin{bmatrix} \dot{\alpha}_{p,e,1} \\ \dot{\alpha}_{p,e,2} \\ \dot{\alpha}_{p,e,3} \\ \dot{\alpha}_{p,e,4} \end{bmatrix} = \begin{bmatrix} \dot{\alpha}_{p,1} * \phi_1 \\ \dot{\alpha}_{p,2} * \phi_4 \\ \dot{\alpha}_{p,3} * \phi_3 \\ \dot{\alpha}_{p,4} * \phi_2 \end{bmatrix} \tag{G.13}$$

The reason for using ϕ_4 together with $\alpha_{p,2}$ and $\dot{\alpha}_{p,2}$ is because a change in the pitch displacement and pitch rate of blade 2 influences blade 1 as a change in the pitch displacement and pitch rate of blade 1 influences blade 4. The same also applies for using ϕ_2 together with $\alpha_{p,4}$ and $\dot{\alpha}_{p,4}$.

The effective pitch displacements and effective pitch rates are shown in Figure G.11 and Figure G.12, respectively, for the variable pitch trajectory. The results in Figure G.11 and Figure G.12 are used to determine the hydrodynamical loads acting on the blade indexed as 1 and the blade position is shown with respect to the blade indexed as 1.

From Figure G.11 and Figure G.12 it is seen that the effective pitch displacement and effective pitch rate for the x- and y-forces and x- and y-torques for blade have a shape similar to each other. It is also clear that there is a reduced amplitude and phase lag. For the z-force there is almost no phase shift and only a small reduction in the amplitude. The z-torque has an increased gain which corresponds to the initial value of the step function being larger than unity in Figure G.10. It is also seen that the effective pitch displacement and pitch rate of blades 2 and 4 are the ones that affect blade 1 the most but in some cases with a large phase shift and amplitude reduction. The pitch displacement and pitch rate of blade 3 do not generally have an effect on blade 1 because it is smoothed out due to the circulative build-up. The exception to this is the effective pitch displacement for the z-torque.

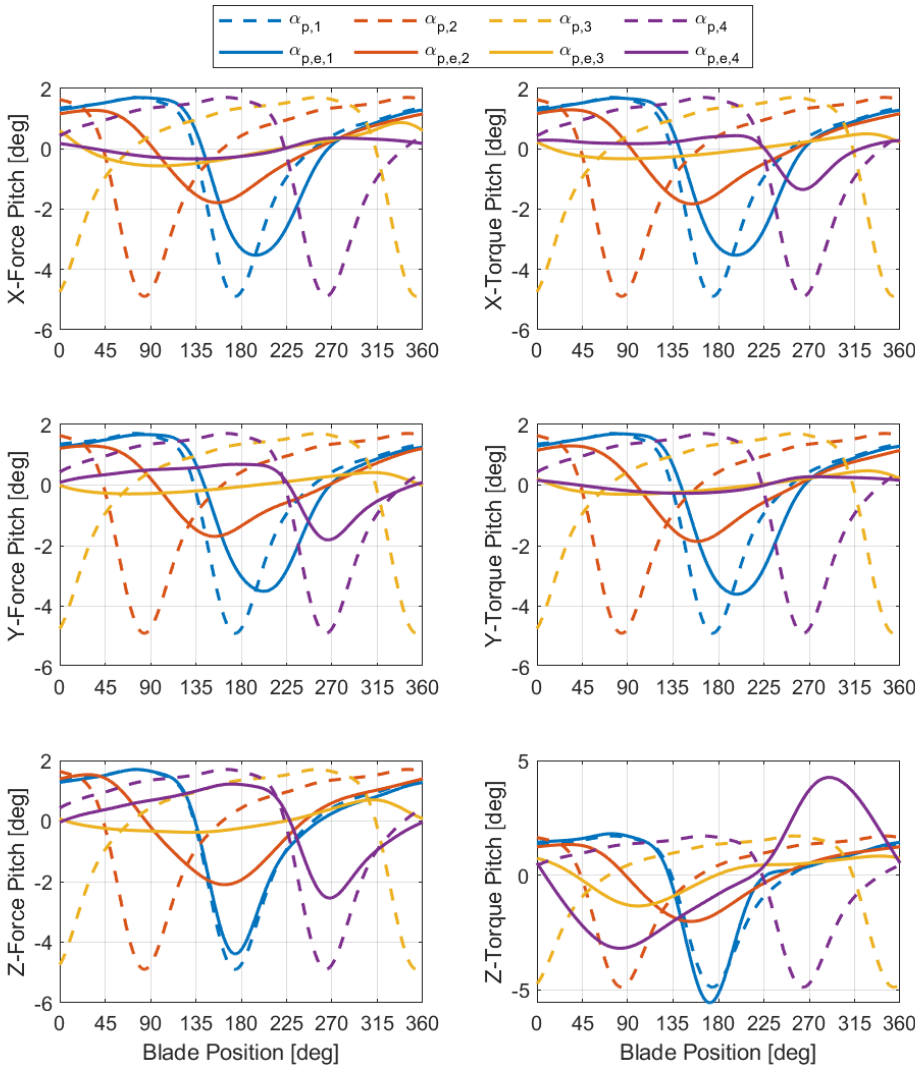

Figure G.11: The effective pitch displacements for the pitch displacements influencing the hydrodynamical loads for the blade indexed as 1 for the variable pitch trajectory.

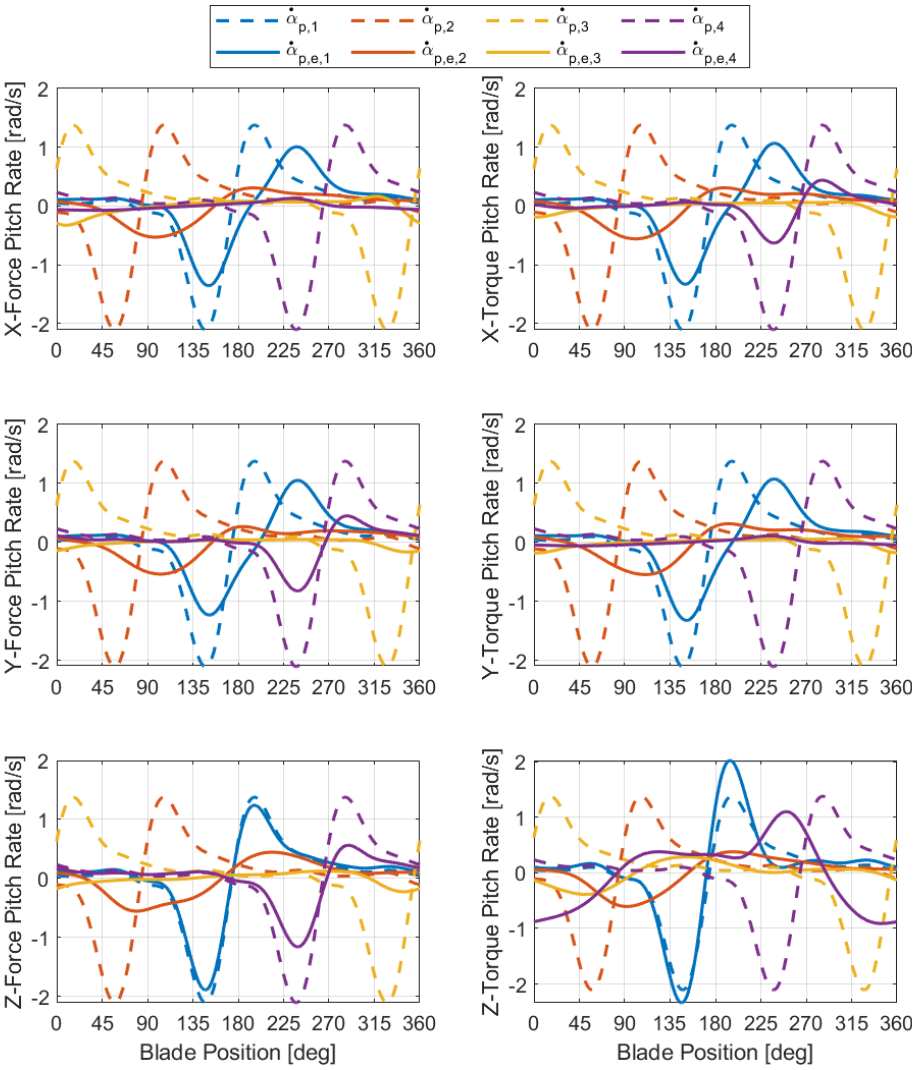

Figure G.12: The effective pitch rates for the pitch rates influencing the hydrodynamical loads for the blade with the blade indexed as 1 for the variable pitch trajectory.

G.4 Determination of the Non-Circulative Effects

The two non-circulative gains are determined through minimising the square of the error between the reduced model and the CFD simulation of the CVP propeller. The error is determined as the difference between the hydrodynamical load using the reduced model and the hydrodynamical load difference between the CVP propeller simulation with the variable pitch trajectory

and the constant pitch trajectory. Using this method gives the non-circulative gains in Table G.5 for each of the hydrodynamical loads.

Table G.5: Non-circulative gains for each hydrodynamical load.

	F_x	M_x	F_y	M_y	F_z	M_z
$K_{NC,\dot{\alpha}}\, 10^{-3}$	79.9	-53.9	33.0	153.1	1.1	4.1
$K_{NC,\ddot{\alpha}}\, 10^{-3}$	-1.1	0.5	-0.3	-1.5	-0.2	-0.7

From Table G.5 it is seen that the non-circulative gain for the pitch rate is significantly larger than the non-circulative gain for the pitch acceleration. To determine which non-circulative effect that is most dominant, it is necessary to consider the ratio between the pitch rate and acceleration. The ratio between the peak pitch acceleration and pitch rate is approximately 40. The non-circulative effect due to the pitch rate is the dominant one for the hydrodynamical loads; F_x, M_x, F_y and M_y. The non-circulative effect due to the pitch acceleration is the dominant one for the other hydrodynamical loads.

G.5 Application and Comparison of the CVP Propeller Model

To evaluate the reduced model's capability to predict the unsteady hydrodynamical loads due to the pitching motion, it is compared to the CFD simulation results of the CVP propeller in Appendix A. The comparison is made for the unsteadiness due to the pitching motion. The hydrodynamical load from the CFD simulation for the constant pitch trajectory is therefore subtracted from the hydrodynamical loads from the cosine and variable pitch trajectory. The hydrodynamical loads due to the pitching motion for the CFD simulations and the reduced model are shown in Figure G.13. All the hydrodynamical loads are shown with their uncertainty as the shaded area. The uncertainty of the reduced model is determined by linear interpolation of the uncertainty of the quasi-steady hydrodynamical loads. The uncertainty also includes two times the standard deviation of the regression model. The uncertainty is therefore only based on the circulative effects of the reduced model.

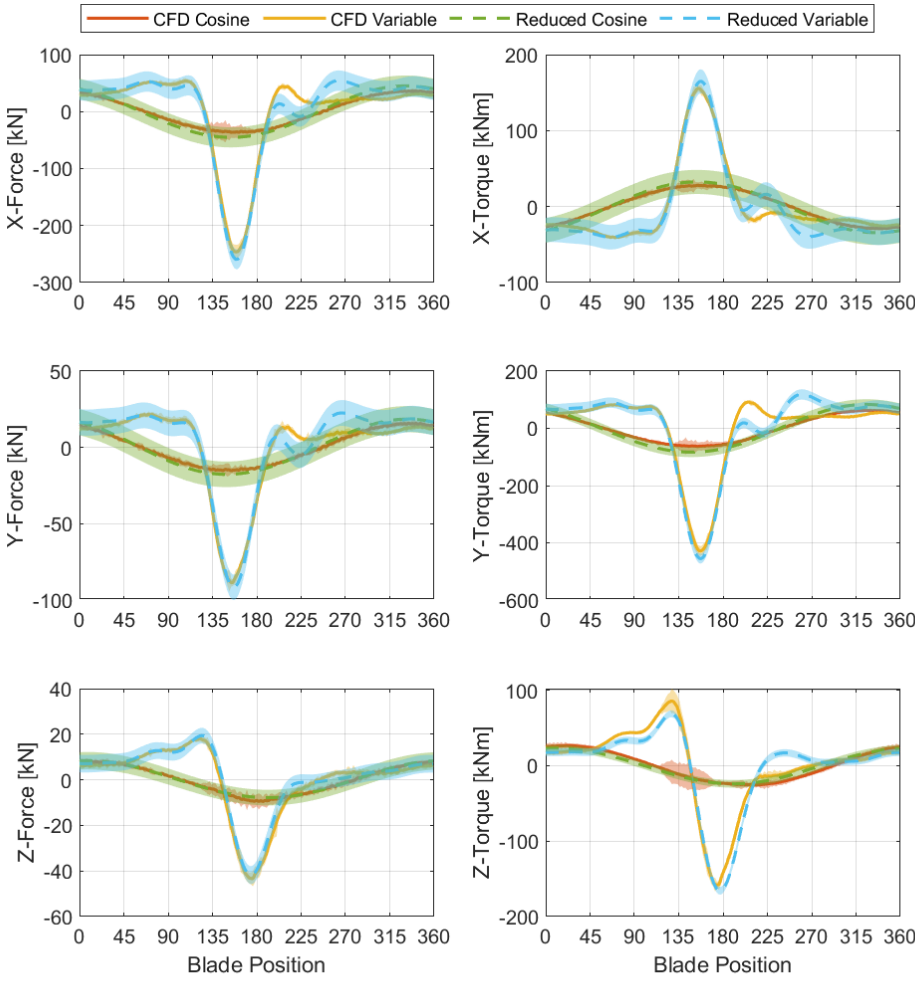

Figure G.13: Comparison of the unsteady hydrodynamical loads from the CFD simulation of the CVP propeller and the reduced model.

From Figure G.13 it is seen that hydrodynamical loads determined using the reduced model generally matches the hydrodynamical loads from the CFD simulations well. The difference between the reduced model and the CFD simulation is the most prominent about the blade position at $225° - 270°$. This may be due to how the step response is determined. The uncertainty of the reduced model is generally larger than the uncertainty for the CFD simulation of the CVP propeller.

ISSN (online): 2446-1636
ISBN (online): 978-87-7210-541-3 AALBORG UNIVERSITY PRESS